MICROCOPY RESOLUTION TEST CHART
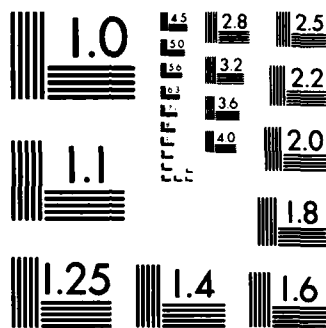
NATIONAL BUREAU OF STANDARDS 1963 A

(12)

RELIABILITY STUDIES OF CERAMIC CAPACITORS

AD-A149 126

Progress Report
for period of
July 1, 1983 to October 1, 1984

W. Huebner, H.U. Anderson and D.E. Day
University of Missouri at Rolla

DTIC
ELECTE
JAN 10 1985
B

October 1984

DTIC FILE COPY

84   11   26   106

TABLE OF CONTENTS

-iii-

INTRODUCTION

1.1 Research Objectives

The major objective of our research program is to determine the mechanisms which induce intrinsic and extrinsic failure of ceramic capacitors. Towards this end we are making extensive electrical measurements and microstructural evaluations on both commercial and laboratory-prepared specimens. The measurements being performed include:

(1) Current as a function of time, temperature, and applied field to evaluate both low and high voltage degradation.

(2) Destructive microstructural evaluations.

(3) Thermally stimulated polarization / depolarization current (TSPC/DC) measurements.

This combination of experiments has provided us with a great deal of information concerning degradation phenomena. The report is divided into three sections:

1) LOW VOLTAGE DEGRADATION

2) HIGH VOLTAGE DEGRADATION

3) TSPC/DC MEASUREMENTS

1.2 Cooperative Programs

In an effort to expand our capabilities and increase our overall knowledge concerning degradation we have established cooperative research programs with Charles Stark Draper Labs, the Materials Research Lab at Penn State University, and Virginia

Polytechnic. These programs are described below.

1.2.1 UMR / Draper Labs

We began the cooperative research program with Draper Labs in June 1983. Draper Labs has obtained several thousand leaded and chip capacitors from commercial manufacturers of which UMR has received half. Our units consist mainly of encapsulated, leaded capacitors while Draper has retained the identical unencapsulated units. The compositions are all NPO, X7R, or Z5U, and cover a wide range of capacitances. A complete listing of the commercial capacitors included in our study is included in the low-voltage degradation portion of this report.

This joint program has allowed us to not only obtain a broader data base from which to work, but to also make a direct comparison of our results with an independent program which is testing nearly identical units from the same manufacturers. Refer to the low-voltage degradation section for the results of measurements carried out on these specimens. This joint effort is an ongoing one, as both Draper Labs and UMR are continuing to collect and compare data.

1.2.2 UMR / Penn State University

Over the past two years UMR has been involved with the Dielectric Center at the Materials Research Lab at Penn State University. The purpose of this interaction has mainly been to coordinate the graduate programs of Wayne Huebner (UMR) and Dean Anderson (PSU) in order to combine the strengths of both

universities as far as experimental capabilities are concerned. The following has been accomplished:

1) UMR has prepared several kilograms of $BaTiO_3$ with variable Ba:Ti ratio for joint use, which should allow for meaningful comparisons of results. UMR is carrying out its work on disk specimens, while PSU will hopefully carry out their measurements on multilayer configuration specimens. A large problem has been encountered with the fabrication of MLC's from the powder prepared by the organnometallic process (see section 3.2.1). Due to the extremely small grain size, agglomeration problems are extensive, which results in porous, nonuniform sintered structures. Several milling techniques and binder/dispersant combinations have been tried, but have not alleviated the problem. However, it appears that a higher calcination temperature will coarsen the grains which minimizes the agglomeration problems. To date, all of the measurements carried out on these compositions have been made using pressed, disk specimens, but it appears that multilayer structures are achievable.

2) UMR and PSU are both studying the high-voltage degradation of $BaTiO_3$ as a function of Ba:Ti ratio. In order to optimize output, the large number of variables involved has been divided, with a deliberate overlap to check for consistency. Results from this joint effort are included in the high-voltage degradation section (see section 3.0).

3)   During the summer of 1984 UMR personell visited PSU in order to make $Q_{i,j}$ measurements on TSPC/DC specimens. These values are needed in order to apply Devonshire theory to the interpretation of the TSPC/DC results. Another trip will be scheduled early in 1985 to continue these measurements and to make Saywer Tower measurements.

4)   UMR and PSU have met three to four times a year in order to discuss future plans and the results of the program.

Results from this joint program are being presented at the Fall Meeting of the Electronics Division of the American Ceramic Society held in San Francisco, California, 1984.

1.2.3 UMR / Virginia Polytechnic

During the summer of 1984 we embarked on a joint program with Virginia Polytechnic. In this program we are mainly exchanging specimens: a) UMR is sending Virginia Polytechnic $BaTiO_3$ specimens with variable composition, density and grain size to be used to make carrier concentration, mobility, thermoelectric power, and I-V measurements. b) Virginia Polytechnic is sending UMR commercial capacitors which exhibit non-ohmic I-V behavior for current injection studies.

To date, this interaction is only partially underway as UMR is still in the process of preparing the needed specimens for shipment. Hopefully this will be completed by the end of October.

1.3 Recent Results and Achievements

Our research program has progressed to the point that a number of the initial goals of the program have been achieved. The most significant accomplishments are listed below:

Low Voltage Degradation

1) 1400 encapsulated, and 600 unencapsulated capacitors were subjected to the methanol test. None of these 2000 capacitors tested as received from the manufacturer failed the methanol test. This implies the either the encapsulant integrity is excellent, or the capacitors contained no physical flaws connecting electrodes of opposite polarity.

2) None of the 1100 capacitors tested using the 85 $^{\circ}$C / 85% RH / 1.5 VDC life test developed the "classic" low voltage short. 3.6% of the capacitors decreased in resistance by two orders of magnitude or greater during life testing. It was evident that gradual degradation of the dielectric was occurring. The low resistance could not be "cleared" by application of a high voltage, or by heating at 125 $^{\circ}$C in a dry atmosphere (except for 1 NPO capacitor).

3) The methanol test was not able to detect those capacitors which failed the 85/85 test; i.e. the failure mode did not seem to be a result of structural imperfections.

4) MLC's exhibit non-ohmic I-V behavior, which may be related to their high voltage degradation. The current flowing through these capacitors may be purely a function of the current injection mode, not the dielectric.

High Voltage Degradation

Compositional Effects

Ti-rich BaTiO$_3$:

1) Increasing the density, thereby decreasing the porosity results in a greater tendency to degrade. This could be indicative of grain boundary diffusion, porosity blocking the movement of $V_O^{\cdot\cdot}$, or a change from intergranular to intragranular porosity resulting in resistivity inhomogeneities due to altered field-splitting.

2) For those samples which degrade, increasing the field substantially reduces the time over which the "rapid degradation region" extends, and increases the current non-ohmically, but does not change the degradation rate in the region of gradual current increase (section 3.4).

3) Increasing the amount of excess Ti decreased the current levels and the tendency to degrade. All compositions with excess Ti exhibited higher current levels and enhanced degradation compared to the stoichiometric composition.

Stoichiometric BaTiO$_3$

1) The stoichiometric composition exhibited the lowest current levels at all fields and temperatures. This would lead one to suspect that the second phases present from the excess Ba and Ti are contributing to the degradation.

Ba-rich BaTiO$_3$

1) At fields 2000 V/cm the excess Ba compositions all exhibited current levels 1-2 orders of magnitude than the excess Ti compositions. This would lead one to suspect the excess Ba second phase increases the mobility of the charge carrier responsible for degradation.

2) Increasing the amount of excess Ba results in overall lower current levels, and improved degradation resistance. All compositions with excess Ba exhibited higher current levels and enhanced degradation compared to the stoichiometric composition.

3) The form of the degradation behavior between the excess Ti and Ba compositions is different. When degradation occurs in the excess Ti compositions, the current rises rapidly (RDR region), and then tapers off to a linear region. The excess Ba compositions which degrade also exhibit two regions of degradation, but the initial rise in the current is never as rapid. This leads one to suspect the mobility of the charge carrier causing degradation changes due to the different grain boundary phases.

Measurement Effects

1) Disc specimens measured for degradation tendicies need to be reequilibrated between current-time runs in order to obtain reproducible results, particularily for those units which degrade. Equilibration of specimens at 1000 $^{\circ}$C for 8 hours

-7-

was found necessary to bring specimens back to a non-degraded state. If reequilibration was not carried out, the specimens exhibited non-reproducible results; increasing the field sometimes resulted in lower current levels, or the current started off at the same level it left off with the previous run.

2) The current-voltage behavior exhibited by the specimens measured for degradation ranged from ohmic to voltage dependencies greater than that predicted by space-charge-limited current. However, the validity of applying non-ohmic current injection analysis to specimens which exhibit degradation is questionable; the high current levels may simply be a result of degradation, not of a non-ohmic current injection mechanism. Specimens which exhibit ohmic behavior are the most releiable.

TSPC/DC Measurements

1) TSPC/DC measurements are capable of determining:
   - phase transformation temperatures
   - formulations of commercial capacitors (i.e. NPO, BX, Z5U) and its useful temperature of constant capacitance
   - the order of the tetragonal-cubic phase transformation in $BaTiO_3$; i.e. first or second order
   - whether or not $BaTiO_3$ is nonstoichiometric; judged through the grain size and its effect on the presence of current peaks
   - the effects of donors, acceptors, shifters, and depressors

-8-

on the ferroelectric behavior, resistivity, and
energy of the conduction process

- the low temperature resistivity and activation
any material

2)   TSPC/DC measurements cannot predict the abil
capacitor to pass life testing. It can distingui
"good" and "bad" capacitors following life testin
TSPC/DC measurements are useful in terms of chan
the failure mechanism.

Degrees, Publications, and Presentations

Degrees:

P.D. Martin, "Thermally Stimulated Current Studies
Titanate Capacitors", M.S. December 1984

Publications

1)   W. Huebner, J.D. Keck, and H.U. Anderson, '
Degradation of High Purity $BaTiO_3$", 4th Capacitor ar
Technology Symposium, March 1984

2)   H.U. Anderson and D.E. Day, "Reliability Studies
Capacitors", Progress Report for the period of July
June 30, 1983, ONR Contract No. N00014-82-K-0294

3)   W. Huebner, H.U. Anderson, and D.E. Day, "Reliabil.
of Ceramic Capacitors", Progress Report for the peri
1, 1983 to October 1, 1984, ONR Contact No. N00014-(

Presentations

1) W. Huebner and H.U. Anderson, "Review of Current Injection Mechanisms in Solid Dielectrics", Electronics Division Meeting of the American Ceramic Society, Sept. 11-14, 1983

2) P.D. Martin, et al, "Thermally Stimulated Polarization and Depolarization Current Measurements for Ceramic Capacitors", ibid.

3) W. Huebner, et al, "Electrical Degradation of Ceramic Dielectrics", 36th Pacific Coast Regional Meeting of the American Ceramic Society, October 3-5, 1983

4) W. Huebner, et al, "Electrical Degradation of High Purity $BaTiO_3$", 4th Annual Capacitor and Resistor Technology Symposium 1984, March 7-8, 1984

5) W. Huebner and H.U. Anderson, " Electrical Degradation Behavior of $BaTiO_3$", 86th Annual Meeting of the American Ceramic Society, April 29 - May 3, 1984

6) P.D. Martin, et al, "Thermally Stimulated Current Aspects of Barium Titanate and Ceramic Capacitors", ibid

7) H.U Anderson, "Degradation of Ceramic Capacitors", Seminar at Sandia Corp., October 5, 1984

8) W. Huebner and D.A. Anderson, "Electrical Degradation Studies of High Purity $BaTiO_3$", Pacific Coast Regional Meeting of the American Ceramic Society, October 29-31, 1984

9)   H.U Anderson and W. Huebner, "Thermally Stimulated Current Measurements on Barium Titanate", 2nd US:Japan, ONR-sponsored Seminar on Dielectrics and Piezoelectrics, Williamsburg, VA, Nov. 4-7, 1984

2.0 Low Voltage Degradation

Introduction

In recent years a problem has been identified concerning the insulation resistance failure of ceramic capacitors biased well below their rated voltage; i.e. "low voltage" failure. As a part of our degradation studies we wished to study low voltage phenomena in order to: a) confirm or reject theories put forth to explain low voltage degradation, and b) develop a testing procedure capable of determining those capacitors likely to fail before they are put into use.

Before presenting the results of our studies on low voltage degradation, a brief literature review is included.

2.1 Literature Review

Low voltage failures of MLC's have been identified as a problem only in recent years[1,2]. As a result, a tremendous effort has focused on determining the cause of low voltage failures, and finding a testing procedure which can effectively screen out those capacitors prone to low voltage failure[1-18].

Failure Mechanisms

Several models have been proposed to explain low voltage degradation in ceramic capacitors, most of which involve the

water-induced electromigration of the electrode materials along structural defects[3-8]. This process involves[7]:

1) Dissolution of the anode material.

2) Transport of the metal towards the cathode in the form of a simple ion, complex ion, or a colloidal ion (oxide or hydroxide).

3) Deposition of a conducting dendrite by electroconduction or precipitation.

The resulting dendrites essentially create a "short" within the dielectric, rendering them useless as a capacitor. This type of low voltage failure can be "cleared", i.e. the capacitor returned to a high resistivity state, with the application of a high voltage which vaporizes the dendrite. Current-time studies exhibit switching between high and low resistivity states, as the dendrite grows, shorts, partially vaporizes, and then grows again.

Other studies[9-12] have found that the failure path is not necessarily a metallic-dendrite, but instead a degraded portion of the dielectric. The reason for the degraded dielectric was not clear, but may have been a result of absorption of water into the dielectric as protons or hydroxyl ions, or possibly the migration of $V_o^{\cdot\cdot}$ (see section 3.1.1). These failures could not be cleared by the application of a high voltage, nor were they low resistance failures (i.e. failure defined by resistance 10 megohms). This gradual compared to abrupt decrease of the resistance has been reported elsewhere[13]. In this study it was found that failed specimens recovered if they were stored in a dry environment at room temperature, or if they were baked at 125

$^{\circ}$C. All specimens which failed had a crack on the chip surface. This is a strong indication the low resistance was due to the presence of water in structural imperfections. The electrode material was not specified, but no evidence of electromigration was found.

Screening Methods

With the knowledge that low voltage failures seemed to be related to the presence of water and structural defects, a large number of screening methods have been tested in order to assess their ability to eliminate capacitors prone to failure.

Methods to determine whether structural imperfections are present include ultrasonic scanning[14], acoustic emission[15-17], and methanol testing[7,8]. These have been reported capable of determining if delaminations or cracks are present in the chip capacitors , the latter pertaining to cracks which extend to the surface of the dielectric. Sweep voltammetry has also been utilized[10,11], but was found incapable of detecting units prone for failure.

The other method of screening parts involves the use of life testing, such as the MIL-C-123; the 85°C/85% RH, 1.5 VDC test[5-13]. This test has been used extensively, with mixed results. It appears capable to detect lots with failure-prone units, but lacks definition in terms of test time. Capacitors subjected to the 85/85 test have been found to exhibit steady or increasing failure rates up to 500 hours, instead of decreasing until no parts failed[11].

2.2 Capacitors Studied

The majority of the capacitors utilized in this study were obtained from the Charles Stark Draper Labs as part of a joint effort to study low voltage degradation (see section 1.2.1). Draper Labs has obtained several thousand leaded and chip capacitors from commercial manufacturers, of which UMR has received half. Our units consist mainly of encapsulated, leaded capacitors, while Draper has retained the identical, unencapsulated units. A complete listing of the capacitors being utilized in our study is contained in Table 2.2a-b. The compositions are all NPO, BX, or Z5U, and cover a wide range of capacitances. Some of these capacitor lots are "suspect", in terms of reliability and structural integrity.

2.3 TESTING / Results

Based upon past results obtained concerning low voltage degradation, the following tests were chosen to be included in our study:

1) MIL-C-123:   85°C / 85% RH 1.5 VDC life test

2) Methanol Testing

3) Current-Voltage measurements

4) Thermally-stimulated polarization / depolarization current measurements

The results obtained from these tests will be discussed separately. First a description of the initial measurements and handling procedure is included.

-14-

LOT #	TYPE	# Units	Size	Cap.	Encap	Comments
545976678909	X7R	100	CACO3	22000 pF	Yes	–
545976678909	X7R	100	CACO3	22000 pF	Yes	Burned-In
CGB 103 KDX	BX	100	–	10 nF	Yes	–
735300	COG	100	CACO4	2200 pF	Yes	–
735300	COG	100	COG	2200 pF	Yes	Burned-In
E424A	BX	100	CGB103	.01 uF	Yes	–
CK14BR104K	BX	157	CK14	100 nF	Yes	–
MA105A301K	NPO	105	MA10	270 pF	Yes	–
MA1015C153J	BX	100	MA10	15 nF	Yes	–
MA105A270K	NPO	108	MA10	270 pF	Yes	–
MA201C682K	BX	100	MA20	100 nF	Yes	–
C124B103	BX	100	K1X5CA	10 nF	Yes	–
8304ZR	NPO	100	K1G5CA	1000 pF	Yes	–
C124C102	NPO	100	J1G5CA	1000 pF	Yes	–
C124B103	BX	42	K5X5EA	10 nF	Yes	–
821J4	NPO	100	B-1805	220 pF	No	–
7943A6	BX	100	B-1805	40 nF	No	–
8137D2	NPO	100	F-2225	20 nF	No	–
8134XE	BX	100	F-2225	450 nF	No	–
8103B8	NPO	100	E-1825	10 nF	No	–
7907JF	BX	100	D-1813	15 nF	No	–

TABLE 2.2a : Commercial Capacitors utilized in the low-voltage degradation study.

Lot #	Type	# Units	Size	Cap.	Encap	Comments
8132A7	NPO	100	A-0805	120 pF	No	-
8201C8	BX	100	D-1813	5000 pF	No	-
8135C5	BX	30	B-1210	100 nF	No	-
CKR11BX680M	BX	330	CKR11	70 pF	Yes	-
CKR12BX103K	BX	256	CKR12	10 nF	Yes	-
CKR11BX105L	BX	160	CKR11	10 nF	Yes	-

TABLE 2.2b :   Commercial capacitors utilized in the low-voltage degradation study.

2.3.1 Initial Measurements

Immediately after receiving, filing, and storing the commercial capacitors, each unit was subjected to initial measurements of capacitance, dissipation factor, and insulation resistance.   Refer to figure 2.3.1 for a flow chart of the overall handling and measurement procedure.   Capacitance and dissipation factor at 1 kHZ were measured at 25°C using a General Radio 1689 LRC meter.   Insulation Resistance was measured at 10 VDC at 25°C using an Hewlett Packard 4140B pA Meter / DC Voltage Source and the shielded HP16055A test fixture.   In order to correlate data with the methanol test results, ten volts was chosen as the applied voltage.   Both meters were operated in conjunction with a Hewlett Packard 85 computer for data storage. Of the 3088 capacitors collected for study , all were measured for initial capacitance and dissipation factor, and 2900 units were measured for insulation resistance (IR) at 10 VDC.

None of the capacitors measured were out of specifications in terms of capacitance, dissipation factor, or insulation resistance.

After life testing the capacitors were remeasured for capacitance, dissipation factor, and IR in order to check for any changes in these parameters.
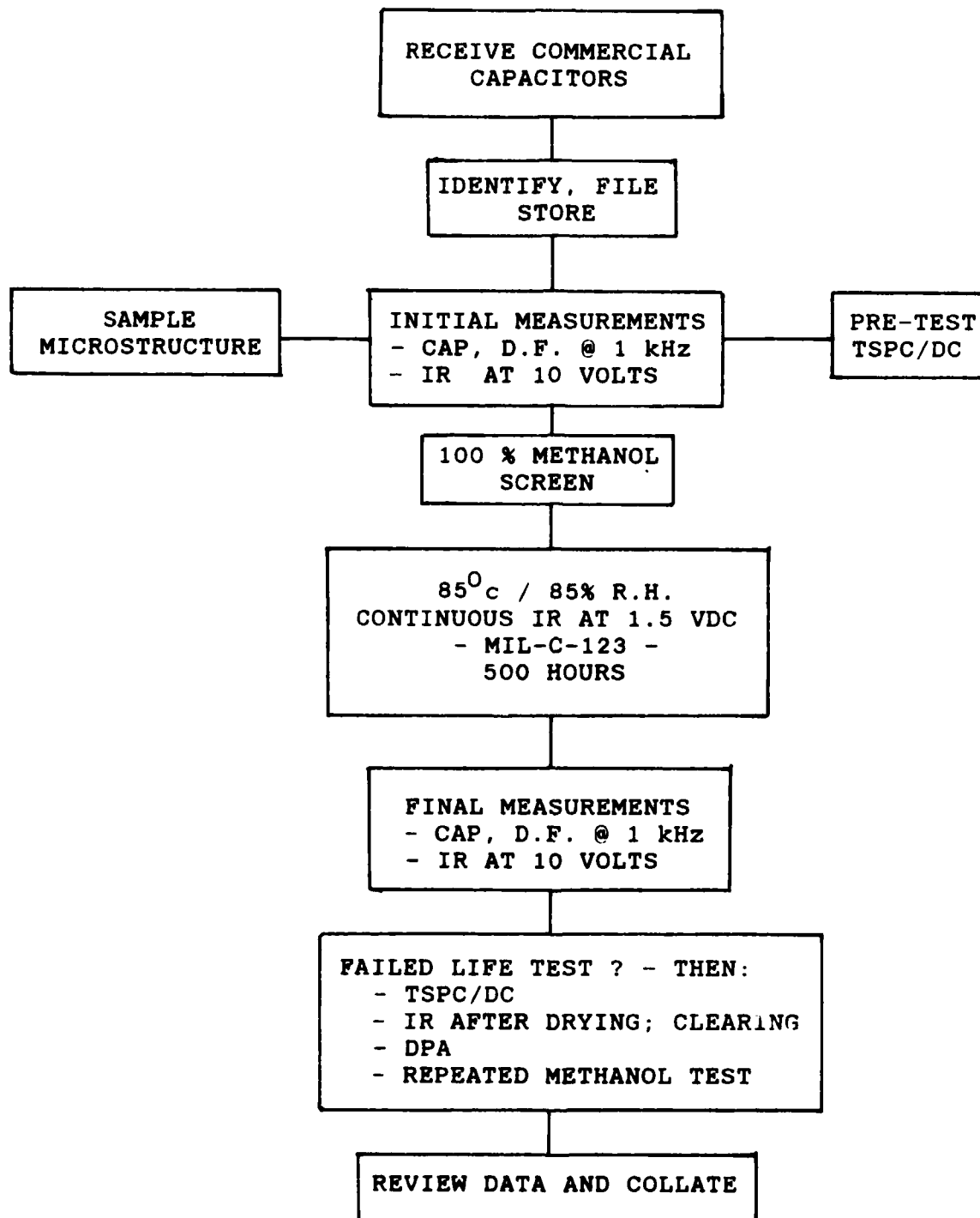
Figure 2.3.1: General flow chart of the handling procedure and measurement process for the low voltage degradation study.

2.3.2 Methanol Testing

Due to the success imparted to the methanol test as an effective screen for low voltage failures[7,8], we chose to subject all of the capacitors being life-tested with the methanol test. In this manner we could determine its effectiveness as a screening method. This test consists of the following steps[7]:

1) 10 VDC is applied to the capacitor and the current (I_1) is measured after 10 seconds.

2) The capacitor is heated to 85 $^{\circ}$C and then immersed in methanol for a minimum time of 15 minutes to allow full penetration into any cracks or open porosity present. We used an ultrasonic cleaner filled with methanol to aid in the penetration.

3) The capacitor is removed from the methanol, dried on a tissue, and blow-dried with air at room temperature to remove all traces of methanol on the surface.

4) Step #1 is repeated immediately after drying and the current (I_2) is measured.

Those capacitors which fail the methanol test have an I_2 several orders of magnitude greater than I_1. In our study, I_1 was determined along with the initial measurements. All current measurements were computer-controlled, as determination of the still rapidly decreasing current is difficult to ascertain accurately manually. Some problems were encountered with instability of the current, i.e. positive/negative fluctuations, despite the use of the shielded HP16055A test fixture in conjunction with the HP4140B pA Meter/DC Voltage Source. In the past, we have used this measurement system to measure stable currents down to 10^{-14} amps. Burton[19] has encountered similiar problems in acquiring stable currents in MLC's at room

-19-

temperature. While this problem should not effect the outcome of the methanol test, it does pose problems when determining the IR.

Results

1400 encapsulated and 600 unencapsulated capacitors were subjected to the methanol test. <u>None of these 2000 capacitors tested as received from the manufacturer failed the methanol test.</u> This was an unexpected result, as some of the capacitors when received were labelled suspect in terms of structural integrity. This implies two things:

1) The encapsulant integrity is excellent.

2) The unencapsulated capacitors contained no physical flaws connecting electrodes of opposite polarity.

After obtaining this result we were very interested in seeing if any low voltage failures would occur at all.

2.3.3 85 ^{O}C / 85% RH / 1.5 VDC Life Testing

As stated previously, the 85 ^{O}C / 85% RH / 1.5 VDC (85/85) life test (MIL-C-123) has proven the most useful in determining the low voltage failure tendencies of ceramic capacitors, with certain limitations. One of the purposes of our program was to determine its effectiveness in identifying low voltage failures in conjunction with the methanol and TSPC/DC testing.

The first year of our program was spent building and refining a computer-controlled capacitor life testing system (Figure 2.3.3a). This system is capable of continuously monitoring the
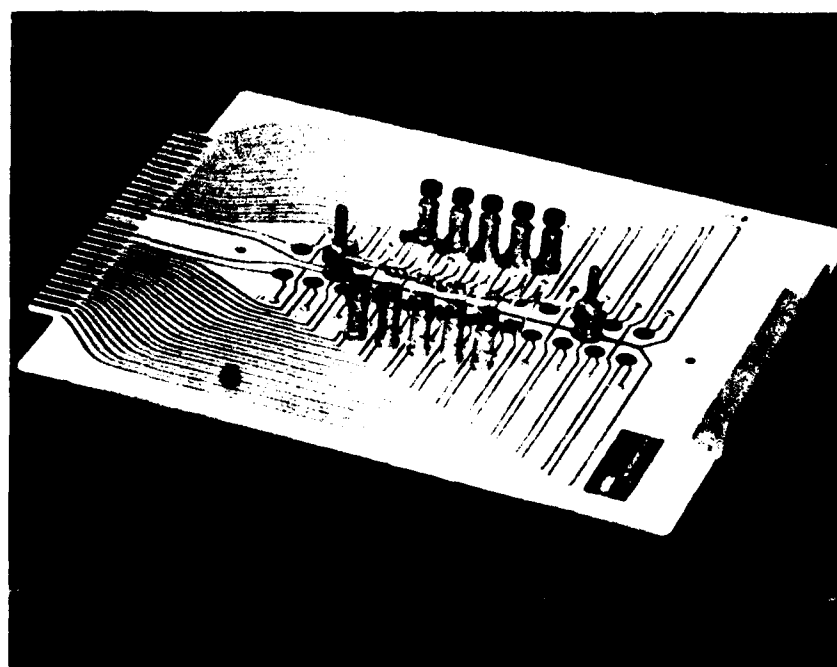
Figure 2.3.3a:

Capacitor Life Testing
System

Figure 2.3.3b: Circuit board used for mounting capacitors to be
tested in the capacitor life testing system.

leakage current of 90 capacitors housed in nine separate furnaces, each of which allows precise variation of the temperature, atmosphere, or voltage. The heart of the system is a Hewlett Packard (HP) 3054 DL Data Logger, which consists of an HP 85 computer and a HP 3497A Data Acquisition Unit. The HP 3054 DL is essentially a 100 channel auto-ranging voltmeter with temperature measurement capabilities. Capacitors are mounted on a circuit board (Figure 2.3.3b) which plugs into a connector sealed into the furnace faceplate. Each channel of the voltmeter is connected to a capacitor on the board by the circuit shown in Figure 2.3.3c.
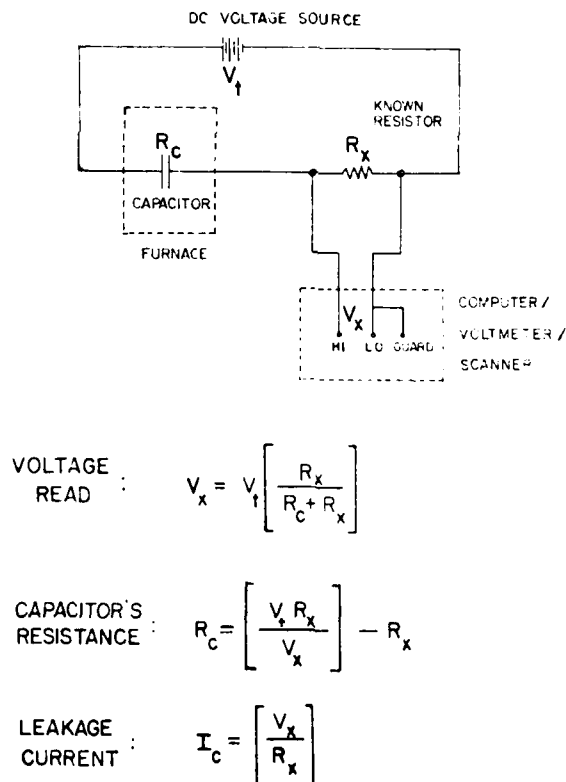

VOLTAGE READ :

$$V_x = V_t \left[\frac{R_x}{R_c + R_x} \right]$$

CAPACITOR'S RESISTANCE :

$$R_c = \left[\frac{V_t R_x}{V_x} \right] - R_x$$

LEAKAGE CURRENT :

$$I_c = \left[\frac{V_x}{R_x} \right]$$

Figure 2.3.3c: Schematic circuit diagram for the low voltage capacitor measurement system.

Results

Of the 3088 capacitors which were being studi

voltage degradation 1100 have been life tested usin

screen. The results of these measurements can be su

follows:

1) <u>None</u> of the 1100 capacitors tested has exh
   "classic" low voltage short due to a dendritic (

2) 40 of the 1100 capacitors tested (3.6%
   resistance by 2 orders of magnitude.

   - These did so in a gradual fashion; no abrup
     resistance was observed during continuous

   - 21 of these were unencapsulated.

   - 12 of these were within the same lot.

   - Only 1 had a resistance less than 10^9
     resistance was 10^6 ohms, a change of fiv
     magnitude. The other 39 had resistances in
     range, representing a change of 2-3
     magnitude.

   - Application of a high field does not
     resistance.

   - Heating the capacitors at 125 $^\circ$C in a dry
     did not change the resistance for 39/40 cap
     lone case an NPO capacitor.

   - These capacitors did not fail the methanol
     life testing.

These 40 capacitors were microstructurally examin

to attempt to determine the cause of these non-cl

resistances. No areas could be found which exhibit

of any sort of degradation, albeit a degraded

dielectric due to anything other than a crack, ext

porosity, or delaminations will be nearly impossible to identify.

From every lot of capacitors we received, an untested capacitor was analyzed microstructurally. Even after repeated polishings none of the capacitors have been found to exhibit any type of gross physical defect in the form of a crack, a delamination, a macrovoid, or extensive, connected, open porosity. The physical integrity of these capacitors is excellent, including the state of the encapsulant as far as bonding and homogeneity are concerned. After seeing the microstructures, the results we have obtained studying low voltage degradation are not too surprising.

Based upon these measurements the following conclusions can be made:

1) The failure mechanism for those capacitors which failed in our study was not the dendritic growth of an electrode material.

2) Based upon the fact that a) heating in a dry atmosphere did not clear the low resistances (except for 1 NPO capaci- tor), b) the encapsulant integrity is excellent, and c) methanol testing did not detect any structural defects both before and after life testing, water does not appear to be the cause of the observed degradation.

3) The methanol test was not able to detect those capacitors which failed the 85/85 test. This result is not too surprising, as the mode of failure did not appear to be due to any sort of cracking or open porosity.

2.3.4 Current-Voltage Studies

Burton[20] has shown that both degraded and new MLC's exhibit non-ohmic I-V behavior, which leads one to suspect that some of the problems associated with degradation may well be related to the current injection mode (see section 3.1 for a review of

current injection mechanisms). Since I-V behavior was being measured for the laboratory-prepared specimens, we recently decided to expand the specimens measured to include MLC's from our low voltage testing program.

Initially we attempted to duplicate Burton's results carried out at room temperature, but found the current levels were too low (10^{-13} amps), and hence the noise level too high to make any accurate I-V determinations. To increase the current substantially, we raised the measurement temperature to 150 $^{\circ}$C and then made I-time (I-t) measurements, from which I-V behavior can be obtained. Figures 2.3.4a-f are representative I-t, I-V curves we have obtained measuring just a few of the MLC's. Refer to section 3.1 for full explanations of non-ohmic current injection modes and the I-V behavior associated with each.

Three types of behavior can be seen. Figures 2.3.4a-b are of an NPO capacitor which reached stable current levels during the I-t measurement. The I-V curve exhibits a distinct transition in slope from 1.2 to 2.13. We suspect this is due to a transition to space-charge-limited current injection. Note the time independence of the high slope region, indicative of the absence of degradation.

Figures 2.3.4c-d are of a BX capacitor which also attains steady-state current levels during the I-t tests. Note the I-V behavior is linear, with slope 1.6, also non-ohmic. This comes close to Burton's value of 1.5, which he has attributed to SCLC injection from a hemispherical electrode, i.e. the electrode protuberances into dielectric layers.
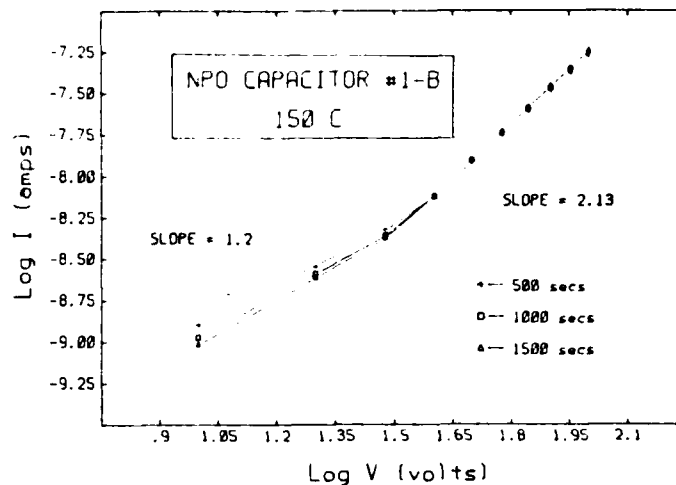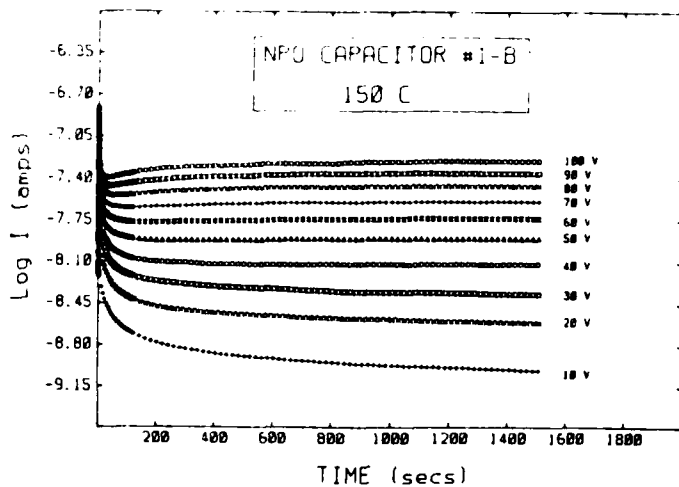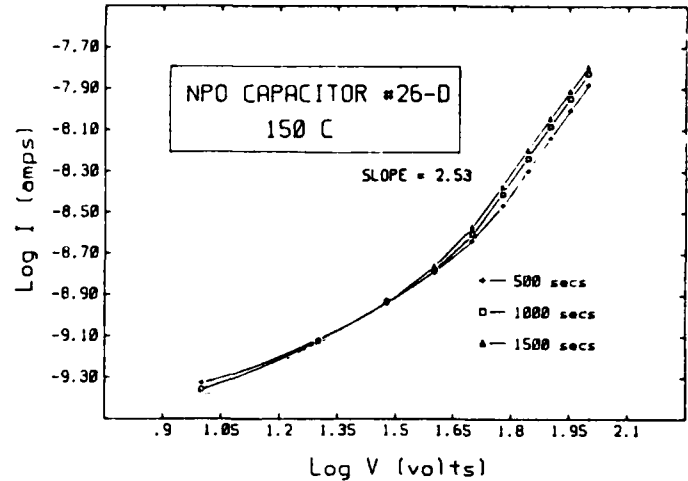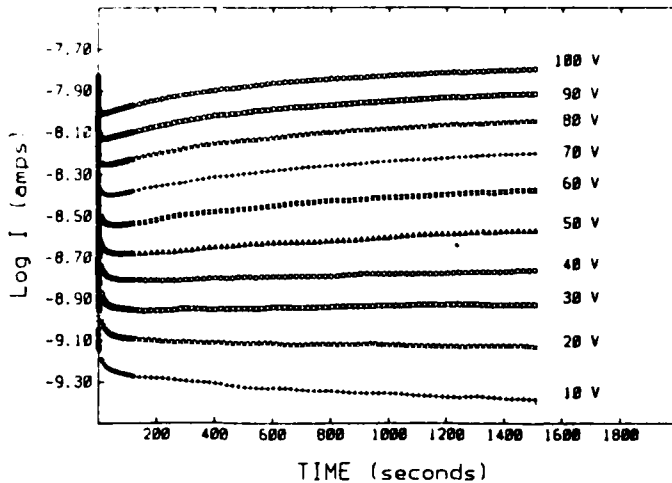
Figures 2.3.4a-b: Current-time, and current-voltage results for NPO capacitor #1-B.
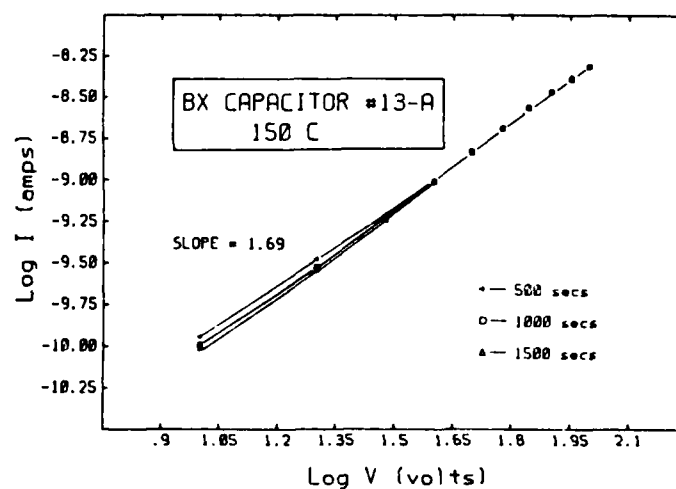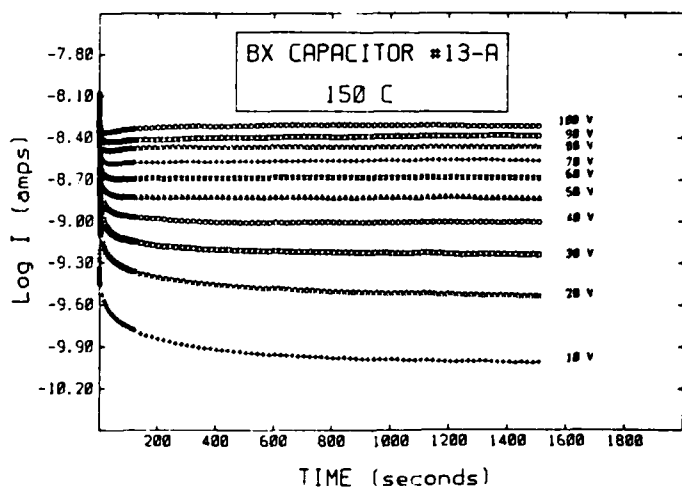
Figures 2.3.4c-d: Current-time, current-voltage results for BX capacitor #13-A.

NPO CAPACITOR #26-D @ 150 C

Figures 2.3.4e-f: Current-time, current-voltage results for NPO capacitor #26-D.

Figures 2.3.4e-f are of an NPO capacitor which does not attain steady-state current values, but exhibits degradation for voltages 40. A distinct transition from ohmic to non-ohmic behavior is also seen at 40 V, the voltage at which degradation is beginning to occur. Note the magnitude of the slope in the non-ohmic region does not change, even though degradation is occurring.

These results represent preliminary measurements we have carried out on a few capacitors, but already a several conclusions can be made:

1) MLC's exhibit non-ohmic I-V behavior, which may or may not be related to degradation. Note the applied voltages are well within the operating range of the MLC's.

2) It's important when gathering data for I-V analysis that the nature of the I-t curves be known.

-27-

2.3.5 TSPC/DC Studies

One of the original goals of our research program was to determine if TSPC/DC measurements could provide an easy way to predict life-testing behavior. The measurements which were carried out to decide if this were the case are contained in section 4.4, the TSPC/DC degradation section. Th' conclusions are summarized here:

1) TSPC/DC measurements have not been found capable of detecting the structural flaws which lead to low voltage degradation. Therefore it is not an adequate method to predict capacitor reliability.

2) TSPC/DC measurements do exhibit a large difference between those capacitors which failed the life test and those which did not. Therefore, TSPC/DC measurements are useful for studying the results of degradation.

3) TSPC/DC measurements would have clearly shown if any of the failures were due to dendritic growth by the temperature dependence of the resistance, i.e. increasing resistance with increasing temperatures for metals.

In recent months the life testing portion of our low voltage degradation program has been halted in order to use the computer system for TSPC/DC and capacitance measurements.

3.0 High Voltage Degradation

The stability of $BaTiO_3$ -based capacitors biased under DC fields has long been recognized as one of the important factors determining the reliability of ceramic capacitors. Electrical degradation, characterized by a gradual increase in the electrical conductivity over a period of time, becomes an increasing problem as dielectric thicknesses decrease, and the corresponding field the dielectric must withstand increases (eg.in MLC's). Even though degradation has been extensively studied in the past, the mechanisms behind the degradation process are not clearly understood. The purpose of our research program is to clarify which mechanisms are responsible for degradation in order that they may be better understood. This section of the report covers the research which has been carried out studying the degradation of laboratory-prepared specimens biased under high DC voltage stress. We are currently studying degradation as a function of:

1) Ba:Ti ratio
2) Acceptor and donor doping
3) Porosity
4) Grain size
5) Applied field
6) Temperature
7) Humidity

Our initial measurements have focused mainly on the effects of excess Ti and Ba. By studying the effects of nonstoichiometry, one also obtains information on the effect of porosity, field, and temperature on the degradation rate. All of the initial measurements have been carried out in a "dry"

atmosphere in order to minimize the possible influence of humidity on the results. The experiments being carried out are:

1) I vs. Short Time
2) I vs. Field
3) I vs. Temperature
4) I vs. Extended Time
5) Thermally-Stimulated Polarization / Depolarization

Current vs. short time (< 5 hours) measurements are the primary source of our conclusions. We have discovered that if a capacitor is going to exhibit degradation behavior, then it does so in the first few minutes. Current vs. field analyses are obtained from the I-time results and are used to see if non-ohmic current injection behavior is occurring. Current vs. temperature measurements are made in order to determine the activation energy of the conduction process. In the past, those specimens exhibiting degradation had a low activation energy. Current vs. extended time (> 5 hours) measurements are made in order to confirm if long term behavior matches that of the short time experiments, i.e., do "good" specimens from the short time tests fail, or begin to degrade at a later time. TSPC/DC measurements are being made in order to see if a relationship exists between degradation phenomena and polarization mechanisms. As it turns out, TSPC/DC measurements have not proven fruitful in terms of degradation, but has provided a wealth of information concerning polarization processes in $BaTiO_3$. This combination of experiments, in conjunction with a thorough microstructural analysis, represents a powerful tool for studying degradation.

3.1 Literature Review

Before presenting the results and discussion of our investigation, a brief literature review will be presented so that the conclusions reached later have meaning to the reader. First a review of the mechanisms which have been found to influence degradation will be presented.

3.1.1 Degradation Mechanisms

Previous studies have shown qualitatively that the degradation of $BaTiO_3$ is dependent upon many factors. These include:

1) Choice of electrode material
2) Incorporation of water
3) Composition
4) Non-ohmic current injection

The first of these, the effect of electrode material, has been found to effect degradation either through electromigration, or by the enhancement of one of the current injection modes. Branwood and Tredgold[21] found that $BaTiO_3$ single crystals tend to degrade only with Ag or Au electrodes; while Cr, Al, or Zn electrodes formed stable combinations. Initially this was thought to be due to an electromigration problem, but was later ascertained to be enhanced hole injection at the anode. This results in abnormally high current levels. Complexing of water with electrode materials and subsequent migration through structural imperfections is also thought to be responsible for the low voltage degradation of multilayer capacitors.

The second mechanism concerns the incorporation of water into

-31-

the dielectric either during firing, or by absorption of water from the atmosphere under ambient conditions. Water incorporated during firing exists in the lattice either as hydroxyl groups, OH^-, or as protons, H^+. These are thought to result in high current levels due to their migration under the influence of a field.[22] Water can also form charged complexes with electrode materials, which may result in dendritic growth through structural imperfections and subsequent failure. Past studies clearly show these mechanisms can be inhibited by annealing $BaTiO_3$ in a dry atmosphere at temperatures greater than 1000 $^\circ C$, and by hermetic sealing.

Varying the composition of $BaTiO_3$ through the Ba:Ti ratio or by doping greatly effects the degradation behavior. Studies in the past qualitatively attribute this directly to the corresponding variation in the oxygen vacancy ($V_o^{\cdot\cdot}$) concentration, and their migration under the influence of a high field. Oxygen migration is thought to effect degradation as illustrated in Figure 3.1.1a.

Positively-charged $V_o^{\cdot\cdot}$ migrate towards the cathode with a corresponding migration of oxygen ions to the anode where oxygen evolves. The $V_o^{\cdot\cdot}$ pile up at the cathode, creating two Ti^{+3} centers (electron binding energy <.1 eV) to maintain electrical neutrality. This region, characteristically blue, has a low resistivity and slowly moves towards the anode, a "virtual moving cathode". Current levels increase, leading to eventual breakdown from ohmic heating or an electron avalanche, "Zener" breakdown.

OXYGEN DIFFUSION MODEL

low ρ

Cathode $-$

moving
virtual cathode

Anode $+$

$V_o^{\cdot\cdot}$ $V_o^{\cdot\cdot}$
$V_o^{\cdot}$ $\leftarrow V_o^{\cdot\cdot}$
$V_o^{\cdot\cdot}$ $V_o^{\cdot\cdot}$
$V_o^{\cdot}$ $\leftarrow V_o^{\cdot\cdot}$
$V_o^{\cdot}$ $V_o^{\cdot}$ $\leftarrow V_o^{\cdot\cdot}$
$V_o^{\cdot\cdot}$
$V_o^{\cdot\cdot}$ $V_o^{\cdot}$ $\leftarrow V_o^{\cdot}$
$V_o^{\cdot\cdot}$
$V_o^{\cdot\cdot}$ $V_o^{\cdot\cdot}$ $\leftarrow V_o^{\cdot}$
$V_o^{\cdot}$

$O'' \rightarrow$
$O'' \rightarrow$
$O'' \rightarrow$
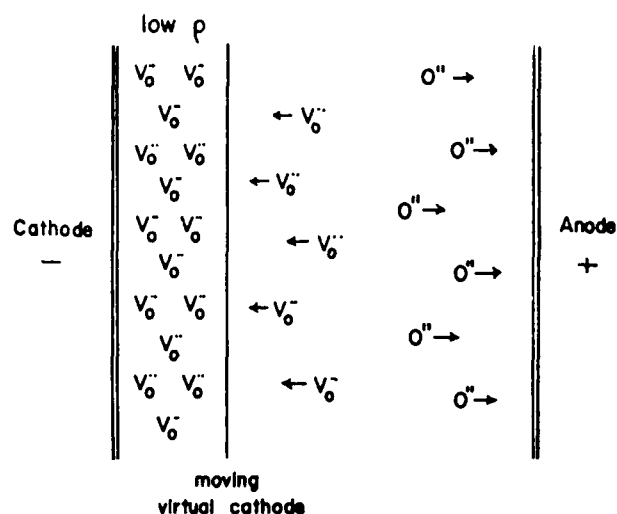$O'' \rightarrow$
$O'' \rightarrow$
$O'' \rightarrow$

Figure 3.1.1a: Illustration of oxygen vacancy migration and its effect on degradation.

Evidence supporting this model is substantial. Lehovic and Shirn[23] found degraded polycrystalline $BaTiO_3$ formed a dark blue low resitivity region at the cathode, and a dark brown high resistivity region near the anode, corresponding to the $V_o^{\cdot\cdot}$ concentration gradient. Glower and Heckman[24], and Payne[25] found from oxygen concentration cell experiments an inordinate proportion of ionic conduction at tempertures below 250 $^{\circ}C$. Payne also found those specimens exhibiting ionic conductivity tended to degrade. Gruver et.al.[22] found that by hermetically sealing the anode with a layer of $BaTiO_3$ they could increase the lifetime by 2-4 orders of magnitude compared with specimens with only the cathode sealed.

The addititon of donor impurities has been found to decrease the degradation rate, due to the corresponding decrease in the $V_o^{\cdot\cdot}$ concentration (refer to Section 3.1.3B). Gruver et. al.[22] found additions of cations with valency greater than +4 on the Ti

site, or anions with valency greater than -2 on the O site substantially improved the resistance to degradation. MacChesney et.al.[26] found additions of La^{+3} to polycrystalline $BaTiO_3$ stabilized its resistivity, with a 0.5 mole % addition being optimal. Lifetime compared to pure $BaTiO_3$ was increased from two hours to over 1000 hours without a failure. Keck[27] found donor additions to improve the degradation resistance of $BaTiO_3$ for Ba:Ti ratios less than one, with a decrease in degradation resistance if the Ba:Ti was greater than one.

Past studies have also indicated, though not conclusively, that $BaTiO_3$ specimens exhibiting non-ohmic current-voltage characteristics were those most likely to degrade (refer to Section 3.1.2). Payne[25] studied two mil thick $BaTiO_3$ capacitors and found the current-voltage behavior to be accurately described by Schottky emission. Those specimens exhibiting this non-ohmic behavior were those most likely to degrade. Keck[27] found the onset of degradation in $BaTiO_3$ to coincide with the field at which space-charge-limited current began to occur.

The degradation of $BaTiO_3$ seems to be dependent upon many factors. In our research program, we hope to delineate many of these factors. The UMR/PSU joint effort on this problem is progressing rapidly, with a substantial data base being established on the undoped compositions before the effects of dopants are considered. The results of this program are included in Section 3.4 .

3.1.2 Current Injection Mechanisms in Solids

Past studies[24,25] have indicated that there exists a possible connection between non-ohmic current injection mechanisms and electrical degradation. Sections 3.4 and 2.3.4 contain the I-V behavior we have measured on various commercial and laboratory-prepared specimens, the results of which are discussed in terms of ohmic and non-ohmic behavior. Understanding the analysis would be difficult without prior knowledge of injection mechanisms. For this reason a brief review of the current-injection mechanisms found to occur in insulators is presented .

Electronic conduction through an insulator can be separated into three distinct phases: 1) carrier injection from the metal electrode to the insulator, 2) carrier motion through the insulator, and 3) carrier extraction from the insulator to the metal. Any observed steady-state electrical behavior exhibited by a specific metal-insulator combination will necessarily be controlled by one or a combination of these three phases.

When a metal and an insulator are joined, carriers such as electrons or holes will diffuse from one into the other until their Fermi energies align. If the work function of the metal is less than that of the insulator (n-type conduction), then electrons will transfer from the metal to the insulator, forming an ohmic contact (Figure 3.1.2a). In this case, electrons are able to move freely in either direction across the interface, not
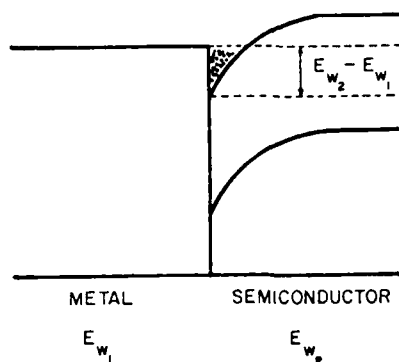
OHMIC CONTACT

Figure 3.1.2a: Energy band structure of an ohmic contact for a
n-type semiconductor - metal junction.

effecting the conduction process. Therefore, for an

insulator with ohmic contacts biased under low fields, observed

steady-state electrical behavior will be controlled by the bulk

properties of the insulator, the second phase of the conduction

process. Ohmic behavior is the simplest case and is governed by:

$$J = q[]uE \qquad (1)$$

where: J = current density
        q = electronic charge
        [] = carrier concentration
        u = carrier mobility
        E = applied field

Note that bulk properties of the insulator control the

conduction process. From this equation it can be seen that a

log J vs. log E plot would have a slope of one if ohmic behavior

were occurring.

For thinner insulators biased under higher fields,

behavior may not be governed by bulk properties, but

three current injection mechanisms. These mecha

Schottky Emission, Tunneling, and Space-Charge-Limit

Each will be discussed separately.

Schottky Emission

Schottky emission of electrons from a metal into a

is analogous to the the thermionic emission of elect

metal into a vacuum. Essentially, this mechanis

the transfer of electrons from the electrode to the i

a result of temperature and field effects alone.

For a metal-vacuum system there exists a potential

the surface of the metal which keeps electrons fro

(Figure 3.1.2b). The height of this barrier is equal

function of the metal.

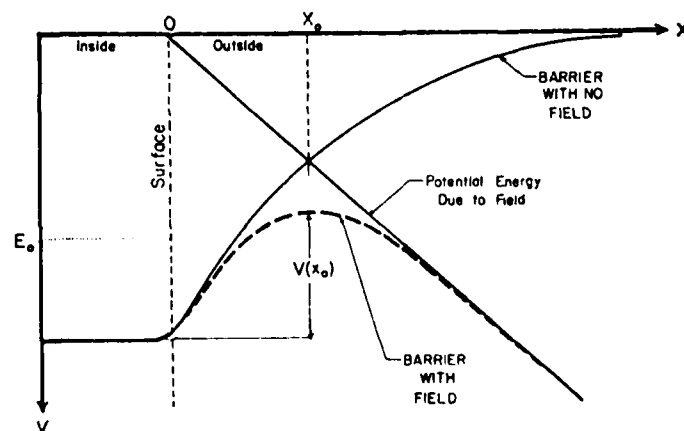Figure 3.1.2b: Surface potential barrier at a metal s

Only those electrons with sufficient thermal energy to surmount this barrier are spontaneously emitted from the metal into the vacuum. Fermi-Dirac statistics describe the energy distribution of electrons in a metal. As can be seen in Figure 3.1.2b, applying an accelerating potential "lowers" the barrier, representing a decrease in the effective work function of the metal. Now, more electrons in the tail of the Fermi-Dirac distribution have sufficient energy to pass over the barrier. The equation relating the current density of electrons being emitted to the temperature and applied field is the equation for Schottky emission:

$$J = \frac{4\pi mek^2}{h^3} \, T^2 \, \exp\left[-\frac{\phi - q\left(\frac{qE}{4\pi\varepsilon_o}\right)^{\frac{1}{2}}}{kT}\right]$$

(2)

J = current density
m = electron mass
q = electronic charge
k = Boltzman constant
h = Planck's constant
T = absolute temperature
E = field
ε_o = permittivity of free space

Note the resulting current density is strongly dependent upon the temperature and the square root of the field. Correspondingly, a plot of log J vs. $E^{1/2}$ (constant temperature), or log J/T^2 vs. 1/T (constant field) would be linear if Schottky emission were occurring (Figure 3.1.2c).

Although the equation for Schottky emission was derived in terms of a metal-vacuum system, the same analysis applies for
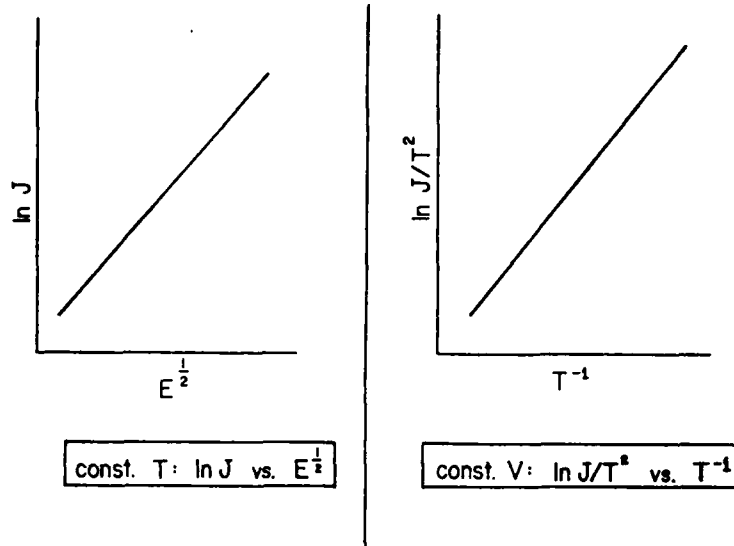
SCHOTTKY   EMISSION

Figure 3.1.2c: Injected current density as a function of field.
and temperature governed by Schottky emission.

a metal-insulator system. The only difference concerns the
height of the surface potential barrier, which will now be
governed by the difference in work functions between the
insulator and the metal. The contact necessarily needs to be a
rectifying one, as the work function of the metal must be greater
than that of the insulator. It is also possible that the
rectification may be a result of a surface depletion layer, or a
surface dipole layer present at the interface[28]. In any case,
electrons which are thermionically emitted from the insulator
enter directly into the conduction band of the insulator and are
swept towards the anode. This constitutes the Schottky emission
current.

Several of the assumptions utilized in this approach which may cause deviations from theory are: 1) interfacial conditions are ignored, 2) the work function may be temperature dependent, and 3) electrons may be reflected at the surface of the metal. As mentioned previously, charge or dipole layers at the surface may alter the effective work function of the the metal-insulator contact. These arise as a result of surface irregularities and interdiffusion of atomic species. The net effect is to change the slope of the log J vs. $E^{1/2}$ graph from expected values, but the observed current density-field behavior does not change if Schottky emission is still occurring. For semiconducting insulators, the temperature dependence of the Fermi energy alters the surface potential barrier. This has the effect of making the constant voltage, log J/T^2 vs. graph nonlinear; however this can be taken into account by determining the temperature dependency of the Fermi energy. Reflection of electrons at the metal interface arises from quantum-mechanical effects, which allow the electrons to be reflected at the potential barrier even though they have sufficient energy to overcome it. A full quantum-mechanical treatment of this phenomonem yields a minor effect at extremely high fields and temperatures but produces a more significant effect at lower fields and temperatures where the electrons barely have sufficient thermal energy to clear the lowered barrier. Certainly the effect could create no more than a 1 % deviation, which is much less than experimental error.

Schottky emission has been found to occur in insulating materials with thicknesses on the order of 2 mils or less under

applied fields of approximately 10^5 V/cm. These conditions correspond to 250 V/mil, well within the fields withstood by most high voltage multilayer capacitors and the grain boundaries in devices such as barrier layer capacitors and varistors. Several authors have found that Scottky emission occurs in insulating materials:

Emtage and Tantraporn[29] first observed Schottky emission in 100 A thick films of polymerized silicon oil with gold electrodes. They concluded that at room temperature the current is totally due to Schottky emission, but at lower temperatures (-70°C) tunnel emission becomes dominant. They also observed Schottky emission in 50 A thick Al_2O_3 and GeO_2.

Lengyel[30] found that 1.1 mil thick films of polyethylene-terephthalate and 2.2 mil thick films of polyvinylformal exhibit Schottky emission as the limiting factor when one tries to establish a steady-state current. The fields varied from 20-200 KV/cm, and temperatures from 25 - 100 ^{O}C.

Tantraporn and Harris[31] observed Schottky emission in 100 A thick mica.

Hacaskaylo[32] measured 100 A thick films of Al_2O_3 and found that Schottky emission accurately described the current-field behavior up to fields of 10^7 V/cm.

Payne [25] studied 2 mil thick $BaTiO_3$ capacitors and found that the current injection mechanism exhibited the current-field, current-temperature characteristics described by Schottky emission. This study is of particular interest as Payne found those capacitors exhibiting non-ohmic behavior tended to degrade.

Johansen[33] studied 0.1-1 u thick films of SiO_2 and observed Schottky emission and the Poole-Frenkel effect. The Poole-Frenkel effect is internal Schottky emission in which the conduction process is limited by the enhanced thermal emission of electrons from a discrete trap level into the conduction band.

Tunneling

Tunnel emission, also known as Fowler-Nordheim tunneling, occurs in very thin insulators, 10-100 A, under fields on the order of 10^7 V/cm. Unlike Schottky emisson in which electrons pass over the surface potential barrier of the metal-insulator contact, "tunneling" electrons pass through the energetically-forbidden region. The current density arising from such an injecton mechanism is directly proportional to a transmission coefficient which describes the fraction of electrons that tunnel through the barrier.

For simple "square" barriers, the Schroedinger equation is directly solvable, and an exact transmission coefficient can be found. However, for barriers such as the effective surface potential barrier of Figure 3.1.2b, the Schroedinger equation is not solvable, and an approximation method must be used. For tunneling, the Jeffreys-Wentzel-Kramers-Brilliouin (JWKB) approximation theory is used. This theory is valid in the region of a slowly varying potential, i.e., the momentum of the electron does not change appreciably over a distance of several deBroglie wavelengths. The current density using this approximation method is given by:

$$J = \frac{q^3 E^2 \alpha}{8\pi h\phi} \exp - \left[\frac{4(2m)^{\frac{1}{2}} \phi^{\frac{3}{2}} \beta}{3hq} \frac{1}{E} \right]$$

J = current density   (3)
q = electronic charge
E = applied field
α = adjustable parameter
h = Planck's constant
ϕ = work function
m = electron mass
β = adjustable parameter

A plot of log J/E^2 <u>vs.</u> E^{-1} yields a straight line (Figure 3.1.2d). The important thing to notice is the temperature independence, which makes it easy to distiguish from Schottky emission.

TUNNELING

$$\boxed{\ln J/E^2 \text{ vs. } E^{-1}}$$
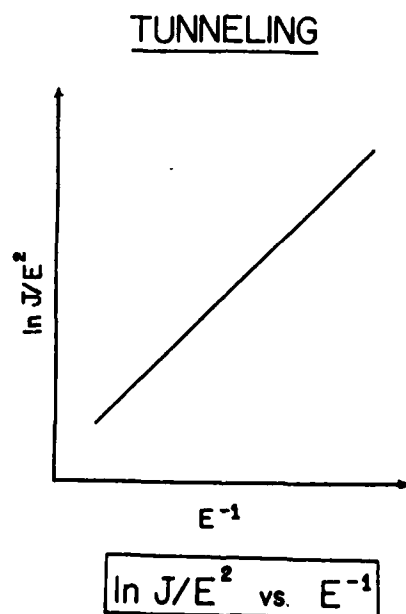
Figure 3.1.2d: Injection current as a function of field for Fowler-Nordheim tunneling.

Tunnel emission in insulators has been identified experimentally by several investigators:

Fisher and Giaever[34] observed that the current injection

-43-

mechanism in 50 A Al_2O_3 is tunneling emission.

Ekrut and Hahn[35] performed extensive studies on tunnel emission in $Ta/Ta_2O_5/Ag$ and Al/Al_2O_3 junctions. Their oxides, which were on the order of 10-50 A thick, were grown by careful oxidation of the electrode.

Maserjian and Zamani[36] studied 50 A thick films of SiO_2 grown on silicon and observed classical Fowler-Nordheim tunneling. An interesting finding of theirs was that the tunnel junction degraded as a function of time, i.e., its current increased. They explained this behavior by introducing the formation of positive-charge centers which form at the interface.

As stated earlier, tunnel emission occurs only in very thin insulators, which are on the order of several hundred / thick under applied fields of 10^7 V/cm. This corresponds to 25,000 V/mil. Obviously, tunneling is not going to occur in multilayer capacitors; however, 10^7 V/cm also converts to 10 V/100 A, which is not an unreasonable field to see applied across a grain boundary. Matsuoka[37] theorized that ZnO varistors work because the electrons tunnel through a double Schottky barrier at the grain boundary when a critical field is reached. Tunneling is easily identified by its temperature independence.

Space-Charge-Limited-Current

For insulators with ohmic contacts biased under high fields, it is possible for electrons to be directly injected into the conduction band of the insulator from the cathode. The injection is at such a rate that all of the electrons cannot immediately

move through the conduction band to the anode. This results in a "space-charge" buildup at the cathode. This space charge of the uncompensated electrons alters the field in such a way as to limit the current, hence the name space-charge-limited current (SCLC). This is analogous to the limited emission of electrons through a vacuum from cathode to anode first described by Child[38] in 1911. Mott and Gurney[39] pointed out that a solid-state analog of this phenomenom would be possible. Rose[40] later developed this idea into a concise theory concerning SCLC and its dependence upon the intrinsic properties of the insulators themselves.

The main point is, insulators with ohmic contacts biased under low fields will initially exhibit ohmic behavior, but at some point the field will become high enough such that SCLC will take over. The field at which this occurs will depend upon the bulk properties of the insulator, such as the free and trapped carrier concentrations, and the overall defect chemistry. Different types of SCLC behavior will be exhibited for various combinations of these quantities. Lampert and Mark[41] explicitly derived the various possible cases and their limitations. Basically there are six cases which can arise: 1) perfect trap-free insulator, 2) trap-free insulator, 3) insulator with shallow traps, 4) insulator with deep traps, 5) insulators with an exponential trap distribution, and 6) insulator with a uniform trap distribution.

The current-field relationships governing each of these six relationships can be derived using Poisson's equation and the

relationships describing the concentrations of free and trapped carriers as a function of temperature and Fermi energy (Figure 3.1.2e). Each is discussed briefly below.
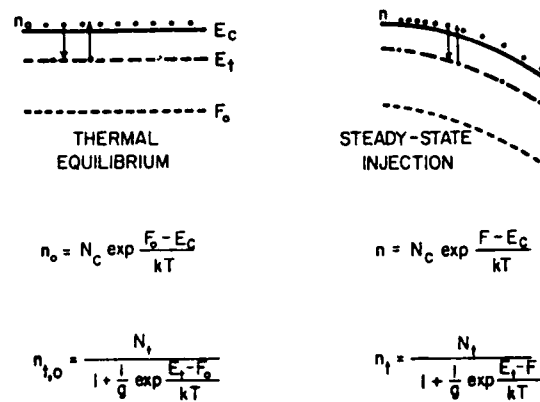
$$n_o = N_C \exp \frac{F_o - E_C}{kT}$$

$$n = N_C \exp \frac{F - E_C}{kT}$$

$$n_{t,o} = \frac{N_t}{1 + \frac{1}{g} \exp \frac{E_t - F_o}{kT}}$$

$$n_t = \frac{N_t}{1 + \frac{1}{g} \exp \frac{E_t - F}{kT}}$$

Figure 3.1.2e: Band structure at thermal equilibrium and for steady-state injection of electrons for SCLC.

Perfect Trap Free Insulator

A perfect insulator is free of traps, and has a negligible concentration of free carriers. All of the injected electrons remain free in the conduction band and contribute to the space charge. The current density is given by:

$$J = \frac{9}{8} \varepsilon \mu \left(\frac{V^2}{L^3} \right) \tag{4}$$

where: ε = permittivity of the insulator
μ = carrier mobility
V = applied voltage
L = electrode separation

Note the current-field behavior; current increases with the

square of the voltage, not linearly as in ohmic behavior. The importance of this simple case is that it represents the highest current which can flow when all traps are filled, and the injected concentration of electrons is much greater than any other contribution. Thus the trap-free insulator case is the limiting case for all of the SCLC injection mechanisms at high fields.

Trap-Free Insulator with Thermal-Free Carriers

In this case carriers are assumed to be present in the conduction band due to the thermal ionization of electrons from band to band processes or from donor levels lying close to the conduction band. If one looks at the concentration gradient of electrons across the insulator (Figure 3.1.2f), it may be seen that at low fields the thermally-ionized electron concentration is greater than the injected concentration, and ohmic behavior is dominant. However, when the injected electron concentration exceeds that of the thermally-ionized concentration, then the SCLC trap-free square law is observed. Graphically this would appear as a change in slope of magnitude 2 on a log J vs. log E plot (Figure 3.1.2g). The critical voltage at the transition point is defined as:

$$V_c = \frac{8qn_oL^2}{9\varepsilon} \qquad (5)$$

n_O = thermally-ion-
zed electron
concentration.

$n_i(x)$ = injected
electron
concentration.
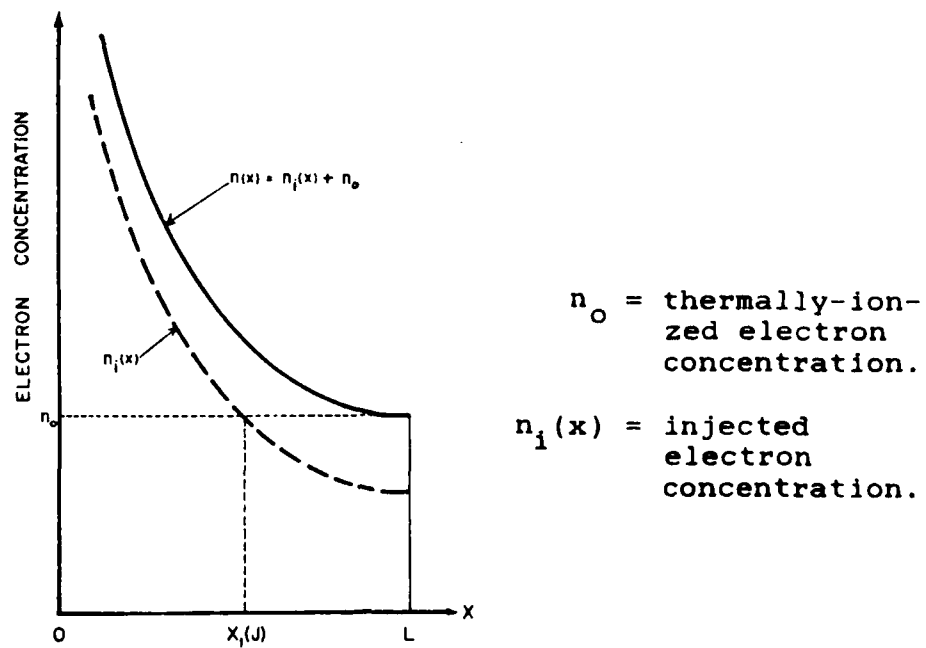
Figure 3.1.2f: Injected electron concentration as a function of distance from the metal-insulator contact.
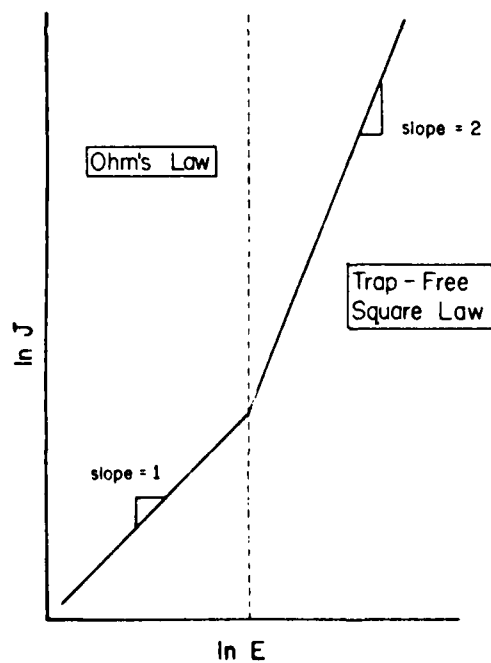

Figure 3.1.2g: Current-field behavior for a transition from ohmic to SCLC behavior when $n_o = n_i(x)$ in Figure 3.1.2f.

Insulator with Shallow Traps

If traps, which are initially empty, exist within the insulator, the net effect would be to decrease the magnitude of the injected current. Electrons which would have stayed in the conduction band and contributed to the space charge, are captured. For shallow traps, which are defined to be those lying between the conduction band and the Fermi energy, the corresponding current density is reduced by an amount , the ratio of free to trapped carriers. Increasing the trap concentration results in a transition to SCLC at a higher field. Shallow traps may arise as a result of low lying acceptor states, or dislocations. This case has been found to be a good approximation for single crystals with a high chemical and structural purity.

Insulator with Deep Traps

Undoubtedly, some crystals will contain traps which lie energetically between the Fermi energy and the valence band, i.e., deep traps. In this case, θ, the ratio of free to trapped carriers, is no longer field dependent. This is a direct result of Poisson's equation and the relationships between the free and trapped carrier concentrations. The result is that at some voltage at which ohmic behavior ceases, there is a region where the current abruptly increases instead of immediately transforming to the trap-free square law. The steep rise corresponds to a filling of the deep traps (Figure 3.1.2h).
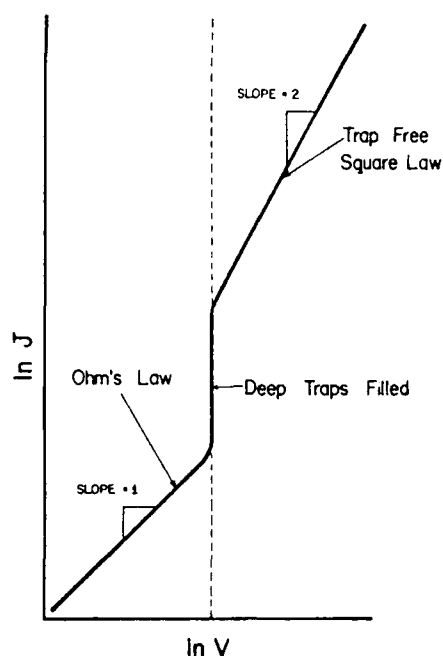
Perfect Insulator with Deep Traps

Figure 3.1.2h: Injected current as a function of field for an insulator with deep traps.

Insulator with a Uniform or Exponential Trap Distribution

Real crystals, particularily those of polycrystalline materials, are unlikely to contain a single, discrete trap energy but will most likely exhibit an energetic distribution of traps. This distribution may be uniform or exponential. In any case, the ratio of free to trapped carriers again becomes field dependent, which results in a more gradual increase in the current after ohmic behavior (Figure 3.1.2i). During trap filling the current becomes dependent upon some power of the field higher than two, dependent upon the trap distribution. Eventually, a point is reached where all of the traps are filled and again the trap-free square law takes over.

INSULATOR with TRAPS
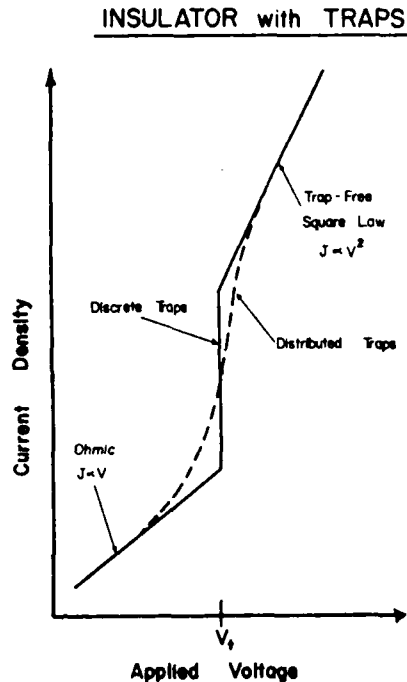
Figure 3.1.21: Injected current as a function of f:
insulator with discrete or distributed

The consequences of the trap-free square law

paramount. In this region the current is limited (

space charge of the injected electrons. It does n(

difference what is in between the electrodes. This

remarkable result. The existence of an abnormally h

current in an insulating device may not be due to pr

the insulator but may be due solely to the onset (

injection mechanism.[27]

The derivation of the preceeding SCLC relationsh

upon two key assumptions: 1) the contacts are

otherwise unimportant, 2) the influence of the conti

conduction band profile, i.e. band bending, is cor

depth that is small when compared to the insulator. O'Reilly and DeLucia[42] and Rosenthal and Sapar[43] investigated thin insulators in which the contact regions are significant. Essentially, the conductivity of the insulator increases as a result of the overlap of the space-charge regions of the two ohmic contacts. In this case, Rose and Lampert's theory become inapplicable. Edwards and Jones[44] addressed themselves to this problem by modeling the the zero-bias conduction band profile and investigated its effects on the current density-voltage characteristics.

Space-charge-limited current has been found to occur in insulators several mils thick under applied fields on the order of 1000-10000 V/cm. This correponds to only 25 V/mil, which is not a high field and is well within the range of that applied to MLC's. Evidence for SCLC in $BaTiO_3$ can be seen in several investigations.

Originally, Smith and Rose[45] observed SCLC behavior in CdS single crystals.

Branwood and Tredgold[21] and Branwood et.al.[46] measured $BaTiO_3$ single crystals and found SCLC behavior described by:

$$J = a \left[\frac{V}{L} \right] + b \left[\frac{V}{L} \right]^2 \qquad (6)$$

where a,b = experimental parameters to fit the data

Their single crystals were 100-600 µ thick with applied fields up to 8000 V/cm.

Rhys-Roberts and Tredgold[47] studied $BaTiO_3$ and found they could accurately describe the resulting SCLC behavior by introducing the effects of a surface trapping layer.

Keck[27] found that SCLC occurs in 10 mil thick specimens of polycrystalline $BaTiO_3$. His data shows a distinct ohmic to SCLC transition. In addition, those samples exhibiting SCLC behavior had the highest tendency to degrade electrically.

More recently Burton[20] has found SCLC behavior to describe the current-voltage behavior of MLC's. The capacitors exhibit a 3/2 power dependency on the field which Burton has attributed to electron emission from electrode protuberances in the dielectric. Mark and Lambert[41] have shown theoretically that electron emission from a hemispherical point results in a 3/2 power dependency on the field. Burton also has shown how carrier characteristics such as concentration and mobility can be determined if trap filling is occurring.

Nepurek and Sworakowski[48] developed an analytical method that enables one to extract qualitative information about the energetic distribution of traps from SCLC measurements. They also described the effects of temperature, current instability, and spatial non-uniformity of traps.

Mathur and Dahura[49] developed a distribution that broadly encompasses all the characteristics of the Gaussian distribution and accurately predicts the current density-voltage dependence in the region from SCLC to ohmic behavior.

Summary

Four current injection mechanisms have been found to occur in solids: ohmic injection, Schottky emission, tunneling, and space-charge-limited current. Figure 3.1.21 summarizes the insulator thicknesses, current-voltage dependencies, and fields under which each has been found to occur. The bottom line concerning all these current injection mechanisms is: current technological advances are aimed towards using thinner and thinner dielectrics as the active layer in various electronic devices. As thicknesses decrease, and the fields increase, a

Mechanism	I-V Behavior	Field	Thickness
Ohmic	$\log J$ vs. $\log E$ slope = 1	low	>several mils
Schottky	$\log J$ vs. $E^{\frac{1}{2}}$	10^5 V/cm	<2 mils
Tunneling	$\log J/E^2$ vs. E^{-1}	10^{7-8} V/cm	<400 Å
Space Charge	$\log J$ vs. $\log E$ slope = 2	10^{3-4} V/cm	several mils

Figure 3.1.21: Summary of the current injection mechanisms with their field, thickness, and I-V behavior.

departure from ohmic behavior becomes more likely, which in turn may have a detrimental effect on the electrical properties of the device. Multilayer capacitors, barrier layer capacitors, varistors, and PTC devices have all been shown to exhibit non-ohmic behavior. In some cases, this deviation results in advantageous properties, whereas in others it limits their capabilities. In any case, a thorough knowledge of the various current injection mechanisms found in insulators is needed.

Since our last progress report, many current-voltage measurements have been made on both commercial and laboratory-prepared specimens. In all cases, non-ohmic behavior has been observed. Whether or not this is due to a non-ohmic current injection mechanism is not known. Many of these same specimens degrade, which may invalidate use of SCLC theory altogether. Refer to Sections 3.3 and 2.3.4 for further analysis of the current-voltage results.

3.1.3 Defect Chemistry

In order to understand the electrical properties and
sintering behavior of BaTiO$_3$ it is particularily important to
have a full working knowledge of the defect chemistry. Our
results indicate degradation is strongly dependent upon the
composition; ie: whether or not nonstoichiometry results in a
second phase or alters the point defect concentration leads to
dramatic differences in the degradation rate. Understanding the
effect of adding dopants to the system also requires full
knowledge of the defect chemistry, as does understanding the
sintering behavior. This section presents the proposed defect
model for BaTiO$_3$ as it has been elucidated in the literature,
mainly through high temperature electrical conductivity and
weight loss measurements. Throughout this section the defect
notation of Kroger and Vink[50] will be used. The first part will
cover the case of undoped BaTiO$_3$.

3.1.3A Undoped Barium Titanate

Three possible configurations need to be covered for undoped
BaTiO$_3$: 1) stoichiometric ; 2) excess barium; and 3) excess
titanium.

Stoichiometric Barium Titanate

Past investigations of stoichiometric BaTiO$_3$[51-62] have shown
it to be an n-type semiconducting oxide. The defect model
developed assumes that the predominating defects are O vacancies

($V_O^{\cdot\cdot}$), electrons (n), holes (p), and Ba vacancies ($V_{Ba}^{''}$). The other major assumption is that the defects are fully ionized, which is supported by numerous experimental results[51-62].

If band to band processes are occurring the intrinsic ionization reaction can be written as:

Intrinsic Reaction: $nil \rightleftharpoons e^{i} + h^{\cdot}$ (1)
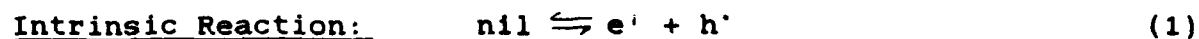
$$K_1 = np \qquad (2)$$

If oxygen leaves its lattice position , it leaves behind a vacancy and the corresponding electronic defects. This can be written as:

Oxygen Deficiency: $O_O^{x} \rightleftharpoons 1/2 \; O_2 + V_O^{\cdot\cdot} + 2 \; e^{i}$ (3)
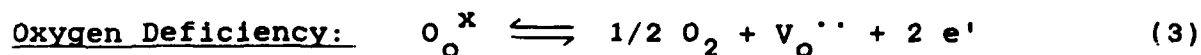
$$K_3 = n^2 \; [V_O^{\cdot\cdot}] \; PO_2^{1/2} \qquad (4)$$

Although unlikely to occur, if excess oxygen is absorbed onto the lattice then Cationic defects, $V_{Ba}^{''}$ and $V_{Ti}^{''''}$, would form. To simplify treatment it will be assumed that only $V_{Ba}^{''}$ form , however if $V_{Ti}^{''''}$ forms the conclusions will not be altered, only the formation reaction. This reaction could be written:

Oxygen Excess : $1/2 \; O_2 \rightleftharpoons O_O^{x} + V_{Ba}^{''} + 2h^{\cdot}$ (5)
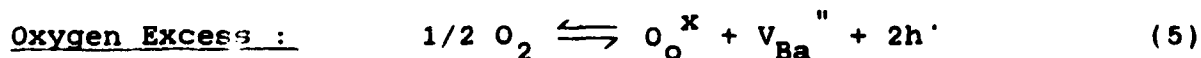
$$K_5 = p^2 \; [V_{Ba}^{''}] \; PO_2^{-1/2} \qquad (6)$$

Nature requires that the material as a whole remains neutral.

The relationship relating the various point and electronic defects is the neutrality condition:

Neutrality Condition : $\quad n + 2\ [V_{Ba}"] = p + 2\ [V_O\ ^{..}]$ \hfill (7)

In general the defect stucture can be broken into three regimes: low, intermediate, and high PO_2's.

$$\underline{Low\ PO_2}\ ;\ n = 2[V_O\ ^{..}]$$

Under highly reducing conditions the oxygen is removed from the lattice, resulting in a conducting oxide . The predominating point defect becomes $V_O\ ^{..}$. Using the preceeding equations the n, p, and $V_{Ba}"$ concentrations are found to be:

$$n = (\ 2K_3\ )^{1/3}\ PO_2^{\ -1/6} \hspace{2cm} (8)$$

$$p = K_1\ (\ 2K_2\ )^{-1/3}\ PO_2^{\ 1/6} \hspace{2cm} (9)$$

$$(V_{Ba}") = (\ K_5\ )\ K_1^{\ -2}\ (\ 2K_3\ )^{2/3}\ PO_2^{\ 1/6} \hspace{1.5cm} (10)$$

Therefore as the PO_2 decreases the concentration of e' and $V_O\ ^{..}$ increases, and the concentration of h˙ and $V_{Ba}"$ decreases. This would continue until a second phase was exsolved.

Intermediate PO_2 : Intrinsic Region

In this region either intrinsic ionization of electrons from the valence band to the conduction band or formation of Schottky

defects may be the dominating defect reaction. For this treatment, we will assume that the band to band process dominates. Usually this region is ignored as the concentration of ionic defects and their corresponding electronic defects is greater than the concentration of intrinsic electronic defects. However, if the the band gap is small enough, and the polycrystalline material is very pure, then this region could occur. For this region then the electronic defect concentration is constant and expressed as:

$$n = p = \text{constant} \tag{11}$$

The corresponding $V_O^{\cdot\cdot}$ and $V_{Ba}"$ concentrations are :

$$(V_O^{\cdot\cdot}) = K_3 \, n^{-2} \, PO_2^{-1/2} \tag{12}$$

$$(V_{Ba}") = K_5 \, p^{-2} \, PO_2^{1/2} \tag{13}$$

Conductivity in this region would be constant, but the concentration of $V_O^{\cdot\cdot}$ would be suppressed.

If Schottky defects prevailed, the cationic defects would be constant and the electron and hole concentration would depend upon $PO_2^{-1/4}$ and $PO_2{+1/4}$ respectively.

$$\underline{\text{High } PO_2} : \quad p = 2 \, [\, V_{Ba}" \,]$$

In this region we are assuming the oxygen is incorporated into the lattice with a subsequent formation of $V_{Ba}"$ ($V_{Ti}""$

could also form). Therefore a transition to p-type behavior would be expected, and has been experimentally verified[51,54,58]. The concentration of the corresponding ionic and electronic point defects are then given by:

$$p = (\ 2K_5 \ )^{1/3} \ PO_2^{\ 1/6} \tag{14}$$

$$n = K_1 \ (\ 2K_5 \ )^{-1/3} \ PO_2^{\ -1/6} \tag{15}$$

$$(\ V_O^{\cdot\cdot}) = K_3 \ K_1^{-2} \ (\ 2K_5 \text{"} \ )^{2/3} \ PO_2^{\ -1/6} \tag{16}$$

Therefore with increasing PO_2 the concentration of $V_{Ba}\text{"}$ and $h^{\cdot}$ would increase, and the concentration of e' and $V_O^{\cdot\cdot}$ would decrease. Figure 3.1.3a is a Kroger Vink diagram representing the defect scheme over the entire pressure regime.

STOICHIOMETRIC UNDOPED BaTiO$_3$
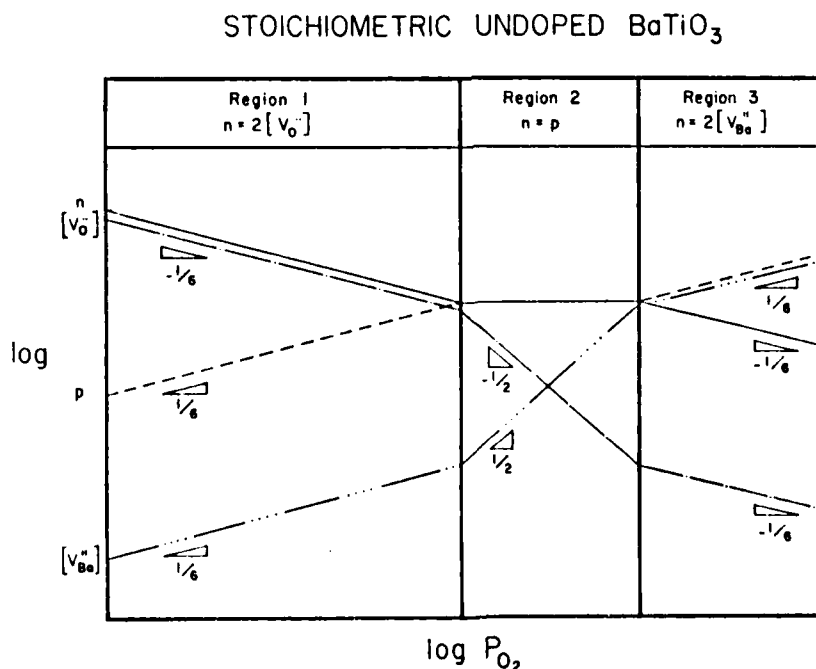
Figure 3.4.1a: Kroger Vink diagram for stoichiometric undoped BaTiO$_3$.

It should be pointed out that another possibile defect reaction could occur in the high PO_2 region.. Chan[57] has pointed out a $PO_2{}^{1/4}$ dependency of the p-type conduction process. This can be explained by assuming oxygen incorporated into the lattice is filling $V_o{}^{\cdot\cdot}$ already present due to acceptor impurities nearly always present in $BaTiO_3$ on the order of 100 ppm[57,58]. In this case the defect reaction may be expressed as:

$$1/2 \ O_2 + V_o{}^{\cdot\cdot} \rightleftharpoons O_o{}^X + 2 \ h^{\cdot} \tag{17}$$
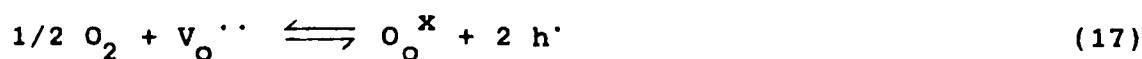
$$K_{17} = p^2 \ [V_o{}^{\cdot\cdot}] \ PO_2{}^{-1/2} \tag{18}$$

If the concentration of holes is negligible compared to the concentration of $V_o{}^{\cdot\cdot}$, then :

$$p = K_{17} \ [V_o{}^{\cdot\cdot}]^{-1} \ PO_2{}^{1/4} \tag{19}$$

Reactions of this sort emphasize the need to distinguish between the two types of excess oxygen :

1) <u>Stoichiometric excess</u> - more oxygen is incorporated into the lattice than is needed to satisfy the valency of the cations.

2) <u>Lattice Excess</u> - more oxygen is present than the available number of lattice positions.

Under atmospheric conditions, $BaTiO_3$ will normally exhibit n-type behavior, with a possibility of p-type behavior occurring at slightly higher PO_2's.

$\underline{TiO_2}$ - Rich Barium Titanate

Considerable controversy has been raised over the issue of the solubility of excess titanium onto the perovskite lattice of $BaTiO_3$[63,64,66]. In 1955 Rase and Roy[65] published the first complete binary phase diagram of $BaO - TiO_2$ (Figure 3.1.3b). It included a substantial amount of Ti^{+4} solubility, nearly four percent at 1400 $^{\circ}C$. Kulcsar[66] examined up to one percent excess Ti^{+4} and found a second Ti-rich phase which he identified as $BaTi_3O_7$. Negas[63] found the Ti-rich phase to be $Ba_4Ti_{13}O_{30}$, and below 1320 $^{\circ}C$ found the adjacent phase on the Ti-rich side to be $Ba_6Ti_{17}O_{40}$. Sharma[56] more recently has found a intergranular second phase which he has identified to be $Ba_6Ti_{17}O_{40}$ from the ratio of Ti/Ba counts from microprobe analysis.
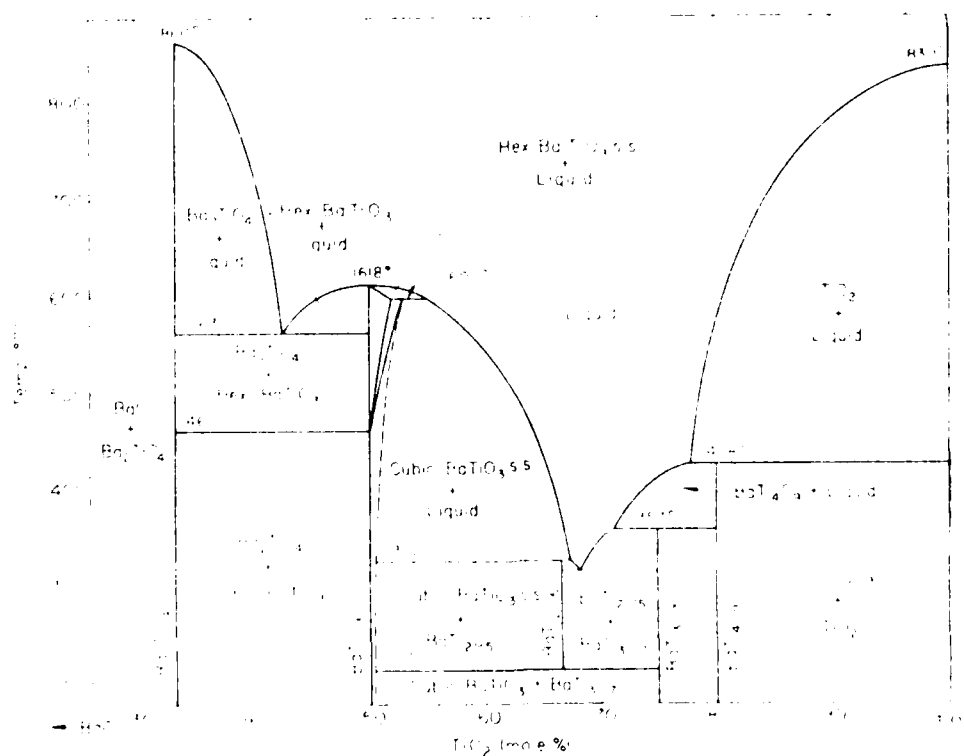
Figure 3.1.3b : Phase diagram of the binary system $BaO-TiO_2$[65].

While the exact composition of the Ti-rich phase is not agreed upon, there is a general consensus that the solubility range of Ti^{+4} onto the lattice is very small, on the order of $\leq$ 0.1 %. The following derivation of the defect chemistry assumes some solubility is possible, and follows closely a method introduced by Smyth[67,68].

One additional equation needs to be introduced in order to derive the defect chemistry. Excess Ti^{+4} absorbed onto the lattice creates an $\underline{V_o}^{\cdot\cdot}$ and a $\underline{V_{Ba}}''$, the underline indicating their source. This reaction is written:

$$TiO_2 \rightleftharpoons Ti_{Ti}{}^x + 2O_o{}^x + \underline{V_o}^{\cdot\cdot} + \underline{V_{Ba}}'' \qquad (20)$$
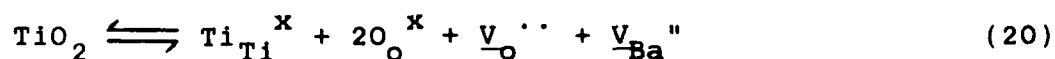
$$K_{20} = [\; \underline{V_o}^{\cdot\cdot}\;]\; [\; \underline{V_{Ba}}''\;]\; a_{TiO2} \qquad (21)$$

The neutrality condition becomes :

$$2[\; \underline{V_{Ba}}''\;] + 2[\; V_{Ba}''\;] + n = p + 2[\; V_o^{\cdot\cdot}\;] + 2[\; \underline{V_o}^{\cdot\cdot}\;] \qquad (22)$$

We define $PO_2{}^o$ to be the oxygen partial pressure where the number of oxygen ions is exactly equal to the number needed to compensate the cations present. ie:

$$N_O = N_{Ba} + 2N_{Ti} \qquad (23)$$

In this case then the only ionic defects present are those due to the excess Ti^{+4}. ie:

$$[\ V_{Ba}{}'' \ ] = [\ V_o{}^{\cdot\cdot} \ ] \qquad\qquad (24)$$

The theoretical PO_2 regime is divided into 5 regions: 1) Very low PO_2; 2) Low PO_2; 3) Intermediate PO_2; 4) High PO_2; and 5) Very high PO_2.

Very Low PO_2 : Two Phase Region

In this region we have removed sufficient oxygen to cause a second phase to exsolve, which for simplicity we assume to be $BaTi_3O_7$. A similiar set of equations could easily be derived assuming the second phase to be either $Ba_4Ti_{13}O_{30}$ or $Ba_6Ti_{17}O_{40}$. The reaction occurring as the second phase exsolves can be written:

$$3BaTiO_3 + 2V_{Ba}{}'' + 2V_o{}^{\cdot\cdot} \rightleftharpoons BaTi_3O_7 + 2Ba_{Ba}{}^x + 2O_o{}^x \qquad (25)$$
$$2O_o{}^x \rightleftharpoons O_2 + 2V_o{}^{\cdot\cdot} + 4e' \qquad (26)$$

$$3BaTiO_3 + 2V_{Ba}{}'' \rightleftharpoons BaTi_3O_7 + 2Ba_{Ba}{}^x + O_2 + 4e' \qquad (27)$$
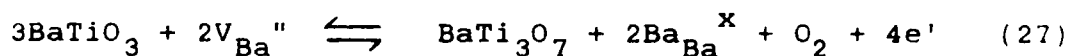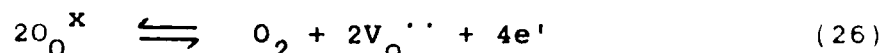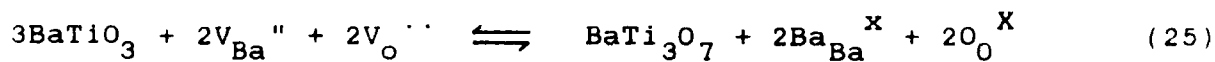
$$K_{27} = n^4 \ [\ V_{Ba}{}'' \ ]^{-2} \ PO_2 \qquad\qquad (28)$$

Essentially then, the second phase exsolving reduces the concentration of the $V_{Ba}{}''$. Utilizing the fact that the activity of the TiO_2 in this region is constant, the concentrations of the other ionic and electronic point defects become:

$$n = (\ 4K_{27}\ )^{1/6} (\ K_{20}\ a_{TiO2}\ )^{1/3} \ PO_2{}^{-1/6} \qquad (29)$$

$$p = (4K_{27})^{-1/6} (K_{20} \, a_{TiO2})^{-1/3} K_1 \, PO_2^{-1/6}$$

$$[V_{Ba}''] = 2K_{27}^{-1/6} (K_{20} \, a_{TiO2})^{2/3} K_1^{-1/2} \, PO_2^{1/6}$$

Therefore the PO_2 dependency of the e' and h˙ co
remains unchanged, as will be seen in the next PO_2 re

Low PO_2 : Single Phase, $n = 2[V_O^{˙˙}]$

Before a second phase exsolves there is a PO_2 reg
the predominate defects are $V_O^{˙˙}$. In this range the
constant, fixed by the excess titanium present in
Also, the concentration of oxygen vacancie
non-stoichiometry, $V_O^{˙˙}$, will be much greater
concentration of oxygen vacancies due to the excess T
$\underline{V}_O^{˙˙}$. The concentrations of the point defects become

$$n = (2K_3)^{1/3} \, PO_2^{-1/6}$$

$$p = K_1 (2K_3)^{-1/3} \, PO_2^{1/6}$$

$$a_{TiO2} = 1/2 \, K_{20}^{-1} [V_{Ba}''] (2K_3)^{1/3} \, PO_2^{-1/6}$$

Intermediate PO_2: Excess Ti^{+4} Dominated

As the PO_2 increases eventually the [$V_O^{˙˙}$] will
than the [$\underline{V}_O^{˙˙}$]. In this region then the exc
dominating the defect scheme. The amount of soli
determine the range over which this region dominate
indicates this range will extend to atmospheric PO_2

-65-

expect this region to be of paticular interest. The excess Ti^{+4} fixes the barium and oxygen vacancy concentration, ie:

$$[\underline{V}_{Ba}"] = [\underline{V}_O^{\cdot\cdot}] = constant \qquad (35)$$

$$[\underline{V}_O^{\cdot\cdot}] >> [V_O^{\cdot\cdot}] \qquad (36)$$

The defect concentrations become:

$$n = K_3^{1/2} [\underline{V}_O^{\cdot\cdot}]^{1/2} PO_2^{-1/4} \qquad (37)$$

$$p = K_3^{-1/2} [\underline{V}_O^{\cdot\cdot}] PO_2^{1/4} \qquad (38)$$

$$a_{TiO2} = K_{20} [\underline{V}_O^{\cdot\cdot}] [\underline{V}_{Ba}"] = constant \qquad (39)$$

Notice the 1/4 power dependencies of the electron and hole concentrations; this would be a likely region for a n-p type transition[51,54,58]. Also note in this region the oxygen concentration is exactly that required to compensate the cations.

High PO_2: $\underline{V}_O^{\cdot\cdot}$ Filling, $[\underline{V}_{Ba}"]$ Constant

As the PO_2 increases further, the $\underline{V}_O^{\cdot\cdot}$ begin to fill, but the $[\underline{V}_{Ba}"]$ remains constant (closed system). This fixes the hole concentration, therefore the conductivity in this region would be constant. The governing releationships become:

$$p = 2[\underline{V}_{Ba}"] = constant \qquad (40)$$

$$n = 1/2 \ K_1 \ [\ \underline{V}_{Ba}" \ ]^{-1} \tag{41}$$

$$[V_O{}^{\cdot\cdot}] = 4 \ K_1{}^{-2} \ K_3 \ [\underline{V}_{Ba}"]^2 \ PO_2{}^{-1/2} \tag{42}$$

$$a_{TiO2} = 4 \ K_1{}^{-2} \ K_{20}{}^{-1} \ [\underline{V}_{Ba}"]^3 \ K_3 \ PO_2{}^{-1/2} \tag{43}$$

Very High PO_2 : $p = 2[V_{Ba}"]$

Eventually the $\underline{V}_O{}^{\cdot\cdot}$ will be filled, and excess O_2 absorbed onto the lattice now creates additional $V_{Ba}"$ (equation 5). In this case the concentration of $V_{Ba}"$ will be greater than the concentration of $\underline{V}_{Ba}"$. Excess O_2 could also be compensated by the formation of $V_{Ti}""$, but for simplicity we will consider only $V_{Ba}{}^{\cdot\cdot}$. If $V_{Ti}""$ do form, the overall behavior remains the same, only the details of the equilibrium constant and power of the PO_2 dependency change. Interstitial O_2 is also unlikely due to the close-packed structure of $BaTiO_3$. The defect scheme corresponding to this region :

$$p = 2[V_{Ba}"] = (\ 2K_5 \ )^{1/3} \ PO_2{}^{1/6} \tag{44}$$

$$n = (\ 2K_5 \ )^{-1/3} PO_2{}^{-1/6} \tag{45}$$

$$[V_O{}^{\cdot\cdot}] = K_3 \ (\ 2K_5 \ )^{2/3} \ PO_2{}^{-1/6} \tag{46}$$

$$a_{TiO2} = K_5 \ K_3 \ K_{20}{}^{-1} = constant \tag{47}$$

This region is one of more theoretical interest, as a substantial PO_2 would be required to reach it. In practical situations the defect scheme will be dominated by the

incorporation of excess Ti^{+4}. Smyth[68] has expanded this analysis

to include the effects of the $\underline{V}_{Ba}$" and the $V_O^{\cdot\cdot}$ forming a neutral

complex. This essentially results in a shorter region over which

the the excess Ti^{+4} dominates the defect chemistry, and decreases

the likelihood of a second Ti-rich phase exsolving as the PO_2 is

reduced.

Figure 3.1.3c is a Kroger-Vink diagram of the five PO_2

regions included in the excess Ti^{+4} analysis.
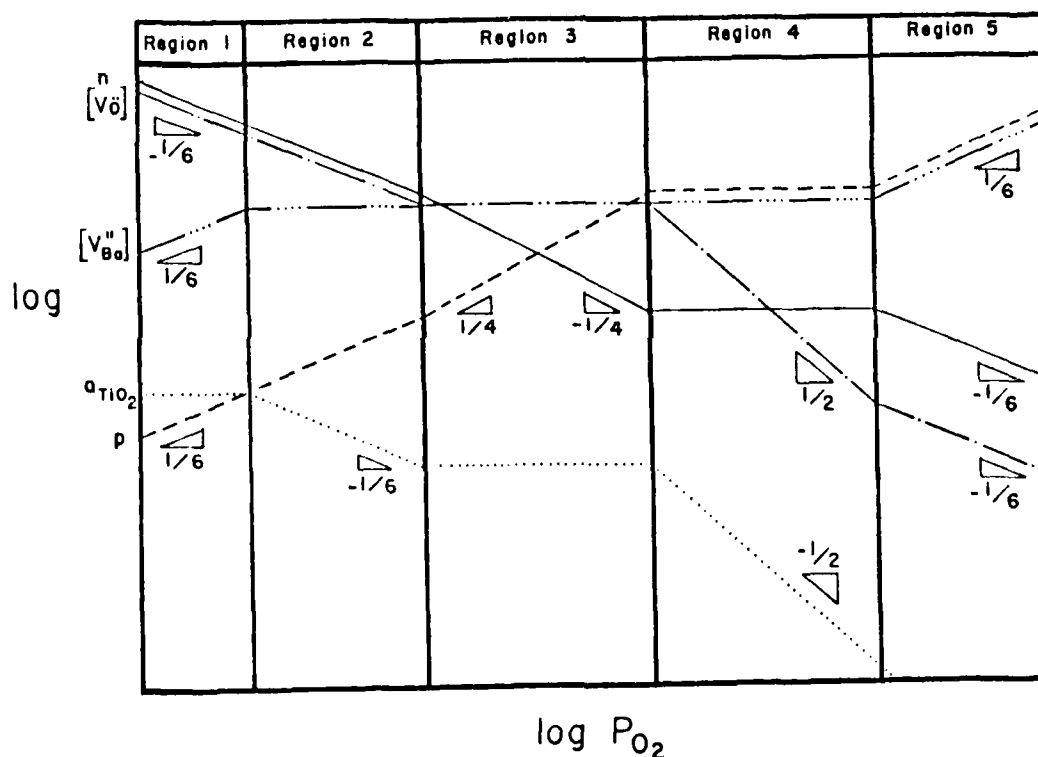
Figure 3.1.3c: Kroger Vink diagram for nonstoichiometric $BaTiO_3$ the case of excess Ti^{+4}.

BaO - Rich Barium Titanate

Past studies have indicated that BaO does not go into solid solution in $BaTiO_3$. The question becomes, where does it go and what phase does it form ? Some studies support the theory that a Ba-rich phase such as Ba_2TiO_4 forms in the grain boundaries. This second phase acts as a grain growth inhibitor, resulting in porous structures. Our study has found sintering to be inhibited the only if the calcination temperature of the $BaTiO_3$ is greater than approximately 800 °C. Ba-rich $BaTiO_3$'s calcined at lower temperatures sinter to dense structures, exhibiting normal grain growth. (refer to Section 3.5: Microstructure) Anderson[69] has attributed this phenomena to the existence of $BaCO_3$ remaining in the ceramic, which turns into a liquid at low temperatures and aids the sintering. However, we do find that the resulting Ba-rich phase is Ba_2TiO_4 and it does reside in the grain boundaries.

It has also been suggested that the excess Ba may form a superlattice accomodation of BaO layers such as the SrO layers theorized to exist in $SrTiO_3$[70]. However, more recent studies seem to indicate these Ruddleson and Popper phases are nonexistent in $BaTiO_3$. Nonetheless, if the excess Ba does not go into solid solution, then it will have no effect on the defect chemistry of $BaTiO_3$. It does have an effect on sintering characteristics and electrical properties, such as resistivity and degradation. These effects are covered in section 3.4.

3.1.3B : Doped Barium Titanate

Two possible schemes need to be derived; 1) Donor doping and 2) Acceptor doping.

Donor Doped BaTiO$_3$

The incorporation of cations onto the Ba^2 lattice position with valency greater than +2, or cations onto the Ti^{+4} site with valency greater than +4 constitutes donor doping. Donors have an effective positive charge with respect to the lattice due to their "donation" of an electron either to the conduction band, or to some ionic point defect. For BaTiO$_3$ common donors are La^{+3} and Nb^{+5}.

Two possible compensation mechanisms occur when a donor is added to BaTiO$_3$, depending upon the dopant concentration. Numerous studies[27,71,72,55,73] have shown that the resistivity of BaTiO$_3$ exhibits a minima with respect to the donor doping levels. This minima occurs for doping levels around several thousand ppm, at which point further additions of dopant dramatically increases the resistivity. This behavior is interpreted as the change in compensation mechanism from ionic to electronic, and back to ionic as doping levels increase. ie:

Resistivity:	High	Low	High
Donor Concentration:	< 1000 ppm	1000-4000 ppm	> 4000 ppm
Compensation Mechanism:	Ionic	Electronic	Ionic

These phenomena are all easily explained by simple analysis of the defect structure. Equations #1-6 still apply; the net effect of the donor dopant is to change the neutrality condition. It becomes:

Neutrality Condition

$$n + 2[V_{Ba}''] = p + 2[V_O^{\cdot\cdot} + [D^{\cdot}] \tag{48}$$

If we assume the donor is electronically compensated, then for every donor added, an electron state is created which lies close to the conduction band in energy (ionization energy <0.1 eV). Physically, the electron lies in the 3d band of the titanium ion; changing it to a +3 valence state. Conduction can be characterized either by a small-polaron hopping model from Ti^{+3} to Ti^{+3}, or by conduction within the 3D band of Ti. The defect scheme can be divided into three PO_2 pressure regimes, as was done for the stoichiometric undoped case in section 3.1.3A. The low and the high PO_2 regions remain unchanged, these being the cases for which the defect chemistry is dominated by $V_O^{\cdot\cdot}$ and V_{Ba}'' respectively. The high PO_2 regime becomes one of more theoretical than practical interest, as the addition of donors will move this region to PO_2's much greater than 1 atm O_2.

The defect chemistry of the intermediate PO_2 regime is dominated by the addition of donors, and represents the only change to the overall defect chemistry.

<u>Intermediate PO$_2$</u>: Donor Dominated

In this region the electron concentration is fixed by the concentration of the donor. ie:

$$n = [D^{\cdot}] = \text{constant} \tag{49}$$

The concentration of the other defects becomes:

$$p = K_1 [D^{\cdot}]^{-1} \tag{50}$$

$$[V_O^{\cdot\cdot}] = K_3 n^{-2} PO_2^{-1/2} \tag{51}$$

The range over which the donor dominates the defect chemistry depends upon its concentration. Several thousand ppm donor added to BaTiO$_3$[51,54] results in a semiconducting material which is dark blue in color; electronic compensation is occurring. Figure 3.1.3d is the Kroger Vink diagram for the doped case.
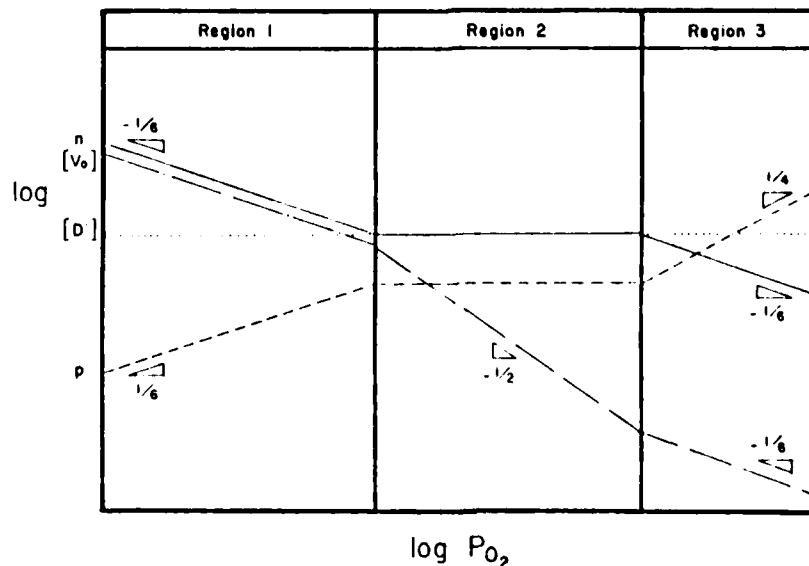
<u>Table 3.1.3d:</u> Kroger Vink diagram for the case of donor-doped BaTiO$_3$.

In the higher PO_2 range lesser or greater additions of donor result in a tan, high resistivity material. In this case the donors are being compensated ionically; for every two donors added one oxygen ion is absorbed into the lattice, and the donors become compensated by the formation of a cationic type defect. The exact mechanism is still not well understood, however the behavior is well described. In the lower PO_2 regions, the excess oxygen is lost and the donors once again are compensated by electrons. It is assumed that oxygen interstitials will not form to compensate the donors due to the close-packed structrure of the perovskite lattice.

Acceptor-Doped $BaTiO_3$

Incorporating cations onto the Ba^{+2} site with valency +1, or cations onto the Ti^{+4} site with valency less than +4 constitutes acceptor-doping. Common acceptor dopants for $BaTiO_3$ are Mg^{+2}, and Al^{+3}, both of which fit onto the Ti^{+4} site. Acceptors are negative with respect to the lattice due to their "acceptance" of an electron from the valence band, an ionic point defect, or a trap. Acceptors can be compensated electronically or ionically, similiar to the donor-doped case. Electronic compensation involves the formation of holes in the valence band, and may result in p-type behavior. Ionic compensation occurs when the acceptor dopant fixes the $V_o^{\cdot\cdot}$ concentration. In $BaTiO_3$, the latter is nearly always the case. The net effect of the acceptors is to change the neutrality condition of the defect

chemistry. It becomes:

$$n + [A'] = p + 2[V_O^{..}] \qquad (51)$$

In the low PO_2 region the defect scheme is dominated by the presence of $V_O^{..}$, equation 3. Increasing the PO_2 moves us into the acceptor-dominated region. Here the $V_O^{..}$ concentration is fixed by the acceptor concentration. ie:

$$2[V_O^{..}] = [A'] \qquad (52)$$

The corresponding defects are given by:

$$n = K_3^{1/2} [V_O^{..}]^{-1/2} PO_2^{-1/4} \qquad (53)$$

$$p = K_1 K_3^{-1/2} [V_O^{..}]^{1/2} PO_2^{1/4} \qquad (54)$$

Therefore the electron concentration is suppressed, which would be reflected by a corresponding decrease in the conductivity. As the PO_2 is increased further the $V_O^{..}$ concentration decreases slightly as excess O_O^{x} is added. We see the hole concentration is increasing while the electron concentration decreases. As long as the number of oxygen ions is less than the number of cations present, n-type behavior will be observed. However, as we pass this point equation 54 will dominate and a switch to p-type conductivity will occur. This corresponds to region #3 on figure 3.1.3e, the Kroger Vink

diagram for acceptor-doped $BaTiO_3$. Note $V_O^{\cdot\cdot}$ are still present due to the acceptor present. The range over which the acceptor dominates the defect chemistry will depend upon its concentration.

ACCEPTOR - DOPED $BaTiO_3$
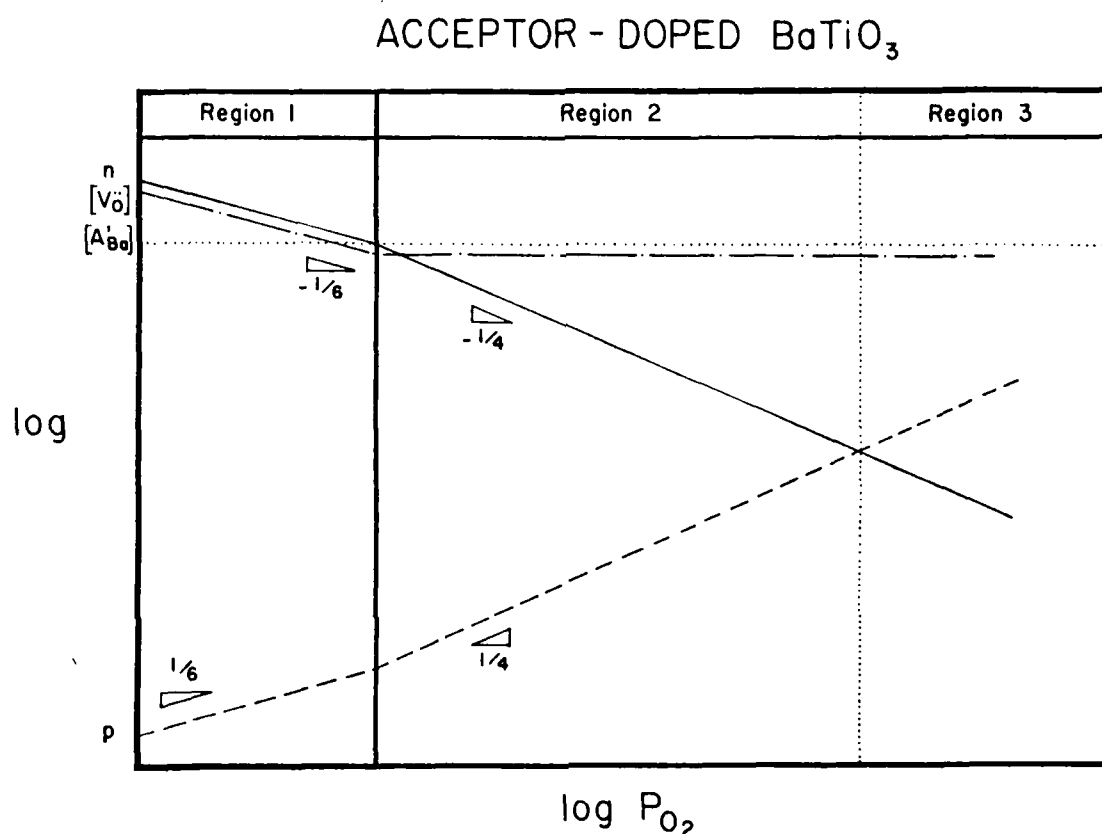
Figure 3.1.3e: Kroger Vink diagram for the case of acceptor-doped $BaTiO_3$.

Sharma[56] found this to be the defect structure of Al-doped $BaTiO_3$. The p-type region was characterized by a $PO_2^{1/4}$ dependency, matching the predicted behavior. An important assumption here is that the change in $V_O^{\cdot\cdot}$ concentration as oxygen is absorbed is small compared to the $V_O^{\cdot\cdot}$ concentration set up by the acceptor dopant.

3.2 Compositions / Test Specimens

3.2.1 Compound Preparation

The method utilized for preparing the barium and strontium titanate compositions used in this study was first described by Pechini . Essentially the process involves the quantitative mixing and and dissolution of the desired cations into an organic solution. The cations link to the oxygen radicals of the organic network in a random fashion, evenly dispersing the cations and dopants . The advantages to using this method include:

1) Powders are chemically homogeneous, with an evenly distributed dopant concentration . This is never the case when using titanates which have been prepared under the assumption that solid-state diffusional processes go to completion.

2) Resulting crystallites are uniformly-sized and very small; approximately 500 angstroms in diameter.

3) Powders require no ball milling or grinding, eliminating the addition of impurities often added during this step.

4) The process is simple and easily repeated. This should allow for meaningful comparison of results; not only of our own but with other studies' results also utilizing this process.

The experimental procedure involved in this process is outlined in Figure 3.2.1. A complete list of the raw materials and their respective sources is contained in Table 3.2.1. The steps in the entire process are as follows:

```
┌──────────────────────────┐   ┌──────────────────────────┐
│   Ethylene glycol         │   │   Ethylene glycol         │
│ Tetraisopropal titanate   │   │   Barium carbonate        │
│ Citric acid monohydrate   │   │ Citric acid monohydrate   │
└──────────────────────────┘   └──────────────────────────┘
          │                               │
     ┌──────────┐                   ┌──────────┐
     │Gravimetric│                  │Gravimetric│
     │ anaylsis  │                  │ analysis  │
     └──────────┘                   └──────────┘
          │                               │
          └──────────┬────────────────────┘
                ┌──────────┐
                │  Dopant  │
                │ Solution │
                └──────────┘
                     │
                ┌──────────┐
                │ Solution │
                │of cations│
                └──────────┘
                     │
                ┌──────────┐
                │Heat until│
                │polymerized│
                └──────────┘
                     │
                ┌──────────┐
                │Calcine at│
                │  800° C  │
                └──────────┘
                     │
          ┌────────────────────┐
          │ Press pellets and  │
          │ paint Pt electrodes│
          └────────────────────┘
                     │
          ┌────────────────────────────────┐
          │ Vacuum fire at 1375°C-1 hr.     │
          │ Anneal in dry air 1050°C-6 hr.  │
          └────────────────────────────────┘
```
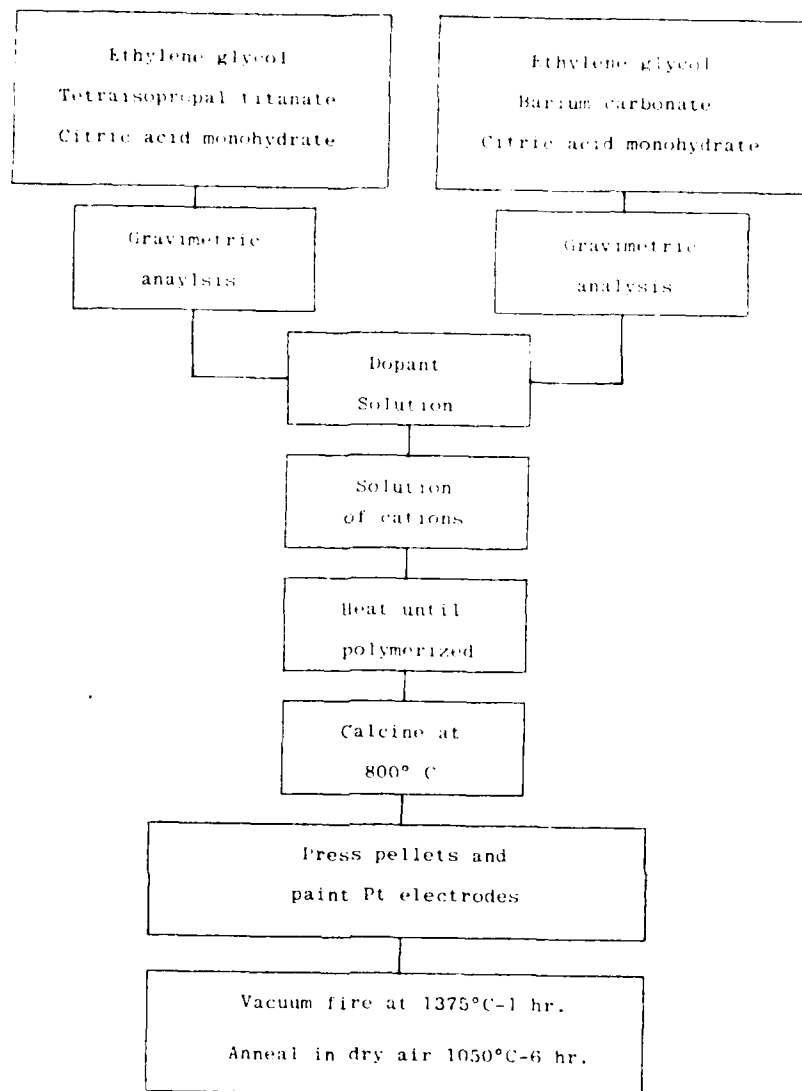
Figure 3.2.1: Typical flow sheet for preparation of $BaTiO_3$ capacitors.

a) An organic Ti^{+4} solution is prepared by mixing 200 ml of tetraisopropyl titanate (TPT) with 400 grams of anhydrous citric acid and 600 ml of ethylene glycol in a 2000 ml beaker. This solution is heated on a hot plate at approximately 150°C to dissolve the citric acid and the white hydrated TiO_2 which forms upon initial mixing. The

-77-

Raw Materials and Sources

Material	Source
$BaCO_3$	E.I. DuPont, De Nemours & Co. Solid State Dielectrics Div.
$SrCO_3$	E.I. DuPont, De Nemours & Co. Solid State Dielectrics Div.
Tyzor TPT (tetraisopropyl titanate)	E.I. DuPont, De Nemours & Co. Chemicals Division
Ethylene Glycol	E.I. DuPont, De Nemours & Co. Chemicals Division
Anhydrous Citric Acid	Chem Tech Industries
$Al(NO_3)_3 - xH_2O$	Apache Chemicals
$La_2(CO_3)_3 - xH_2O$	Apache Chemicals
Niobium Oxalate	Fisher Scientific
Zirconium Acetate	Fisher Scientific
$Mg(NO_3)_2$	Fisher Scientific
$PbCO_3$	Fisher Scientific

Table 3.2.1 Raw materials and their respective sources.

----

concentration of Ti^{+4} in this solution is determined by careful thermogravimetric analysis.

b) The cationic sources of $BaCO_3$, $SrCO_3$, $MgCO_3$, $La_2(CO_3)_3 - xH_2O$, $Al(NO_3)_3 - xH_2O$, and $PbCO_3$ are also thermogravimetrically analyzed. Reaction products are always X-rayed to ensure completion of the reaction and purity of the end product. These sources readily dissolve in the organic Ti^{+4} solution, hence it is not necessary to predissolve them.

COMPOSITIONS STUDIED

Nonstoichiometric:

Ba_xTiO_3 : x = 0.96, 0.97, 0.98, 0.99, 0.995, 0.998, 0.999, 1.000 1.001, 1.002, 1.005, 1.01, 1.02, 1.03, 1.04

Donor - Doped:

$Ba_{1-x}La_xTiO_3$ x = 0.001, 0.005, 0.01, 0.05

$BaTi_{1-x}Nb_xO_3$ x = 0.001, 0.005, 0.01, 0.05

Acceptor - Doped

$BaTi_{1-x}Al_xO_3$ x = 0.001, 0.005, 0.01, 0.05

$BaTi_{1-x}Mg_xO_3$ x = 0.001, 0.005, 0.01, 0.05

Curie Point Shifted

$Ba_{1-x}Sr_xTiO_3$ x = 0.05, 0.10, 0.15, 0.20, 0.25

$Ba_{1-x}Pb_xTiO_3$ x = 0.05, 0.10, 0.15, 0.20, 0.25

$BaTi_{1-x}Zr_xO_3$ x = 0.05, 0.10, 0.15, 0.20, 0.25

Table 3.2.2: Compositions prepared for degradation study.

----

degradation. This variation will also allow us to study the effect of density, grain size, and porosity on the degradation. The doped compositions were chosen in order to study the affect of both donor and acceptor dopants on the degradation. Note both A and B site dopants have been chosen. All the compositions have also been prepared for strontium titanate.

Twenty-five gram batches of all 73 compounds have been prepared. Larger quantities of the compounds have been made in

order to restock supplies and to supply the UMR / PSU program. (see section 1.2.2)

3.2.2 Pressing Test Specimens

After the calcination step of the preparation process, the powders are transferred to a Spex mill jar and subsequently "Spex-milled" to help break up the agglomerates present. Then, six weight percent polyvinyl alcohol solution (PVA) is added and thoroughly mixed , again with the Spex mill. The powder is now ready for pressing.

The powder is pressed into disks using a 1.25 cm diameter stainless steel die at a compaction pressure of 3500 kg/cm^2 (50000 psi). The thickness of the specimen depends upon the experiment in which it will be used. Previously, Keck[27] had encountered rupture problems during die release which he solved using a vacuum die. Our PVA binder system eliminates this problem.

To date, a complete set of ten .5 gram pellets has been pressed for each of the 73 compositions being studied. In addition, nearly 750 pellets have been pressed (and fired) for the joint PSU/UMR program.

3.2.3 Sintering

After pressing, the pellets were sintered in a SiC muffle tube furnace. An additional furnace was built in order to facilitate rapid firing of all of the initial 730 pellets, which is now complete.

Several problems were encountered during the sintering process which delayed electrical measurements until they were solved. These problems and the solutions we found to them are included here in order that it may be of some help to others who have encountered the same difficulties.

1) Initially the pellets were fired on a zirconia setter covered with ZrO_2 powder, but this resulted in unwanted surface contamination. Therefore, a layer of $BaTiO_3$ was substituted, both above and below the specimens. This solved the contamination problems but introduced problems with sticking. Powder stuck to the surface can be ground away; but we have found that those specimens which are ground contain impurities from the polishing media or suffer mechanical damage which alters the electrical properties. Though expensive, our final solution has been to sinter the samples on platinum foil. This also allows for stack firing of up to 24 pellets at a time. Since we started this practice, no problems with contamination have occurred.

2) The next problem encountered was sintering the pellets to a high density. The doped compositions sintered to high densities, 95 % theoretical at 1375 $^{\circ}C$ - 4 hours, but the undope. compositions proved to be more difficult to sinter. While we

found these easy to sinter to any density 92 %, increasing the density above this point using the compounds prepared by the organnometallic technique was difficult. This is particularily true for the nonstoichiometric $BaTiO_3$'s, as the presence of excess barium or titanium drastically changes the sintering characteristics. Many studies in the past[74-79] have addressed this problem. Bratschun[74] found the final density of stoichiometric $BaTiO_3$ is limited by the entrapment of pores due to rapid grain growth. He obtained high densities by firing at 1350 $^{\circ}$C for times of 50 hours or greater. Miller[75] sintered $BaTiO_3$ to 99% theoretical using an addition of 0.8 wt % sugar, but this required a firing time of 200 hours at 1350 $^{\circ}$C. Anderson[76] studied the initial sintering characteristics of $BaTiO_3$ and found oxygen ion vacancy diffusion through the grain boundaries controlled the initial sintering rate. Hyatt et.al.[77] found maximum densities were achieved in the 1260-1320 $^{\circ}$C range, generally on the order of 93-95 % theoretical. Kulcsar[78] sintered $BaTiO_3$ with variable Ba:Ti ratio and found excess barium inhibited grain growth, while excess titanium did not. Anderson[79] found the sintering rate of Ba-rich $BaTiO_3$, prepared by the organometallic technique, depended strictly upon the calcination temperature. Calcining at 700 $^{\circ}$C results in the excess barium existing as $BaCO_3$, which was found to increase the densification rate due to enhanced grain boundary diffusion of oxygen ions. Calcining at 1000 $^{\circ}$C results in the formation of BaO, which was found to hinter the sintering kinetics.

The problem became one of obtaining a high density without

firing the pellets for 200 hours. Initially, samples were sintered by placing them in a cool furnace, heating the furnace to either 1325, 1350, 1375, or 1400 $^{\circ}$C at 7 $^{\circ}$C/minute, holding the temperature from 1-4 hours, and then cooling at approximately 4 $^{\circ}$C/minute. Densities for the Ti-rich compositions were never above 91 % theoretical due to rapid grain growth entrapping pores. Maximum densities were obtained at 1325 $^{\circ}$C, but resulted in a non-uniform grain size due to exaggerated grain growth. Ba-rich compositions, which were calcined at 850 $^{\circ}$C, sintered to 92 % theoretical. Ba-rich compositions calcined at 750 $^{\circ}$C sintered to 97 % theoretical, reflecting the results obtained by Anderson[65]. Stoichiometric compositions sintered to 93 % theoretical. Obviously, only the excess barium compositions calcined at low temperatures gave satisfactory results.

The next step tried was vacuum firing for short times at the temperatures which had previously yielded the maximum densities, generally 1350 $^{\circ}$C. This resulted in an increase in the density on the order of 1-2 % across the board, but unfortunately resulted in not only extremely large grain sizes for the excess titanium compositions, but also reduced the specimens, thereby decreasing their resistivity. Subsequent annealing in air at the sintering temperature never seemed to completely bring the samples back to a fully-oxidized condition.

The last step tried was to leave the furnace constantly at the sintering temperature, and push the samples directly into the hot zone after binder burnout in a region at 450 $^{\circ}$C. After various sintering times the pellets were pulled out and quenched

into a region of the furnace at 700 ^{O}C. After half an hour the pellets were moved to the "cool" end of the muffle tube, still 300 ^{O}C, from which point they were transported into the room and cooled on an insulator. The results of this method are contained in Tables 3.2.3a-d. In all cases, the density was substantially improved. We are not sure why rapid sintering results in this behavior, but it may be due to lesser time being spent in a temperature region where the grain growth mechanism does not result in densification (i.e. surface diffusion).

Maximum densities for the excess-titanium compositions are still only 94-95 % theoretical, but this is quite good considering the sintering time. Density in this case is limited by the entrapment of pores, which can be seen in the microstructures of Section 3.2.4. A great deal of grain growth has occurred for all these compositions due to exaggerated grain growth. The excess-barium compositions sintered up to 97.5 % theoretical, without any excessive grain growth. This is due, again, to the $BaCO_3$ leftover from the low calcination temperature. Refer to this Section 3.2.4 for a complete microstructural analysis of the undoped $BaTiO_3$ compositions.

<u>Summary</u>

All of the specimens required to carry out our degradation and TSPC/DC measurements have been prepared. This represents about 1500 specimens, including those prepared for joint use with PSU. Numerous problems were encountered, but were overcome to a great degree. In general:

$$Ba_{.98}TiO_3$$
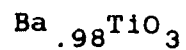
Firing (C/hrs)	Density (g/cm^3)	% Theoretical	% Open Porosity
1250 / 4	5.07	84.5	8.2
1325 / 2	5.48	91.3	1.6
1325 / 4	5.60	93.3	0.0
1375 / 1	5.53	92.2	0.1
1375 / 2	5.57	92.9	0.5
1375 / 4	5.61	93.5	0.1
1400 / 4	5.46	91.0	0.4

$$Ba_{.99}TiO_3$$
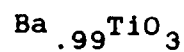
Firing (C/hrs)	Density (g/cm^3)	% Theoretical	% Open Porosity
1250 / 4	5.05	84.2	8.4
1325 / 2	5.39	89.9	2.2
1325 / 4	5.68	94.7	0.0
1375 / 4	5.65	94.1	0.5
1400 / 4	5.42	90.4	0.0

TABLE 3.2.3a: Densities of barium titanates : Ba:Ti = .98, .99

$$Ba_{.995}TiO_3$$

Firing (C/hrs)	Density (g/cm^3)	% Theoretical	% Open Porosity
1200 / 4	4.63	77.2	14.9
1250 / 4	5.39	89.8	4.3
1325 / 2	5.47	91.2	0.9
1325 / 4	5.64	94.0	0.0
1375 / 4	5.42	90.3	0.3
1400 / 4	5.54	92.4	0.0

$$Ba_{1.000}TiO_3$$

Firing (C/hrs)	Density (g/cm^3)	% Theoretical	% Open Porosity
1200 / 4	5.14	85.6	7.3
1250 / 4	5.60	93.3	1.6
1325 / 2	5.62	93.6	0.7
1325 / 8	5.66	94.4	0.3
1375 / 4	5.69	94.9	0.1

TABLE 3.2.3b: Densities of barium titanates: Ba:Ti = .995, 1.000

$$Ba_{1.005}TiO_3$$
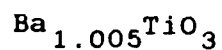
Firing (C/hrs)	Density (g/cm^3)	% Theoretical	% Open Porosity
1200 / 4	5.41	90.1	3.5
1250 / 4	5.53	92.1	2.6
1325 / 2	5.60	93.3	1.1
1325 / 4	5.65	94.1	0.8
1375 / 2	5.63	93.8	1.2
1375 / 4	5.66	94.3	0.6
1400 / 4	5.55	92.5	0.0

$$Ba_{1.01}TiO_3$$
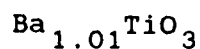
Firing (C/hrs)	Density (g/cm^3)	% Theoretical	% Open Porosity
1200 / 4	5.40	90.0	4.1
1250 / 4	5.52	92.0	1.7
1325 / 2	5.54	92.3	1.4
1325 / 4	5.63	93.8	0.2
1375 / 8	5.60	93.4	0.6
1400 / 4	5.55	92.5	0.0

TABLE 3.2.3c: Densities of barium titanates : Ba:Ti = 1.005, 1.01

$$Ba_{1.02}TiO_3$$
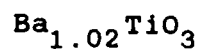
Firing (C/hrs)	Density (g/cm^3)	% Theoretical	% Open Porosity
1200 / 4	5.57	92.8	1.9
1250 / 4	5.68	94.6	0.8
1325 / 2	5.64	94.0	1.9
1325 / 4	5.75	95.9	0.3
1375 / 4	5.74	95.6	0.7
1400 / 4	5.84	97.3	0.0

TABLE 3.2.3d: Density of barium titanate : Ba:Ti = 1.02

1) Pellets need to be fired on platinum to eliminate surface contamination and sticking problems which result from the use of ZrO_2 or $BaTiO_3$ powder to cover a setter.

2) The best densification for the undoped compositions is obtained by rapid firing the pellets. The sintering temperature and time is dependent upon the degree of nonstoichiometry.

3.2.4 MICROSTRUCTURE

A thorough microstructural analysis is necessary in order to characterize the specimens in terms of grain size, porosity, and chemical homogeneity. Towards these ends a scanning electron microscope (SEM) is being used to take micrographs of the fired surface and the fracture surface of the specimens being used for degradation. Initially, optical micrographs of these specimens were being made but problems associated with polishing and etching were too numerous to obtain sufficient resolution and quality.

Figures 3.2.4 - 1 through 3.2.4 - 50 represent the microstructures of the undoped $BaTiO_3$ compositions which were used for degradation and TSPC/DC studies (section 4). A complete listing of the grain sizes for these specimens is contained in Tables 3.2.4a-b. The densities and porosity values are contained in Tables 3.2.3a   . Keep in mind the amount of porosity as seen in the fracture surfaces may appear higher than measured values due to the effect of porosity on cleavage paths, and grain pullouts. Kevex measurements were made on various specimens to detect possible second phases; these analyses are contained within the individual microstructural evaluations. Not all of the conclusions drawn on the microstructures are evident in the micrographs; notes were taken during SEM sessions to allow for a more complete analysis than could be covered by pictures alone. A short analysis of each specimen studied follows:

Ba:Ti Ratio	Firing (^{O}C/hrs)	Grain Size Range (microns)	Average (microns)
	1250 - 4	<1 - 6	2
.980	1325 - 4	<1 - 2	1
		10 - 50 EGG	35
	1375 - 4	10 - 80 EGG	40
	1250 - 4	<1 - 2	1
.990	1325 - 4	<1 - 2	1
		10 - 40 EGG	30
	1375 - 4	10 - 50 EGG	25
	1250 - 4	<1 - 2	1
.995	1325 - 4	<1 - 2	1
		10 - 80 EGG	45
	1375 - 4	10 - 40 EGG	20
	1250 - 4	1 - 8	4
1.000	1325 - 4	1 - 12	5
	1375 - 4	1 - 11	4
	1250 - 4	<1 - 8	3
1.005	1325 - 4	<1 - 15	10
	1375 - 4	3 - 30	13

Table 3.2.4a : Grain size ranges and averages for the undoped BaTiO$_3$ compositions.

Ba:Ti Ratio	Firing (^{O}C/hrs)	Grain size Range (microns)	Average (microns)
	1250 - 4	<1 - 8	3
1.010	1325 - 4	<1 - 10	2
	1375 - 8	1 - 10	5
	1250 - 4	<1 - 8	2
1.020	1325 - 4	<1 - 12	6
	1375 - 4	<1 - 15	7

Table 3.2.4b : Grain size ranges and averages for the undoped
BaTiO$_3$ compositions.

The micrographs utilize the following abbreviations:

TD = theoretical density
OP = open porosity
GS = average grain size (line intercept method)
S   = fired surface
F   = fracture surface

MICROCOPY RESOLUTION TEST CHART
NATIONAL BUREAU OF STANDARDS-1963-A

$$\underline{Ba}_{.98}TiO_3$$
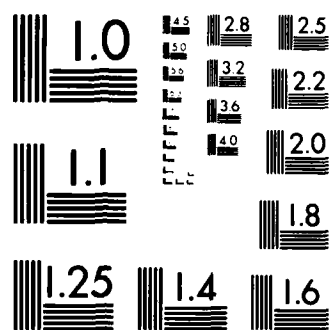
$1250\,^{\circ}C$ - 4 hours : At this sintering temperature we do not expect liquid-phase sintering to occur. The microstructure exhibits a variable grain size ranging from sub-micron to 8 microns in diameter, the variability probably due to agglomerates which sintered together. Normal grain growth is occurring, but not with a great deal of densification, indicating the sintering at this temperature may be surface-diffusion controlled. Porosity is entirely intergranular, the majority of which is open. No evidence of a second phase is detectable.

$1325\,^{\circ}C$ - 4 hours : At this firing temperature liquid forms (refer to Section 3.2.3) and enhances the sintering. This specimen *exhibits exaggerated* grain growth (EGG). The larger grains are 10-50 microns in size, with the small grain matrix 1-2 microns. The distribution is approximately 50/50. From the fracture surface it can be seen that the small grains are sintered well, with a small amount of intergranular porosity. Porosity is nearly entirely closed, as evidenced by the large amount of intragranular porosity contained in the large grains. Not evident on the micrograph, but a recrystallized second phase was evident in the grain boundaries. Note the large grains fractured through the grains.

$1375\,^{\circ}C$ - 4 hours : Increasing the sintering temperature resulted in virtually no increase in density, but did allow EGG to completely absorb the smaller grains. The grain size now

Ba:Ti = .98   1250°C 4hrs
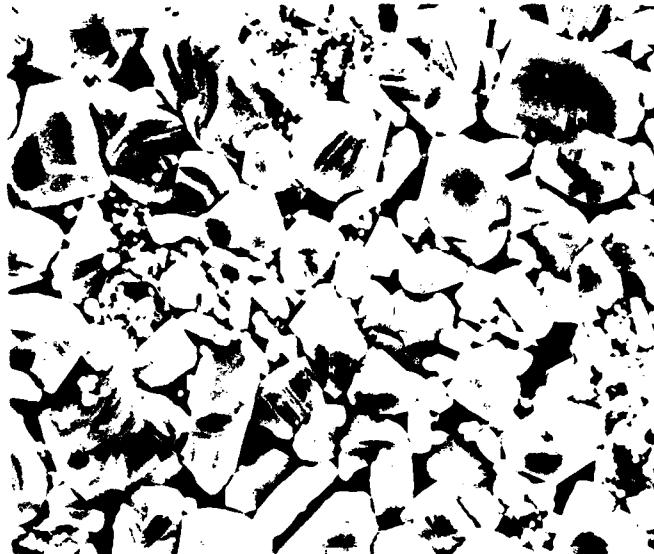
84.5 % TD   GS=2μ |————————|
8.2 % OP   10μ

Figure 3.2.4-1: S

Ba:Ti = .98   1250°C 4hrs

84.5 % TD   GS=2μ |————|
8.2 % OP   1μ

Figure 3.2.4-2: F

Ba:Ti = .98   1325°C 4hrs
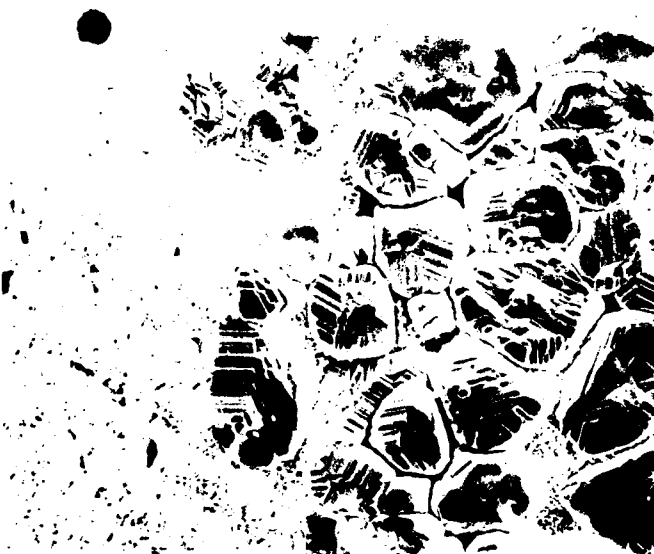
93.3 % TD   GS=1μ |—|
0.0 % OP   =35μ EGG   10μ

Figure 3.2.4-3: S

Ba:Ti = .98   1325°C 4hrs
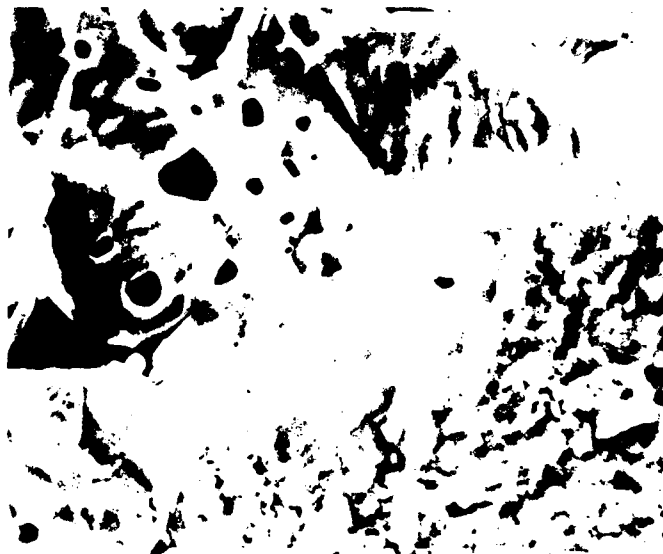
93.3 % TD   GS=1μ |————|
0.0 % OP   =35μ EGG   10μ

Figure 3.2.4-4: F

Figures 3.2.4,1-4:   Microstructures of the undoped BaTiO$_3$'s.
                     Ba:Ti = .98

Ba:Ti = .98   1375°C   4 hrs

93.5 % TD   GS = 40μ

0.1 % OP   10μ
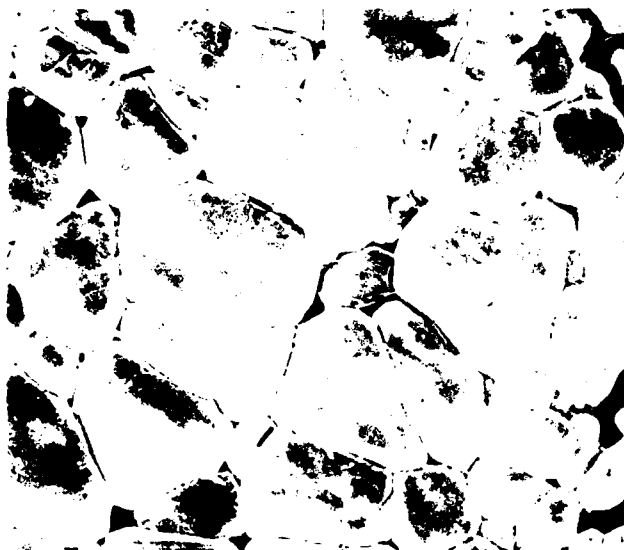
Figure 3.2.4-5: S

Ba:Ti = .98   1375°C   4hrs

93.5 % TD   GS = 40μ

0.1 % OP   10μ
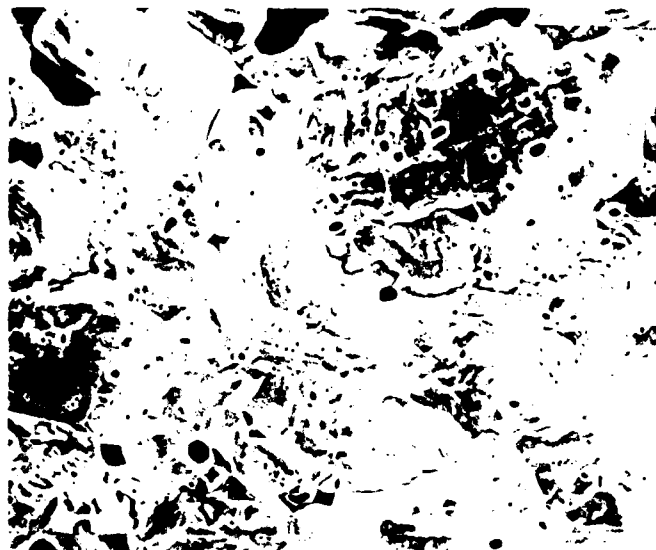
Figure 3.2.4-6: F

Ba:Ti = .98   1375°C   4hrs

92.2 % TD   GS = 40μ

0.1 % OP   1μ

Figure 3.2.4-7: F

Ba:Ti = .99   1250°C   4hrs

84.2 % TD   GS = 1μ

8.4 % OP   1μ
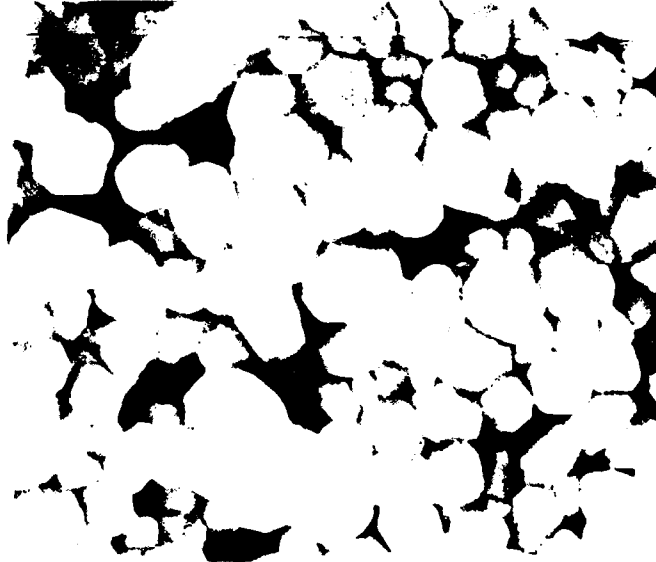
Figure 3.2.4-8: S

Figures 3.2.4 ; 5-8:   Microstructures of the undoped $BaTiO_3$'s.
Ba:Ti = .98, .99

ranges from 10-80 microns, with nearly total intragranular porosity. A second phase is evident in the grain boundary, with the Kevex unit finding the Ba:Ti ratio in this region to be around three. Whether this phase is $BaTi_3O_7$, $Ba_4Ti_{13}O_{30}$, or $Ba_6Ti_{17}O_{40}$[56,64,70] is indeterminable, as the Ba:Ti ratios of all of these Ti-rich phases lie close to three.

$$\underline{Ba}_{.99}TiO_3$$

1250 °C - 4 hours : This porous specimen exhibits a grain size on the order of 1-2 microns, with a great deal of open, intergranular porosity. Normal grain growth is occurring, as evidenced by the uniform size and shape of the grains. Some clustering is seen, probably due to agglomeration of the powder. No evidence of a second phase can be seen.

1325 °C - 4 hours : Increasing the firing temperature results in EGG as in the Ba:Ti = .98 specimen. However, the portion of large grains has decreased to approximately 30 % of the specimen, due to the lesser amount of the Ti-rich liquid phase. The 1-2 micron grains have sintered to a dense structure, the majority of the porosity being intragranular within the large, 10-40 micron grains. Small amounts of a second phase are in the grain boundaries.

1375 °C - 4 hours : Exaggerated grain growth has engulfed the smaller grain matrix, resulting in large grains 10-60 microns in diameter. This specimen decreased slightly in density, which is

Ba:Ti = .99   1250°C 4 hrs

84.2 % TD   GS=1μ

8.4 % OP   1μ

Figure 3.2.4-9: S

Ba:Ti = .99   1325°C 4 hrs

94.7 % TD   GS=1μ

0.0 % OP   =30μEGG   10μ

Figure 3.2.4-10: S

Ba:Ti = .99 1325°C 4hrs
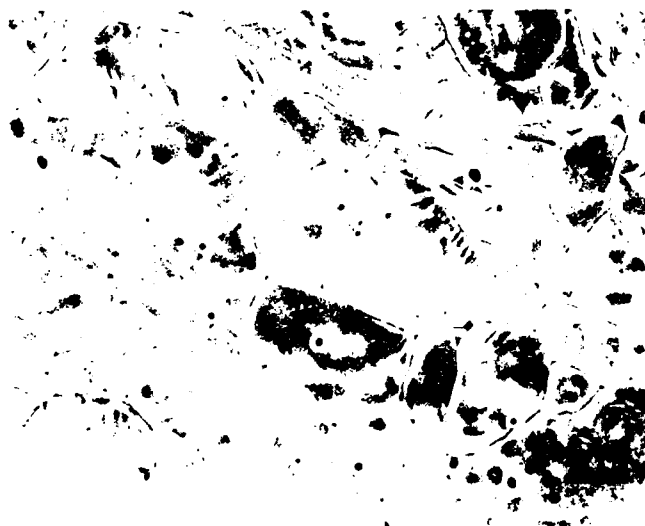
94.7 % TD   GS=1μ

0.0 % OP   =30μ EGG   10μ

Figure 3.2.4-11: F

Ba:Ti = .99 1375°C 4 hrs

94.1 % TD   GS=25μ

0.5 % OP   10μ

Figure 3.2.4-12: S

Figures 3.2.4 ; 9-12: Microstructures of the undoped $BaTiO_3$'s.
                       Ba:Ti = .99

probably due to the high grain growth rate and the resulting large amount of intragranular porosity. A second phase is evident in the grain boundary.

$\underline{Ba}_{.995}TiO_3$

1250 ^{O}C - 4 hours : This porous specimen exhibits 1-2 micron grains, with a large amount of intergranular porosity. Normal grain growth is occurring, as evidenced by the uniform grain size and shape. No second phase is evident. This specimen is very similiar in appearance to the Ba:Ti =.98, and .99 specimens fired at the same temperature.

1325 ^{O}C - 4 hours : This firing temperature results in a duplex structure of large, 10-80 micron grains, interdispersed with small, 1-2 micron grains. This is due to EGG. Porosity is intragranular and closed. The large grains exhibit an interesting phenomena on their surfaces, appearing to have recrystallized from surface diffusion or an evaporation-condensation process.

1375 ^{O}C - 4 hours : This specimen has large grains, 10-40 microns in size, as a result of liquid phase sintering. The grain size is somewhat smaller than the 1325 ^{O}C firing due to uniform liquid-phase sintering of the entire matrix compared to the EGG of a few large grains. Porosity is closed and intragranular. Less second phase is evident in the grain boundaries compared to the Ba:Ti =.98, and .99 specimens.

Ba:Ti=.99 1375°C 4hrs

94.1% TD GS=20μ   ⊢─┤

0.5%OP   10μ
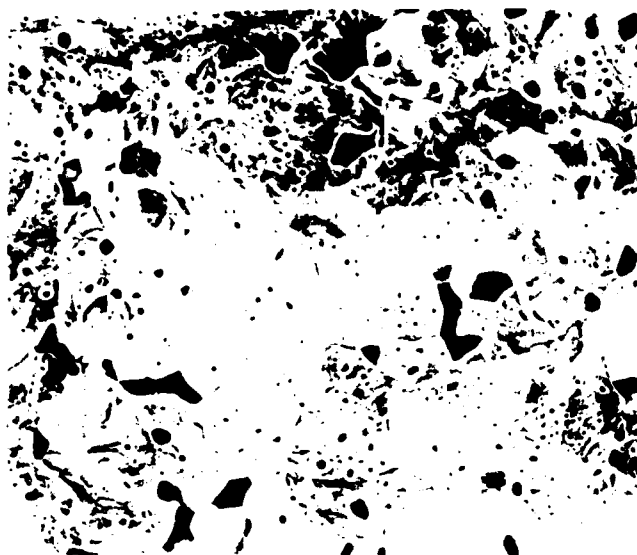
Figure 3.2.4-13: F

Ba:Ti=.995 1250°C 4hrs

89.8 % TD GS=1μ   ├────┤

4.3 % OP   10μ
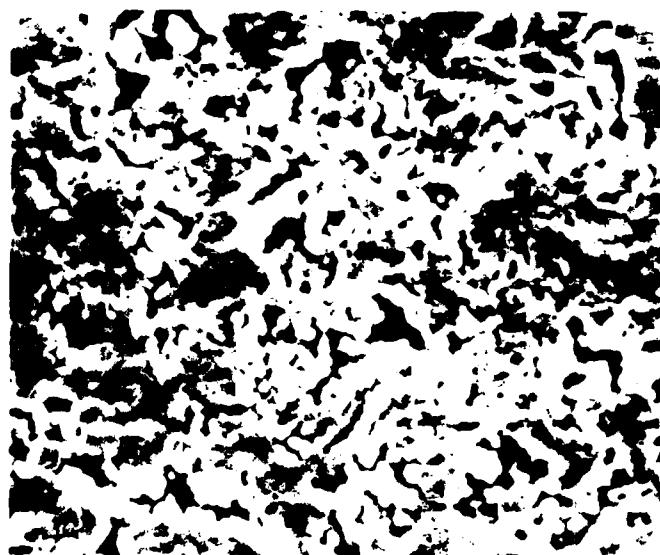
Figure 3.2.4-14: S

Ba:Ti=.995 1250°C 4hrs

89.8 % TD GS =1μ   ├───┤

4.3 % OP   1μ
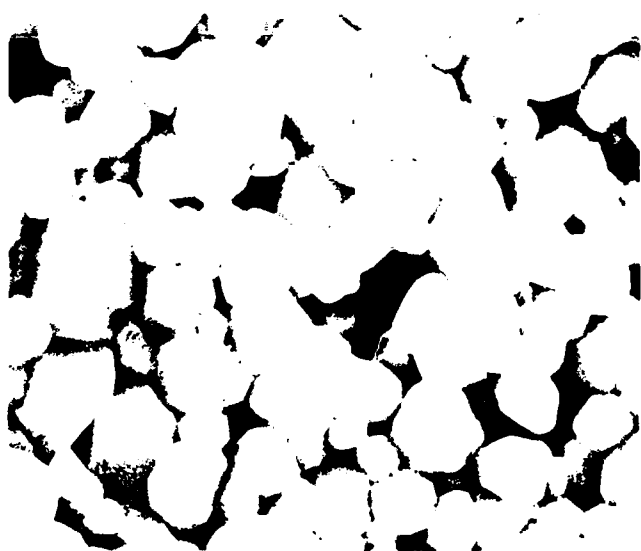
Figure 3.2.4-15: F

Ba:Ti=.995 1325°C 4hrs

94.0 % TD GS=1μ   ├────┤

0.0 % OP =45μEGG 100μ

Figure 3.2.4-16: S

Figures 3.2.4 ; 13-16: Microstructures of the undoped BaTiO$_3$'s.
Ba:Ti = .99, .995

-99-

Ba:Ti =.995 1325°C 4hrs

94.0 % TD   GS = 1μ

0.0 % OP   = 45μ EGG   10μ

Figure 3.2.4-17: F

Ba:Ti =.995 1325°C 4hrs

94.0% TD   GS = 1μ

0.0 % OP   = 45μ EGG   10μ

Figure 3.2.4-18: S

Ba:Ti =.995 1325°C 4hrs

94.0 % TD   GS = 1μ

0.0 % OP   = 45μ EGG   10μ

Figure 3.2.4-19: S

Ba:Ti =.995 1325°C 4hrs

94% TD   GS = 1μ

0.0% OP   = 45μ EGG   1μ

Figure 3.2.4-20: S

Figures 3.2.4 - 17-20:   Microstructures of the undoped BaTiO$_3$'s
Ba:Ti = .995

Ba:Ti = .995   1375°C 4hrs

90.3 % TD   GS=20μ   ⊢————⊣

0.3 % OP   10μ
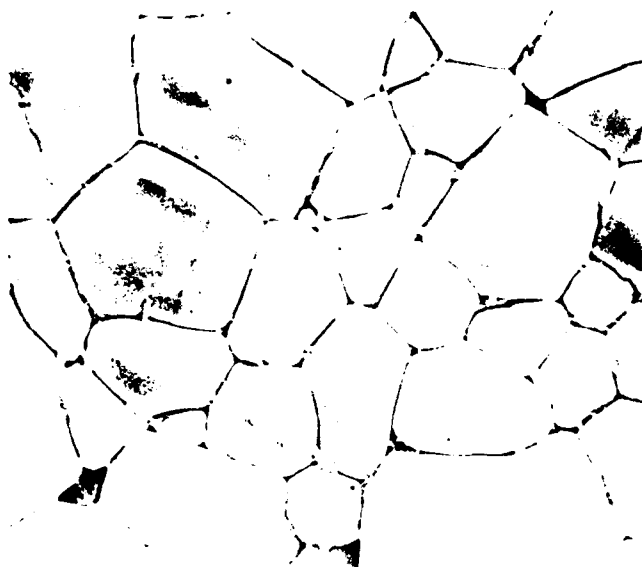
Figure 3.2.4-21: S

Ba:Ti = .995   1375°C 4hrs

90.3 % TD   GS =20μ   ⊢————⊣

0.3 % OP   10μ
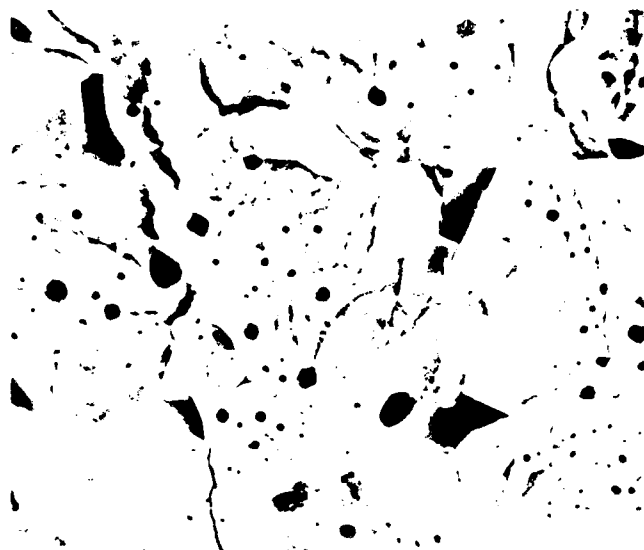
Figure 3.2.4-22: F

Ba:Ti = 1.00   1250°C 4hrs

93.3 % TD   GS= 4μ ⊢————⊣

0.6 % OP   10μ

Figure 3.2.4-23: S

Ba:Ti = 1.00   1250°C 4hrs

93.3 % TD   GS = 4μ ⊢————⊣

0.6 % OP   10μ
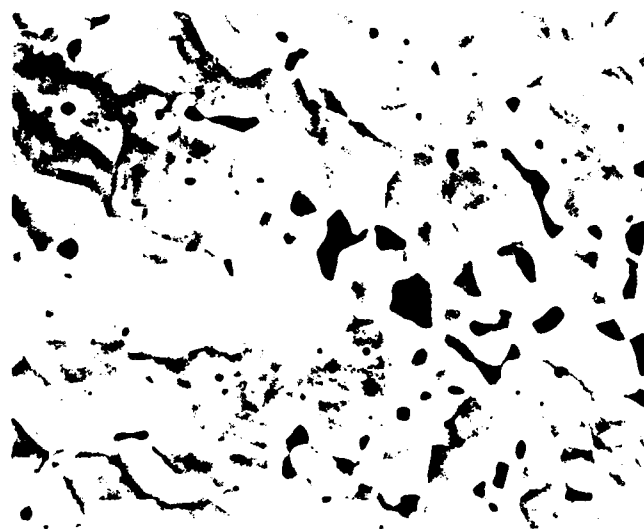
Figure 3.2.4-24: F

Figures 3.2.4 ; 21-24: Microstructures of the undoped BaTiO$_3$'s.
Ba:Ti = .995, 1.000

$$\underline{Ba}_{1.000}TiO_3$$
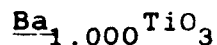
<u>1250</u> ^oC - 4 hours : This specimen exhibits a grain size ranging from 1-8 microns, with an average size of 4 microns. Normal grain growth is occurring. With a density of 93.3 % theoretical, this sample sintered amazingly well. The fracture surface broke through the grains, unlike any of the other 1250 ^oC specimens with Ba:Ti < 1. Porosity is mostly intergranular, and slightly connected, with a very small amount of intragranular porosity. This particular specimen showed regions within the dielectric that were very porous, Figures 3.2.4: 25-26 , which are probably due to uneven distribution of the PVA binder sytem.

<u>1325</u> ^oC - 4 hours : This specimen differs from all those with Ba:Ti < 1 in that it exhibits no trace of exaggerated grain growth. This indicates the composition must be stoichiometric, or very nearly so. Normal grain growth is occurring, with the grain size ranging from 1-8 microns. The fracture surface reveals some intragranular porosity, but the majority is intergranular.

<u>1375</u> ^oC - 4 hours : Even 60 ^oC above the eutectic temperature of Ti-rich $BaTiO_3$ this specimen shows no sign of liquid formation and the associated increase in the sintering rate. Normal grain growth is occurring, with a grain size ranging from 1-10 microns. A slightly larger amount of intragranular porosity is present, which is not surprising as the increased grain growth rate will allow more pores to be absorbed rather than expelled.

Ba:Ti=1.00   1250°C   4 hrs
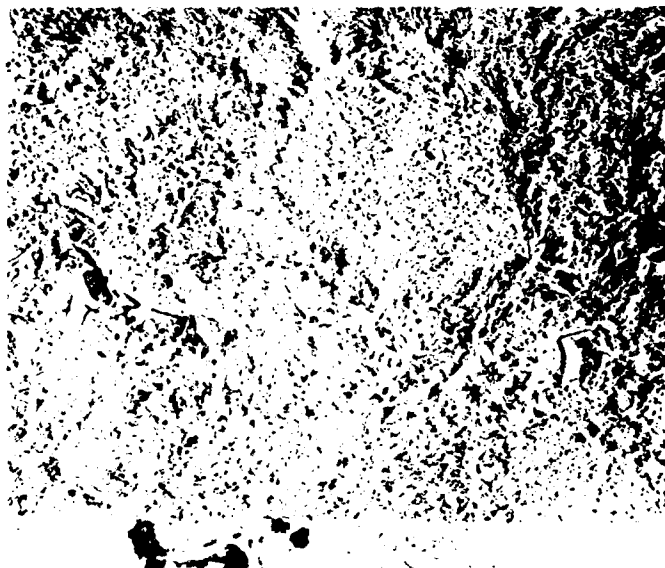
93.3% TD   GS=4μ   ⊢————⊣
1.6 %OP   100μ

Figure 3.2.4-25: F

Ba:Ti=1.00   1250°C   4 hrs

93.3% TD   GS=4μ   ⊢————⊣
1.6 % OP   10μ

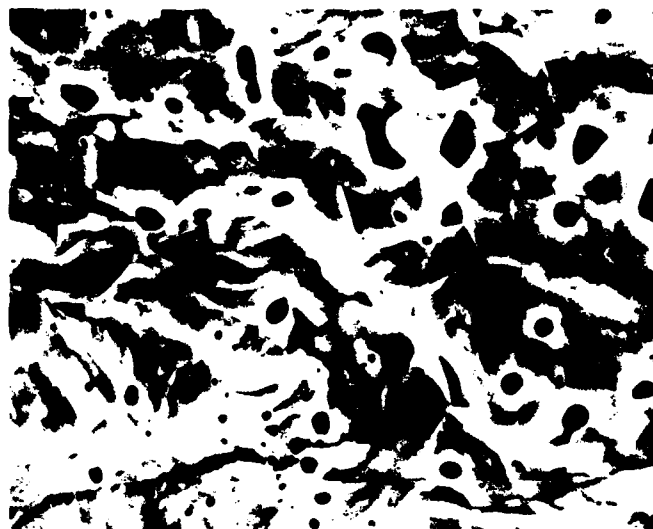Figure 3.2.4-26: F

Ba:Ti=1.00   1325°C 4hrs
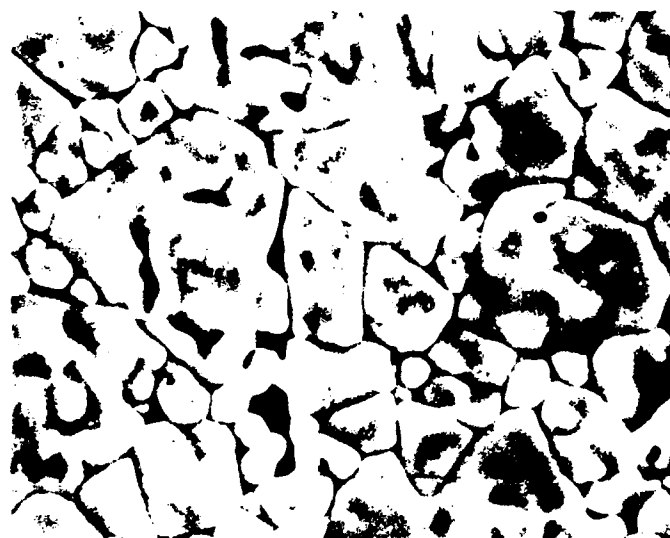
93.6 % TD   GS=5μ   ⊢————⊣
0.7 %OP   10μ

Figure 3.2.4-27: S

Ba:Ti=1.00   1325°C 4hrs
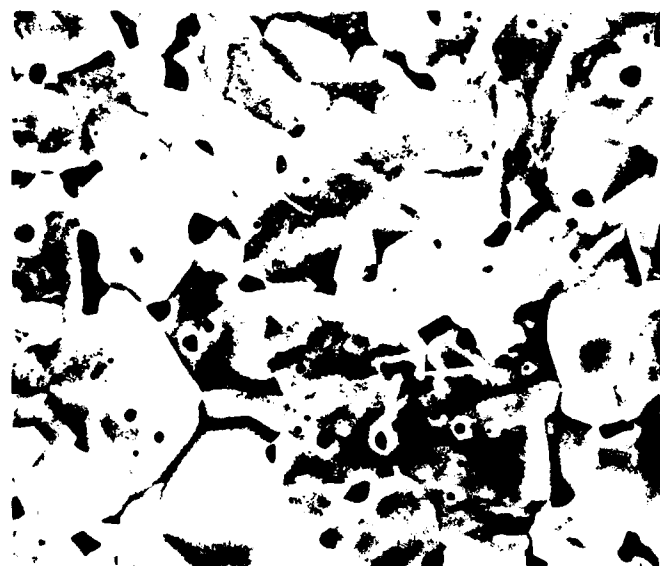
93.6 %TD GS=5μ   ⊢————⊣
0.7 %OP   10μ

Figure 3.2.4-28: F

Figures 3.2.4 ; 25-28: Microstructures of the undoped BaTiO$_3$'s.
                        Ba:Ti = 1.000

Ba:Ti=1.00   1375°C 4hrs

94.9 % TD   GS=4u ⊢————⊣
0.1 % OP   10u

Figure 3.2.4-29: S

Ba:Ti=1.00   1375°C 4hrs
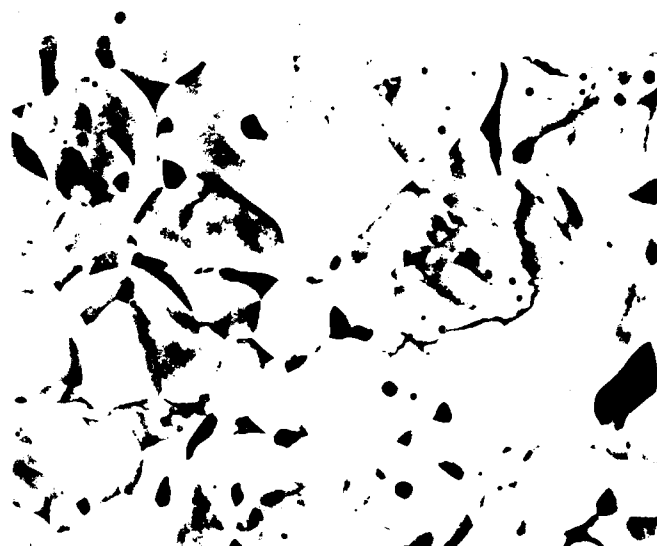
94.9 % TD   GS=4μ ⊢————⊣
0.1 % OP   10μ

Figure 3.2.4-30: F

Ba:Ti=1.00   1375°C   4hrs
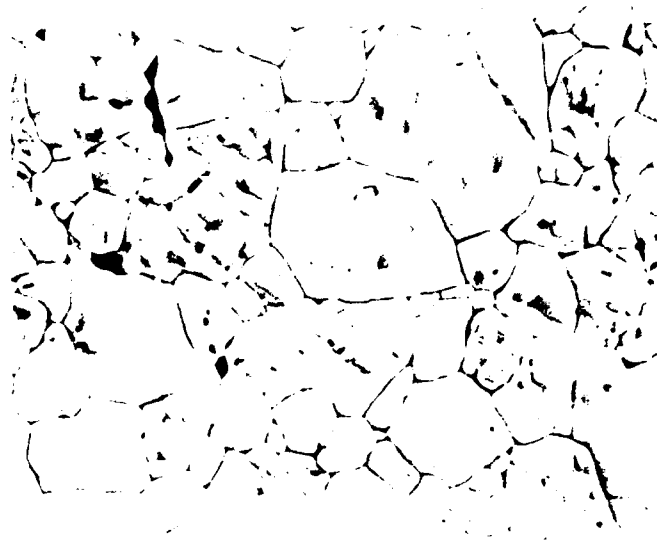
94.9% TD   GS=4μ   ⊢——⊣
0.1 % OP   10μ

Figure 3.2.4-31: S

Ba:Ti=1.00   1375°C   4hrs
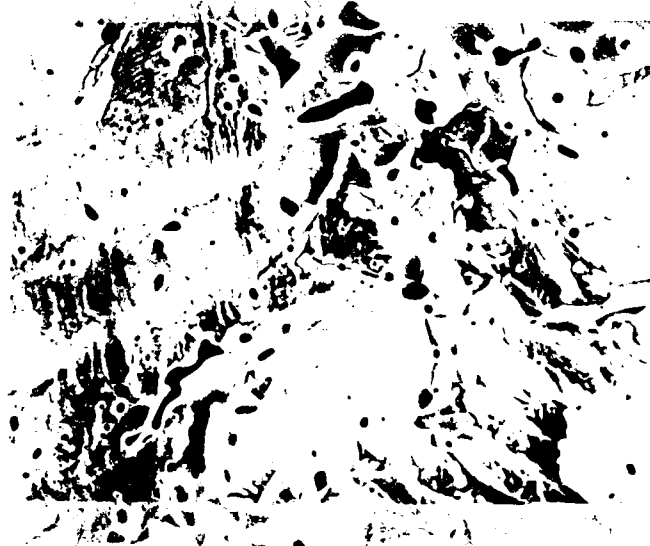
94.9% TD   GS=4μ   ⊢——⊣
0.1 % OP   10μ

Figure 3.2.4-32: F

Figure 3.2.4 : 29-32:   Microstructures of the undoped BaTiO$_3$'s.
Ba:Ti = 1.000

$$\underline{Ba}_{1.005}TiO_3$$
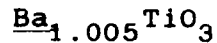
<u>1250</u> ^{O}C - 4 hours : The compositions with excess barium sintered much better than expected. Refer to Section 3.2.3 for a full explanation . At this firing temperature the specimen exhibits normal grain growth, the grains ranging from 1-8 microns in size. Several porous regions were found within the dielectric, but it is not known if this is due to a processing step, or some inherent result of the excess barium. Porosity is both intergranular and intragranular, the value of open porosity being 2.6 %. The intragranular porosity is rectangular in shape, which is unusual. No evidence of a second phase present.

<u>1325</u> ^{O}C - 4 hours : At this sintering temperature grain growth is markedly increased. The specimen consists mainly of grains on the order of 10-15 microns in size. Very few regions of 1-2 micron grains are seen. The density of this sample is only 2% more than the 1250 ^{O}C firing run, but it has much larger grains. Porosity is mostly intergranular, but closed. No evidence of a second phase is present.

<u>1375</u> ^{O}C - 4 hours : The grains have grown very large at this firing temperature, ranging from 5-30 microns. Although no second phase is detectable, something in addition to the pure $BaTiO_3$ must be present to sinter these specimens so well (see section 3.2.3). The porosity is mixed evenly between intragranular and intergranular. The fracture surface shows the fracture plane passing through the grains instead of strictly

Ba:Ti = 1.005   1250°C 4hrs

Ba:Ti = 1.005   1250°C 4hrs

92.1 % TD   GS = 3μ

2.6 % OP   10μ

92.1 % TD   GS = 3μ

2.6 %   10μ
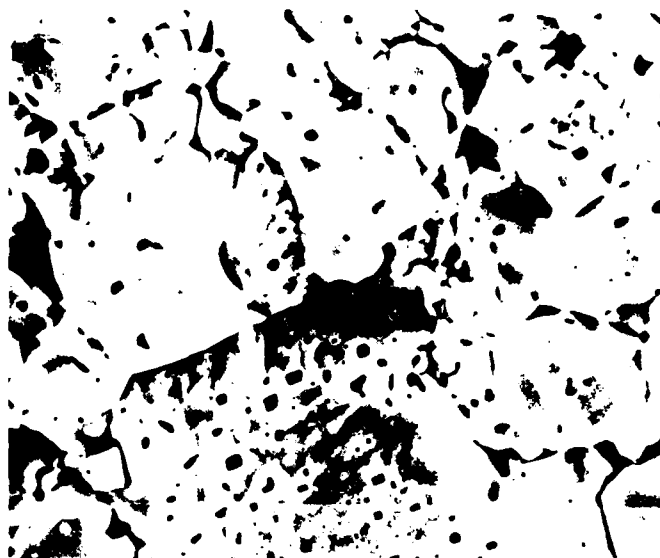
Figure 3.2.4-33: S

Figure 3.2.4-34: F
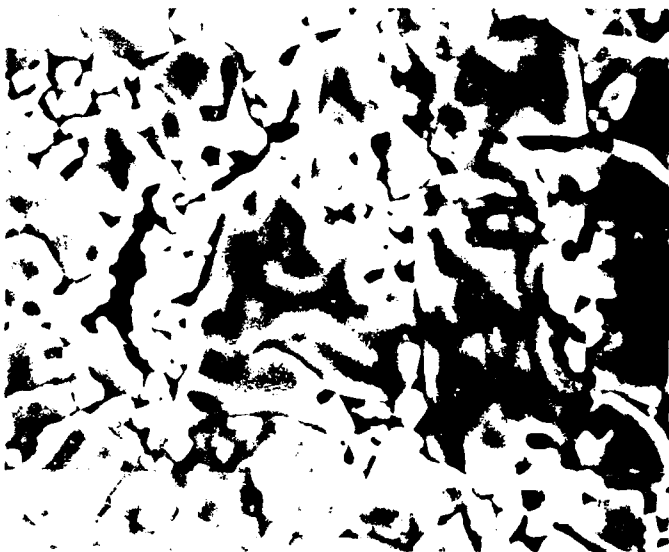
Ba:Ti = 1.005   1325°C 4hrs

Ba:Ti = 1.005   1325°C 4hrs

94.1 % TD   GS = 10μ

0.8 % OP   10μ

94.1 % TD   GS = 10μ

0.8 % OP   10μ

Figure 3.2.4-35: S

Figure 3.2.4-36: F

Figures 3.2.4 ; 33-36: Microstructures of the undoped BaTiO$_3$'s.
Ba:Ti = 1.005

Ba:Ti=1.005 1375°C 4hrs

94.3 % TD   GS=13μ ┣━━━━━┫

0.6 % OP   10μ

Figure 3.2.4-37: S

Ba:Ti=1.005   1375°C 4hrs

94.3 % TD   GS=13μ ┣━ ━━┫

0.6 % OP   10μ

Figure 3.2.4-38: F

Ba:Ti=1.01   1250°C 4hrs

92.0 % TD   GS=3μ   ┣━┫

μ
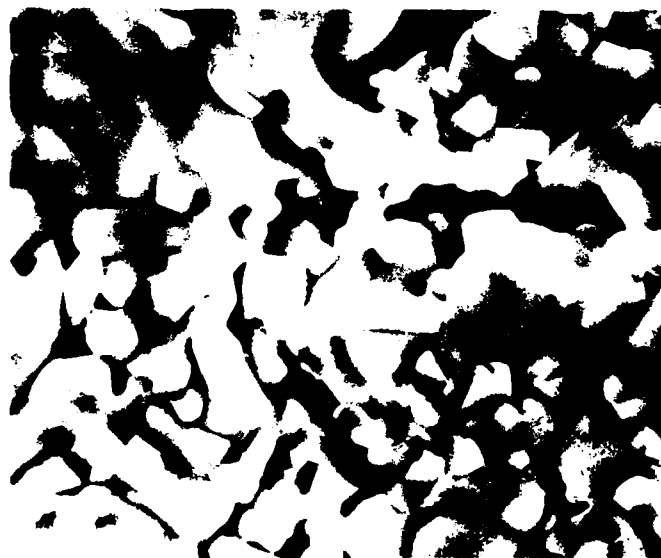
Figure 3.2.4-39: S

Ba:Ti=1.01   1250°C 4hrs

92.0 % TD   GS=3μ ┣━━━━━┫

10μ
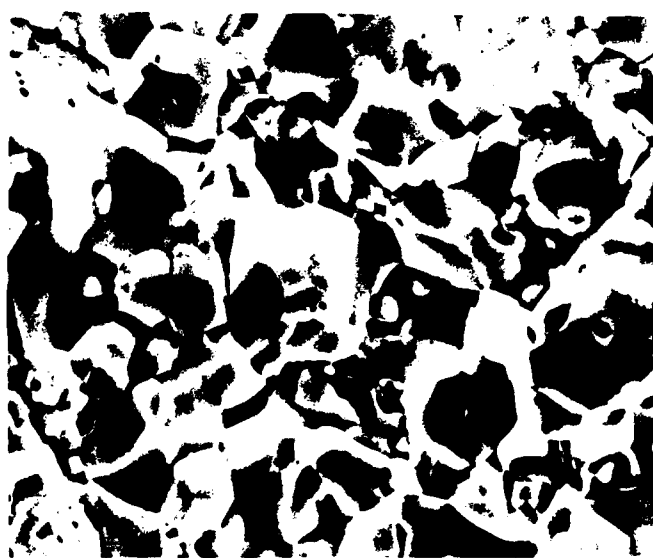
Figure 3.2.4-40: F

Figures 3.2.4 ; 37-40: Microstructures of the undoped BaTiO$_3$'s.
Ba:Ti = 1.005, 1.01

through the grain boundaries, indicating some sort of reaction is occurring in the grain boundaries during sintering. No evidence of a second phase is present by inspection and Kevex.

$$Ba_{1.01}TiO_3$$
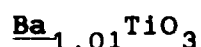
1250 °C - 4 hours : This specimen has a density 92.0 % of theoretical, with only 1.7 % open porosity. The grains range in size from submicron to 8 microns, with the porosity being mostly intergranular. A few very porous regions appeared in the interior of the dielectric, probably due to improper binder mixing. This composition sinters better than expected, refer to Section 3.2.3 for a full explanation. No evidence of a second phase by inspection or Kevex.

1325 °C - 4 hours : Surprisingly this specimen does not exhibit grains larger than the 1250 °C specimen. These range from 1-2 microns, with only a few areas exhibiting 7-10 micron grains. Density increased only 0.3 %, and the open porosity decreased to 0.3 %. Normal grain growth appears to be occurring. Porosity is intergranular, with a small amount of intragranular porosity evident in the larger grains. The large grains are probably agglomerates which sintered together. Still no evidence of a second phase.

1375 °C - 8 hours : At this temperature normal grain growth is occurring, the grains ranging in size from 3-10 microns. The density is up to 93.4 % theoretical, with the open porosity down to .6 %. Porosity is mostly intergranular. Some areas appear to

Ba:Ti = 1.01   1325°C 4hrs

10μ   1μ
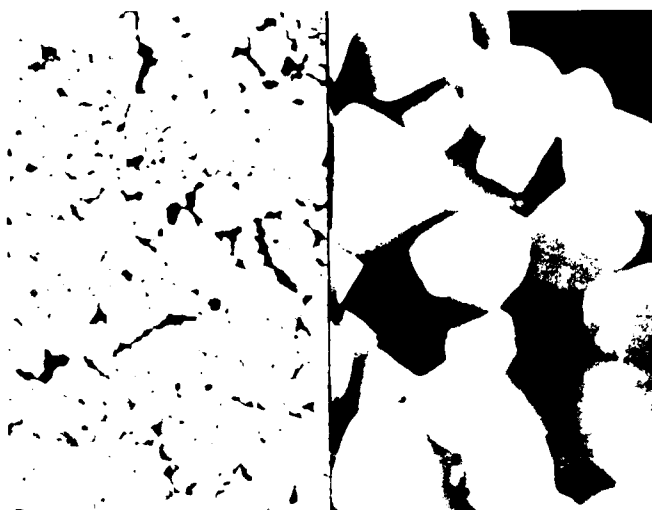
93.8 % TD 0.2 % OP   GS = 2μ
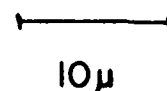
Figure 3.2.4-41: S

Ba:Ti = 1.01   1325°C 4hrs
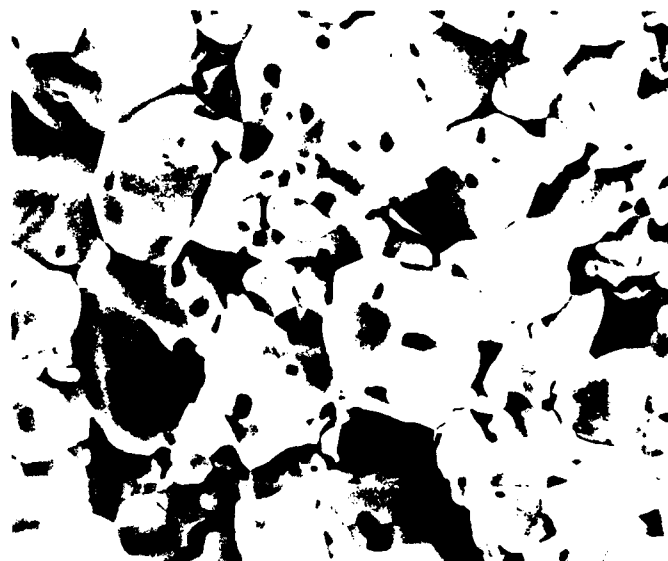
93.8 % TD   GS = 2μ

0.2 % OP   10μ

Figure 3.2.4-42: F

Ba:Ti = 1.01   1375°C 8hrs
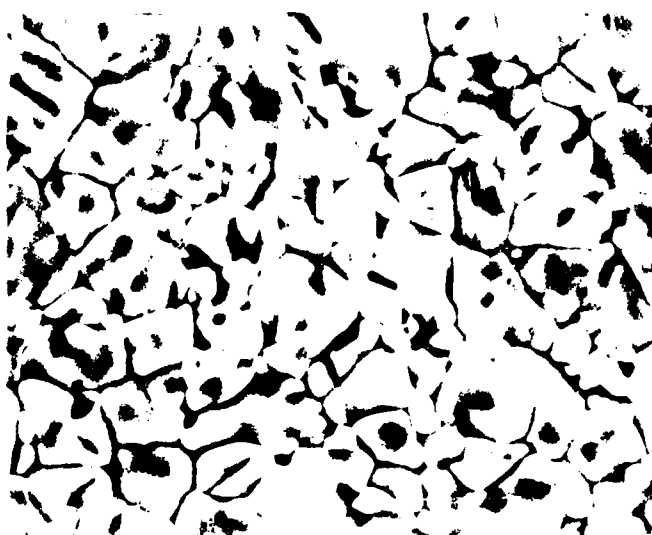
93.4 % TD   GS = 5μ

0.6 % OP   10μ

Figure 3.2.4-43: S

Ba:Ti = 1.01   1375°C 8hrs

93.4 % TD   GS = 5μ

0.6 % OP   10 μ

Figure 3.2.4-44: F

Figures 3.2.4 ; 41-44:   Microstructures of the undoped BaTiO$_3$'s.
Ba:Ti= 1.01

have a second phase present, appearing as small globules, but Kevex results show these to be $BaTiO_3$.

$$\underline{Ba}_{1.02}TiO_3$$
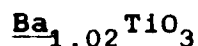
<u>1250</u> ^{O}C - 4 hours : This specimen sintered to 92.8 % theoretical, which was unexpected. Grains are mostly 1-2 microns in size, with a few areas of 8-10 micron grains. Whether these areas are due to agglomerates or the presence of a barium-rich phase is indeterminable. Porosity is mostly intergranular, and only slightly connected (open porosity = 1.9%). Still no evidence of a second phase with the Kevex unit.

<u>1325</u> ^{O}C - 4 hours : Increasing the sintering temperature in creased the overall grain size; now the microstructure exhibits only a few regions of 1-2 micron grains. Porosity is intergranular, and closed. Density is 95.9 % theoretical, which is very high for a barium-rich $BaTiO_3$. No evidence of a second phase is present.

<u>1375</u> ^{O}C - 4 hours : Increasing the sintering temperature again has increased the grain size, but this time it has a detrimental effect on the density, decreasing it 0.3 %. As is evident from the micrographs, the increase in grain growth rate has resulted in more intragranular porosity than the 1325 ^{O} specimen. The grain size ranges from 1-15 microns, but only a few regions of the smaller grains is can be seen. Surprisingly, still no evidence of a second phase is observed.

Ba:Ti = 1.02   1250°C 4hrs
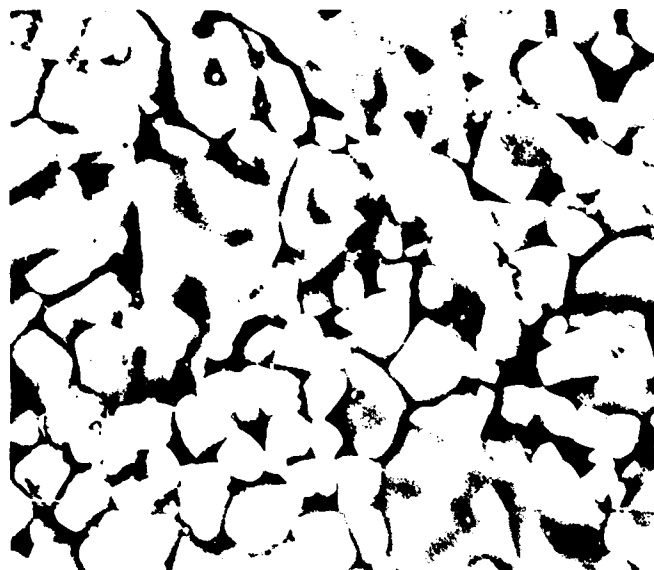
94.6.% TD   GS = 2μ
0.8 % OP   1μ

Figures 3.2.4-45: S

Ba:Ti = 1.02   1250°C 4hrs
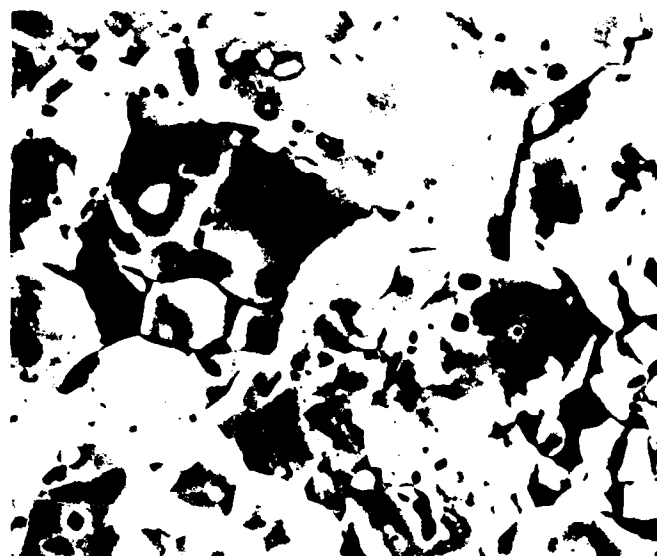
94.6 % TD   GS = 2μ
0.8 % OP   10μ

Figure 3.2.4-46: F

Ba:Ti = 1.02   1325°C 4hrs
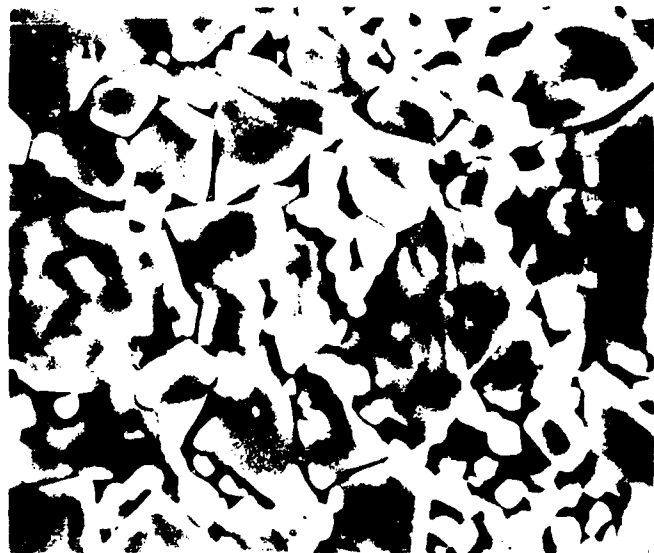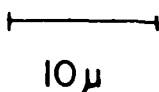
95.9 % TD   GS = 6μ
0.3 % OP   10μ

Figure 3.2.4-47: S

Ba:Ti = 1.02   1325°C 4hrs

95.9 % TD   GS = 6μ
0.3 % OP   10μ
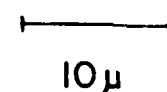
Figure 3.2.4-48: F

Figures 3.2.4 ; 45-48: Microstructures of the undoped BaTiO$_3$'s.
                        Ba:Ti=1.02

Ba:Ti = 1.02   1375°C 4hrs   Ba:Ti = 1.02   1375°C 4hrs

95.6 % TD   GS = 7μ ⊢——⊣   95.6 % TD   GS = 7μ ⊢————————⊣

0.7 % OP   1μ   0.7 % OP   10μ

Figure 3.2.4-49: S   Figure 3.2.4-50: F

Figures 3.2.4 : 49 - 50: Microstructures of the undoped BaTiO$_3$'s
                          Ba:Ti = 1.02

Microstructure Summary

The results of the microstructural analysis on the undoped BaTiO$_3$ compositions can be summarized as follows:

Ba:Ti Ratio < 1.000

1) Compositions fired at 1250 °C - 4 hours exhibit normal grain growth, intergranular porosity, a 1-2 micron grain size, intergranular fracture, and no evidence of a second phase. No liquid-phase sintering.

2) Increasing the sintering temperature to 1325 °C - 4 hours

results in a duplex structure of very large, 10-80 micron grains interdispersed with small, 1-2 micron grains. This is due to exaggerated grain growth, the degree of which increased as the amount of excess titanium increased. The excess titanium forms a liquid phase at 1312 ^{O}C. Porosity is intergranular in the small grain matrix, and intragranular in the large grains. Fracture is through the grains. A second recrystallized phase is evident in the grain boundaries.

3) Increasing the sintering temperature to 1375 ^{O}C - 4 hours results in a completely large-grained microstructure, on the order of 10-80 microns. This is due to uniform liquid-phase sintering of the matrix compared to the EGG of a few grains. Increasing the amount of excess titanium increases the final grain size. Porosity is closed and mostly intragranular. Fracture is through the grains. A second, recrystallized phase is evident in the grain boundaries.

4) Individual grain surfaces on the fired surface exhibit a great deal of angular "steps" and planes, which are indicative of the crystal orientation. This type of surface is usually generated by either an evaporation-condensation process or surface diffusion process.

Ba:Ti = 1.000

5) The stoichiometric composition exhibits normal grain

growth at all sintering temperatures, indicating the absence of a Ti-rich phase. Grain sizes range from 1-10 microns. Porosity is mostly intergranular.

Ba:Ti > 1.000

6) The excess barium compositions sintered better than expected. This is believed to be due to the presence of $BaCO_3$ leftover from the preparation process, which dissociates at low temperatures (811 ^{O}C) and aids the sintering. This is supported by the fact that changing the sintering temperature from 1250 ^{O}C to 1375 ^{O}C did not change the porosity or density significantly (< 2%) for any of the barium-excess compositions.

7) Compositions sintered at 1250 ^{O}C - 4 hours exhibit normal grain growth, grains in size from submicron to 8 microns, and intergranular porosity.

8) Increasing the sintering temperature to 1325 ^{O}C - 4 hrs results in similiar structures with a slight increase in the density and grain size (3-10 microns), and a decrease in the porosity. Only the Ba:Ti = 1.005 deviates from this behavior. It exhibits a larger grain size, 10-15 microns, and as a result contains a greater amount of intragranular porosity. No reasons as to why this occurs is evident from the microstructure.

9) Increasing the sintering temperature to 1375 ^{O} C - 4 hours results in structures similiar to that of the 1325 ^{O}C - 4 hours specimens with an increase in the grain size and a

decrease in the density. This is due to the enhanced grain growth rate allowing more pores to be absorbed instead of expelled. Again the Ba:Ti = 1.005 specimen deviates, exhibiting a larger grain size.

Specimens with excess barium contained a large number of grains with "lines" through them, which may be indicative of twinning. The excess titanium specimens did not exhibit this structure. The variations in microstructure between these compositions had a large effect on the degradation; refer to Section 3.4.1 for an analysis of the current-time behavior of these specimens.

3.2.5 Electroding

After sintering, the pellets were electroded with a fritless Pt paste and subsequent heating to 800 ^{o}C for 3 hours. The circular electrodes were kept at least 1 mm from the edge to prevent surface conduction problems. The choice of Pt as the electrode material for the specimens was based upon past studies which have found that other electrode materials such as Ag, Au, Pd, or combinations thereof can result in electromigration, enhancement of current injection mechanisms etc. Platinum has never been found to exhibit such problems.

Prior to testing the electroded units are stored in a dry atmosphere to prevent adsorption of water from the environment. Failure to do so results in erratic I-time behavior.

To date, all of the pellets needed for our studies have been eletroded.

3.3 ELECTRICAL MEASUREMENTS

High-voltage degradation measurements have been carried out on the undoped $BaTiO_3$ compositions with Ba:Ti = 0.980, 0.990, 0.995, 1.000, 1.005, 1.010, and 1.020 at 85 $^{\circ}$C and 150 $^{\circ}$C with applied fields ranging from 500 to 8000 V/cm. All measurements have been made in a dry atmosphere to date. The majority of these measurements are a result of the UMR/PSU joint program described in Section 1.2.2. . Both universities are making I-time measurements, with a purposeful overlap to ensure consistency of results.

3.3.1 Measurement System

The experimental apparatus used to make these measurements is illustrated in Figure 3.3. Each component will be described separately:

Furnace - The furnace consists of a Cu inner shell with a heavy Cu faceplate, which is wrapped with heat tape and surrounded by one inch of fibre insulaton. Copper was chosen to insure an even temperature distribution. The entire unit is surrounded by an Al box which not only physically contains the insulation and inner shell, but when grounded serves as the shielding. An Omega 6100 temperature controller with a variable autotransformer is capable of varying the furnace temperature up to 300 $^{\circ}$C, with a variation of $\pm$ 0.7 $^{\circ}$C maintainable for an indefinite period of time.
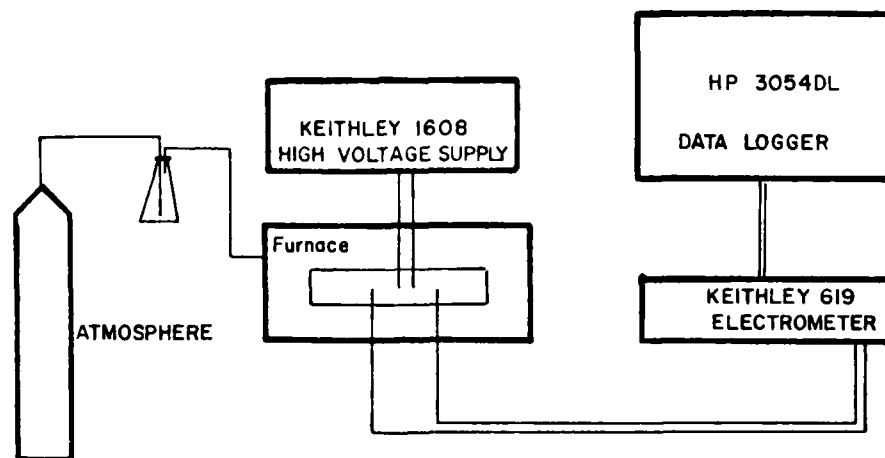
Figure 3.3.1 : Current-time, voltage measuring system.

Atmosphere System - The atmosphere system is used to run either dry or humid atmospheres through the furnace. Dry atmospheres are obtained by passing air through an in-line dessicant. Humid atmospheres are obtained by passing the furnace air through water, which is heated in an Erlenmeyer flask wrapped with heat tape. A dew point hygrometer was used to calibrate the relative humidity as a function of water temperature, keeping the gas flow rate constant.

Electrical Measurement System - The current readings are collected using a Keithley 619A two-channel electrometer operated by a Hewlett Packard 85 computer. The voltage supply is a Keithley 1608 high-voltage supply, capable of delivering 3100

VDC. The system is currently capable of measuring two specimens at a time. Specimens are mounted in spring-loaded test fixture which is connected to the electrometer with coaxial cable to minimize noise problems.

3.3.2 Experimental Procedure

Current-time Studies

Numerous difficulties were encountered collecting the I-time data. A precise procedure must be followed in order to get reproducible results. A review of the problems is included here in order that they may be helpful to someone else making these measurements.

1) Specimen Handling - In order to obtain high fields across a specimen with minimum voltages it is necessary to use the thinnest specimens practical. Unfortunately, the thinnest disk units obtainable by dry pressing are about 10 mils thick. In our joint PSU/UMR program we initially tried to press thicker units, and then subsequently ground them thinner using a diamond wheel with alcohol as the lubricant. This worked just fine until the current measurements were analyzed. Random results were the norm, no matter how we re-sintered or dried the specimens. The specimens appear to have suffered irreparable damage, probably surface cracks.

The problem was eliminated by building a protection circuit for the electrometer, which allowed the use of higher voltages to be used without concern for a sample short. This circuit can be a simple neon bulb placed in parallel with the electrometer,

across which the voltage will drop should a short develop. PSU has developed an alternate, more sophisticated protection circuit.

Another important precaution to take is to store the specimens to be measured in a sealed container with dessicant immediately after heating to attach the electrodes. Samples stored under ambient conditions yield inconsistent results, undoubtedly due to the absorption of water.

2) <u>Requilibration</u> - Two questions arise when studying degradation concerning the measurement procedure. a) Does allowing a specimen to degrade invalidate further data taken on the same sample at higher fields ? b) Is the degradation of a specimen a reversible process ? ie: Can a degraded sample be brought back to an undegraded state ? Past studies[27,80] only monitored the leakage current until degradation became evident, at which time the field was removed in order to not destroy the specimen. A standard wait time was employed between measurements. In our study we wish to monitor specimens degrading in order to obtain further clues as to what is happening.

With this in mind I-time measurements were initially carried out to standard times independent as to whether degradation was occurring or not. A standard wait time (30 minutes) was used, after which the field was increased and the next I-time measurement was performed. The results obtained in this manner can be summarized by:

1) The current does not always increase as the field is

increased.

2; Sometimes the current value starts off at the same level at which it ended on the previous run.

These results could imply that the resistivity of the sample is dependent upon the field, but this is unlikely in light of the magnitude of the field increase. It is unlikely that the carrier mobility is sufficiently dependent on the field to account for the observed behavior. In addition, if the same field is successively applied the current does not duplicate the previous result, but instead starts off at a level corresponding to the previous run's final current. Obviously the degradation is permanently affecting the resistivity of the specimen. Any current measurements taken on a sample which had been previously degraded were meaningless. Increasing the wait time or shutting off the field when degradation began resulted in the same unrepeatable results.

The question then is, can a degraded specimen be brought back to an undegraded state? To answer this question we measured the leakage current of a specimen which exhibited degradation, then removed the sample and heated it at an elevated temperature. The I-time experiment was repeated, and compared to the previous run. In this manner we have determined the answer to be yes; a sample can be brought back to an undegraded state if the refiring is sufficiently high. Our degraded specimens required firings of at least 1000 $^{\circ}$C for 8 hours in order to be "re-equilibrated". To be on the safe side a 1200 $^{\circ}$C – 8 hour reequilibration is currently being used in our studies. Following this treatment

the samples give reproducible results.

This type of behavior in itself is an important clue to the mechanism behind the degradation process, the consequences of which are discussed in Section 3.4.

Even those samples not exhibiting degradation gave improved repeatibility of results if a reequilibration was performed between I-time measurements.

I-time Procedure - Based upon the previous mentioned problems the following procedure was adopted for the I-time measurements:

1) Following electroding, specimens are stored in a sealed container with a dessicant.

2) Specimens are loaded in the furnace, the temperature equilibrated, and the I-time data collected.

3) Regardless if degradation occurred or not, the specimens are removed and reequilibrated at 1200 $^\circ$C for 8 hours.

Ferroelectric-Paraelectric Behavior - Some doubt arises concerning the value of measuring the degradation tendencies of BaTiO$_3$ above the Curie temperature, where the crystal structure is cubic. In our study we are measuring the degradation tendencies at 150 $^\circ$C. If the trends remain the same for both the ferroelectric and the paraelectric regions, then we could conclude that degradation is not dependent upon the lattice structure. This would be another important clue in determining the mechanism behind degradation.

Current-Voltage Studies

Past studies have indicated that degradation is due to, or

perhaps results in, non-ohmic current injection behavior. For this reason we are interested in studying the I-V characteristics of the specimens being studied for degradation behavior. This analysis requires no additional results other than the I-time data which was collected as a function of applied field. Simple plots of log current density (J) vs. log field (E) will reveal if non-ohmic behavior is occurring. Refer to Section 3.1.2 for background information on current injection mechanisms. Several important problems need to be considered:

1) A matter of what time to take a current reading for I-V analysis arises. Should the current reading be the minimum value, equilibrium value, or a value at constant time ? There are arguments in favor of each, so in Section 3.4.2 the figures appear with the I-V behavior at various times.

2) The validity of applying non-ohmic current injection analysis to specimens which exhibit degradation is questionable. Equations describing the current injection mechanisms assume equilibrium is attained, which obviously never happens if degradation is occurring. What has been referred to in the past[38] as non-ohmic behavior based upon I-V curves may be nothing more than high current levels due to the degradation process.

For those specimens which attain equilibrium current values for various fields, current injection analysis may be utilized with confidence, but that is the only case.. Any other behavior makes the analysis uncertain.

3.4 Results and Discussion

High-voltage degradation measurements have been made on the the undoped $BaTiO_3$'s for Ba:Ti = 0.98, 0.99, 0.995, 1.000, 1.005, 1.01, and 1.02, at 85 and 150 ^{o}C under applied fields ranging from 500 to 8000 V/cm. In order to obtain a matrix of varying densities, porosities, and grain sizes, specimens were sintered at three temperatures (1250, 1325, 1375 ^{o}C - 4 hours) . In this manner, the effect of each of these variables on degradation can be evaluated. All measurements have been carried out in a dry atmosphere. The majority of these measurements are a result of the UMR/PSU joint program. PSU has made the electrical measurements at 85 ^{o}C, while UMR has provided the test specimens and made the degradation measurements at 150 ^{o}C. A purposeful overlap of I-time measurements were initially made in order check consistency, the results of which were excellent. Analysis of these data will be broken up compositionally, and by the measurement temperature. References to the microstructure, density, porosity, and grain size sections of this report are numerous, and therefore referall between sections is recommended. Data is presented in the form of I-time results, with the corresponding I-V curves. The results from the 85 ^{o}C measurements will be presented first, followed by those made at 150 ^{o}C. Tables 3.4.a, 3.4.b, and 3.4.c contain the current density values for the undoped $BaTiO_3$'s sintered at 1250, 1325, and 1375 ^{o}C under applied fields of 500, 1000, 2000, 4000, and 8000 V/cm at 9000 seconds .

Field (V/cm)	Ba:Ti Ratio	Current Density (amps/cm^2)
	0.980	1.02×10^{-9}
	0.990	1.86×10^{-9}
	0.995	4.24×10^{-10}
500	1.000	4.81×10^{-10}
	1.005	2.87×10^{-8}
	1.010	6.08×10^{-8}
	1.020	7.97×10^{-8}
	0.980	3.86×10^{-9}
	0.990	4.19×10^{-9}
	0.995	8.95×10^{-10}
1000	1.000	9.12×10^{-10}
	1.005	1.03×10^{-7}
	1.010	1.33×10^{-7}
	1.020	1.08×10^{-7}
	0.980	1.24×10^{-8}
	0.990	1.15×10^{-8}
	0.995	2.47×10^{-9}
2000	1.000	1.88×10^{-9}
	1.005	6.89×10^{-7}
	1.010	8.53×10^{-7}
	1.020	3.40×10^{-7}
	0.980	3.49×10^{-8}
	0.990	2.12×10^{-8}
	0.995	5.41×10^{-9}
4000	1.000	3.59×10^{-9}
	1.005	2.21×10^{-6}
	1.010	1.99×10^{-6}
	1.020	5.28×10^{-7}
	0.980	4.44×10^{-8}
	0.990	1.82×10^{-8}
	0.995	7.84×10^{-9}
8000	1.000	1.08×10^{-8}
	1.005	5.98×10^{-6}
	1.010	5.33×10^{-6}
	1.020	1.79×10^{-6}

TABLE 3.4a: Current density values at 9000 seconds for the undoped $BaTiO_3$'s fired at 1250°C for 4 hours.

Field (V/cm)	Ba:Ti Ratio	Current Density (amps/cm^2)
	0.980	7.57×10^{-10}
	0.990	1.51×10^{-9}
	0.995	1.22×10^{-9}
500	1.000	5.19×10^{-10}
	1.005	4.34×10^{-8}
	1.010	1.00×10^{-7}
	1.020	2.86×10^{-8}
	0.980	2.18×10^{-9}
	0.990	3.83×10^{-9}
	0.995	3.18×10^{-9}
1000	1.000	6.97×10^{-10}
	1.005	8.37×10^{-8}
	1.010	1.37×10^{-7}
	1.020	3.62×10^{-8}
	0.980	4.42×10^{-9}
	0.990	1.04×10^{-8}
	0.995	1.65×10^{-8}
2000	1.000	3.48×10^{-9}
	1.005	3.60×10^{-7}
	1.010	5.62×10^{-7}
	1.020	2.30×10^{-7}
	0.980	1.33×10^{-8}
	0.990	5.18×10^{-8}
	0.995	2.46×10^{-7}
4000	1.000	5.15×10^{-9}
	1.005	1.53×10^{-6}
	1.010	3.05×10^{-6}
	1.020	9.48×10^{-7}
	0.980	9.32×10^{-8}
	0.990	3.40×10^{-6}
	0.995	6.93×10^{-6}
8000	1.000	2.21×10^{-8}
	1.005	7.19×10^{-6}
	1.010	1.90×10^{-5}
	1.020	5.01×10^{-6}

TABLE 3.4b: Current density values at 9000 seconds for the undoped BaTiO$_3$'s fired at 1325°C for 4 hours.

Field (V/cm)	Ba:Ti Ratio	Current Density (amps/cm^2)
	0.980	9.56×19^{-10}
	0.990	2.06×10^{-9}
	0.995	1.81×10^{-9}
500	1.000	1.79×10^{-9}
	1.005	1.13×10^{-8}
	1.010	2.58×10^{-8}
	1.020	6.57×10^{-9}
	0.980	2.84×10^{-9}
	0.990	6.77×10^{-9}
	0.995	6.48×10^{-9}
1000	1.000	4.28×10^{-9}
	1.005	4.93×10^{-8}
	1.010	9.89×10^{-8}
	1.020	3.60×10^{-8}
	0.980	1.45×10^{-8}
	0.990	7.98×10^{-8}
	0.995	5.50×10^{-8}
2000	1.000	1.14×10^{-8}
	1.005	3.02×10^{-7}
	1.010	6.16×10^{-7}
	1.020	1.01×10^{-7}
	0.980	6.58×10^{-7}
	0.990	4.13×10^{-6}
	0.995	8.74×10^{-8}
4000	1.000	7.85×10^{-8}
	1.005	1.42×10^{-6}
	1.010	1.40×10^{-6}
	1.020	2.06×10^{-7}
	0.980	4.99×10^{-6}
	0.990	8.10×10^{-5}
	0.995	5.49×10^{-5}
8000	1.000	1.45×10^{-6}
	1.005	1.16×10^{-5}
	1.010	6.33×10^{-6}
	1.020	1.14×10^{-6}

TABLE 3.4c: Current density values at 9000 seconds for the undoped BaTiO$_3$'s fired at 1375°C for 4 hours.

==

Ti-Rich BaTiO$_3$

==

3.4.1 : Ba$_{.98}$TiO$_3$ - 85 °C

1250 °C - 4 hours: 84.5 % TD   2 um ave. GS
                     8.2 % OP   Figures 3.4.1a-b

This is the most porous specimen, and it exhibited the best
resistance to degradation of all the samples studied. This is
quite a surprising result, as it contradicts nearly all the
results which have been collected in past studies. Even at 8000
V/cm it exhibited no tendency to degrade. This particular
specimen was tested at fields up to 25000 V/cm, and it still
showed no tendency to degrade; the sample's breakdown strength
was reached first. The I-V curves appear to exhibit non-ohmic
behavior, however the current values are non-equilibrium and
still decreasing. This is reflected by by an overall lowering of
the I-V curves as time increases. Note the slope of the I-V
curve decreases with increasing field, indicative of the more
rapid achievement of a steady-state current.

1325 °C - 4 hours: 93.3 % TD   1 um ave. GS
                     0.0 % OP   Figures 3.4.1c-d

Increasing the sintering temperature increased the density
and decreased the amount of open porosity. This sample exhibited
exaggerated grain growth (EGG), a result of which is a large
amount of intragranular porosity. Current levels at low fields

Ba.98TiO3 1250C 4HRS .074 CM. THICK T=85C
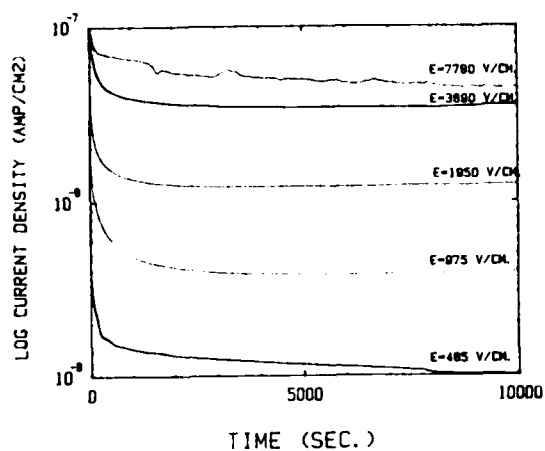
Figure 3.4.1a

Ba.98TiO3 1250C 4HRS. .074 CM. THICK.
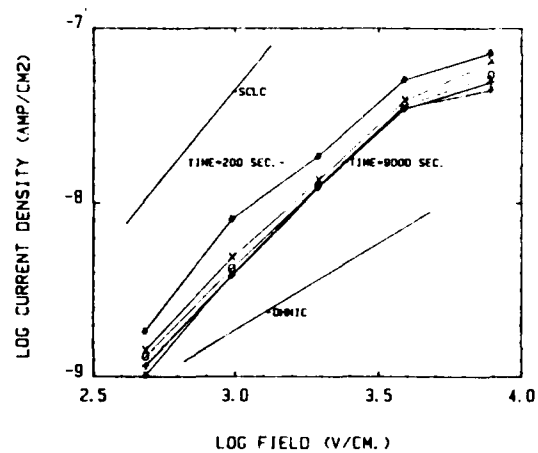
Figure 3.4.1b

Ba.98TiO3 1325C 4HRS. .075 CM. THICK. T=85C
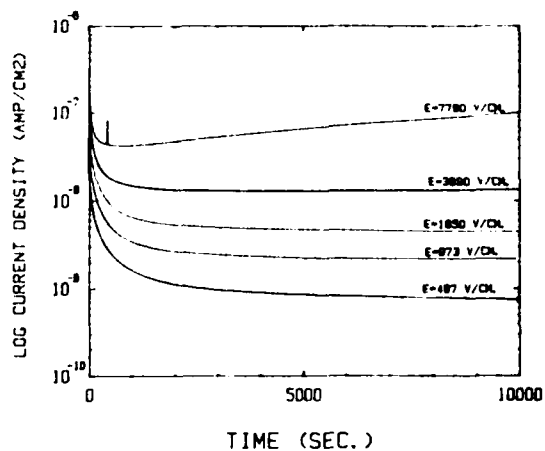
Figure 3.4.1c

Ba.98TiO3 1325C 4HRS. .075 CM. THICK. T=85C

Figure 3.4.1d

-128-
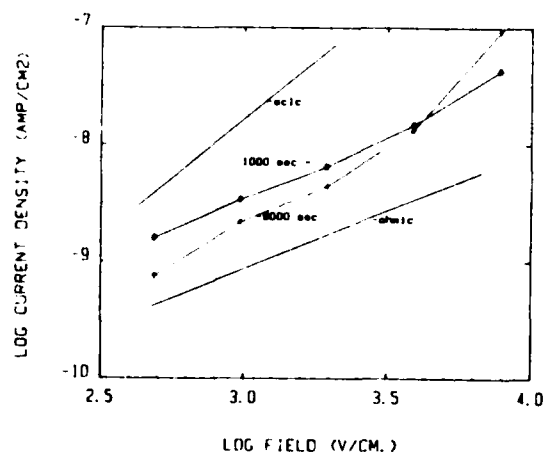
remain unchanged, with less time for a steady-state current to be achieved. However, at 4000 V/cm and above degradation begins to occur. I-V behavior is ohmic, with a transition to a higher slope at 8000 V/cm, measured at 9000 seconds. This change, however, is due to the onset of degradation, not a switchover to a non-ohmic current injection mechanism.

1375 $^\circ$C - 4 hours: 93.5 % TD   40 μm ave. GS
                      0.1 % OP   Figures 3.4.1e-f

Increasing the sintering temperature results in a matrix of large grains, with a great deal of intragranular porosity. Again, the behavior remains unchanged at fields 2000 V/cm, but at 4000 and 8000 V/cm the current dramatically increases and degradation occurs at an enhanced rate. Note only a small change in density produced these results. The shape of the I-time curve is also important: a rapid increase in current occurs over a period of several hundred seconds (termed the "rapid degradation region" → RDR), followed by a gradual decrease of the slope until a linear region is reached. Increase the field, decrease the time of the RDR. The I-V behavior is ohmic at low fields, with a jump in the current and increase in slope at 4000 V/cm, again due to degradation.

A complete analysis of this observed behavior is included with the summary of results for the excess Ti compositions.

Ba. 98TiO3 1375C 4HRS. .073 CM. THICK. T=85C
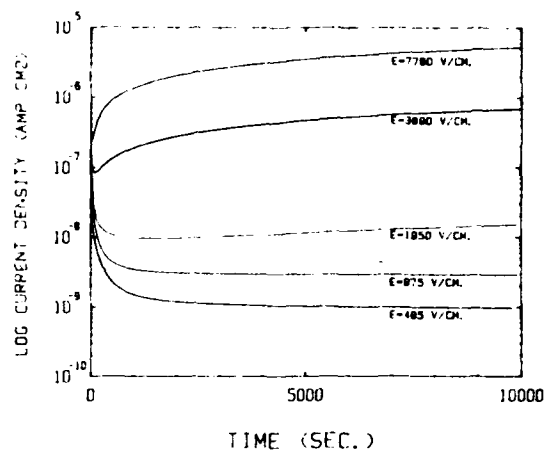
Figure 3.4.1e

Ba. 98TiO3 1375C 4HRS. .073 CM. THICK. T=85C
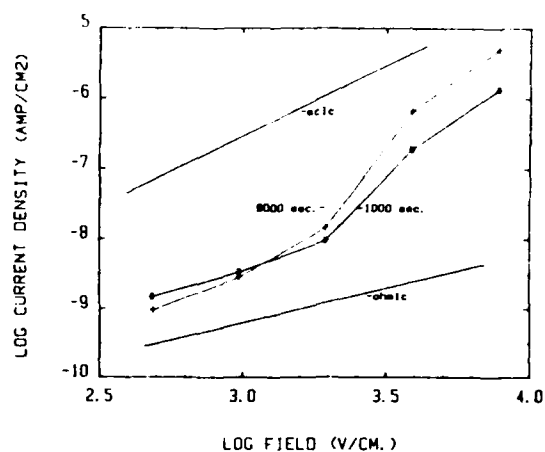
Figure 3.4.1f

Ba. 99TiO3 1250C 4HRS. .07XICM. THICK. T=85C
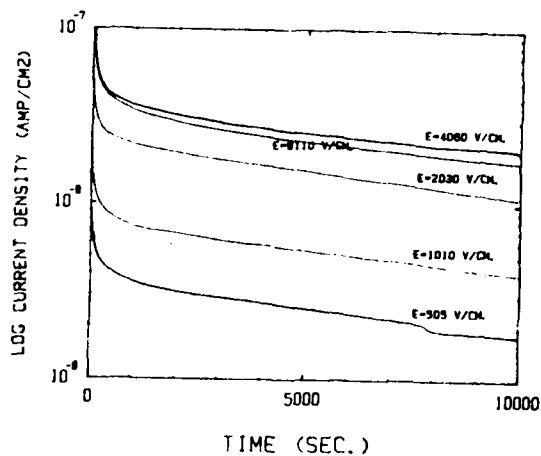
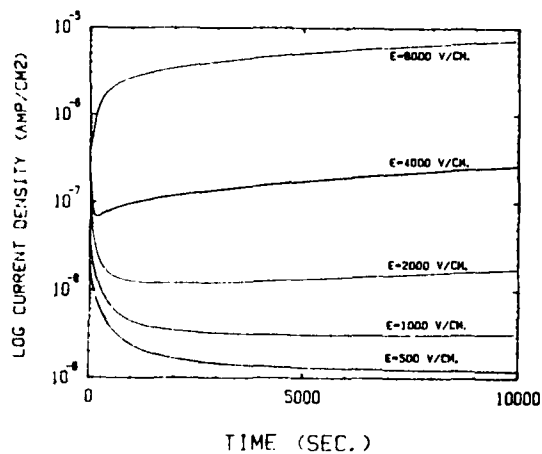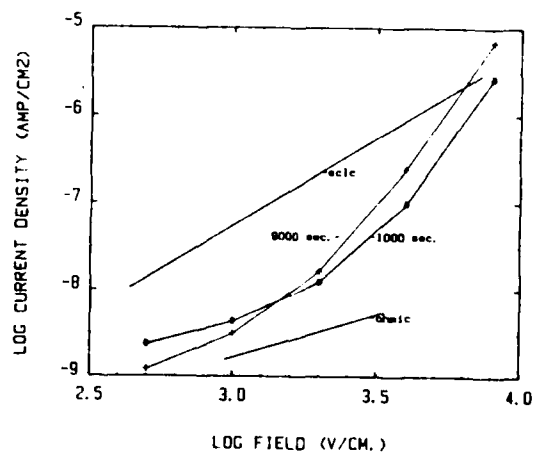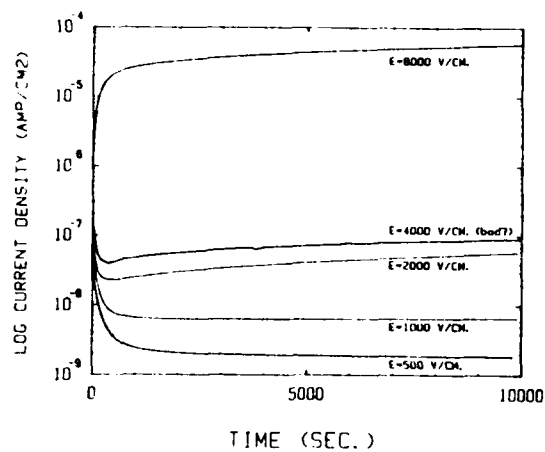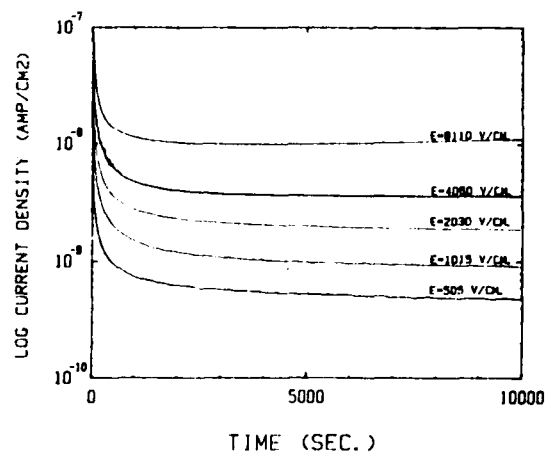Figure 3.4.2a

Ba. 99TiO3 1250C 4HRS. .07i CM. THICK. T=85C

Figure 3.4.2b

-130-

==
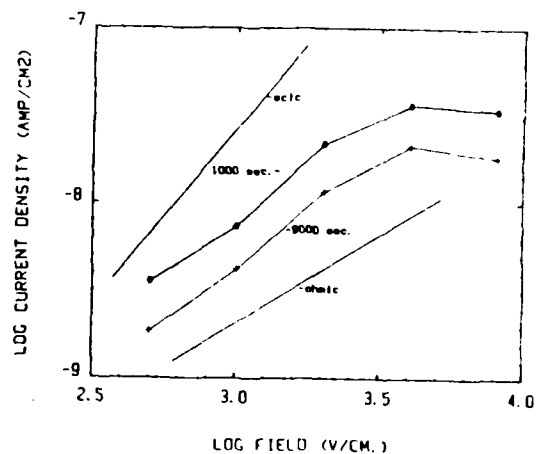
$$\underline{3.4.2} \text{ Ba}_{.99}\text{TiO}_3 - 85 \ ^\circ\text{C}$$

1250 $^\circ$C - 4 hours: 84.2 % TD   1 um ave. GS
                           8.4 % TD   Figures 3.4.2a-c

Again the most porous specimen exhibits the best resistance

to degradation. No degradation occurred for all fields studied.

Current levels are approximately the same as for the 0.98

specimen. I-V behavior is nearly ohmic, the erratic slope due to

the non-steady-state current.

1325 $^\circ$C - 4 hours: 94.7 % TD   1 um ave. GS
                           0.0 % OP   30 um EGG
                                                      Figures 3.4.2c-d

Increasing the sintering temperature results in a duplex

structure of large 30 um grains interdispersed with small 1

um grains; approximately a 50/50 mix. Degradation begins to

occur at 4000 V/cm, with a dramatic increase in degradation and

current levels (2 orders of magnitude) at 8000 V/cm. This is the

same behavior that the 0.98 specimen exhibited, except for the

large increase at 8000 V/cm. I-V behavior is ohmic up to 4000

V/cm, with an increase in slope at 8000 V/cm due to the

degradation, not necessarily due to a non-ohmic current injection

mechanism.

1375 $^\circ$C - 4 hours: 94.1 % TD   25 um ave. GS
                           0.5 % OP   Figures 3.4.2e-f

This specimen exhibits a large grain matrix with nearly all

Ba.99TiO3 1325C 4HRS, .077 CM. THICK, T=85C
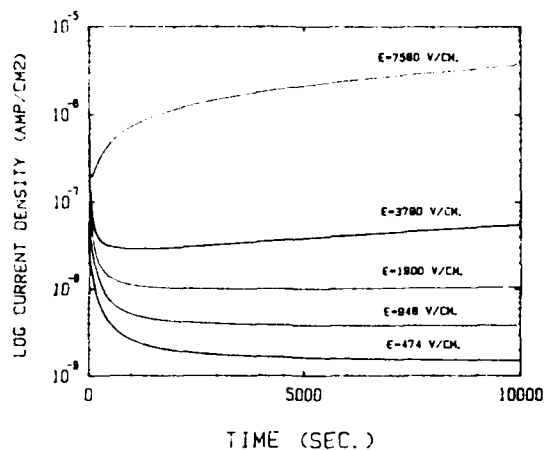
Figure 3.4.2c

Ba.99TiO3 1325C 4HRS, .077 CM. THICK, T=85C
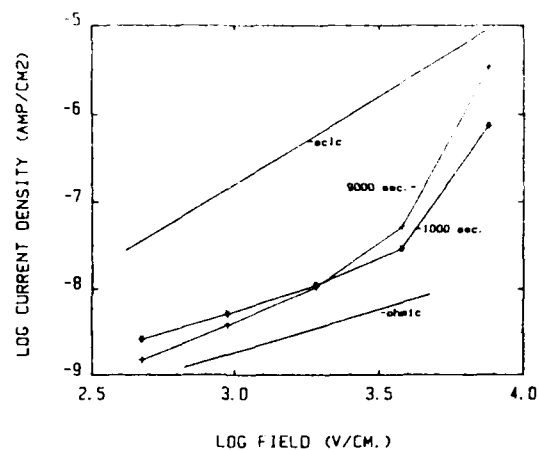
Figure 3.4.2d

Ba.99TiO3 1375C 4HRS, .071 CM. THICK, T=85C
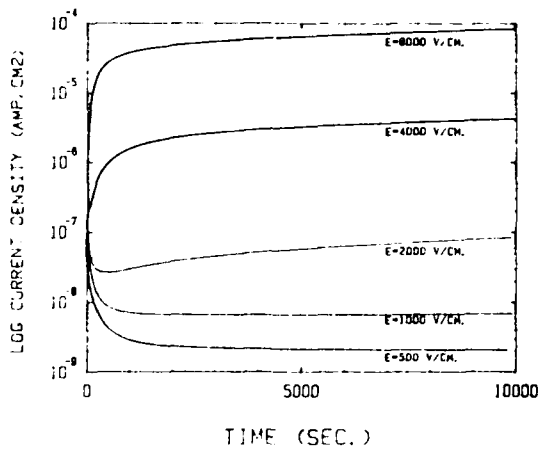
Figure 3.4.2e

Ba.99TiO3 1375C 4HRS, .071 CM. THICK, T=85C

Figure 3.4.2f

-132-
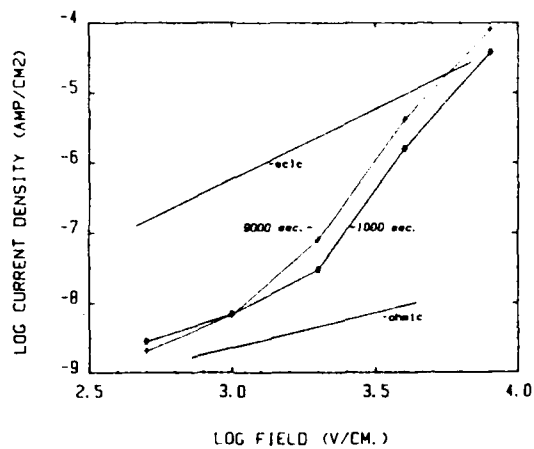
the porosity intragranular. At 500 and 1000 V/cm the sample does not degrade, with a transition to degradation for fields 2000 V/cm. This represents a substantial change from the behavior exhibited by the 0.98 specimen. Degradation occurs more rapidly, and the current levels are 1.5 times higher. Note that the density has decreased for this sample compared to the 1325 $^{\circ}$C specimen due to the increased grain growth rate entrapping more pores. Also, the RDR occurs over a shorter time with increasing fields, but the slope of the degradation rate does not change in the linear region. I-V behavior appears to exhibit a transition to a slope greater than two, but again this is due to the degradation.

==

3.4.3 Ba$_{.995}$TiO$_3$ - 85 $^{\circ}$C

1250 $^{\circ}$C - 4 hours: 89.8 % TD   1 um ave. GS
                            4.3 % OP   Figures 3.4.3a-b

Similiar to the 0.98 and 0.99 specimens, this porous specimen exhibits no degradation. I-V behavior is approximately ohmic. No other significant changes.

1325 $^{\circ}$C - 4 hours: 94.0 % TD   1 um ave. GS
                            0.0 % OP   45 um EGG
                                           Figures 3.4.3c-d

Increasing the sintering temperature, thereby increasing the density, and decreasing the open porosity results in dramatically different behavior. No change in the current levels or behavior at 500 and 1000 V/cm, but at 2000 V/cm degradation begins to

Ba.995Ti03 1250C 4HRS. .073 CM. THICK. T-85C
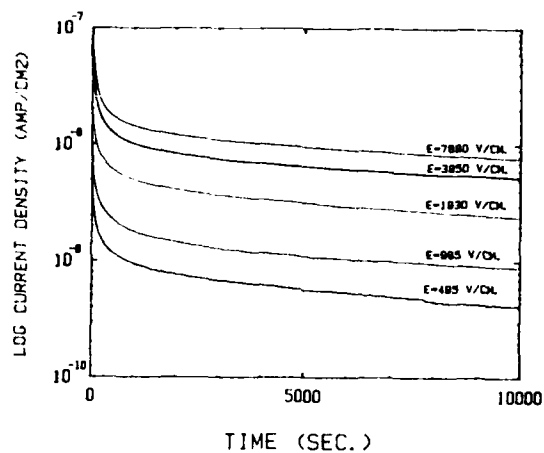
Figure 3.4.3a

Ba.995Ti03 1250C 4HRS. .073 CM. THICK. T-85C
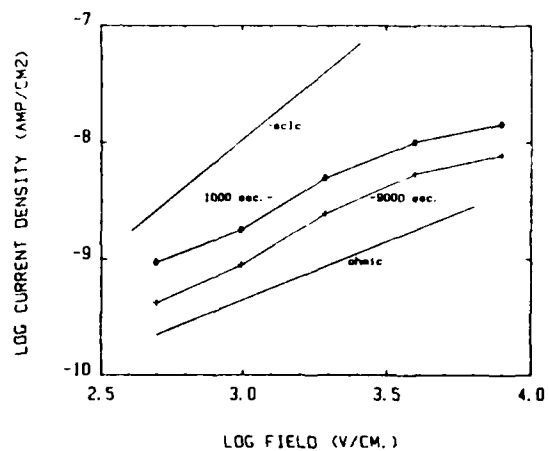
Figure 3.4.3b

Ba.995Ti03 1325C 4HRS. .073 CM. THICK. T-85C

Figure 3.4.3c

Ba.995Ti03 1325C 4HRS. .073 CM. THICK. T-85C

Figure 3.4.3d

-134-

occur, with la ge increases in current and degradation at 4000 and 8000 V/cm. This also represents an increase in the current and degradation rate compared to the 0.98 and 0.99 specimens. I-V behavior exhibits a deviation to non-ohmic behavior, due to the onset of degradation.

1375 ^{O}C – 4 hours: 90.3 % TD   20 um ave. GS
                       0.3 % OP   Figures 3.4.3e-f

Increasing the sintering temperature resulted in a decrease in the the density, due to rapid grain growth and the corresponding increase in the intragranular porosity. This is readily visible in the microstructure. Current levels remain essentially unchanged compared to the 1325°C specimen for fields 2000 V/cm. The 4000 V/cm I-time run is suspect and marked thus. However, at 8000 V/cm the current level is an order of magnitude greater. I-V behavior is ohmic up to 4000 V/cm.

Summary of the High-Voltage Degradation Behavior
for the Excess Titanium Compositions

1) In general, increasing the sintering temperature resulted in an increase in the density, a decrease in the open porosity, an increase in the intragranular porosity, and an increase in the grain size. <u>This resulted in a greater tendency to degrade.</u> There are several things this behavior could be attributed to:

- Increasing the grain size decreases the grain boundary diffusion length. This points towards the diffusion of a grain boundary species, such as $V_O^{\cdot\cdot}$, as the possible cause of

Ba.995TiO3 1375C 4HRS. .071 CM. THICK. T=85C

Figure 3.4.3e

Ba.995TiO3 1375C 4HRS. .071 CM. THICK. T=85C
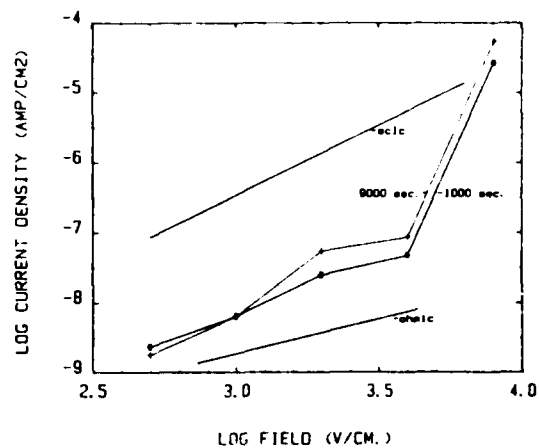
Figure 3.4.3f

Ba1.00TiO3 1250C 4HRS. .071 CM. THICK. T=85C

Figure 3.4.4a

Ba1.00TiO3 1250C 4HRS. .071 CM. THICK. T=85C

Figure 3.4.4b

-136-
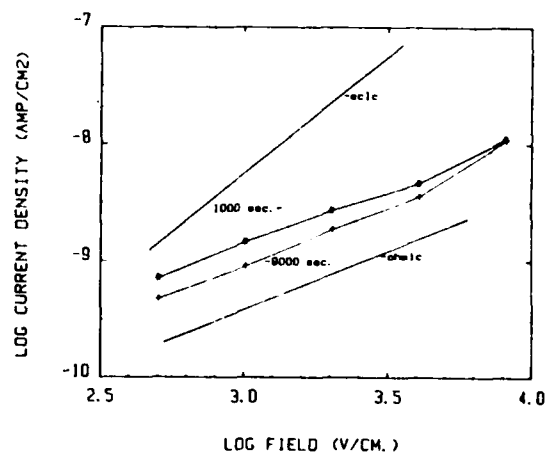
degradation.

- Increasing the sintering temperature above $1311^{\circ}C$ results in the excess titanium phase forming a liquid which recrystallizes in the grain boundary upon quenching. The composition of this second phase is not agreed upon (refer to Section 3.1.3). Below $1311\ ^{\circ}C$ the excess titanium exists as TiO_2. Perhaps the excess-titanium eutectic composition is causing the degradation. Smyth et.al.[81] prepared a sample of the excess-titanium composition and found it did not degrade, but whether or not the same applies when it is in the grain boundary is unknown.

- If $V_o^{\cdot\cdot}$ diffusion is the cause of degradation (Section 3.1.1), then perhaps the large amount of intergranular porosity in the porous specimens somehow blocks their migration, and thereby improves the degradation resistance. An $V_o^{\cdot\cdot}$ encountering a pore could only "transport" across it either by circumvention, or by oxygen evolution at the other side. Both of these processes would inhibit the migration process.

- The porosity of those specimens with the greater tendency to degrade was intragranular. This could indicate only intragranular porosity has a large effect on resistivity inhomogeneities within individual grains due to field-splitting.

- Other than the effects of field-splitting, we cannot think of any reasons why porosity would increase a specimen's tendency to degrade, <u>assuming the I-time measurement is made in a dry atmosphere</u>. In a humid environment one would expect an

increase in open porosity would increase the degradation.

2) Degradation does not specifically seem to be dependent upon the density. Comparing the 1325 and 1375 $^{\circ}$C - 4 hours specimens shows that while the density increases only a small amount (< 1%), or even decreases (0.99 and 0.995 specimens), the degradation behavior substantially worsens. This implies either the grain size, porosity type, or the existence of a second phase must be causing the change in behavior.

3) For those samples which degrade, increasing the field substantially decreases the RDR time, and increases the current non-ohmically, but does not change the degradation rate in the region of gradual current increase. Current levels also "jump" several orders of magnitude when a field sufficient to induce degradation is applied. These observations could be a result of several things:

- Whatever is causing the degradation has a field-activated mobility or concentration. A critical fieldis reached, and either the mobility or concentration of the migratory species suddenly increases, which results in degradation.

- The shape of the I-time curves is an important clue as to what is happening. The RDR has to be due to the rapid migration of some mobile species initially in the specimen, or it could be due to the buildup of a space-charge at the cathode associated with the SCLC injection mechanism. The sustained high current level would then be due to the current injection mechanism itself. The gradual increase in conductivity could then be attributed to the migration of $V_o^{\cdot\cdot}$ due to the non-linaer

potential drop across the dielectric.

4) Changing the degree of nonstoichiometry did not change the current levels at fields < 2000 V/cm. However, at 4000 and 8000 V/cm the degradation behavior was substantially different; increasing the excess titanium decreases the current levels and the tendency to degrade. Increasing the excess titanium concentration past several hundred ppm does not change the defect chemistry of the primary phase, $BaTiO_3$, but it does increase the amount of the intergranular Ti-rich phase. Perhaps this "blocks" the migrating species by decreasing its mobility.

As is usual with this kind of research, more questions seem to be raised rather than answered. The next section covers the analysis of the stoichiometric composition.

==

3.4.4 Stoichiometric BaTiO$_3$

The stoichiometric specimens exhibit the overall lowest current levels and the best resistance to degradation of all the compositions studied. Individual analyses:

1250 ^{O}C - 4 hours: 93.3 % TD   4 um ave. GS
                          1.6 % OP   Figures 3.4.4a-b

This sample exhibits normal grain growth, with a grain size ranging from 1-8 um, and only 1.6 % open porosity. No evidence of intragranular porosity is evident from the microstructure. Steady-state currents are achieved at all fields, with no evidence of degradation occurring. I-V curves are ohmic.

Bal.OOTiO3 1325C 4HRS. .072 CM. THICK. T=85C
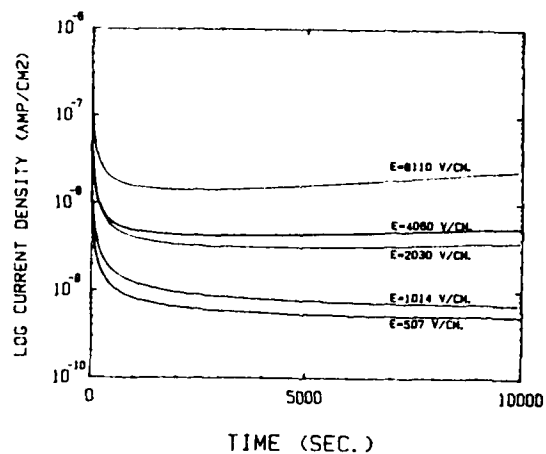
Figure 3.4.4c

Bal.OOTiO3 1325C 4HRS. .072 CM. THICK. T=85C
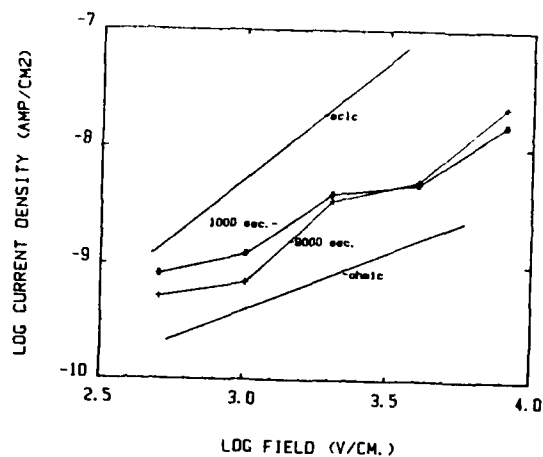
Figure 3.4.4d

Bal.OOTiO3 1375C 4HRS. .069 CM. THICK. T=85C
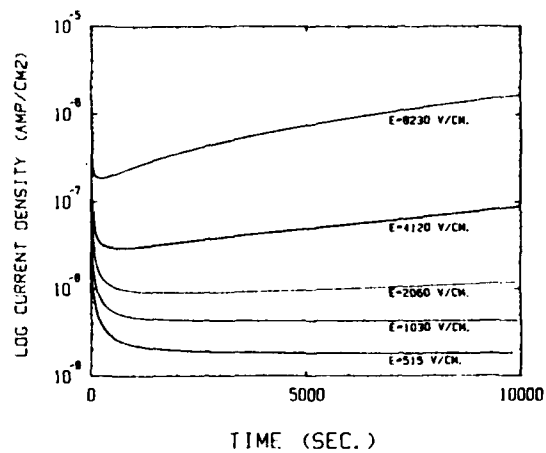
Figure 3.4.4e

Bal.OOTiO3 1375C 4HRS. .069 CM. THICK. T=85C

Figure 3.4.4f

-140-
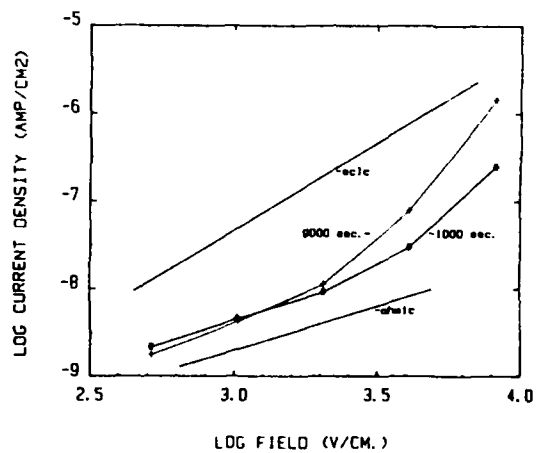
1325 ^{O}C – 4 hours: 94.3 % TD   5 um ave. GS
                         0.3 % OP   Figures 3.4.4c-d

Increasing the sintering temperature increased the density slightly, decreased the open porosity, and increased the grain size. There is no evidence of exaggerated grain growth, indicative of the lack of a Ti-rich phase. Current levels are the same as the 1250 ^{O}C specimen, except at 8000 V/cm where degradation begins. I-V curves are erratic, but approximately ohmic.

1375 ^{O}C – 4 hours: 94.9 % TD   4 um ave. GS
                         0.1 % OP   Figures 3.4.4e-f

Increasing the sintering temperature results in only a minor increase in the density and decrease in the open porosity, leaving the grain size virtually unchanged. However, the current levels and degradation behavior have substantially increased at 4000 and 8000 V/cm. I-V behavior shows a change in slope from ohmic to non-ohmic.

Summary for the Stoichiometric Composition

Evidently, for the stoichiometric case the change in degradation behavior is not due to a change in the grain size, porosity,or density. This may lend evidence towards the $V_O^{\cdot\cdot}$ diffusion model of degradation. Samples sintered at 1375 ^{O}C and then quenched would have a higher $V_O^{\cdot\cdot}$ concentration than those specimens sintered at 1325 or 1250 ^{O}C, which could explain the difference in behavior.

The fact that the stoichiometric composition exhibited the

lowest current levels indicates the excess Ba or Ti
decreases the resistivity, either through the presence of a
second phase or by alteration of the defect chemistry. The
latter is unlikely in light of the limited solubility (Section
3.1.3) of Ba or Ti onto the $BaTiO_3$ lattice.

The next section covers the results obtained for the
Ba-rich compositions.

===

Ba-Rich $BaTiO_3$

===

The excess Ba compositions sintered exceptionally well, due
to the presence of $BaCO_3$ (Section 3.2.3). The Ba-rich phase in
the past has been found to be Ba_2TiO_4, which exists in the grain
boundaries. All of the excess Ba compositions exhibited higher
current levels, > 1-2 orders of magnitude, than the excess Ti
compositions. The individual analyses follow.

===

3.4.5 $Ba_{1.005}TiO_3$ - 85 ^{O}C

1250 ^{O}C - 4 hours: 92.1 % TD   3 um ave. GS
                         2.6 % OP   Figures 3.4.5a-b

This specimen exhibited degradation at all fields.
Increasing the field again results in a decrease in time over
which the RDR extends, with no effect on the degradation rate in
the linear region. The I-V behavior exhibits ohmic behavior at

Bal.005TiO3 1250C 4HRS, .068 CM. THICK, T=85C

LOG CURRENT DENSITY (AMP/CM2)

E=8000 V/CM.
E=4000 V/CM.
E=2000 V/CM.
E=1000 V/CM.
E=500 V/CM.

TIME (SEC.)

Figure 3.4.5a

Bal.005TiO3 1250C 4HRS, .068 CM. THICK, T=85C

LOG CURRENT DENSITY (AMP/CM2)

aclc
8000 sec.
1000 sec.
ohmic

LOG FIELD (V/CM.)

Figure 3.4.5b

Bal.005TiO3 1325C 4HRS, .071 CM. THICK, T=85C

LOG CURRENT DENSITY (AMP/CM2)

E=8230 V/CM.
E=4110 V/CM.
E=2080 V/CM.
E=1020 V/CM.
E=514 V/CM.

TIME (SEC.)

Figure 3.4.5c

Bal.005TiO3 1325C 4HRS, .071 ′ THICK, T=85C

LOG CURRENT DENSITY (AMP/CM2)

aclc
8000 sec.
1000 sec.
ohmic

LOG FIELD (V/CM.)

Figure 3.4.5d

-143-

1000 seconds, and non-ohmic behavior at 9000 seconds. This is due to the degradation, which occurs at a faster rate at higher fields.

1325 $^{\circ}$C - 4 hours: 94.1 % TD   10 μm ave. GS
                        0.8 % OP   Figures 3.4.5c-d

Increasing the sintering temperature increases the density by 2 %, decreases the open porosity by 0.8 %, and increased the grain size to 10 μm. These changes had no effect on the degradation tendencies or the current levels. I-V behavior also remains unchanged, still reflecting the the differing degradation rates as a function of field.

1375 $^{\circ}$C - 4 hours: 94.3 % TD   13 μm ave. GS
                        0.6 % OP   Figures 3.4.5e-f

This increase in the sintering temperature resulted in only a 0.2 % increase in density, a 0.2 % decrease in the open porosity, and an average grain size of 13 μm. Again, no change in the degradation behavior is observed. I-V behavior is initially ohmic, but as degradation proceeds the slope of the I-V curve increases.

==

3.4.6 Ba$_{1.01}$TiO$_3$ - 85 $^{\circ}$C

1250 $^{\circ}$C - 4 hours: 92.0 % TD   3 μm ave. GS
                       1.7 % OP   Figures 3.4.6a-b

This specimen, unlike the 1.005 specimen, reaches a steady-state current at 500 V/cm. Increasing the field results

Bal.005TiO3 1375C 4HRS. .072 CM. THICK. T=85C

Figure 3.4.5e

Bal.005TiO3 1375C 4HRS. .072 CM. THICK. T=85C

Figure 3.4.5f

Bal.01TiO3 1250C 4HRS. .069 CM. THICK. T=85C

Figure 3.4.6a

Bal.01TiO3 1250C 4HRS. .069 CM. THICK. T=85C
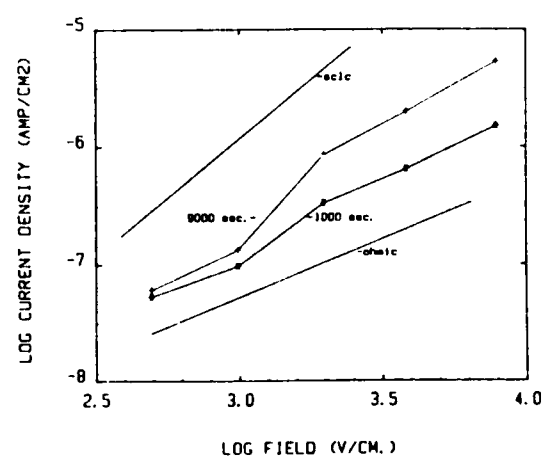
Figure 3.4.6b

in a non-ohmic increase in the current, and an increase in the degradation rate. Current levels are lower than for the 1.005 specimen. I-V behavior, which is non-ohmic, reflects degradation.

1325 ^{O}C - 4 hours: 93.8 % TD   2 um ave. GS
                         0.2 % OP   Figures 3.4.6c-d

Increasing the sintering temperature results in a 0.8 % increase in the density, a 1.5 % decrease in the open porosity, and virtually no change in the average grain size. I-time degradation behavior remains unchanged, as does the I-V behavior.

1375 ^{O}C - 4 hours: 93.4 % TD   5 um ave. GS
                         0.6 % OP   Figures 3.4.6e-f

A further increase in the sintering temperature resulted in a 0.4 % decrease in density, a 0.4 % increase in the open porosity, and a 5 um average grain size. Grain growth is occurring at a faster rate. No changes in the current or degradation behavior is observed. The I-V curve, which is linear and has a slope of two, would lead one to suspect SCLC is occurring, but again this is probably due to the degradation.

==

3.4.7 $Ba_{1.02}TiO_3$ - 85 ^{O}C

1250 ^{O}C - 4 hours: 94.6 % TD   3 um ave. GS
                         0.8 % OP   Figures 3.4.7a-b

Bal.01TiO3 1325C 4HRS. .071 CM. THICK. T=85C
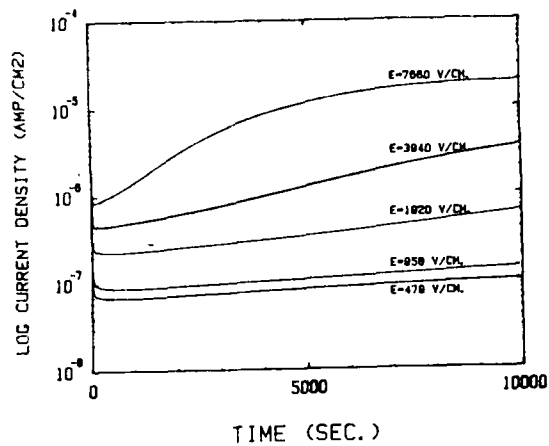
Figure 3.4.6c

Bal.01TiO3 1325C 4HRS. .071 CM. THICK. T=85C
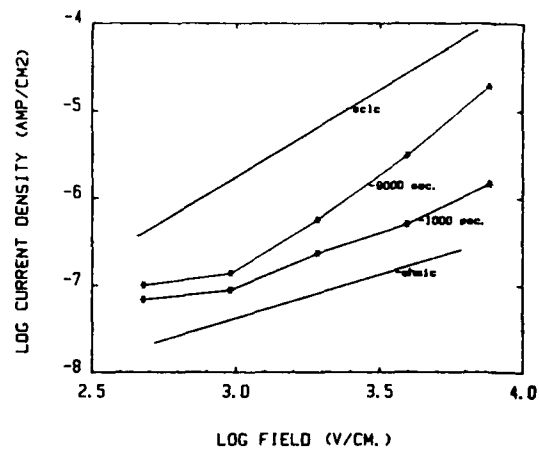
Figure 3.4.6d

Bal.01 1375C 8HRS. .071 CM. THICK. T=85C
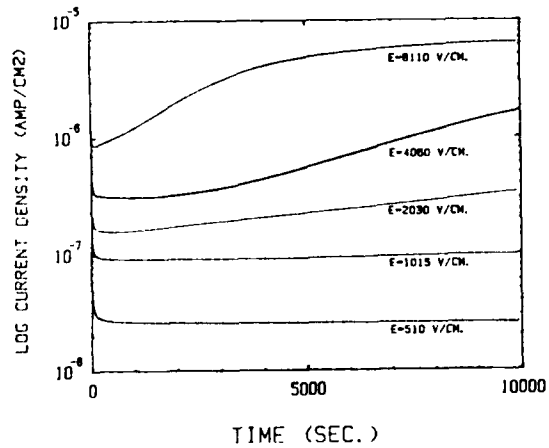
Figure 3.4.6e

Bal.01TiO3 1375C 8HRS. .071 CM. THICK. T=85C

Figure 3.4.6f

-147-
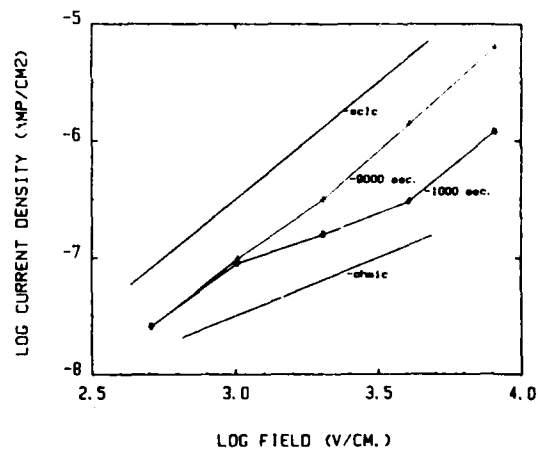
This specimen sintered to a high density, despite the low firing temperature. Current levels are nearly the same as the other excess barium compositions, but degradation does not occur significantly until 8000 V/cm. I-V behavior is nearly ohmic.

1325 $^{\circ}$C - 4 hours: 95.9 % TD   6 μm ave. GS
                            0.3 % OP   Figures 3.4.7c-d

Increasing the sintering temperature increased the density by 1.3 %, decreased the open porosity by 0.5 %, and increased the average grain size to 6 μm. Initial current levels are lower than the 1250 $^{\circ}$C specimen, but degradation occurs at all fields. I-V behavior reflects the occurrence of degradation as the curve switches from ohmic to non-ohmic behavior as the time increases.

1375 $^{\circ}$C - 4 hours: 95.6 % TD   7 μm ave. GS
                            0.7 % OP   Figures 3.4.7e-f

Increasing the sintering temperature resulted in a 0.3 % decrease in the density, an average grain size of 7 μm, and an 0.4 % increase in the open porosity. This specimen behaves nearly the same as the 1250 $^{\circ}$C specimen, with slightly lowered current levels. The specimen exhibits only slight degradation at 4000 and 8000 V/cm. I-V behavior lies between that of SCLC and ohmic.

Ba1.02TiO3 1250C 4HRS, .068 CM. THICK, T=85C
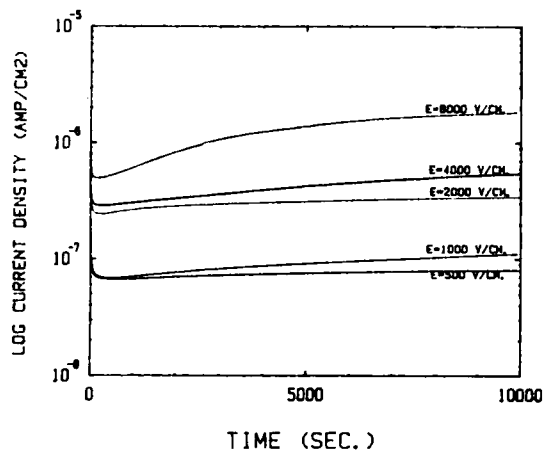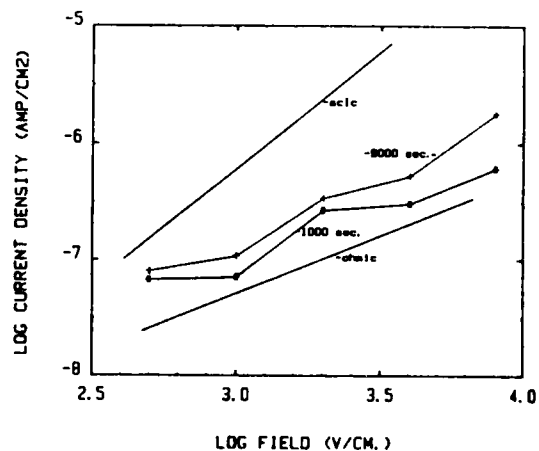
Ba1.02TiO3 1250C 4HRS, .068 CM. THICK, T=85C

Figure 3.4.7a

Figure 3.4.7b

Ba1.02TiO3 1325C 4HRS, .068 CM. THICK, T=85C
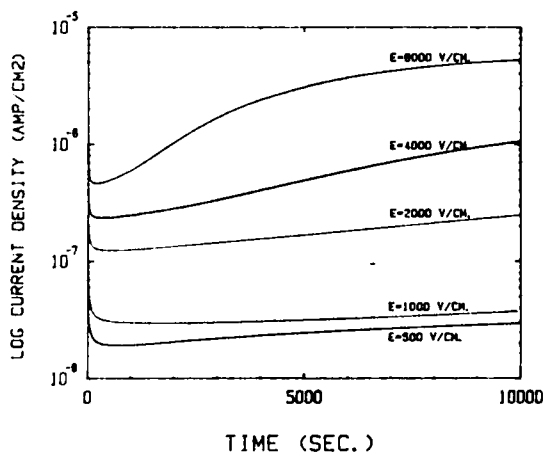
Ba1.02TiO3 1325C 4HRS, .068 CM. THICK, T=85C
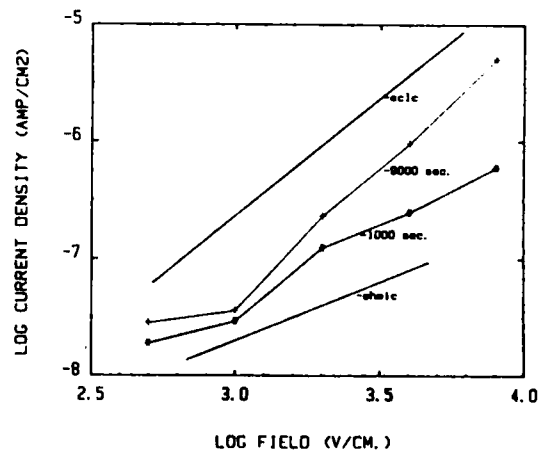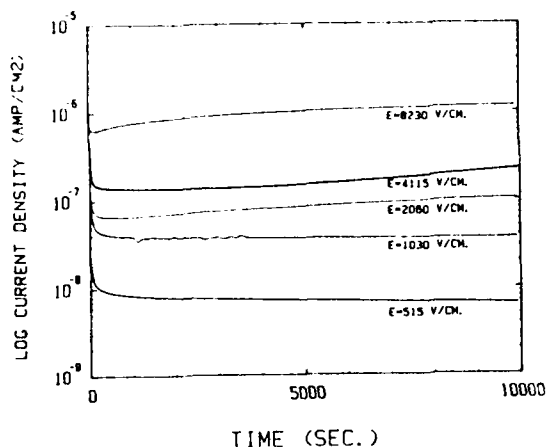
Figure 3.4.7c

Figure 3.4.7d
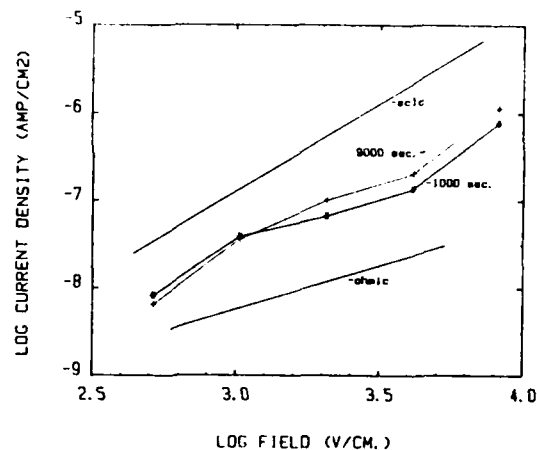
Figure 3.4.7e

Figure 3.4.7f

Summary of the High Voltage Degradation Behavior
for the Excess Barium Compositions
at 85 ^{o}C

Increasing the sintering temperature of these compositions resulted in little change in either the density, porosity, or grain size. Correspondingly, very little change was observed in the current levels or degradation behavior within individual compositions. The results and analysis can be summarized as follows.

1) The excess barium compositions all exhibited current levels 1-2 orders of magnitude greater than those of the excess Ti compositions, for fields 2000 V/cm. This would suggest that the Ba-rich phase is somehow decreasing the resistivity of the

specimens. However, increasing the amount of excess Ba results in overall lower current levels, thereby increasing the resistivity. The 1.005 composition exhibits the worst behavior. It also has the largest grain size and the most amount of intragranular porosity. The microstructures of the 1.01 and 1.02 specimens does not appreciably change. These facts, as for the excess titanium compositions, would suggest either : a) Grain boundary diffusion is causing the degradation; i.e., increasing the amount of excess Ba decreases the grain size, thereby increasing the grain boundary diffusion length, or b) The larger percentage of intragranular compared to intergranular porosity is detrimentally effecting the resistivity of the grains through field-splitting effects.

3) Comparison of the degradation behavior between the excess Ba and Ti compositions reveals a major difference. When degradation occurs in the excess Ti compositions, the current rises rapidly (the RDR), and then tapers off to a linear region. The excess Ba compositions which degrade also exhibit two regions of degradation, but the initial rise in current is never as rapid. Yet, at the end of 10000 seconds, the overall change in current level is the same. This would suggest several things:

   a) The degradation mechanisms for the excess barium and titanium compositions are different.

   b) The mobility of the migratory species changes in the grain boundaries due to the different grain boundary phases. We expect little difference in the defect

-151-

chemistry of the primary phase, $BaTiO_3$, when excess Ba or Ti are present.

===
$150\ ^oC$ Measurements
===

In order to study degradation as a function of temperature, we have begun making I-time measurements at $150\ ^oC$. At this temperature $BaTiO_3$ is in a paraelectric, cubic state. We seek to determine if the change in lattice structure changes the degradation phenomena. If it does not, then evidence points further towards grain boundary phenomena causing degradation. If it does, then we'll need to focus our attention more on the structural properties and defect chemistry of the primary, $BaTiO_3$ phase. To date, I-time measurements at $150\ ^oC$ have been made on only the porous specimens which were sintered at $1250\ ^o$ - 4 hours. Figures 3.4.8 - 3.4.14 contain the I-time, I-V results of these measurements. Individual analyses follow.

===
3.4.8 $Ba_{.98}TiO_3$ - $150\ ^oC$
- -

$1250\ ^oC$ - 4 hours: 84.5 % TD   2 um ave. GS
                       8.2 % OP   Figures 3.4.8a-b

This specimen exhibits interesting behavior. At the lowest field, degradation occurred almost immediately, following the type of curve exhibited by the $85\ ^oC$ I-time runs. However, increasing the field to 1000 V/cm and greater resulted in a different form of curve, even though degradation occurred. No
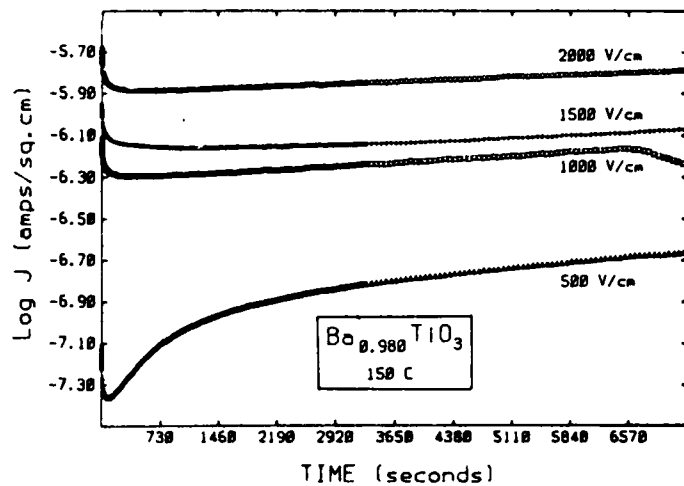
Figure 3.4.8a
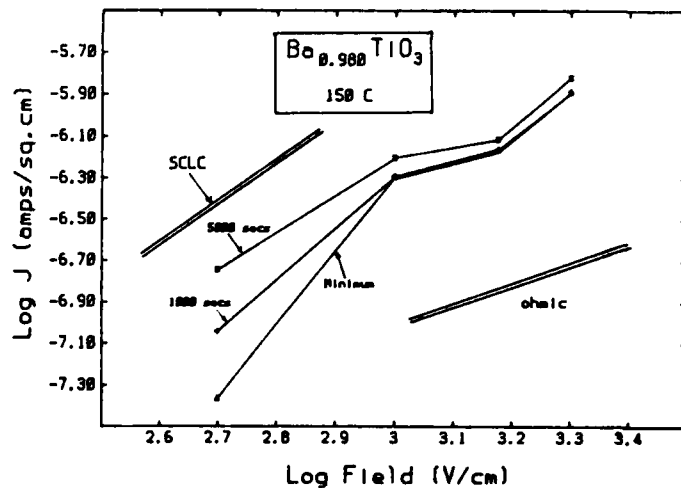
Figure 3.4.8b
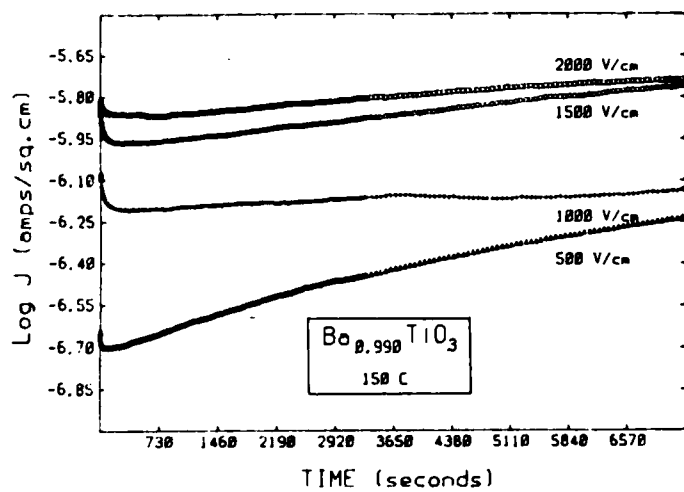
Figure 3.4.9a
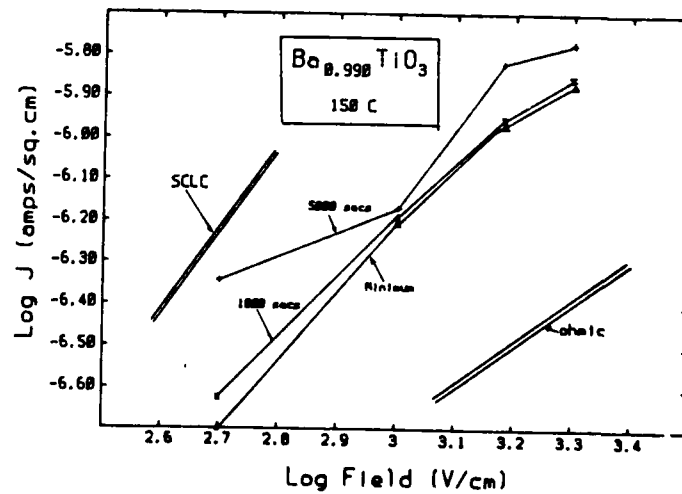
Figure 3.4.9b

rapid degradation region is observed. This particular specimen was measured on the I-time apparatus before it was discovered that reequilibration at 1200 ^{o}C - 8 hours is needed to remove the effects of previous degradation. In this case, the migratory species would already have a concentration gradient built up within the specimen due to the previous degradation run. Similiar curves were obtained in the past on all of the specimens run without requilibration. I-V behavior lies between that of ohmic and SCLC, but these curves probably mean nothing in light of the requilibration problem. This curve was included even though the data is suspect, in order to show the effects of previous degradation.

===

3.4.9 Ba$_{.99}$TiO$_3$ - 150 ^{o}C

1250 ^{o}C - 4 hours: 84.2 % TD   1 um ave. GS
                          8.4 % OP   Figures 3.4.9a-b

This specimen was also ran at successively higher fields without reequilibration. The results are similiar to the .98 specimen in that degradation at the lowest field, 500 V/cm, is rapid and exhibits a RDR region. Further increases in the field still result in degradation, but the shape of the curve is different. Current levels are approximately the same as for the 0.98 specimen. I-V behavior is non-ohmic, but is probably without meaning due to the lack of reequilibration. The remaining compositions were run with reequilibration.

===
3.4.10 Ba$_{.995}$TiO$_3$ - 150 ^{O}C
_____

1250 ^{O}C - 4 hours: 89.8 % TD   1 μm ave. GS
                        4.3 % OP   Figures 3.4.10a-b

This specimen exhibits current levels which are lower than for the 0.98, and 0.99 specimens, and approximately 2 orders of magnitude greater than for 85 ^{O}C. The latter is expected considering the activation energy is on the order of 1 eV. The former was not expected since the 0.995 specimen exhibited the highest current levels for the 85 ^{O}C I-time runs. Note at 500 V/cm the sample approaches a steady-state current, but at higher fields degrades. I-V behavior is nearly ohmic.

===
3.4.11 Ba$_{1.000}$TiO$_3$ - 150 ^{O}C

1250 ^{O}C - 4 hours: 93.3 % TD   4 μm ave. GS
                        1.6 % OP   Figures 3.4.11a-b

The stoichiometric specimen exhibits degradation at all of the fields studied. Current levels compared to the Ti-rich compositions are approximately the same for the first 100 seconds, but then degradation occurs rapidly, resulting in final current levels 1-2 orders of magnitude higher. This is surprising considering the stoichiometric composition exhibited the best behavior during the 85 ^{O}C I-time run. Current levels are 2-3 orders of magnitude greater than the 85 ^{O}C run, which is unexpected in light of the activation energy of 1 eV.
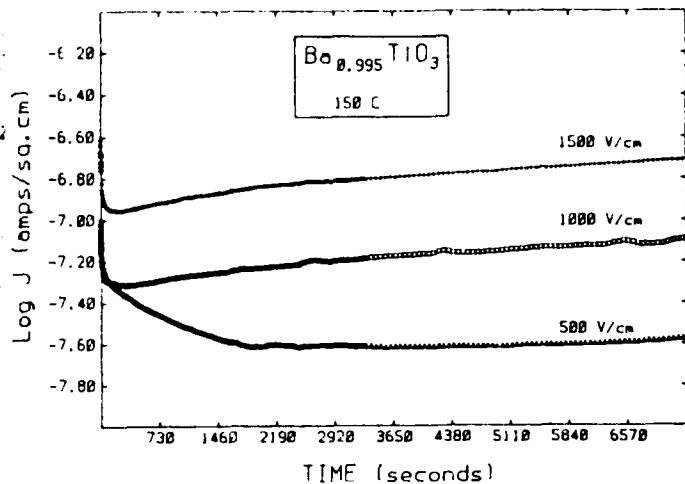
Figure 3.4.10a
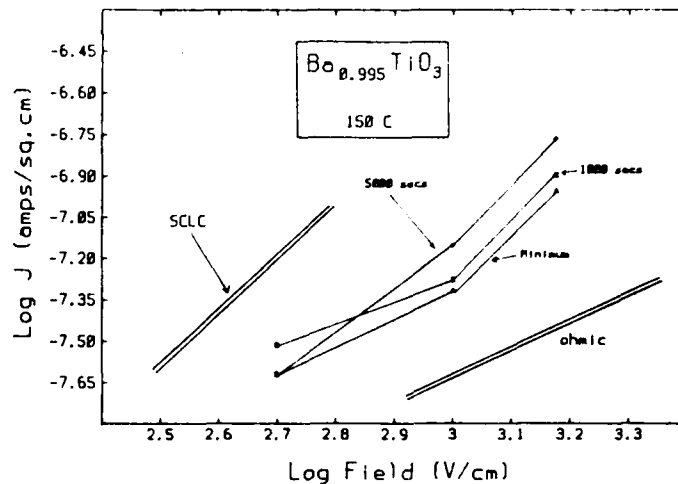
Figure 3.4.10b
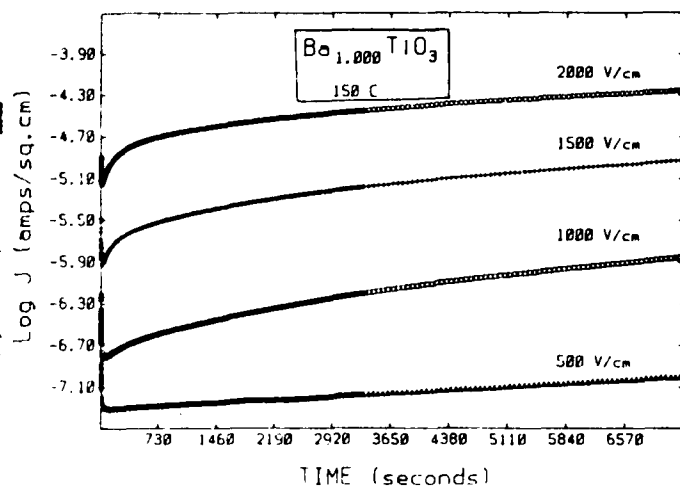
Figure 3.4.11a

Figure 3.4.11b

-156-
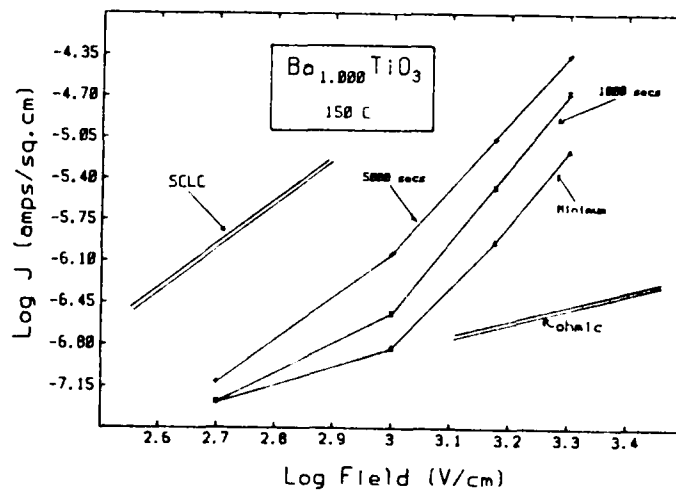
Note although the increase in field results in higher current levels, it <u>does not change the degradation rate</u>. This could mean the mobility of the species causing degradation is not field dependent. I-V behavior is non-ohmic, but may be due to the degradation occurring.

===

3.4.12 $Ba_{1.005}TiO_3$ - 150 ^oC

1250 ^oC - 4 hours: 92.1 % TD   3 um ave. GS
                        2.6 % OP   Figures 3.4.12a-b

This specimen exhibits degradation at all fields. Current levels are 2 orders of magnitude greater than the 85 ^oC run, but exhibit nearly identical behavior. Note the field does not change the degradation rate. Current levels are higher than the excess Ti compositions. I-V behavior appears to be described accurately by the SCLC injection mechanism.

===

3.4.13 $Ba_{1.01}TiO_3$ - 150 ^oC

1250 ^oC - 4 hours: 92.0 % TD   3 um ave. GS
                        1.7 % OP   Figures 3.4.13a-b

Again, degradation is observed at all the fields, but at 500 V/cm degradation does not set in until nearly 6000 seconds. Current levels are an order of magnitude greater than the 1.005 specimen, and 2 orders of magnitude greater than the 85 ^oC run. The former is unexpected as the 1.005 specimen exhibited worse behavior at 85 ^oC. Again, the field has no effect on the degradation rate. I-V behavior approaches that predicted by the SCLC injection mechanism.
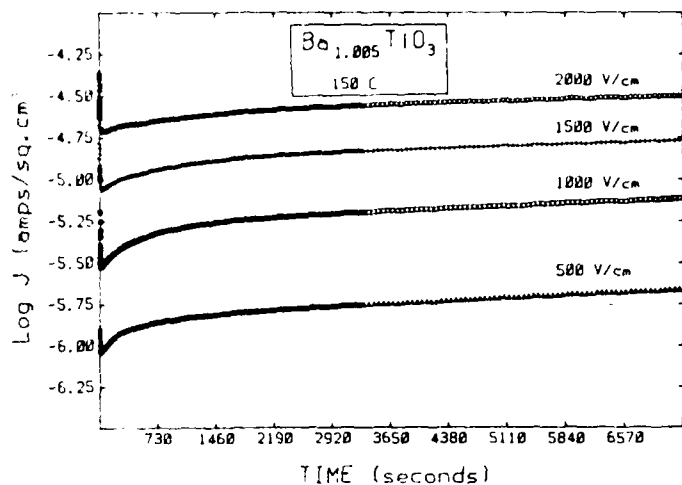
Figure 3.4.12a
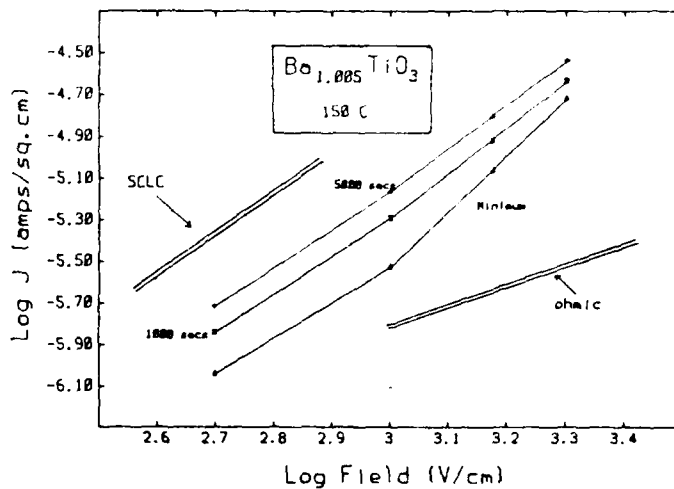
Figure 3.4.12b
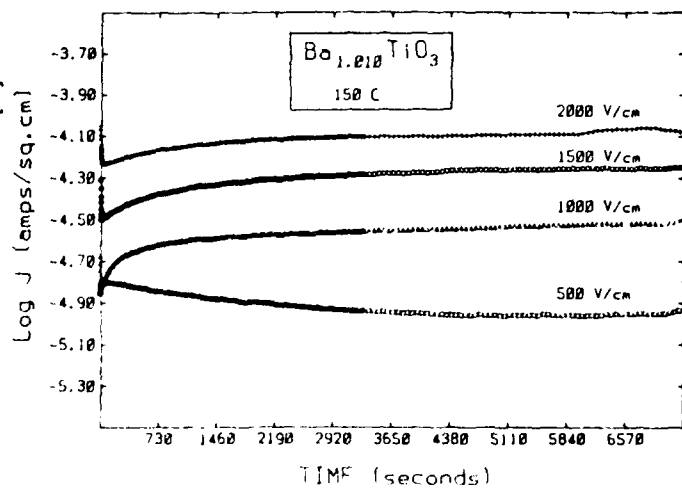
Figure 3.4.13a
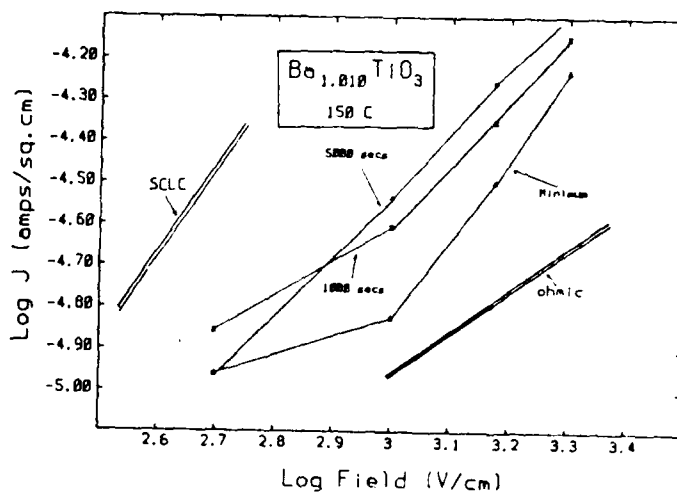
Figure 3.4.13b

===

3.4.14 $Ba_{1.02}TiO_3$ - 150 $^{\circ}C$

1250 $^{\circ}C$ - 4 hours: 94.6 % TD   3 um ave. GS
                       0.8 % OP   Figures 3.4.14a-b

This specimen exhibits slightly different behavior from the rest. At all fields, a rapid increase in current occurs, but past this point the current levelled off and achieved a steady-state condition. This could be indicative of the SCLC injection mechanism, as a large initial rise would occur due to the build-up of the space-charge, with an equilibrium established thereafter. However, the I-V curve, which is linear for this specimen, has a slope of 1.5, not two as expected for the trap-free square law of SCLC. More work needs to be done on these specimens to confirm or reject this possibility.

Overall current levels are slightly lower than in the 1.01 specimen, and 2 orders of magnitude greater than the same specimen run at 85 $^{\circ}C$.

Summary of High Voltage Degradation Measurements
for the Undoped Compositions at 150 $^{\circ}C$

High-voltage degradation measurements are being made to determine not only the temperature dependence of the degradation, but to also determine the effect of changing the crystalline structure of $BaTiO_3$ from tetragonal to cubic. The results, which have been carried out only at 150 $^{\circ}C$ on the 1250 $^{\circ}C$ - 4 hours

-159-
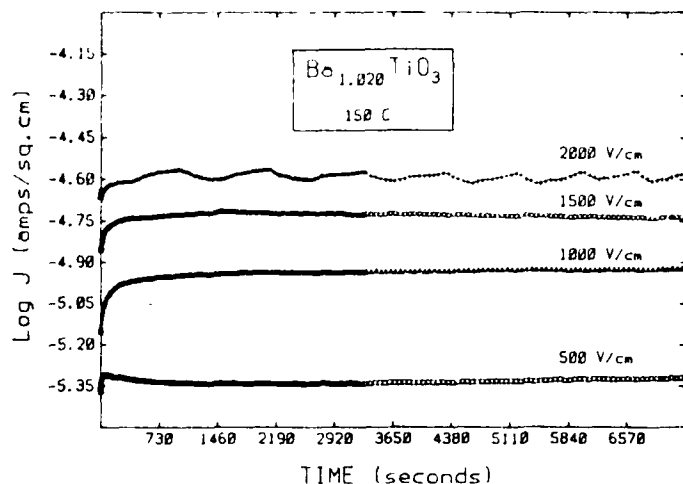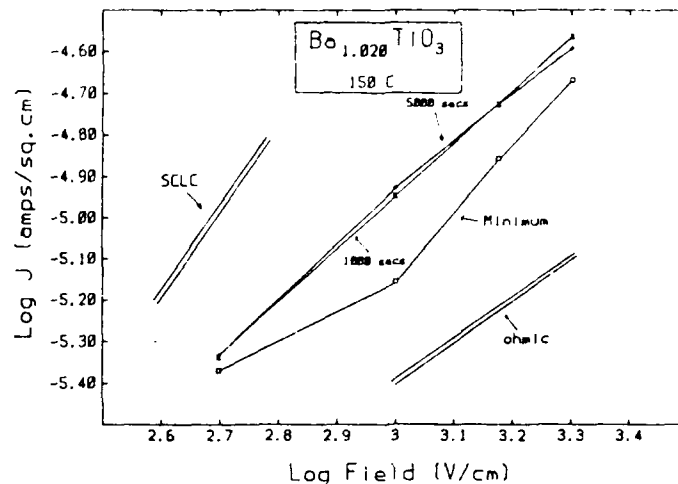
Figure 3.4.14a

Figure 3.4.14b

specimens, were closely related to the 85 $^{\circ}$C measurements, with the following differences noted:

1) Degradation did not occur for the excess Ti compositions at 85 $^{\circ}$C, however, at 150 $^{\circ}$C they all degraded to some extent. This could be indicative of several things:

- The degradation mechanism is activated, which would be related to the mobility or perhaps the concentration of the charge carriers.

- Changing the crystal structure of $BaTiO_3$ changes its degradation behavior. $BaTiO_3$ exhibits large differences in electrical characteristics between the paraeletric and ferroelectric states; the same may be true for degradation.

2) The stoichiometric composition exhibits higher current levels

and a greater degradation tendency than the excess Ti specimens. This would lead one to believe that the Ti-rich second phase lowers the field-enhanced diffusion coefficient of the migratory species. It is possible that the slightly larger grain size of the stoichiometric composition is causing this effect.

Further comparisons could be made, but a complete set of data needs to be collected at 150 $^{\circ}$C before the full story can be elucidated.

3.5 Future studies

From the results we have obtained thus far in our high voltage degradation study, many clues have been obtained concerning the mechanism behind degradation. However, more research needs to be made before the mechanism can be delineated. Future studies include:

1) Continuation of the I-time studies of the undoped compositions, expanding the range of densities and porosities for the excess Ba and stoichiometric compositions.

2) Calcining the excess barium powders at a higher temperature to remove the $BaCO_3$, with subsequent sintering and degradation studies.

3) Completing the I-time studies at higher temperatures, namely 150 and 125 $^{\circ}$C.

4) Repeating the entire I-time studies, this time in a humid atmosphere. In this manner the effect of water on the

degradation rate can be determined.

5) Begin the I-time studies on the doped compositions in order to see if altering the defect chemistry alters the degradation behavior.

6) PSU will soon have the technique established for tape casting the powders obtained from the organometallic technique. By using multilayer configurations we hope to study the thickness dependency, and the effect of sealing the electrodes on the degradation behavior.

4. Thermally-Stimulated Polarization / Depolarization Measurements

Thermally-stimulated polarization / depolarization (TSPC/DC) measurements are sensitive tools by which polarization phenomena and charge transport in insulators can be studied. The measurement basically involves monitoring the leakage/charging current passing through a material as a function of temperature. Current minima/maxima are observed when charges are released from localized trapping states (i.e. donor or acceptor states, ionic point defects), or when crystal structure changes occur. We believe this sensitivity of the current spectra to material properties could make TSPC/DC measurements a useful tool for studying degradation phenomena.

Initial TSPC/DC measurements were made on the $BaTiO_3$ compositions and commercial capacitors which were used to study degradation phenomena. From these measurements it became apparent that TSPC/DC current spectra yield much more information concerning material properties than was expected. We believe TSPC/DC measurements also yield information concerning spontaneous polarization, domain switching rates, aging phenomena, phase transitions, energy levels of point defects, and overall defect chemistry; all of which help us further understand the underlying nature of the material being studied.[*]   In

---

addition, TSPC measurements are an excellent way to determine the low-temperature resistivity and activation energy of resistivity.

Based upon these expectations and early results, the program concerning TSPC/DC measurements has been expanded beyond studying only degradation phenomena. To date we have collected a large data base of TSPC/DC spectra, and are in the process of interpreting the results. This requires analysis in terms of the thermodynamics[82] and lattice dynamics[83] of ferroelectricity.

Several auxiliary measurements, such as polarization vs. field, and the piezoelectric and electrostrictive coefficients, $Q_{i,j}$, need to be made on our specimens before a full interpretation of the results in these terms can be made. A Sawyer-Tower apparatus is currently being rebuilt and interfaced with our computer system at UMR. This will allow us to determine the temperature dependency of the spontaneous polarization, as well as the nature of the phase transitions; i.e. first or second order. During August 1984, a trip was made to Penn State to begin measuring the $Q_{i,j}$ coefficients of our samples. Future trips will hopefully allow us to complete these measurements.

Before presenting the results and discussion of the TSPC/DC measurements collected to date, in order to acquaint the reader with what TSPC/DC measurements have been used for in the past, a short literature review is included.

4.1 Literature Review

As stated previously, TSPC/DC spectra reflect the resistivity, the energetic distribution of traps, and changes in

crystal structure of a material. TSPC measurements examine the current behavior of a material subjected to a DC stress while being heated at a constant rate from low temperatures. If charges are released from traps during heating, the magnitude of the current released can be expressed by[84]:

$$I(T) = A \exp\left[\frac{-E_a}{kT}\right] \exp - \left[B \int_{T_o}^{T} \exp \frac{-E_a}{kT'} dT'\right] \qquad (1)$$

where: E_a = activation energy of localized trapping state
k = Boltzmann constant
T = absolute temperature
T_o to T = temperature range over current release
A,B = constants; dependent upon trapping state and experimental parameters.

This equation pertains primarily to the thermal ionization of carriers into the conduction band (electrons) either from band to band processes or from donor and impurity centers during "polarization" (i.e. heating with an applied field). The magnitude of current minima and maxima resulting from changes in crystalline structure will be dependent upon resistivity differences between crystal structures, and whether the structure change represents a ferroelectric-cubic (F-C), or ferroelectric-ferroelectric (F-F) transition. The latter is of particular interest to us in the study of polarization phenomena in $BaTiO_3$, which exhibits two F-F transitions and one F-C transition. During a F-F transition a current peak will be produced in the TSPC spectrum, the magnitude of which will depend upon the change in magnitude and direction of the spontaneous

polarization, P_s. During a F-C transition, the P_s goes to zero; the presence and magnitude of a current peak during this transition will then depend upon how P_s varies with temperature, i.e. : is the transitio. first or second order ?[85] These effects as they pertain to the TSPC/DC results obtained on the BaTiO$_3$ compositions are contained in Section 4.3.2.

TSDC measurements involve measuring the charge released from a polarized material which is being heated at a constant rate from low temperatures. Again, current peaks will appear as the direction and magnitude of the P_s changes with crystal structure and temperature. Essentially, dipoles will reorient to the lowest free energy position, if they are not locked in place due to physical constraints imposed by the crystal structure or microstructure. An equation for the magnitude of the current produced by dipole reorientation during heating can be represented by[84]:

$$I(T) = \frac{N_d u^2 a E_p}{k T_p t} \exp\left[\frac{-E_a}{kT}\right] \exp\left[\frac{-1}{b t_o} \int_{T_o}^{T} \exp\frac{-E_a}{kT'} \, dT'\right] \quad (2)$$

where: T_p = polarization temperature
        N_d = dipole concentration
        u = dipole moment
        t= dipole relaxation time
        a = factor of dipole orientation freedom
        b = heating rate
        E_p = applied field
        E_a = trap depth
        T to T = heating range

with other terms being defined previously.

Chen[86] reviewed methods for the kinetic analysis of thermally

stimulated processes. These methods included thermoluminecence (TL), thermally-stimulated current (TSC), ionic thermocurrents (ITC), and thermally-stimulated electron emission (TSEE). Shindo[87] reviewed formula derivations for the spectral peaks occurring in TSPC/DC measurements, and recognized the spectra caused by reorientation of permanent dipoles were similiar to those caused by ionic transfer.

Hong and Day[88] studied ionic motion in glasses using TSPC/DC measurements. Polarization peaks were attributed to to bulk polarization and were dependent upon glass composition. A type of dipole orientational polarization involving Na ion movement around nonbridging oxygen ions were also found. Similiar work by Agarwal and Day[89] investigated alkali ion motion in both single alkali silicate glasses and in mixed alkali glasses to determine polarization and conduction mechanisms.

Bucci and Fieschi[90] investigated thermally-activated dipole reorientation in Sr and Ca-doped NaCl using the ITC technique. They were able to use this technique to determine impurity solubility and activation energy. In addition, qualitative measurements on Teflon, calcite, and quartz were performed to illustrate polarization in non-ferroelectric dielectrics. McKevver and Hughes[91] measured the TSPC/DC behavior in alkali halides and found the resulting spectra was due to impurity/vacancy dipoles. In related studies, Hino[92] made TSPC measurements on solid dielectrics such as organic polymers, ZnTe, and $Al-SiO_2-Si$ metal oxide semiconductor compositions. Through his measurements Hino was able to determine dipolar

relaxation times, trap levels, and ionic space charge polarization.

Morin and Oliver[93] studied ionic and electronic point defect energy levels in the band gap in $SrTiO_3$ using TSPC/DC measurements. Al^{+3} acceptors were found to be 0.18 eV above the valence band, Fe^{+3} acceptors 0.075 eV above the conduction band, and oxygen ion vacancies 0.085 eV below the conduction band. Siegwarth and Morrow[94] made TSPC measurements on $SrTiO_3$ ceramics doped with V^{+5} and Nb^{+5}. The observed current peaks were not due to ferroelectric or antiferroelectric transitions but to the presence of of a thermoelectric state existing for permanent dipoles in the material. Lebedeva et.al.[95] investigated $SrTiO_3$ using TSPC techniques to measure electron trapping levels in the band gap and found them to range from 0.50 to 0.92 eV.

4.2 Experimental Procedure

In our program we are studying the following variables and their effect on TSPC/DC behavior of $BaTiO_3$:

Variables Studied in the TSPC/DC Program

1) Compositional

  - Donor and Acceptor doping (La, Nb, Al, Mg)

  - Nonstoichiometry (A:B = 0.96 - 1.04)

  - Shifters (Sr, Zr, Pb)

  - Commercial capacitors (NPO, BX, Z5U)

2) Microstructural

  - Porosity

- Grain size / distribution

3) Experimental

- Applied field

- Heating Rate

- Aging time following poling

To date, forty-three compositions have been measured, including a number of commercial capacitors; only the La and Mg-doped, and Zr and Pb-shifted compositions have not been measured. The measurements have been carried out on only maximum density specimens, which still allows determination of the effect of grain size and porosity due to the vastly different sintering characteristics of the nonstoichiometric specimens. Applied fields range from 250 to 8000 V/cm, with a constant heating rate. The effect of poling and subsequent aging, and variation of the heating rate on TSPC/DC behavior has not yet been measured.

4.2.1 Compositions/Specimens

In order to determine if the technique could predict degradation tendencies, initial TSPC/DC measurements were made on $BaTiO_3$ compositions and commercial capacitors. These initial results prompted the expansion of the program in order to study the value of TSPC/DC measurements in terms of understanding ferroelectric behavior. In addition to the original forty-six $BaTiO_3$ compositions which were prepared for degradation analysis, an additional twenty-one Sr-shifted $BaTiO_3$ compositions with A:B = 0.995 to 1.005 were prepared for this study (Section 3.2.1).

The excess barium powders used for the TSPC/DC runs were calcined at 850 ^{O}C, which results in large differences in sintering behavior, and hence the microstructure of the specimens (section 3.2.3). In all cases the excess Ba acted as a grain growth inhibitor, the resulting grain size of the specimen typically on the order of 1 micron or less.

Disk specimens electroded with platinum were prepared as outlined in Section 3.2, with the maximum density specimens being chosen for initial study.

4.2.2 Electrical Measurements

In order to monitor the TSPC/DC behavior at low temperatures (-100°C), a sensitivity of 10^{-14} amps is required. This sensitivity was achieved by building a completely enclosed, shielded test chamber which is connected to an electrometer with grounded triaxial cable. Figure 4.2.2a is an illustration of the TSPC/DC chamber. It essentially consists of a stainless steel outer chamber which houses a removable inner assembly. This assembly contains a spring-loaded test fixture and thermocouples, separated and supported by teflon to insure electrical isolation. Three valves connect the chamber to a vacuum supply (mechanical), a dry inert atmosphere (helium), and a bubbler exhaust. The dry inert atmosphere is passed through the system to insure a moisture-free environment. Heating is provided by heat tape wrapped around the stainless steel outer chamber, and is
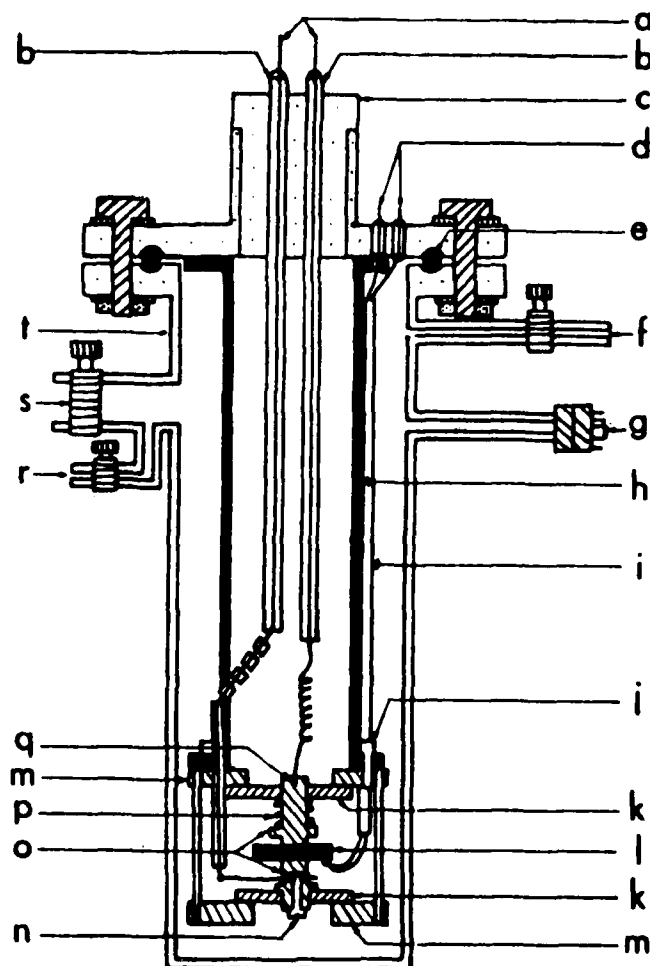
Figure 4.2.2a: Diagram of the TSPC/DC test chamber. a) copper wire to the electrodes, b) alumina tube, c) Teflon insulation, d) thermocouple, e) O-ring, f) helium inlet, g) vacuum gauge, h) inner copper tube, i) thermocouple spaghetti, j) screw, k) Teflon insulation, l) test sample, m) metal frame, n) set screw, o) electrodes, p) spring, q) set screw, r) exhaust outlet, s) vacuum outlet, and t) stainless steel container[88].

controlled with a Eurotherm temperature controller capable of controlling the heating rate.

A Hewlett-Packard 4140B picoammeter / DC voltage source measures the current and supplies the DC voltage; its sensitivity is 10^{-15} amps. All measurements are made with this picoammeter

in conjunction with a HP 85 3497A Data Acquisition Control Unit which monitors the temperature and stores the data on disk. A X-Y recorder also records the current-temperature results; which serves as a backup in the event of disk failure.

Capacitance measurements are made using a General Radio GR1689 Precision RLC Digibridge, which is also connected to the HP3497A system. Data is plotted with a Bausch and Lomb DMP-29 X-Y graphics plotter.

The procedure to make TSPC/DC measurements is as follows:

TSPC/DC Measurement Procedure

1) Desired test specimen is loaded, sealed into the test chamber, and connected to the picoammeter.

2) The chamber is evacuated and then heated to 165 $^{\circ}$C for two hours to aid in moisture removal from the system.

3) The test chamber is purged with dry helium gas and cooled to -100 $^{\circ}$C by immersing the test chamber in liquid nitrogen.

1st Polarization

4) Heating is started at a controlled rate (4.4 $^{\circ}$C/min), the desired field is applied, and the current is monitored. Data is taken at a minimum of 10 second intervals, the rate proportional to the time rate of change of the current. Monitored temperature range is from -100 to 165 $^{\circ}$C.

2nd Polarization

5) Once 165 $^\circ$C is reached, the sample is immediately
    quenched to -100 $^\circ$C with the field still applied.
    The measurement cycle is repeated, constituting the 2nd
    polarization.

Depolarization

6) Upon completion of the 2nd polarization, the sample is
    again quenched to -100 $^\circ$C, the field removed, contacts
    shorted to eliminate space charges, and then heating
    begins and the measurement cycle repeated.

Capacitance vs. temperature measurements at 1000 Hz are made
using the same procedure, with the same heating rate.

Initially, three polarization measurements were made, but in
nearly all cases the sample is fully poled by the 2nd
polarization. 3rd polarization measurements exactly duplicated
the 2nd polarization runs; a reassuring result.

The remainder of this section concerning TSPC/DC measurements
will be divided into two sections: 1) TSPC/DC measurements, and
2) TSPC/DC measurements and their relationship to degradation
phenomena. A full interpretation of these measuremnts is not yet
complete in terms of ferrolectric behavior. However, general
observations can be made which support the viewpoint that the
current spectra's behavior is directly related to atomic
processes characteristic of ferroelectric materials.

4.3 Observed TSPC/DC Behavior

Since our last report the TSPC/DC program has been greatly expanded in an effort to determine its value in terms of elucidating ferroelectric behavior. This section presents the results and preliminary analyses of the measurements which have been carried out on single crystals, commercial capacitors, and polycrystalline $BaTiO_3$. Complete analysis of the data will not be possible until Sawyer-Tower, and $Q_{i,j}$ measurements are made, but general trends are included.

Data is presented in three forms: 1) $\pm$ Log J (amps/sq.cm) vs. Temperature, 2) Dielectric Constant vs. Temperature, and 3) 1/K vs. Temperature. The first of these is simply the TSPC/DC spectrum, usually containing the first and second polarization currents, and the depolarization current. Knowledge of how the dielectric constant changes as a function of temperature aids in the "visual" interpretation of the TSPC/DC spectrum, as well as yielding fundamental numerical information concerning the nature of the phase transitions, and the expected magnitude of current peaks. 1/K vs. Temperature graphs, which are obtained from the dielectric constant data, are useful in: a) illustrating the Curie-Weiss law, b) determining the Curie constant (C.C) and the Curie temperature (T_c), and c) determining if the phase transition is first or second order (i.e. studying the temperature dependence of the spontaneous polarization, P_S). All of these are needed in order to analyze the results in terms of Devonshire theory of ferroelectricity.

This section of the report will be divided into the analyses of the various specimens measured:

1) Single Crytals

2) Commercial Capacitors

3) Undoped $BasTiO_3$'s

4) Acceptor and Donor-doped $BaTiO_3$

5) Sr-shifted $BaTiO_3$

Before presenting the results, a simplified analysis of what TSPC results signify needs to be presented. Figure 4.3a is a graph of Log J vs. T with four simple curves. Positive current on these graphs correponds to leakage current; i.e. normal electron flow in the direction of the anode. Negative current on these graphs corresponds to electron flow in the opposite direction, and is indicative of the charging, or displacement current in a ferroelectric as its dipoles align with the field.

Curve #1 would be the type exhibited by a nonferroeletric ceramic material as it is heated. The slope of the line would be proportional to the activation energy of the conduction process. Curve #2 is similiar, but contains a peak in the positive direction. The peak could correspond to several things, but in this case we will assume it is due to a discrete electron trap, such as a donor impurity, reaching a sufficient "kT" to empty its electrons into the conduction band. The temperature at which this occurs is proportional to the energy depth of the impurity, and the magnitude of the peak proportional to the impurity concentration.
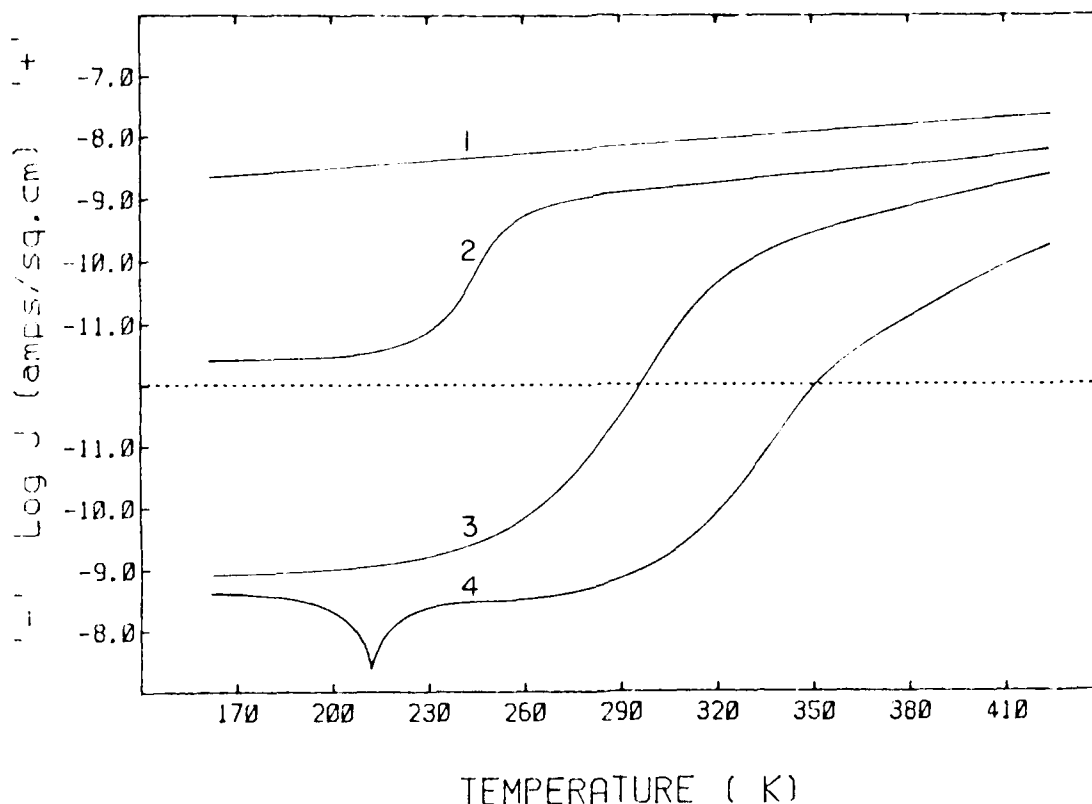
Figure 4.3a: Simplified TSPC behavior of ideal systems described in the text.

Curve #3 exhibits a transition from negative to positive current, and is characteristic of polarizable, high-resistivity solids. When a field is applied at low temperatures, the specimen begins to polarize (i.e. negative current), the degree or magnitude of which is dependent upon the temperature and, if the material is ferroelectric, how "locked-in" the dipoles are. At this low temperature the leakage current of the solid is less than that of the charging current due to its high resistivity; i.e. low concentration and mobility of the charge carrier. However, as the temperature increases, the leakage current will eventually increase to a value greater than the charging current and a transition to positive current will occur.

-176-

Curve #4 is similiar to curve #3 but in this case a peak in the negative direction is included. This peak may be attributed to the occurrence of a phase transition; for later purposes it will be assumed to be due to a ferroelectric-ferroelectric transition. In this case, as the phase transition occurs, the value of the spontaneous polarization, P_S, abruptly increases, resulting in a current peak in the negative direction. The magnitude of this peak will depend primarily on the change in magnitude of P_S, and the ability of the dipoles to align in the direction of the field. It would be possible for P_S to increase, yet the number of polarization directions accessible to decrease, resulting in an overall lessening of the net polarization. Note we can also correlate these peaks to the variation of the dielectric constant with temperature. If P_S decreased we would expect the current to peak upwards into the positive current regime.

In reality no systems are so simply described. The P_S is not the only thing which will effect the magnitude, direction, and presence of peaks in the TSPC/DC spectra. Electrostrictive effects, microstructure, and the nature of the phase transition will all play a role; the purpose of our TSPC/DC program is to determine them.

In the following analyses frequent reference will be made to the four examples c. Figure 4.3a; references will be termed as curve #1,2,3, or 4.

4.3.1 Single Crystal Measurements

Initial TSPC/DC measurements were carried out on a variety of single crystal specimens in order to: 1) Study both ferroelectric and nonferroelectric "simple" systems (i.e. non-polycrystalline) in order to achieve an understanding of the results, and 2) To establish a base line from which to compare the results from polycrystalline materials. Figures 4.3.1a-f contain the results of the TSPC/DC behavior of the single crystals measured.

Figure 4.3.1a is of Al-doped $SrTiO_3$. This paraelectric crystal initially exhibited negative current as it polarized (i.e. space charge buildup and electron cloud distortion), and then switched to positive current as the leakage current increased. Surprisingly, the current increased rapidly with increasing temperature, indicative of the occurrence of some form of degradation. This specimen mimics the behavior of curve #3, Figure 4.3a.

Figures 4.3.1b-d are of undoped, Nb-doped, and Al-doped TiO_2. Figure 4.3.1b, the undoped crystal, is an excellent example of curve #3; in this case for a paraelectric material. Note the low current levels of the TSDC; due to its low dielectric constant TiO_2 does not store much charge. Nb acts as a donor-dopant in TiO_2, and Figure 4.3.1c reflects this fact. Current levels are several orders of magnitude greater, which is expected due to the rise in carrier concentration. The depolarization current is constant throughout the temperature range, but at a unexpected high value. Possibly ionic point defects present due to the
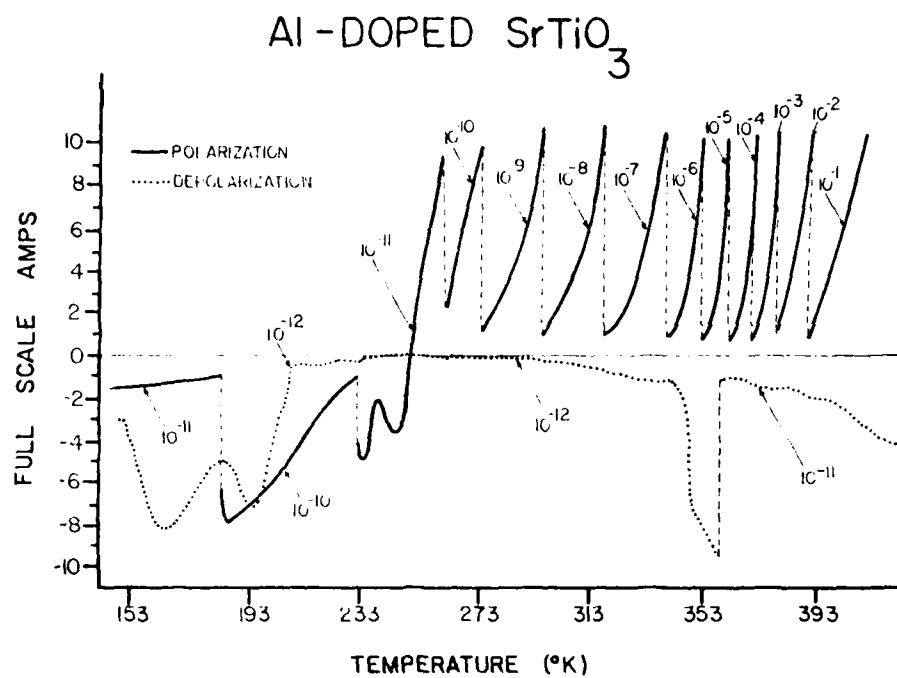
Al-DOPED SrTiO₃

Figure 4.3.1a: TSPC/DC behavior of an Al-doped SrTiO₃ single crystal.
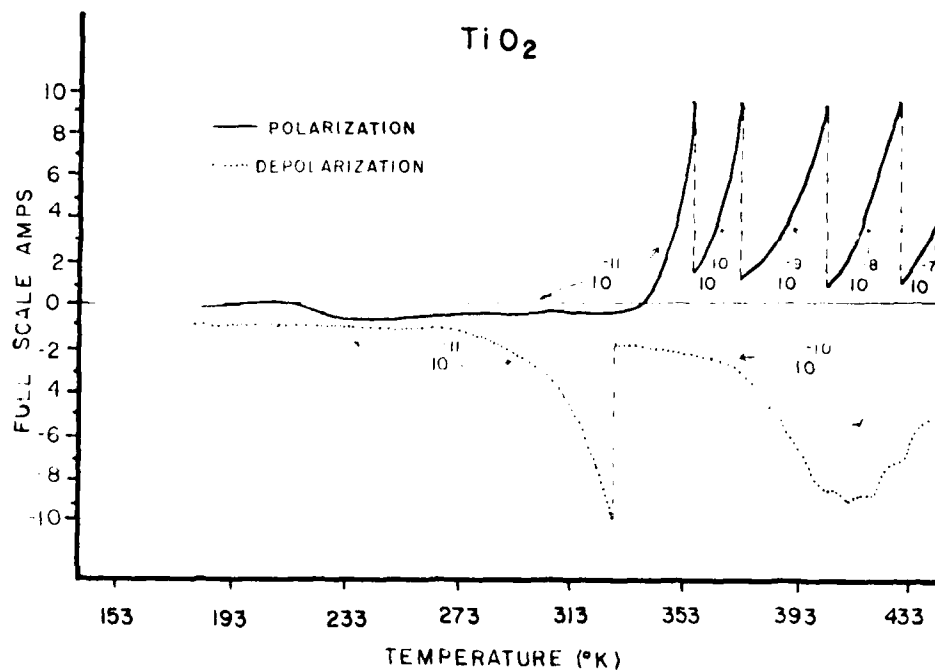
TiO₂

Figure 4.3.1b: TSPC/DC behavior of an undoped TiO₂ single crystal.
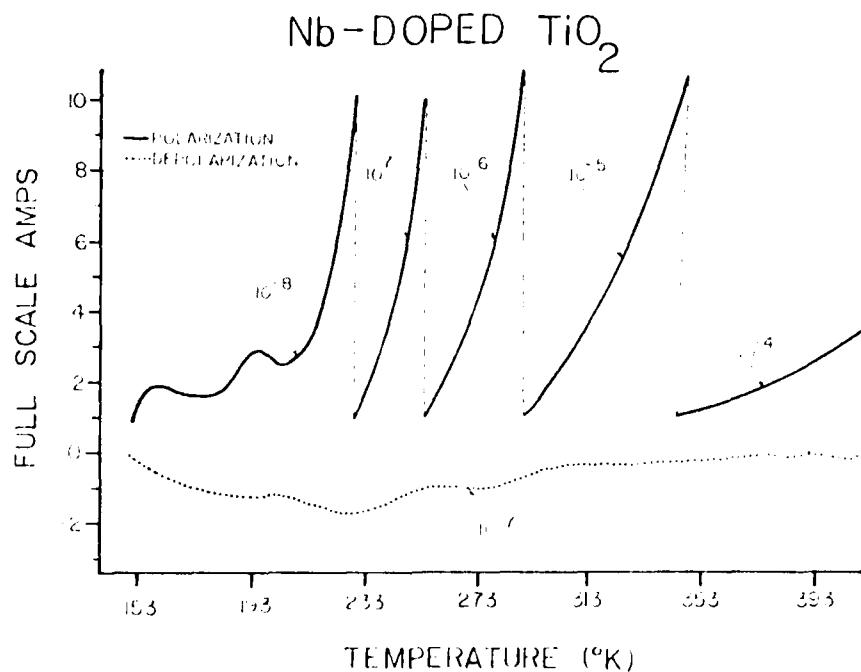
Figure 4.3.1c: TSPC/DC behavior of a Nb-doped TiO_2 single crystal.
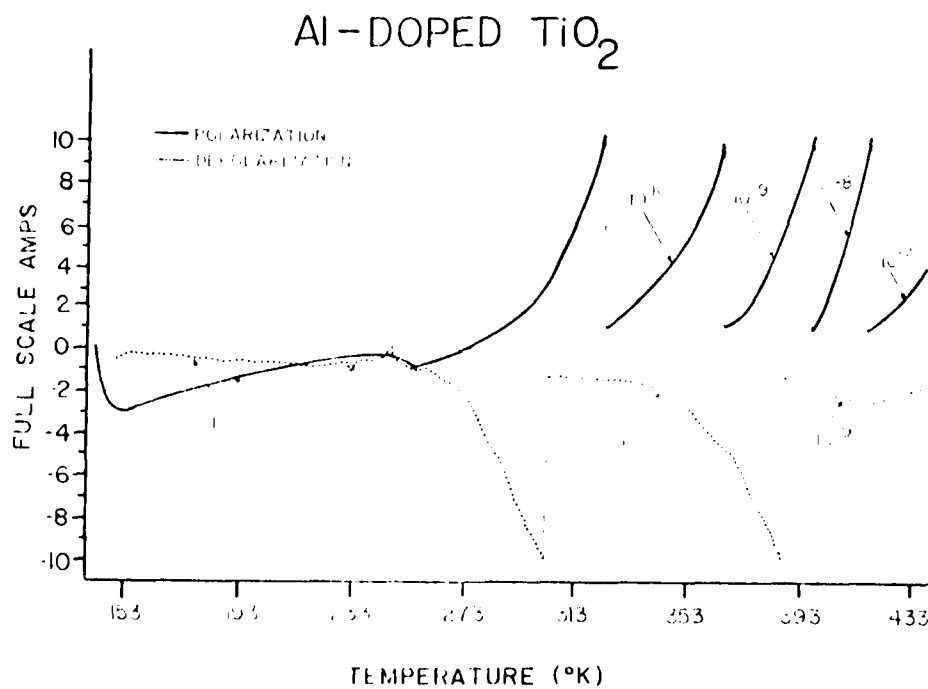
Figure 4.3.1d. TSPC/DC behavior of an Al-doped TiO_2 single crystal.

doping have migrated, resulting in ionic polarization of the solid. Al acts as an acceptor in TiO_2, and will either have the effect of increasing the $V_O^{\cdot\cdot}$ concentration (ionic compensation), or will act as an electron trap through hole generation (electronic compensation). In either case we would expect the conductivity of the crystal to decrease. Figure 4.3.1d shows the TSPC/DC curve appears to be nearly duplicate of the undoped single crystal, which leads to questions concerning the efficiency of Al acting as an acceptor. Nonetheless, it can be seen how the TSPC/DC behavior serves as a useful tool in determining the low temperature resistivity characteristics of a solid.

Figure 4.3.1e-f are TSPC and TSDC curves for a $BaTiO_3$ single crystal. The three phase transitions which occur over a -100 to 165 ^{O}C temperature range are clearly seen. The interpretation of this graph is not yet complete, particularily in terms of why the current is positive throughout the entire range with the exception of the Curie point; here the current peaks strongly into the negative region as P_S goes to zero and the sample discharges. These results are significantly different from the polycrystalline specimens, which is not unexpected, yet to date not clearly understood. The TSDC behavior is typical; negative current peaks are due to charge release as dipoles are free to reorient in the absence of a field.

The results from these measurements are particularily useful in analyzing the TSPC/DC behavior of the commercial capacitors, which is contained in the next section.
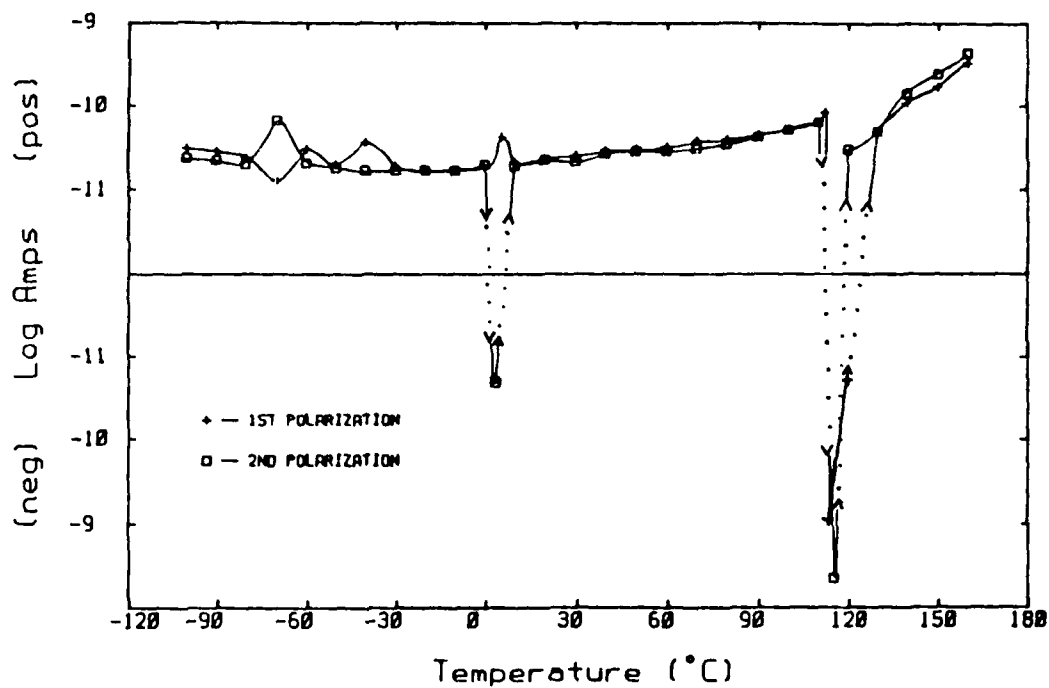
Figure 4.3.1e: TSPC behavior for a BaTiO$_3$ single crystal.
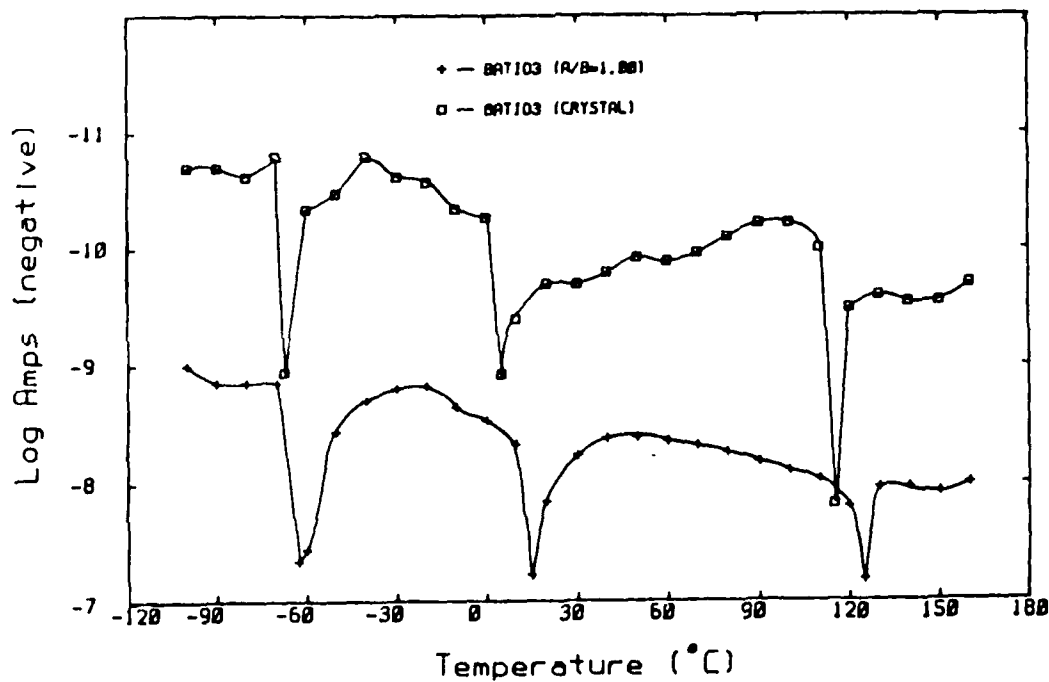
Figure 4.3.1f: TSDC behavior of a BaTiO$_3$ single crystal.

4.3.2 Commercial Capacitor Measurements

In connection with our effort to use TSPC/DC measurements as a tool for studying degradation, we have measured the TSPC/DC current spectra of a number of commercial capacitors. Figures 4.3.2a-f are TSPC/DC graphs and capacitance curves for NPO, and BX formulations, and are representative of the measurements carried out on other capacitors measured with similiar formulations.

Figures 4.3.2a,b and c are TSPC/DC and capacitance results of a NPO capacitor. Note the simple behavior is similiar to that of curve #3, figure 4.3a, and to the results on the undoped TiO_2 single crystal. The second polarization of figure 4.3.2a remains positive because the capacitor is already polarized. The depolarization curve initially starts off positive, due to "freezing in" the charges, but as the temperature increases they once again become free to move and the sample discharges. The capacitance curve is nearly constant over the entire temperature range. NPO capacitors are made primarily from paraelectric TiO_2, which is reflected by the TSPC/DC results.

Figures 4.3.2d, e, and f are TSPC/DC and capacitance results for a BX capacitor. The range of constant capacitance from figure 4.3.2f is reflected by the TSPC results of figure 4.3.2d. Note in figure 4.3.2e, which are the results for another BX capacitor plotted without the log scale to exhibit more detail, the presence of a whole series of peaks in the TSPC curve. BX capacitors are primarily made from $BaTiO_3$, with shifters added to
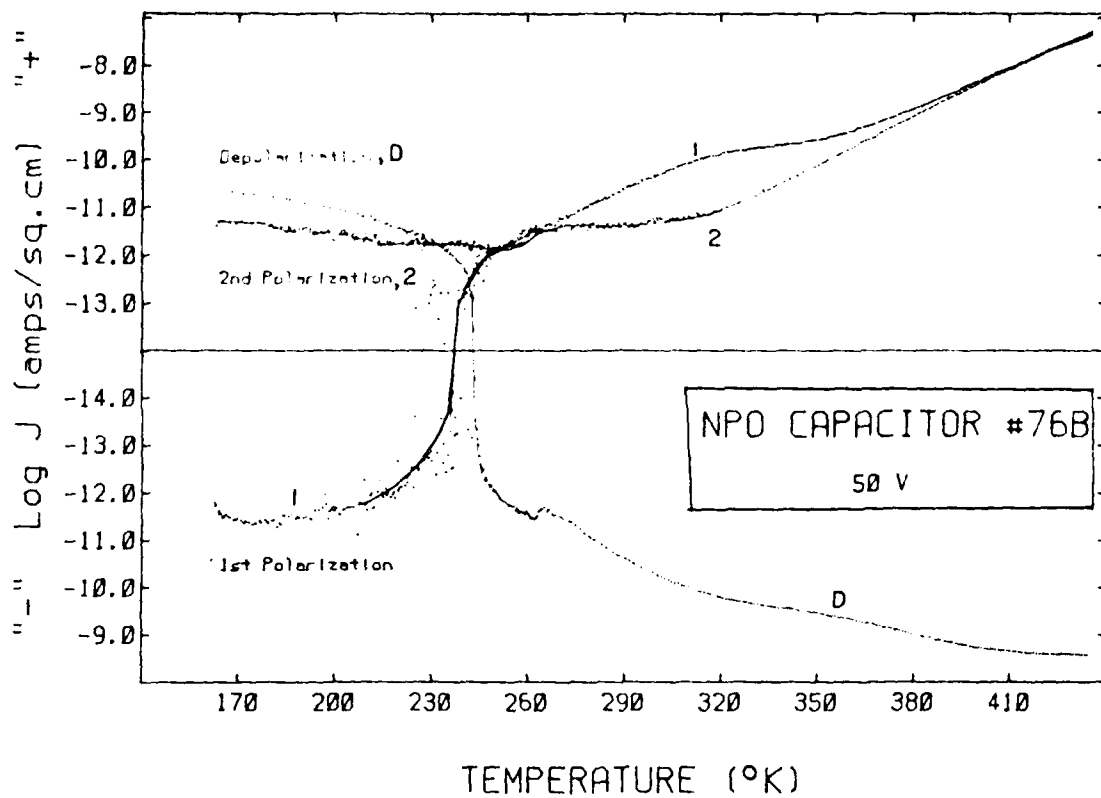
Figure 4.3.2a: TSPC/DC behavior of NPO capacitor #76B.
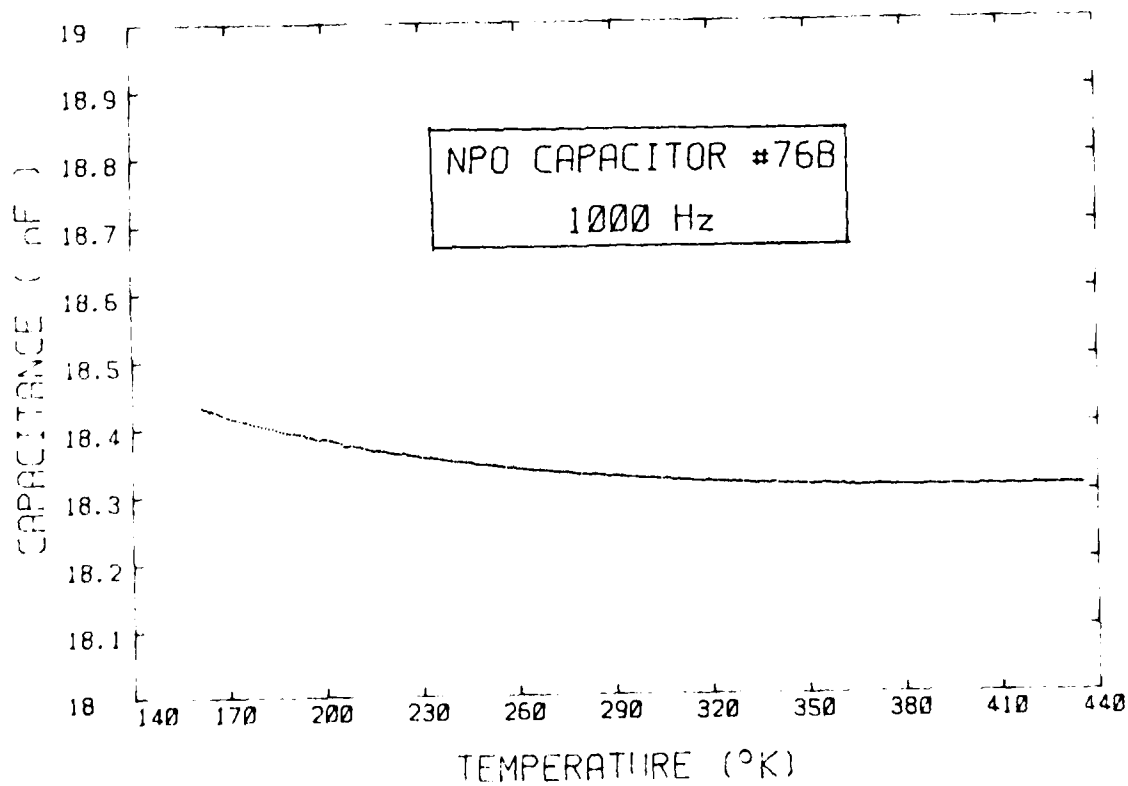
Figure 3.4.2b: Capacitance vs. Temperature curve for NPO capacitor #76B.

NPO CAPACITOR
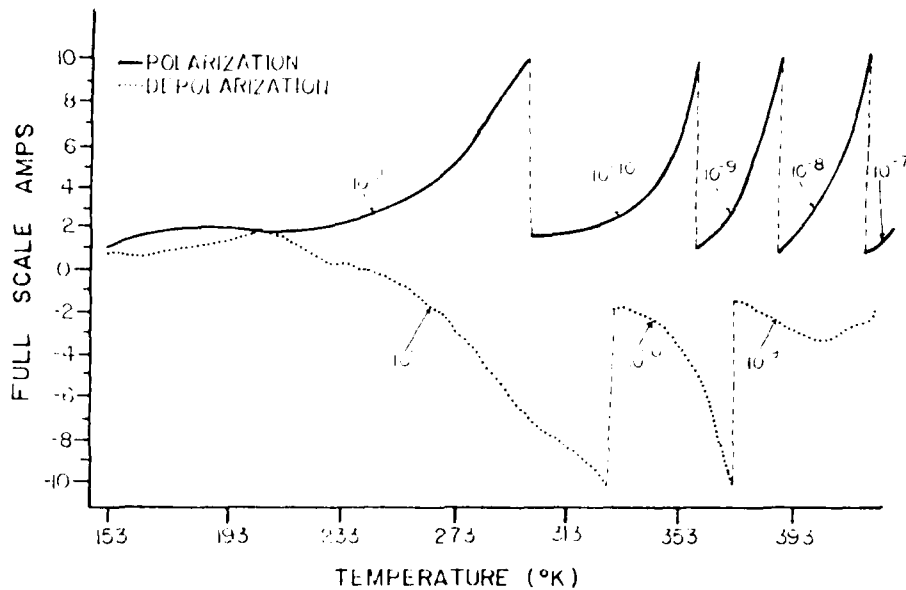
Figure 4.3.2c: TSPC/DC behavior for an NPO capacitor, plotted without the logarithm of the current to show detail.

BX CAPACITOR
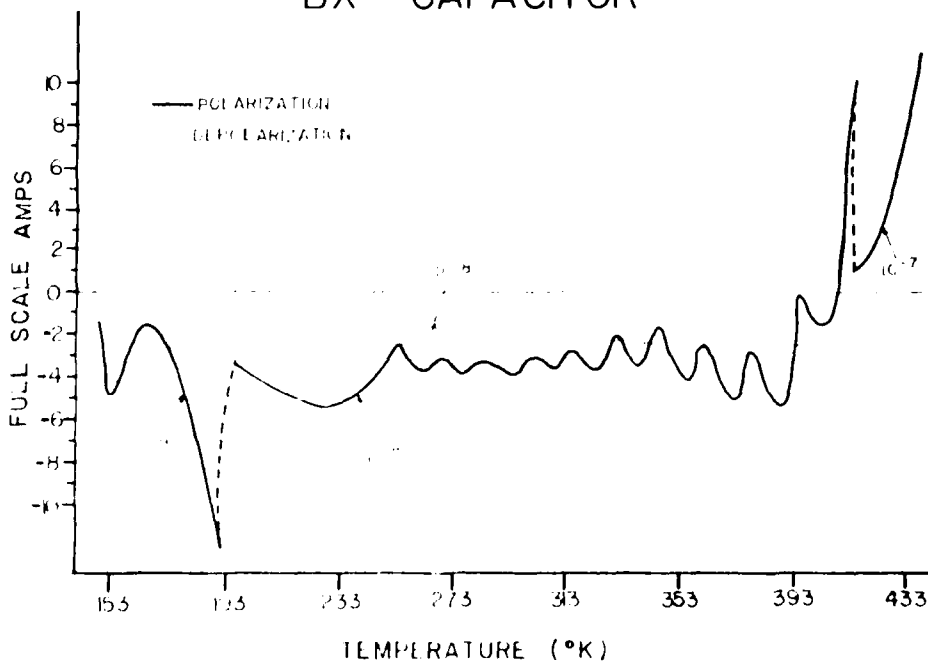
Figure 4.3.2d: TSPC/DC behavior of a BX capacitor, plotted without the logarithm of the current to show
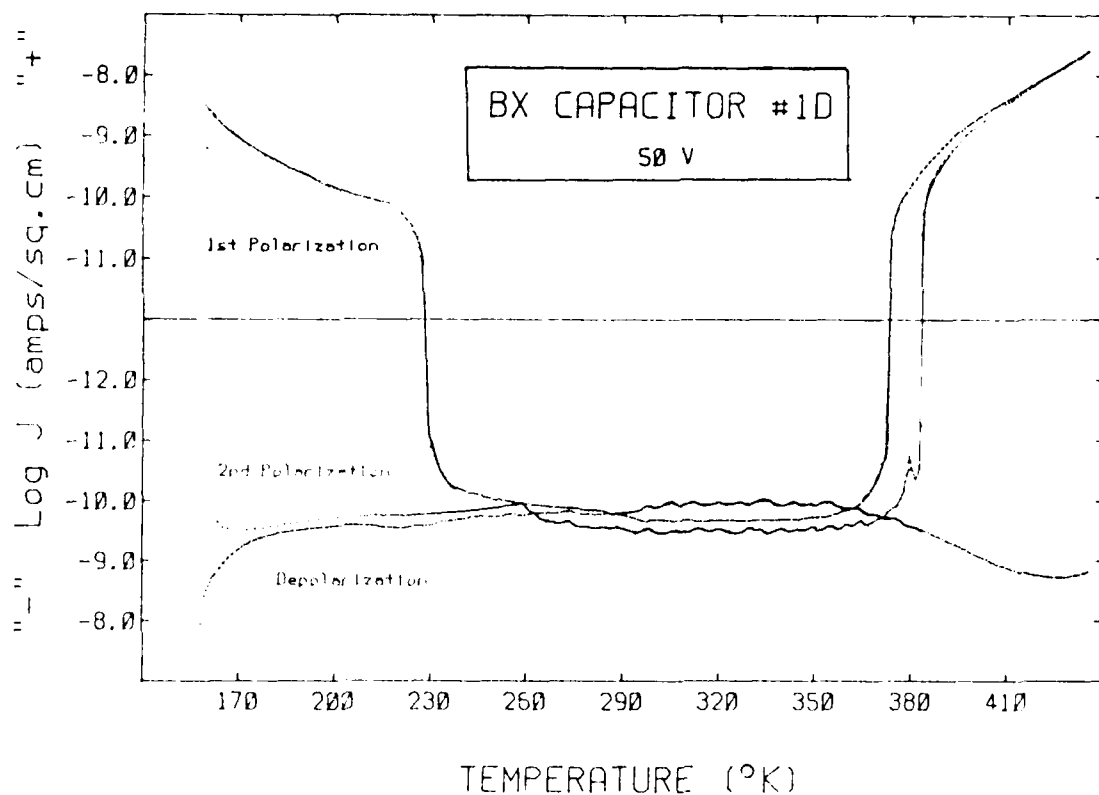
Figure 4.3.2e: TSPC/DC behavior of BX capacitor #1D.
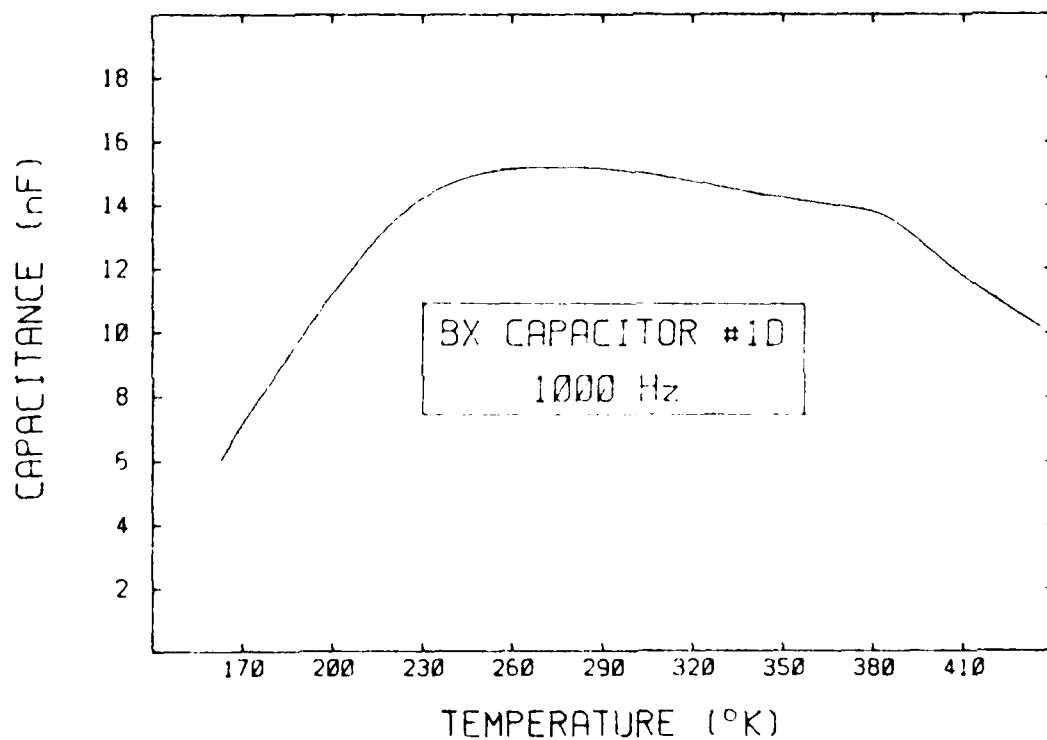
Figure 4.3.2f: Capacitance vs. temperature curve for BX capacitor #1D.

-186-

lower the Curie point. The TSPC spectrum illustrates how these shifters actually result in a whole series of Curie points which are spread out over a large temperature range due to chemical inhomogeneities. If the capacitor formulation were fired for a sufficiently long time we would expect homogenization to occur and the series of peaks to coalesce into one. This simple experiment is being carried out now.

4.3.3 Undoped BaTiO$_3$ Measurements

TSPC/DC and capacitance measurements have been carried out on undoped BaTiO$_3$'s with Ba:Ti ratio ranging from .96 to 1.04. For simplicity the results of only three of these compositions will be presented here, figures 4.3.3 d, e, and f are of Ba:Ti = 0.995, 1.000, and 1.005. They are fairly representative of the other Ba:Ti ratios, at least in terms of the analyses we have made to date. Table 4.3.3 contains a summary of the Curie analyses in terms of the transition temperature, Curie temperature, and Curie constant. These data are included in spite of the fact they have not yet been fully analyzed. Microstructures are the same as those presented in section 3.2.4.

The analysis of these results in terms of positive/negative current, peak direction and magnitude, and ferroelectric theory are not yet completely understood, but many general points can be pointed out. The analysis will be divided into individual explanations of the 1st and 2nd polarization, and depolarization currents, followed by compositional and microstructural effects.

Composition	T_{TR} (^{O}K)	T_C (^{O}K)	$T_{TR} - T_C$ (^{O}K)	Curie Constant
$Ba_{.96}TiO_3$	403.8	351.3	52.5	6.40 E-06
$Ba_{.97}TiO_3$	403.3	371.0	32.3	6.70 E-06
$Ba_{.98}TiO_3$	405.7	374.0	31.7	7.71 E-06
$Ba_{.99}TiO_3$	403.0	356.9	46.1	6.15 E-06
$Ba_{.995}TiO_3$	403.8	356.0	47.8	7.18 E-06
$Ba_{.998}TiO_3$	404.3	369.5	34.8	7.60 E-06
$Ba_{1.000}TiO_3$	401.8	377.3	24.5	5.36 E-06
$Ba_{1.002}TiO_3$	403.1	374.2	28.9	6.94 E-06
$Ba_{1.005}TiO_3$	405.8	369.7	36.1	7.91 E-06
$Ba_{1.01}TiO_3$	404.2	360.7	43.5	5.11 E-06
$Ba_{1.02}TiO_3$	402.6	354.6	48.0	5.15 E-06
$Ba_{1.03}TiO_3$	404.0	294.2	109.8	4.85 E-06
$Ba_{1.04}TiO_3$	402.0	348.1	53.9	9.17 E-06

Table 4.3.3: Curie-Weiss analysis for the undoped $BaTiO_3$ compositions.

First Polarization

Figure 4.3.3a is a TSPC graph of the 1st polarization of $BaTiO_3$ under an applied field of 500 V/cm. In general, this figure is representative of all the 1st polarization runs made on the undoped $BaTiO_3$'s, with the exception of behavior at the tetragonal-cubic transition point, and the magnitude of the

END

FILMED

DTIC
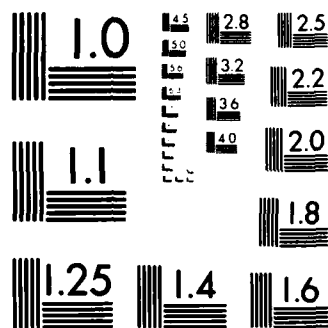
MICROCOPY RESOLUTION TEST CHART

NATIONAL BUREAU OF STANDARDS 196 A

Figure 4.3.3a: TSPC behavior of the first polarization, in this case for pure BaTiO$_3$.

current levels. At -100 $^\circ$C, where the field is first applied and heating begun, BaTiO$_3$ is in a rhombohedral crystal phase: point group 3m, eight possible polar axes along the <111> directions, and P$_S$ equals $\approx$ 8 uC/cm^2. In all cases, for virgin specimens, a positive current was initially observed. This is possibly indicative of the inability of the dipoles to align with the field, allowing the IR leakage current of the specimen to dominate the current spectrum.

At $\approx$ -65 $^\circ$C BaTiO$_3$ changes crystal structure to orthorhombic symmetry: point group mm, twelve possible polar axes along the <110> directions, and P$_S$ equals $\approx$ 10 uC/cm^2. The temperatures of the phase transitions observed in our measurements are a little high compared to values reported. This

is probably due to the fact that our measurements are dynamic, and the fact that increasing the D.C. bias voltage increases the temperature of the phase transitions. Nonetheless, at -65 ^{O}C the current rises, and then immediately changes sign. As the temperature is increased further, the leakage current becomes dominant once again and a transition to positive current is exhibited.

At $\approx$ 15°C BaTiO$_3$ changes crystal structure to tetragonal symmetry: point group 4mm, six possible polar axes along the <100> directions, P$_S$ equals $\approx$ 16 μC / cm^2. The current abruptly changes sign to negative, which is probably due to the sudden increase in P$_S$. This transition appears to be much more sudden than the rhombohedral-orthorhombic transition. Increasing the temperature again results in a transition to positive current as the leakage current increases.

At $\approx$ 125 ^{O}C the Curie point is reached, and BaTiO$_3$ changes to a nonferroelectric, cubic state. The TSPC behavior at this transition varies widely, and seems to be dependent upon the grain size. Large grains (i.e. > 5 microns) do not restrict domain wall motion, allowing P$_S$ to spontaneously disappear; this is characteristic of a first order phase transition. Correspondingly, at the Curie point a large peak into the negative region is seen. Small grains clamp the domains, resulting in a more gradual change of P$_S$ near the phase transition; this is characteristic of a second order transition. Since P$_S$ does not change discontinuously no peak into the negative region is observed. Refer to Figure 4.3.3b for a

FIRST ORDER   **SECOND ORDER**

P_S

K^{-1}
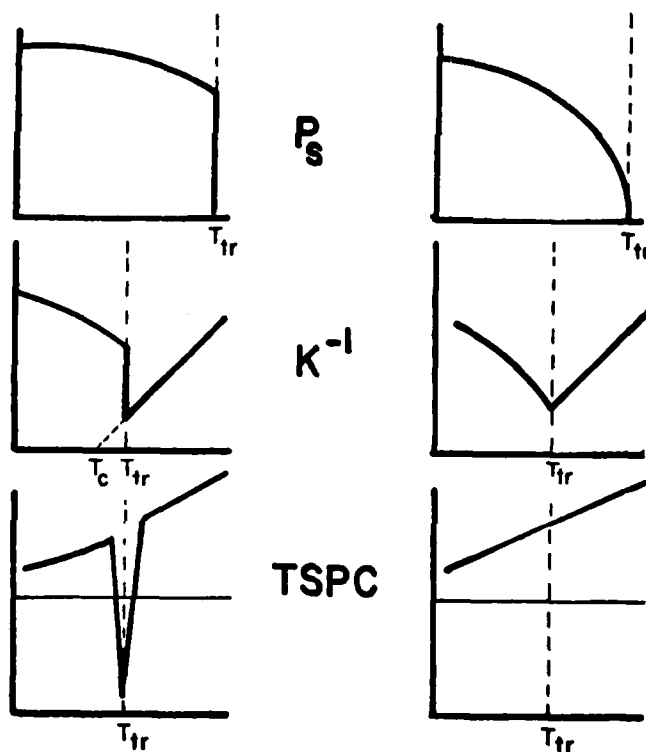
TSPC

<u>Figure 4.3.3b:</u> Variation of the spontaneous polarization and its observed effect on TSPC and inverse susceptibility behavior.

graphical representation of the variation of P_S as a function of temperature for first and second order phase transitions, and its effect on the TSPC and inverse susceptibility behavior.

Following the transition to cubic symmetry the TSPC behavior simply exhibits the temperature dependence of the leakage current, the slope of which is dependent upon the activation energy of the material, the magnitude of which is dependent upon the resistivity of the specimen. Refer to section 4.5 for an analysis of the activation energies obtained from TSPC measurements on the undoped $BaTiO_3$'s.

Second Polarization

Figure 4.3.3c is a graph of TSPC behavior during a second polarization for undoped $BaTiO_3$ under an applied field of 500 V/cm. The sample is already poled from the first polarization run. At the beginning of the measurement at -100 $^{\circ}C$ the sample exhibits negative current, with a transition to positive current as the leakage current increases. Now when the rhombohedral-orthorhombic phase transition occurs a peak in the negative direction is observed, opposite from the first polarization measurement. Why this occurs is not yet clear, but it must be related to differences in domain wall movement for the unpoled and poled states. Note also that now as the temperature
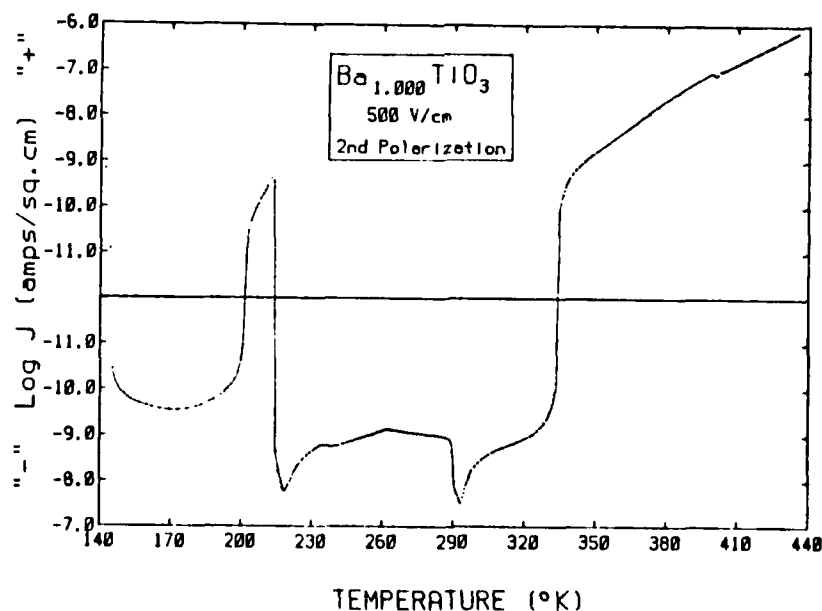
Figure 4.3.3c: General TSPC behavior during the second polarization, in this case for $BaTiO_3$.

increases, the current stays negative up until the temperature reaches the orthorhombic-tetragonal transition. Evidently the field induced from the polarization exceeds the effects of the external field. For higher temperatures the second polarization phenomena is similiar to that of the first polarization, with slight changes in the current magnitude, but no changes in the current behavior. There are exceptions to this rule for some of the $BaTiO_3$ compositions that have been studied, but as of yet no explanation for this behavior has been found.

Depolarization

Figure 4.3.3d is a TSDC graph for $BaTiO_3$ which was poled at a field strength of 500 V/cm. The sign of the current is negative throughout the entire spectrum, with the exception of behavior at the Curie point. The negative current is expected, as the field acting on the dielectric now is due to the net polarization which was induced during the polarization runs; i.e. the + - is reversed. At the two low temperature phase transitions negative peaks are observed, the magnitude of which are nearly always the same as the magnitude exhibited during the second polarization. The behavior at the Curie point again seems to be dependent upon the grain size and its effect on whether the transition is first or second order, but the magnitude and direction of the depolarization peak is not yet understood.

Compositional Effects

Figures 4.3.3e, f, and g are TSPC/DC, capacitance, and
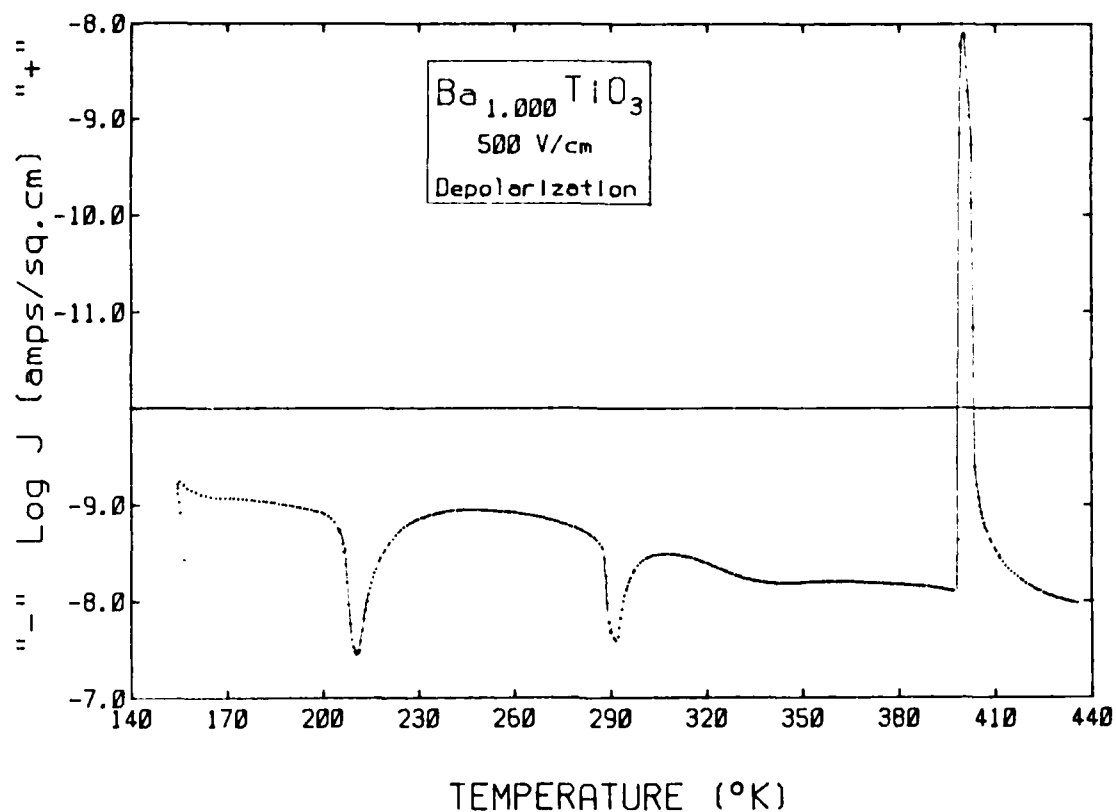
Figure 4.3.3d: General TSDC behavior, in this case for BaTiO$_3$ depolarized from 500 V/cm.

Curie-Weiss graphs for the undoped BaTiO$_3$ compositions with Ba:Ti = 0.995, 1.000, and 1.005. These are fairly representative of all the TSPC/DC results collected on the excess Ti and excess Ba compositions. Analyses of the individual polarizations / depolarizations follow those presented in the previous section. The compositional effects between these spectra can be summarized as follows:

1) For Ba:Ti < 1.000, a large negative peak appears at the Curie point, whereas for excess Ba compositions the peak is absent. From the dielectric constant curves we can see this is not due to a difference in magnitude of the dielectric constant. However, a large difference can be seen in the
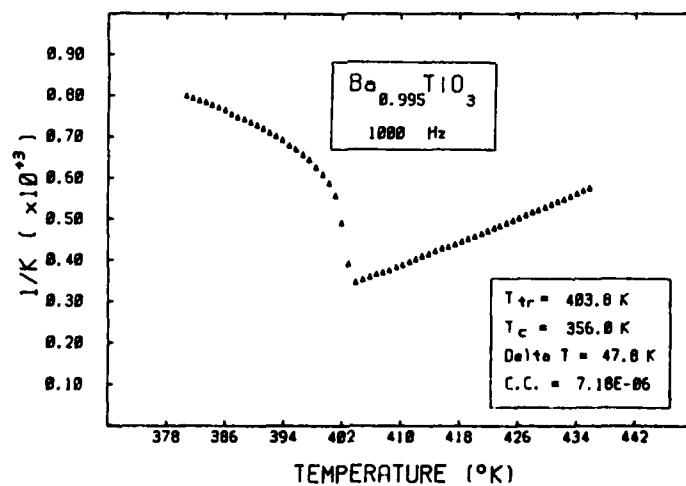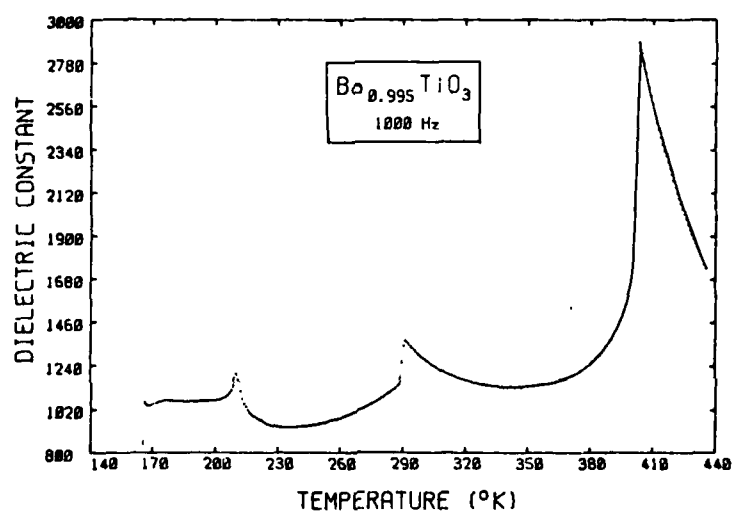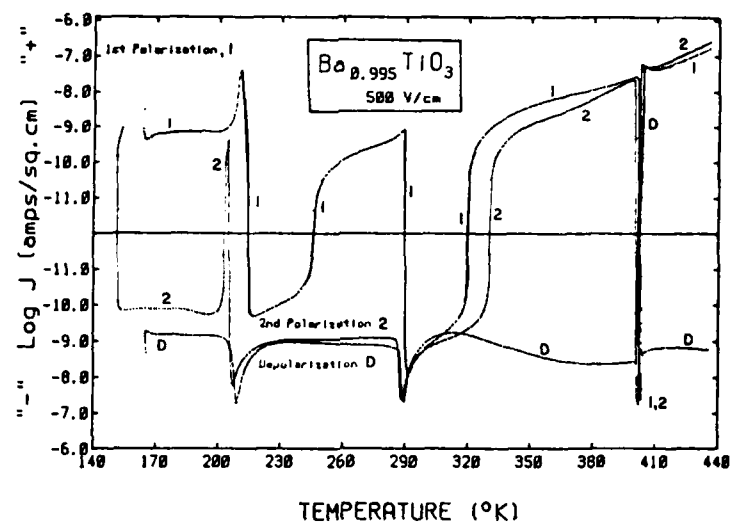
Figure 4.3.3e: TSPC/DC, dielectric constant, and Curie-Weiss vs. Temperature plots for Ba:Ti = 0.995.

-195-
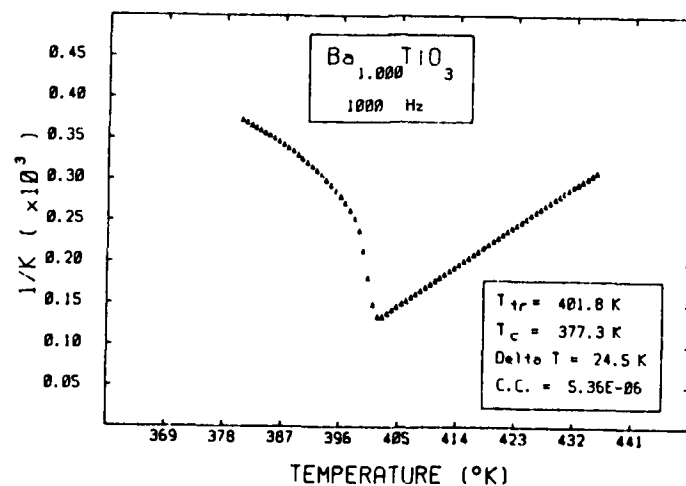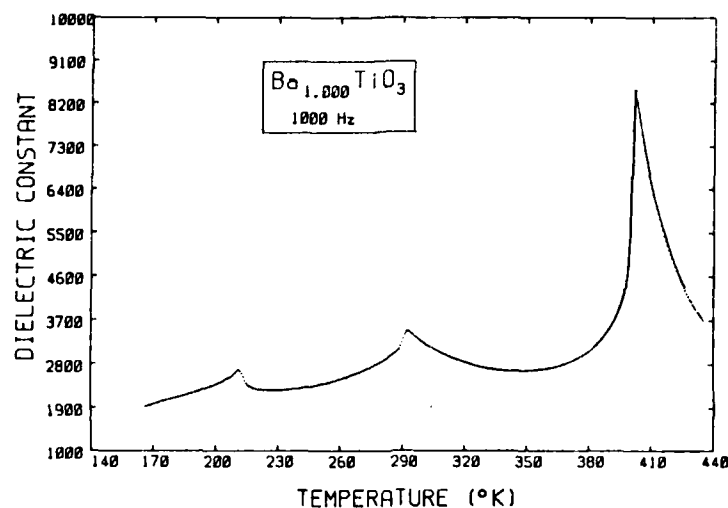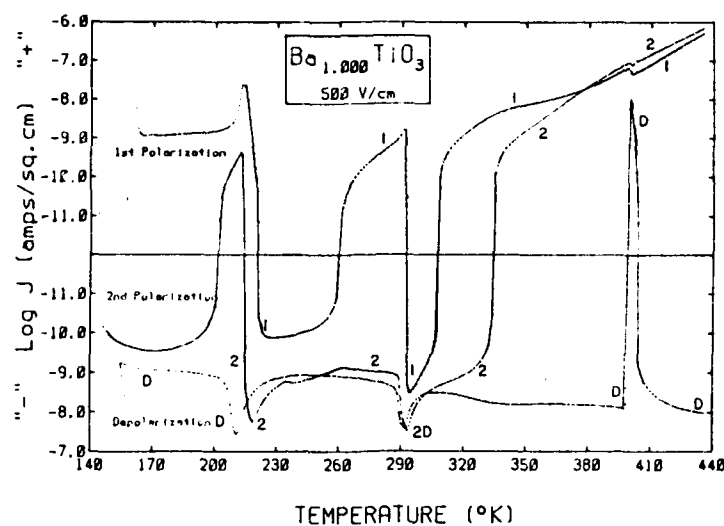
Figure 4.3.3f: TSPC/DC, dielectric constant, and Curie-Weiss vs.
temperature plots for Ba:Ti = 1.000.
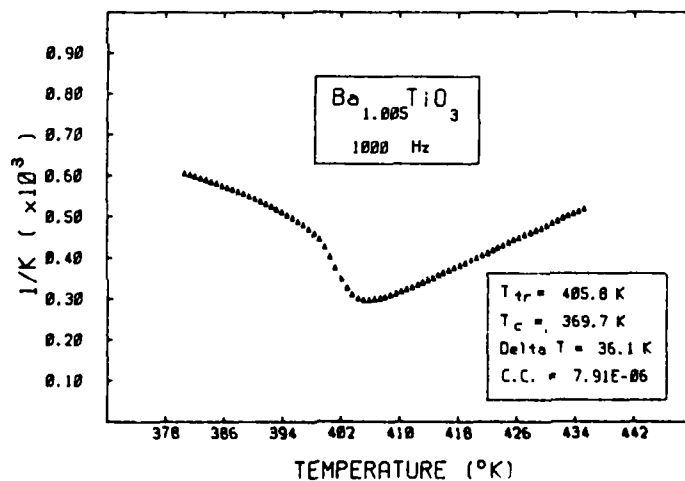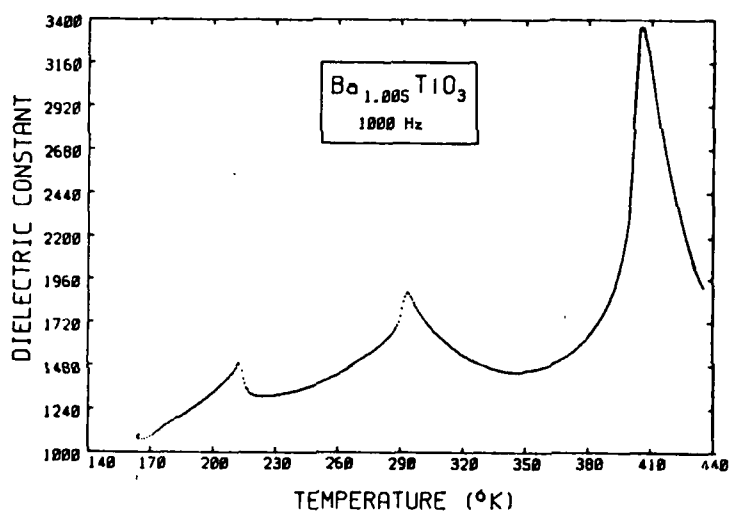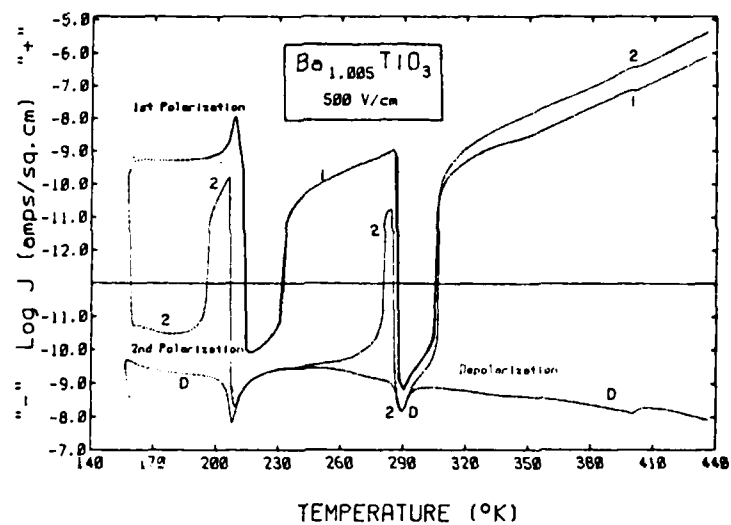
Figure 4.3.3g: TSPC/DC, dielectric constant, and Curie-Weiss vs. temperature plots for Ba:Ti = 1.005.

Curie-Weiss behavior. The 0.995 specimen exhibits behavior indicative of a first order transition, while the 1.005 specimen exhibits behavior indicative of a second order transition. We believe this variation in the P_S vs. temperature is the cause for the difference in the TSPC behavior.

The question becomes, why do excess Ba compositions exhibit second order behavior in contrast to the excess Ti compositions ? Due to the limited solubility of either excess Ba or Ti we would not expect the defect chemistry to be altered to such an extent as to change the nature of the phase transition. Besides compostional differences, the other major difference lies in the microstructure of these specimens. From section 3.2.4 we know that the grain size of the .995 specimen is $\approx$ 20 um due to exaggerated grain growth. The grain size of the 1.005 specimen is $\approx$ 2 um. (Note: the Ba-rich compositions used for the TSPC/DC measurements were calcined at a high temperature, which changes the sintering behavior. Refer to section 3.2.3) We believe this is the cause of the change in TSPC/DC behavior. Large grains act essentially as a group of single crystals, which offer little resistance to the the movement of domains in response to fields or stresses. Small grains clamp the domains, making it difficult for them to move or form 90° domain walls to relieve stresses. It appears TSPC measurements are an excellent way to determine stoichiometry.

2) The current peak and change in the dielectric constant during the orthorhombic-tetragonal phase transition is more abrupt for the Ti-rich compositions. We believe this is also a consequence of the grain size.

3) The magnitude of the leakage current levels as a function of composition closely follow the results obtained in the high-voltage degradation section. Refer to section 3 for an analysis of the effect of second phases on the leakage current, sintering behavior, and grain size.

4.3.4 Acceptor and Donor-doped $BaTiO_3$ Measurements

Figures 4.3.4 a, b, c, and d contain the TSPC/DC, capacitance, and Curie-Weiss results for Nb and Al doped $BaTiO_3$, with dopant levels of 1% and 5%. Each will be discussed separately.

Nb-doped $BaTiO_3$ Measurements

Niobium acts as a donor when incorporated into the perovskite lattice on the Ti site. Refer to section 3.1.3 for an analysis of how a donor alters the defect chemistry. Niobium is also known to shift and depress the Curie point of $BaTiO_3$, making it a useful additive in altering the dielectric properties. We would expect that due to our powder preparation process, the Nb would only act as a shifter; it is evenly distributed throughout the powder. Curie points broadened over a wide temperature range are a result of chemical inhomogeneity.

Figure 4.3.4a contains the results for a Nb doping level of

1%. Note the current levels are no higher than for a pure $BaTiO_3$ specimen, nor are sudden increases in the current present which could be related to a donor level suddenly emptying its electrons into the conduction band. The Nb dopant is being ionically compensated. The capacitance curve shows the Curie point has been shifted down to $\approx 100\ ^{\circ}C$, with the other low temperature transitions being "washed-out", typical of an impurity addition which shifts the tetragonal-cubic transition. The TSPC/DC behavior reflects this behavior; the phase transitions are barely evident. No negative peak is exhibited at the Curie point, the transition is second order.

Figure 4.3.4b contains the results for a Nb doping level of 5%. At this dopant level Nb is still being ionically compensated. The dielectric constant maximum has been shifted to room temperature. The TSPC behavior reflects these results nicely. The temperature at which the dielectric constant reaches a maximum value corresponds to point at which the 1st polarization curve changes sign. The second polarization remains negative over the entire temperature range until the leakage current dominates at $\approx 90\ ^{\circ}C$. In general, the TSPC mimics the behavior of curve #3, figure 4.3a.

Al-doped BaTiO$_3$ Measurements

Al^{+3} acts as an acceptor when incorporated into the perovskite lattice on the Ti^{+4} site. Refer to section 3.1.3 for an analysis of how an acceptor alters the defect chemistry.
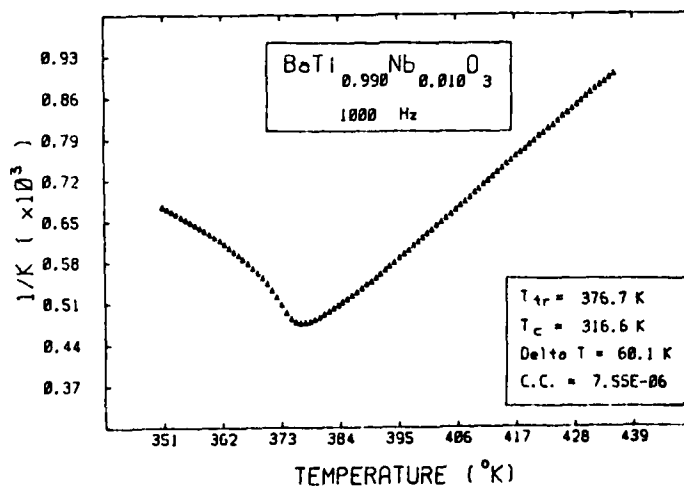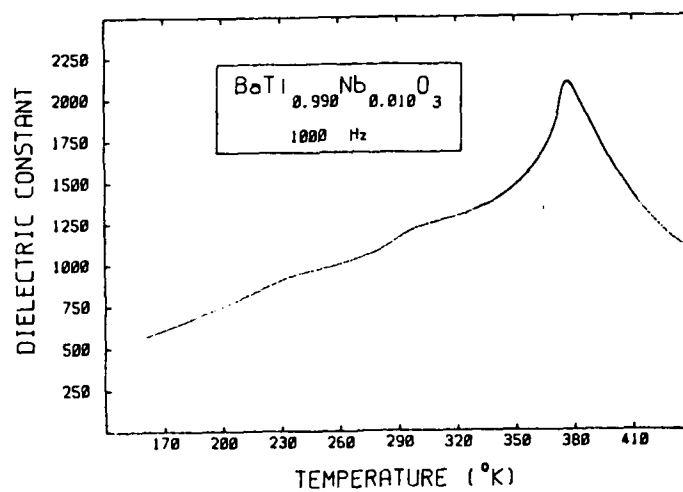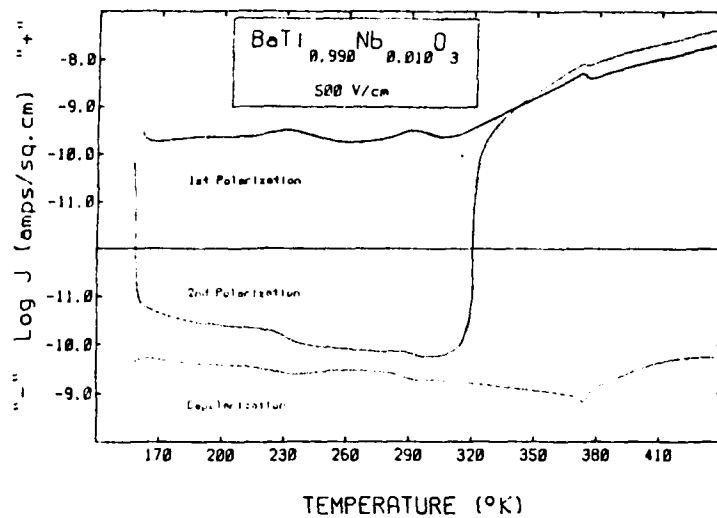
Figure 4.3.4a: TSPC/DC, dielectric constant, and Curie-Weiss vs. temperature plots for $BaTi_{.99}Nb_{.01}O_3$.
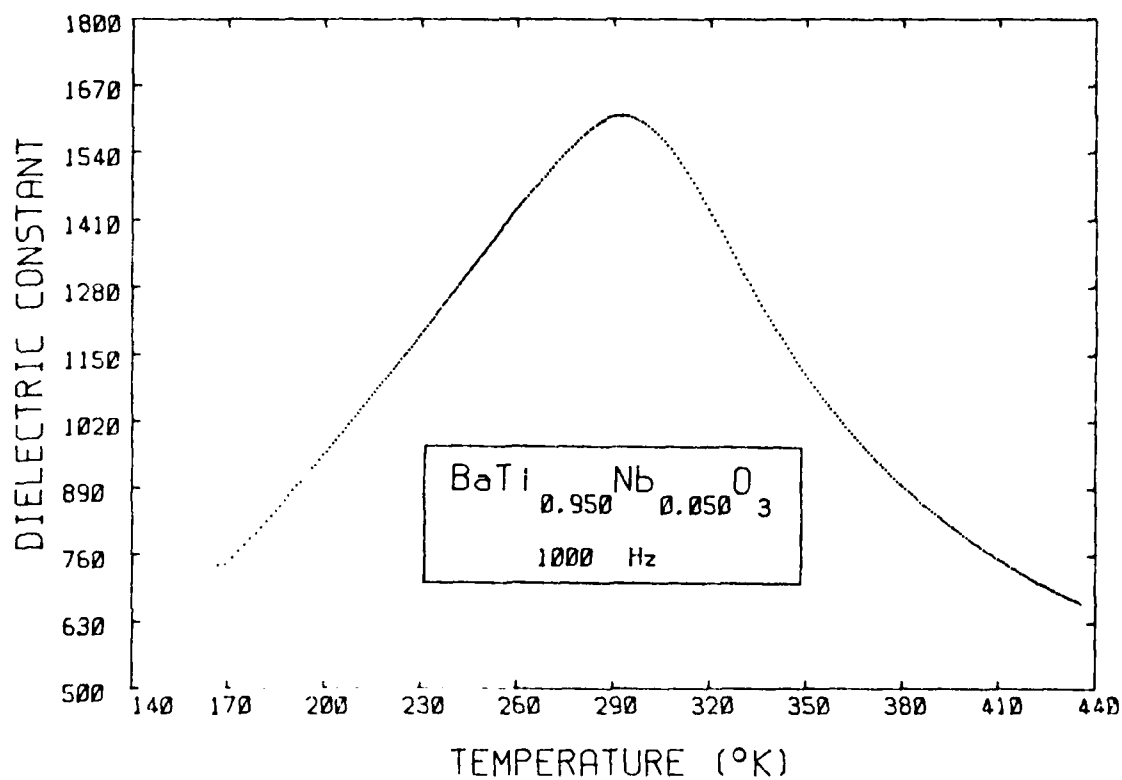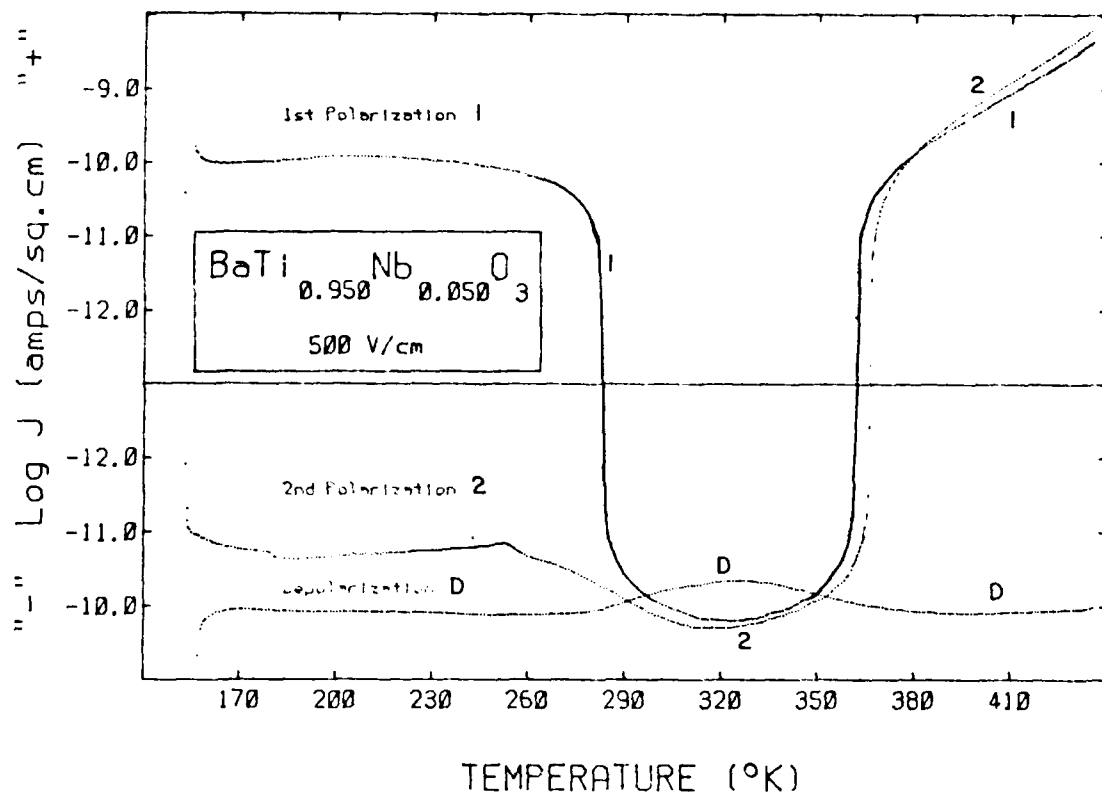
Figure 4.3.4b: TSPC/DC and dielectric constant vs. temperature plots for BaTi$_{.95}$Nb$_{.05}$O$_3$.

Figure 4.3.4c contains the TSPC/DC results obtained for an Al doping level of 1%. As can be seen from the graphs, Al does not shift the Curie point. In addition, the magnitude of the dielectric constant does not seem to be changed, although the relative maxima at the lower two phase transitions have been reduced. This is also reflected by the TSPC behavior; the magnitude of the current levels has not changed but the magnitude of the current peaks at the two lower phase transition temperatures has been lowered. From these results it is impossible to judge whether or not the Al is acting as an effective acceptor.

Figure 4.3.4d contains the TSPC/DC results for an Al doping level of 5%. Again the Curie point is not shifted, but the magnitude of the dielectric constant is drastically reduced. Al appears to be eliminating the ferroelectric behavior. This is confirmed by the TSPC/DC results, which show no trace of current peaks at any of the phase transitions. The specimen is behaving as a simple high resistivity ceramic. It can not be determined whether a high concentration of $V_o^{\cdot\cdot}$ is destroying the behavior, or if it's due to the presence of a second phase.

Future studies concerning the effect of doping are being carried out on donor and acceptor-doped nonferroelectric $SrTiO_3$.
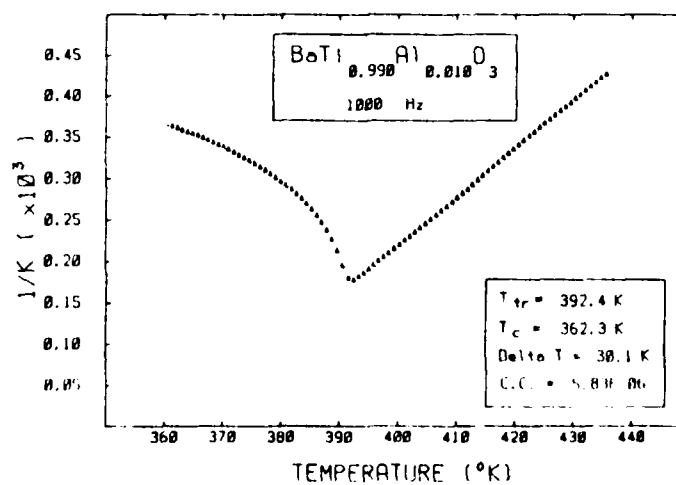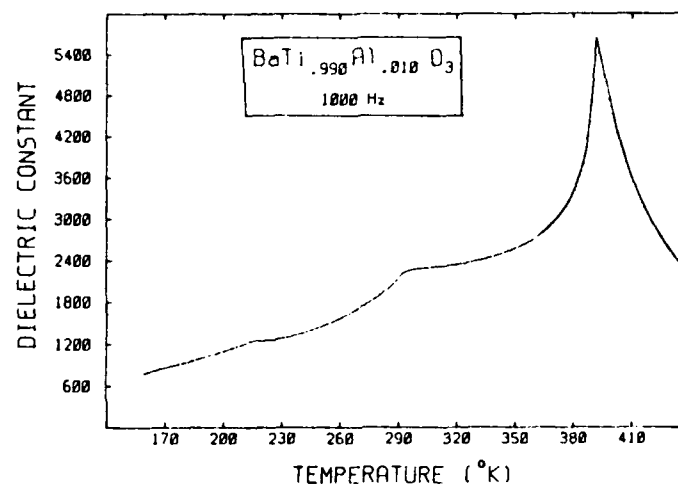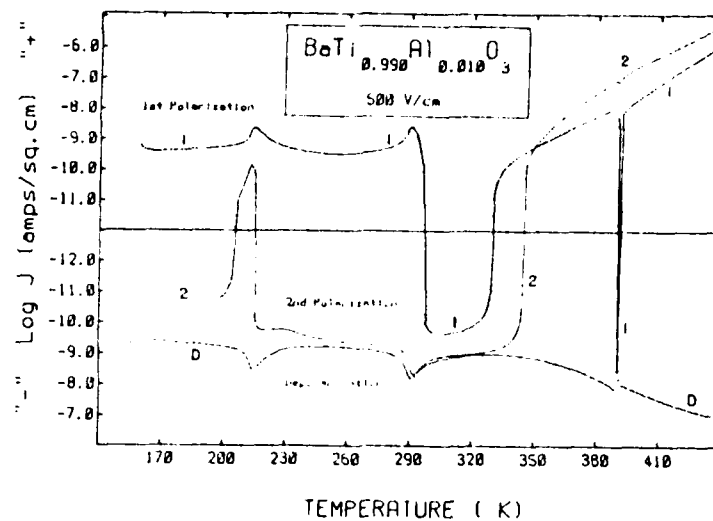
Figure 4.3.4c: TSPC/DC, dielectric constant, and Curie-Weiss vs. temperature plots for $BaTi_{.99}Al_{.01}O_3$.
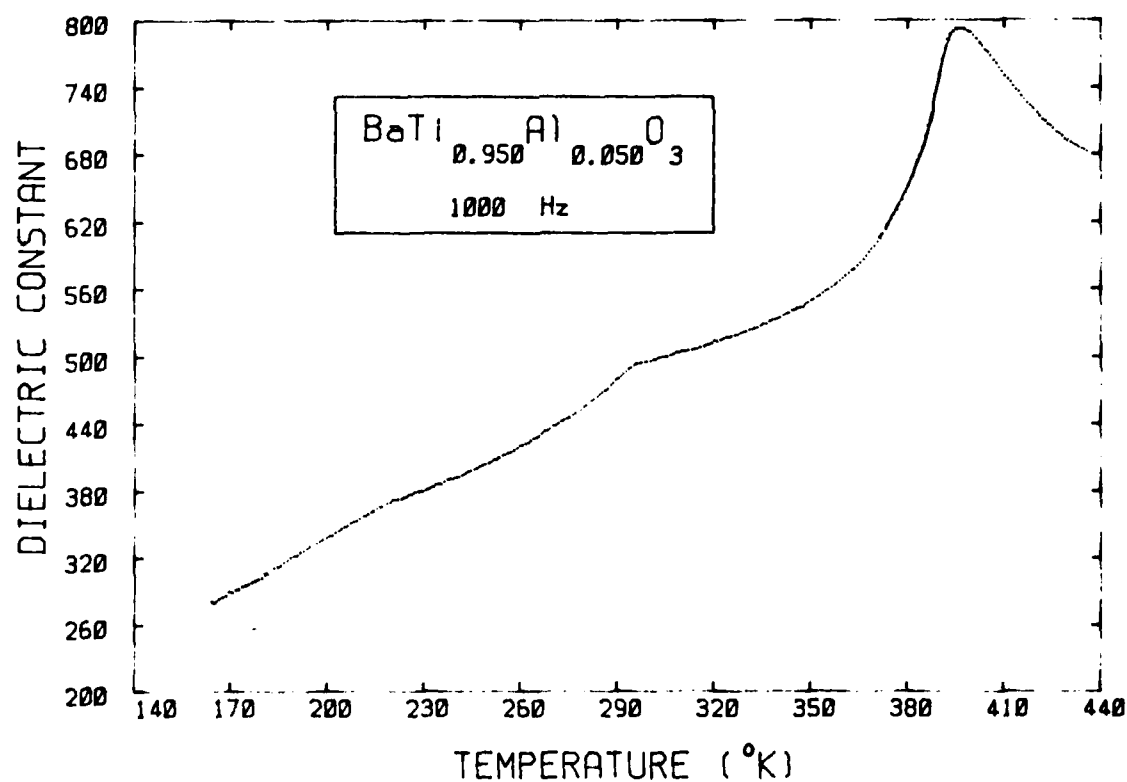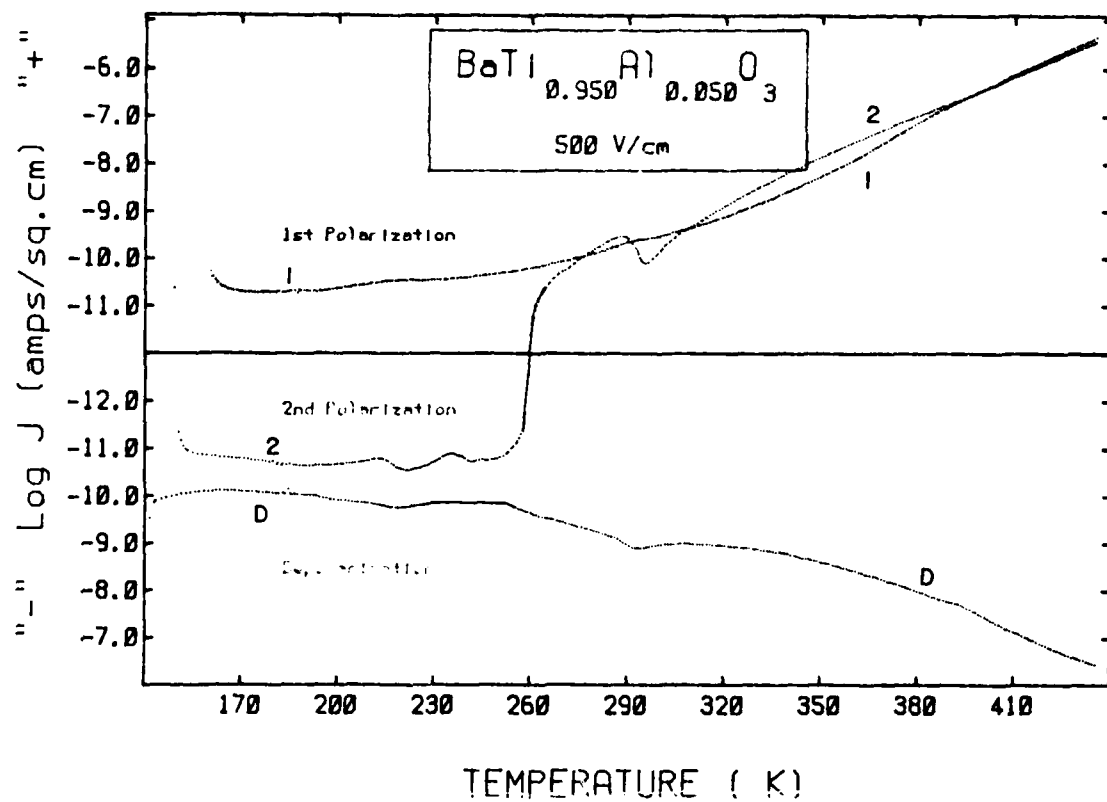
Figure 4.3.4d: TSPC/DC and dielectric constant vs. temperature plos for BaTi$_{.95}$Al$_{.05}$O$_3$.

4.3.5 Sr-shifted BaTiO$_3$ Measurements

In order to observe the relative movement of phase
transitions and its effect on the current spectra the first
TSPC/DC measurements were made on Sr-shifted BaTiO$_3$.During this
time 25 mole% Sr sample was tested which had an unbelievably high
dielectric constant at the Curie point, $\approx$ 29000 (figure
4.3.5a).   This immediately created interest in: 1) What is
causing this anomaly ?, 2) Is it reproducible ?, 3) Can this
abnormally high dielectric constant be shifted to room
temperature with a higher Sr doping level ?, and 4) How is the
TSPC/DC behavior affected, and can it help explain the phenomena
?
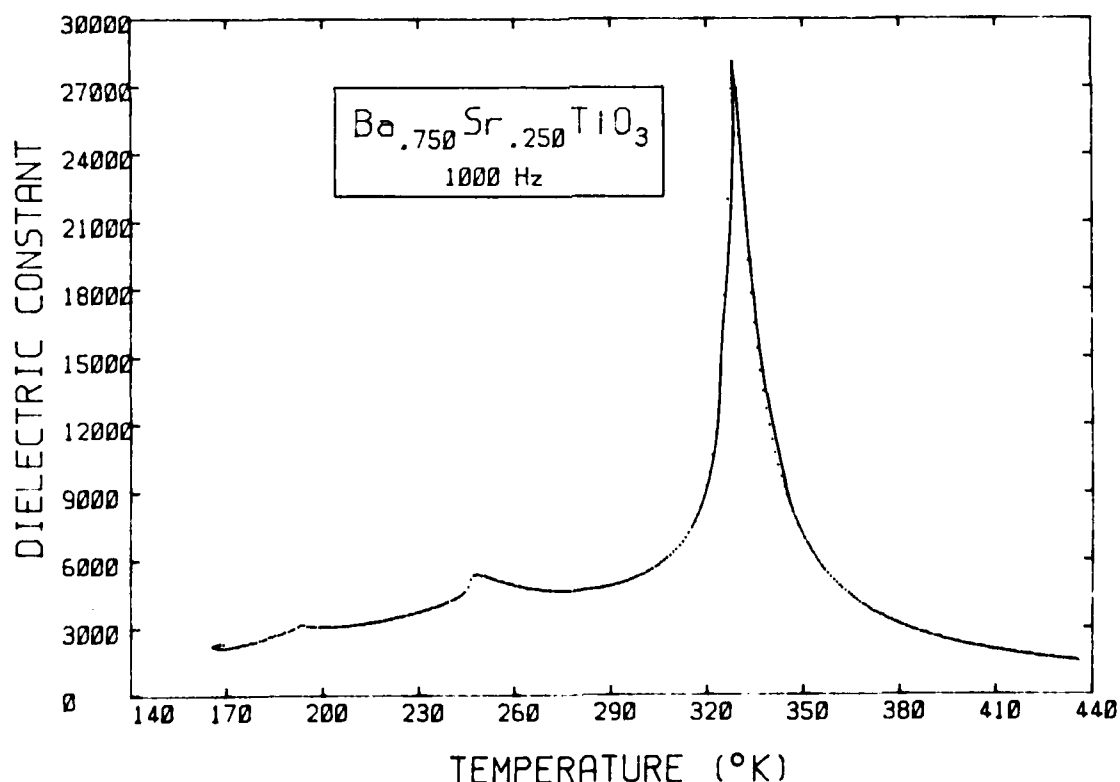
Figure 4.3.5a: Anamolous dielectric constant behavior of the 25
                 mole % Sr-shifted specimen.

In order to answer these questions we prepared another 21 compositions with the formulae: $[Ba_{1-x}Sr_x]_yTiO_3$; $x = 0.25$, 0.30, and 0.35, and $y = 0.995$, 0.998, 0.999, 1.000, 1.001, 1.002, and 1.005. The increased amount of Sr should shift the Curie point down to room temperature. The small variations of nonstoichiometry were chosen in order to determine stoichiometry, since it was suspected that the high dielectric constant of the 25 mole % specimen was due to cation stoichiometry. In addition, since sintering is dependent upon cation stoichiometry, the influence of both grain size and density can be studied. Only half of the needed microstructures have been analyzed on an SEM, but in general these compositions follow the same trends as the undoped $BaTiO_3$'s presented in section 3.2.4. Table 4.3.5 contains the densities of the specimens prepared from the 21 compositions; maximum density specimens were chosen for study. Note: the densities were calculated assuming a linear change in density between $SrTiO_3$ and $BaTiO_3$; see Figure 4.3.5.

To date, TSPC/DC and capacitance measurements have been carried out on all 21 compositions. Figures 4.3.5a-i contain the results for 9 of these 21 compositions, representing all three Sr-shifted levels with cuts above and below stoichiometry for each one. Tables 4.3.5a and b contain the results of the Curie-Weiss analysis carried out on these compounds. These results were collected recently and have not yet been fully analyzed. However, some of the questions raised earlier can be answered in simple terms for each Sr-shifting level:

MOLE % Sr	A:B Ratio	Bulk Density (g/cm^3)	% Theoretical
	0.995	5.31	91.9
	0.998	5.45	94.4
	0.999	5.55	96.1
25	1.000	5.57	96.4
	1.001	5.53	95.7
	1.002	5.49	95.1
	1.005	5.54	95.9
	0.995	5.58	97.4
	0.998	5.55	96.8
	0.999	5.54	96.6
30	1.000	5.46	95.2
	1.001	5.54	96.6
	1.002	5.48	95.5
	1.005	5.55	96.8
	0.995	5.47	96.1
	0.998	5.48	96.3
	0.999	5.47	96.1
35	1.000	5.53	97.2
	1.001	5.47	96.2
	1.002	5.45	95.8
	1.005	5.46	96.0

TABLE 4.3.5 : Densities of Sr-shifted barium titanates by ASTM C-20; Xylene immersant.

Mole % Sr	A:B Ratio	T_{TR} (^{O}K)	T_C (^{O}K)	$T_{TR} - T_C$ (^{O}K)	Curie Constant
	0.995	317.7	308.4	9.3	8.91 E-06
	0.998	323.8	314.7	9.1	6.08 E-06
	0.999	323.0	314.1	8.9	7.85 E-06
25	1.000	323.0	307.7	15.3	7.14 E-06
	1.001	324.2	264.5	59.7	5.22 E-06
	1.002	324.1	314.5	9.6	6.92 E-06
	1.005	323.3	300.3	23.0	8.06 E-06
	0.995	308.5	302.8	5.7	7.78 E-06
	0.998	308.1	301.5	6.6	7.48 E-06
	0.999	307.7	300.2	7.5	7.20 E-06
30	1.000	308.5	302.6	5.9	6.63 E-06
	1.001	307.5	296.0	11.5	7.88 E-06
	1.002	307.4	259.8	47.6	6.35 E-06
	1.005	306.9	277.0	29.9	9.86 E-06

TABLE 4.2.1a: Curie analysis for the Sr-shifted $BaTiO_3$ composition: titanates : Sr = 25, 30 mole %

Mole % Sr	A:B Ratio	T_{TR} (^{O}K)	T_C (^{O}K)	$T_{TR} - T_C$ (^{O}K)	Curie Constant
	0.995	293.0	286.3	6.7	8.13 E-06
	0.998	292.5	286.9	5.6	8.45 E-06
	0.999	290.8	284.5	6.3	7.49 E-06
35	1.000	290.9	284.2	6.7	7.65 E-06
	1.001	291.5	284.1	7.4	7.88 E-06
	1.002	291.1	284.5	6.6	7.69 E-06
	1.005	291.2	281.8	9.4	8.28 E-06

<u>TABLE 4.2.3 :</u> Curie analysis for the Sr-shifted $BaTiO_3$ composition :
Sr = 35 mole %

THEORETICAL DENSITY vs. COMPOSITION
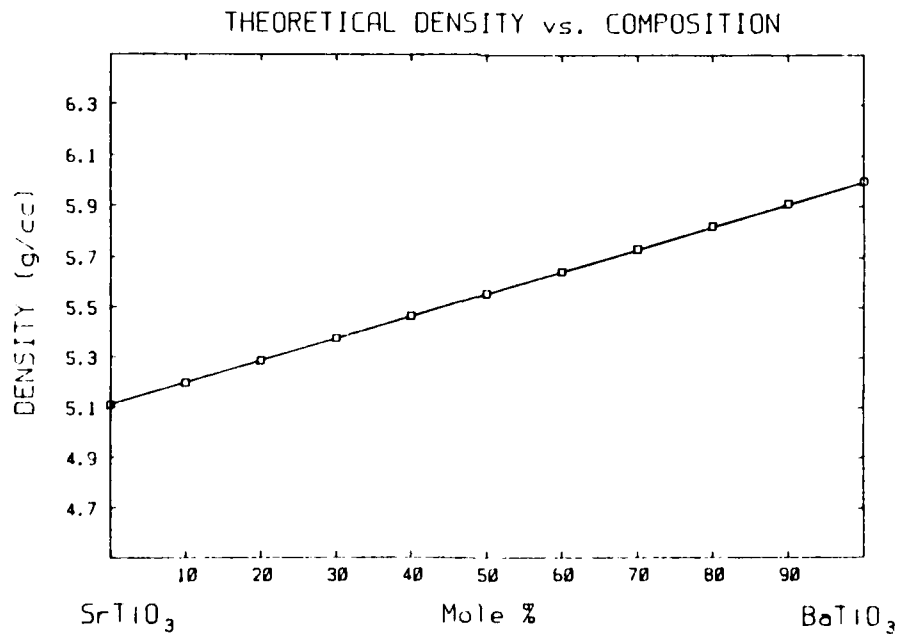
<u>Figure 4.3.5:</u> Assumed variation in theoretical density for the
$BaTiO_3$-$SrTiO_3$ system.

25 mole % Sr-shifted BaTiO$_3$

Figures 4.3.5a-c contain the TSPC/DC, dielectric constant, and Curie-Weiss graphs for A:B ratios of 0.990, 1.000, and 1.001. Doping with 25 mole % Sr has resulted in the Curie point being shifted to $\approx$ 50 $^{\circ}$C, a decrease of $\approx$ 75 $^{\circ}$C. Note the orthorhombic-tetragonal transition is shifted to $\approx$ -30 $^{\circ}$C, a decrease of $\approx$ 50 $^{\circ}$C, and the rhombohedral-orthorhombic transition is shifted to $\approx$ - 85 $^{\circ}$C, a decrease of only $\approx$ 22 $^{\circ}$C. Obviously each phase transition is not affected the same by the addition of Sr.

Changing the stoichiometry has a drastic effect on the dielectric constant and the Curie-Weiss behavior. Excess Ti has reduced the magnitude by a factor of two, while the excess Ba has decreased the magnitude by a factor of ten. It seems the high dielectric constant is highly dependent upon the degree of stoichiometry, although the excess Ti composition still has a dielectric constant of nearly 13000. The Curie-Weiss plots for these compositions also differ significantly; as we move from excess Ti to excess Ba through stoichiometry, we see the order of the tetragonal-cubic transition continually changes more towards second order, and the Curie constant increases. We're not sure why these occur yet.

The TSPC/DC behavior of these compositions differ in several respects: 1) The magnitudes of the current peaks decrease from the excess Ti to Ba compositions. 2) The shapes of the current peaks depend upon the order of the phase transition. Even the
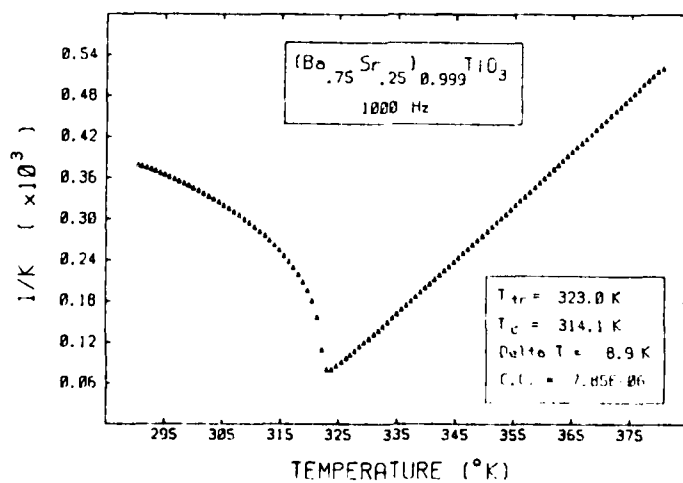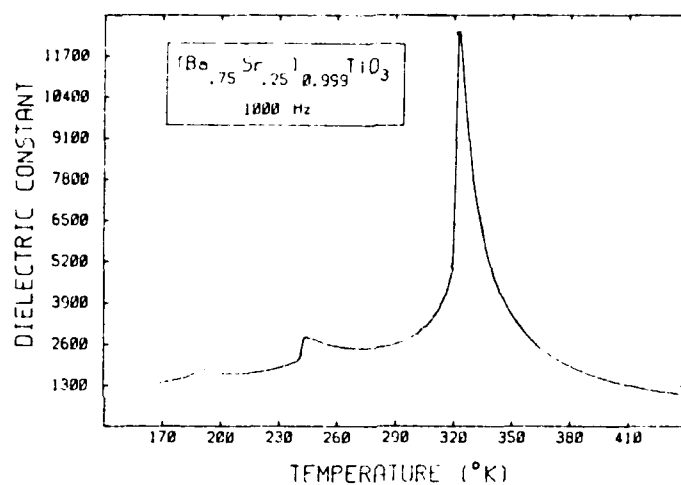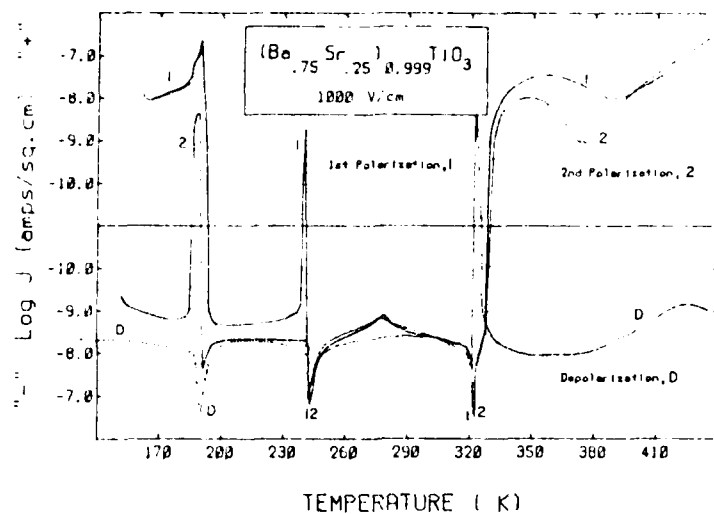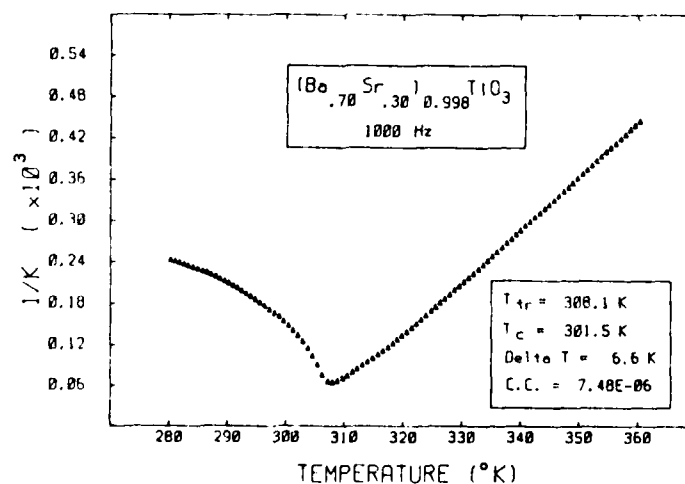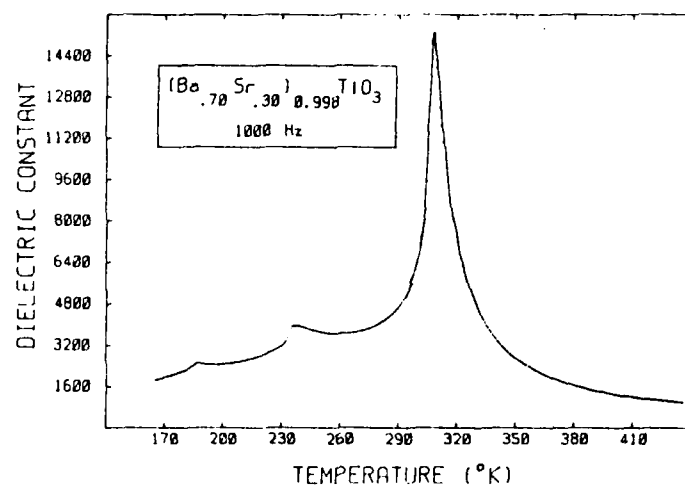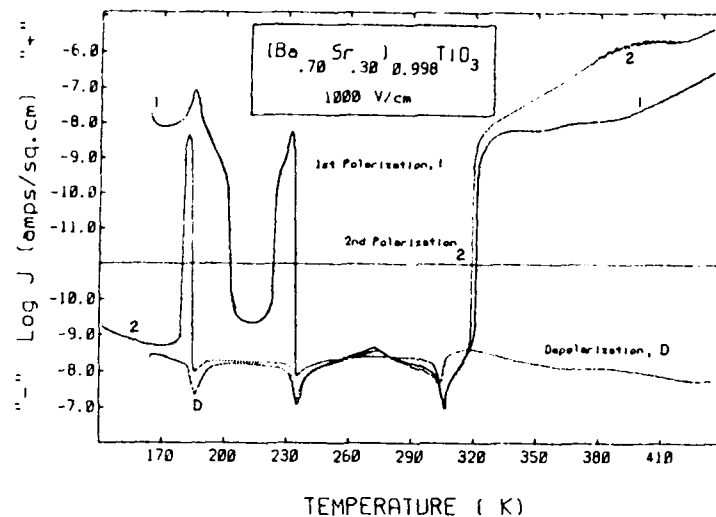
Figure 4.3.5a: TSPC/DC, dielectric constant, and Curie-Weiss vs. temperature plots for Sr = 0.25, A:B = 0.999.
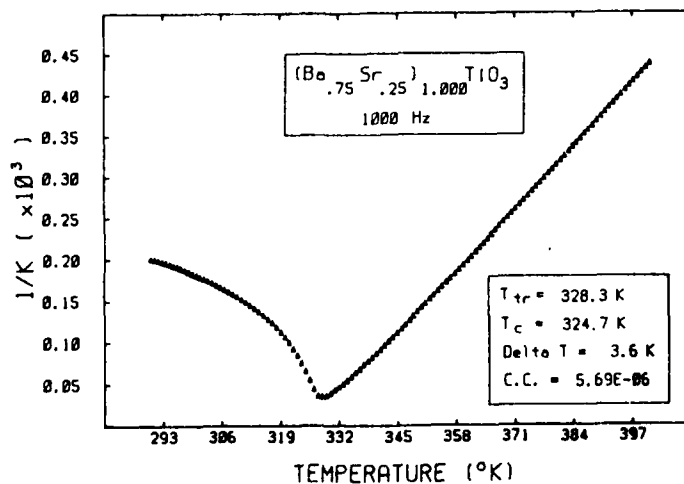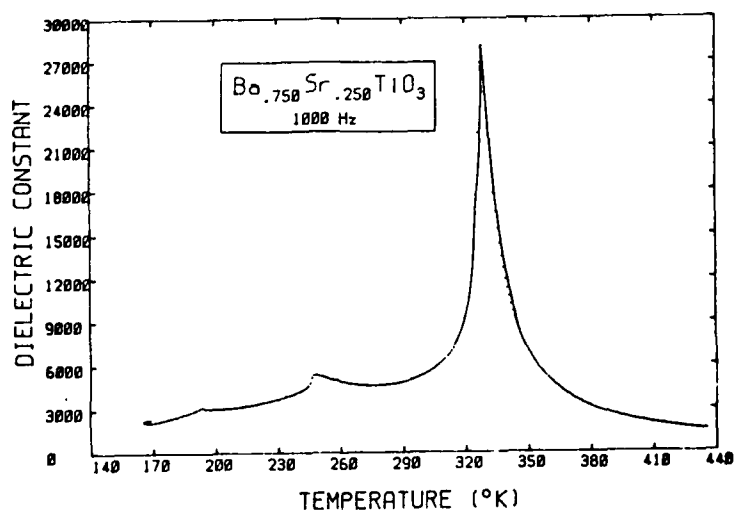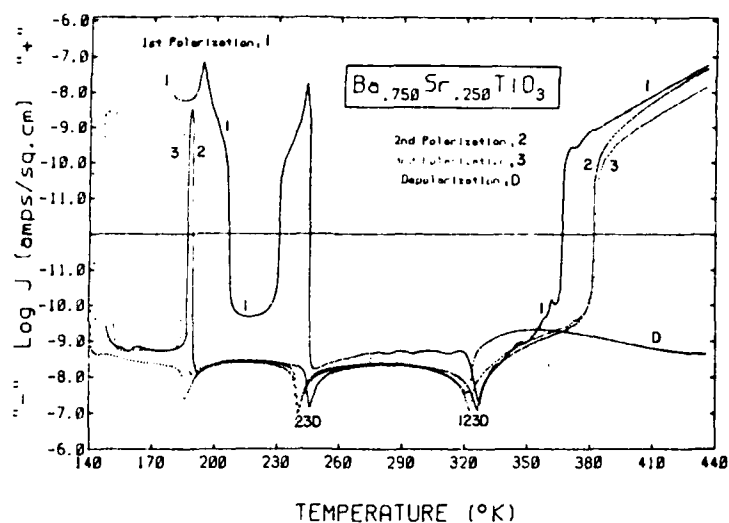
Figure 4.3.5b: TSPC/DC, dielectric constant, and Curie-Weiss vs.
temperature plots for Sr = 0.25, A:B = 1.000.

-213-
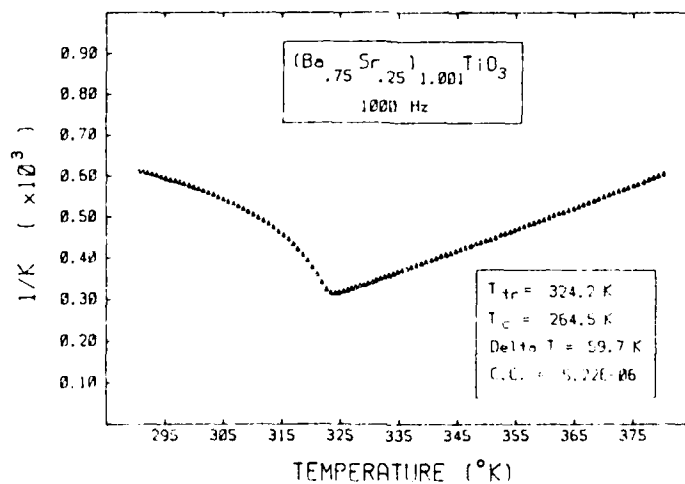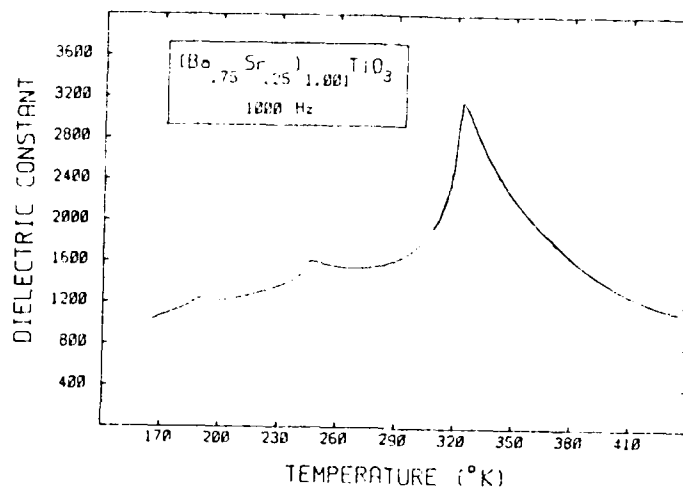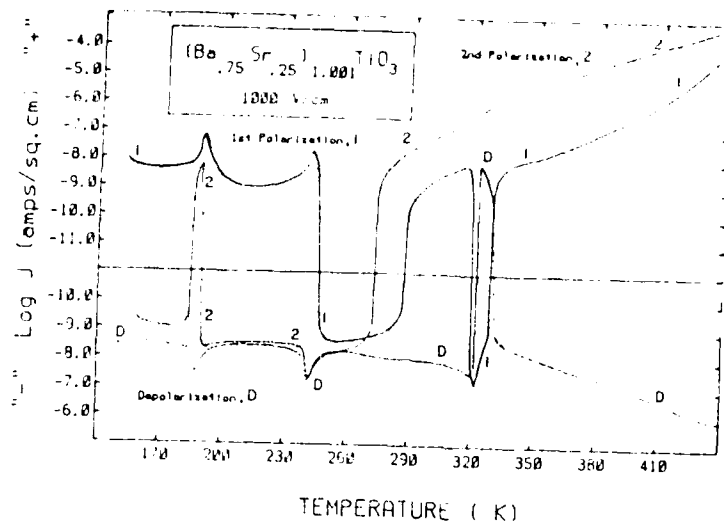
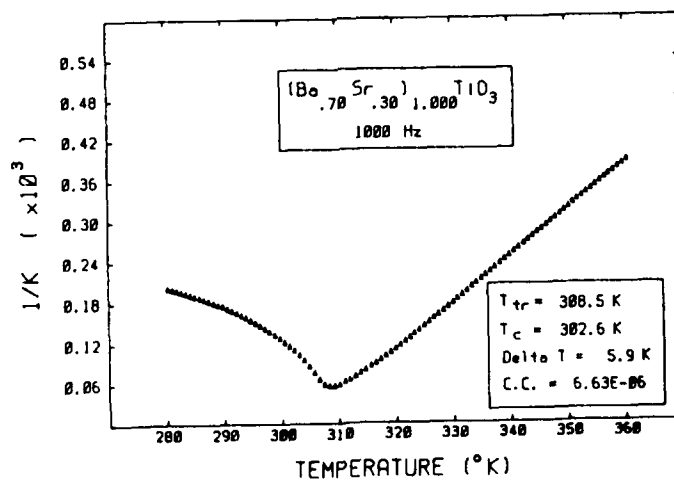**Figure 4.3.5c:** TSPC/DC, dielectric constant, and Curie-Weiss vs. temperature plots for Sr = 0.25, A:B = 1.001.

low temperature peaks reflect the temperature rate of change of the dielectric constant. 3) The excess Ba composition exhibits higher current levels from room temperature and up. 4) The major difference between the high and low dielectric constant compositions is the TSDC behavior. The lower dielectric constant compositions exhibit a peak into the positive region during depolarization.

30 mole % Sr-shifted BaTiO$_3$

Figures 4.3.5d-f contain the TSPC/DC, dielectric constant, and Curie-Weiss plots for A:B ratios of 0.998, 1.000, and 1.002. Doping with 30 mole % Sr has resulted in the Curie point being shifted to $\approx$ 35 $^{\circ}$C, a decrease of $\approx$ 90 $^{\circ}$C from undoped BaTiO$_3$. Note the low temperature transitions are shifted to $\approx$ -38 and -88 $^{\circ}$C, changes of $\approx$ 58 and 25 $^{\circ}$C respectively. Compared to the 25 mole % specimens, it appears the phase transitions are moving closer together.

The composition with the highest dielectric constant was again stoichiometric, but only peaked at $\approx$ 18000. However, this is still quite high. Varying the stoichiometry had the same effect on the results as the 25 mole % Sr specimen, in terms of dielectric and TSPC/DC behavior.

35 mole % Sr-shifted BaTiO$_3$

Figures 4.3.5g-i contain the TSPC/DC, dielectric constant, and Curie-Weiss plots for A:B ratios of 0.995, 1.000, and 1.005. Doping with 35 mole % Sr has resulted in the Curie point being shifted to $\approx$ 20 $^{\circ}$C, a decrease of $\approx$ 105 $^{\circ}$C from undoped

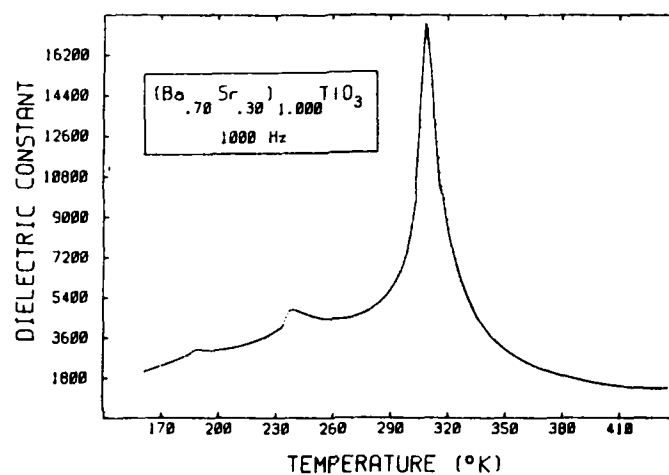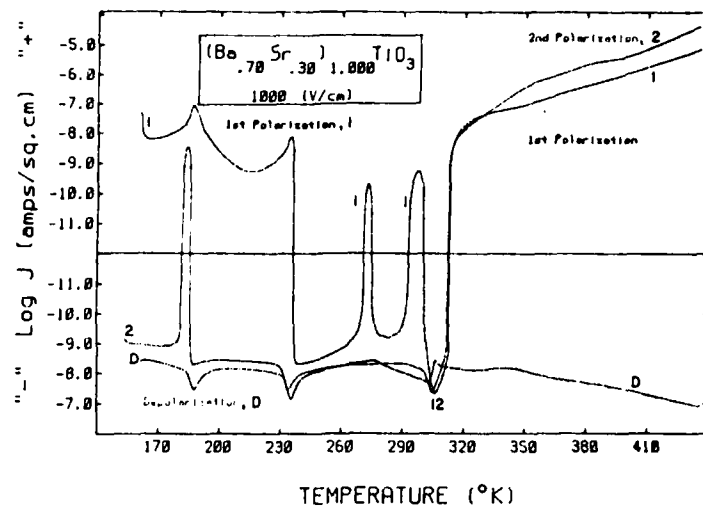Figure 4.3.5d: TSPC/DC, dielectric constant, and Curie-Weiss vs. temperature plos for Sr = 0.30, A:B = 0.998.

Figure 4.3.5e: TSPC/DC, dielectric constant, and Curie-Weiss vs.
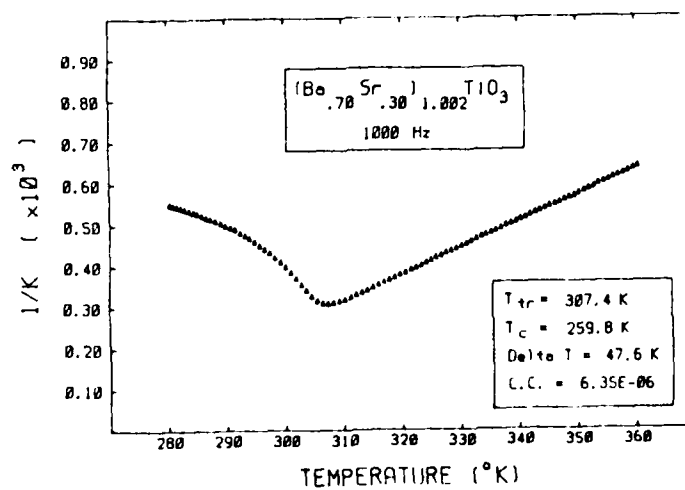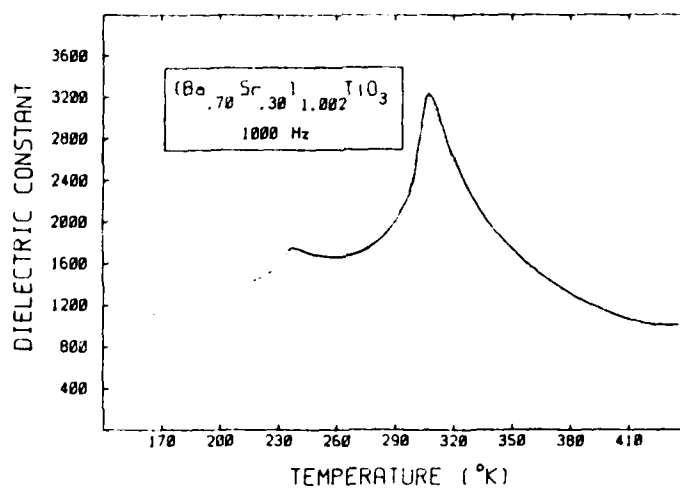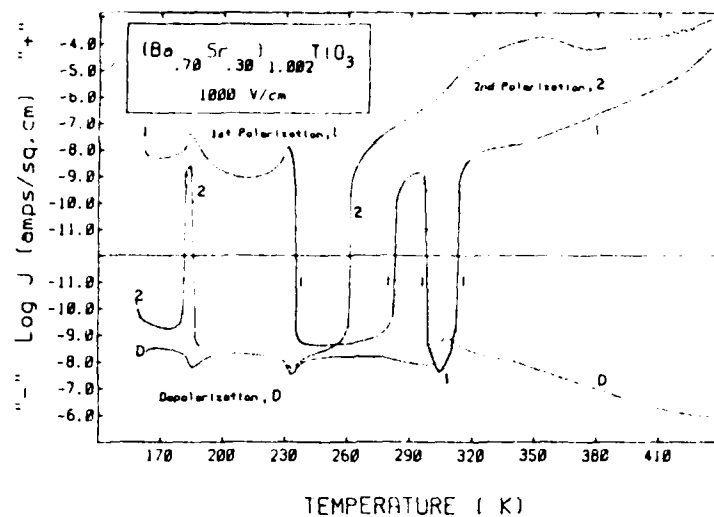temperature plots for Sr = 0.30, A:B = 1.000.

Figure 4.3.5f: TSPC/DC, dielectric constant, and Curie-Weiss vs. temperature plots for Sr = 0.30, 3 = 1.002.

$BaTiO_3$ behavior. Note the low temperature phase transitions occur at $\approx$ -48 and -88 $^{\circ}C$, decreases of 68 and 25 $^{\circ}C$ respectively. The temperature at which the rhombohedral-orthorhombic phase transition occurs is not changing as we add more Sr; it occurs at $\approx$ -85 $^{\circ}C$ for all three doping levels. The other two transition temperatures are steadily decreasing.

The dielectric constant behavior for 35 mole % Sr does not follow the same pattern as the 25 and 30 mole % additions. All of the excess Ti compositions have a dielectric constant of $\approx$ 15000, the stoichiometric composition 13000, and the excess Ba compositions 9000-12500. However, the dielectric constant everywhere else is higher as we move from excess Ti to excess Ba. This is reflecting the grain size dependence of the dielectric constant. The Curie-Weiss plots also reflect the transition in grain size by a transition to second order behavior. Otherwise, the TSPC/DC plots are very similiar to those of the 25 and 30 mole % Sr specimens.

In terms of the questions raised at the beginning of this section: 1) No, we have not yet been able to determine the exact cause of the anomaly; several clues have been found, but more experimental work is needed. 2) Yes, the behavior does seem to be experimentally repeatable, though a dielectric constant of 30000 has not yet been produced other than in the 25 mole % stoichiometric composition. 3) Yes, the Curie point anomaly can be shifted down to $\approx$ room temperature by adding 35 mole % Sr. 4) As of yet we cannot say if the TSPC/DC behavior will give us
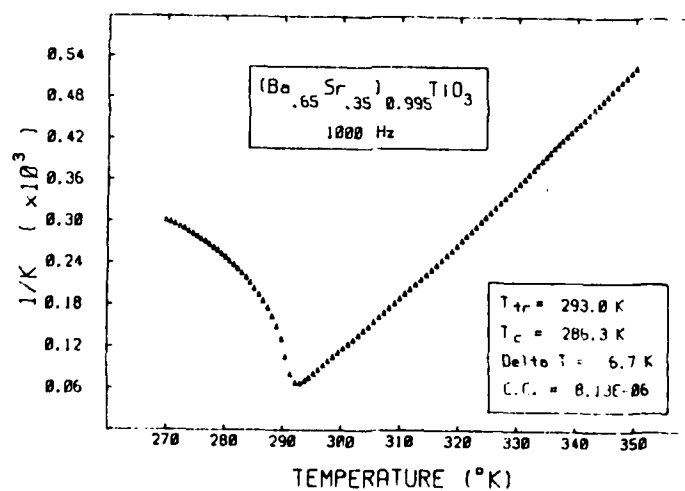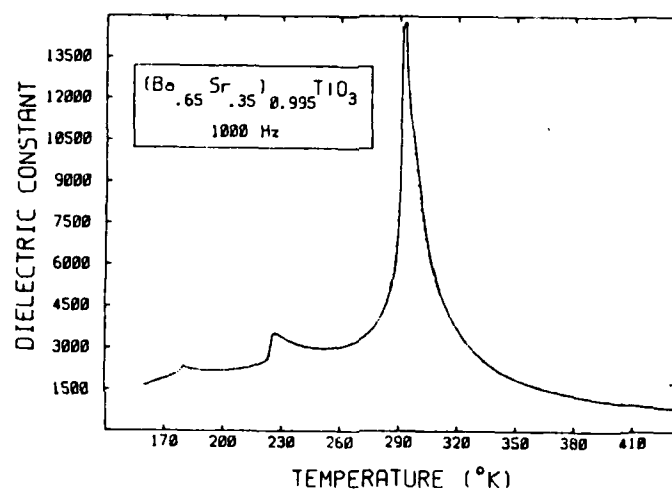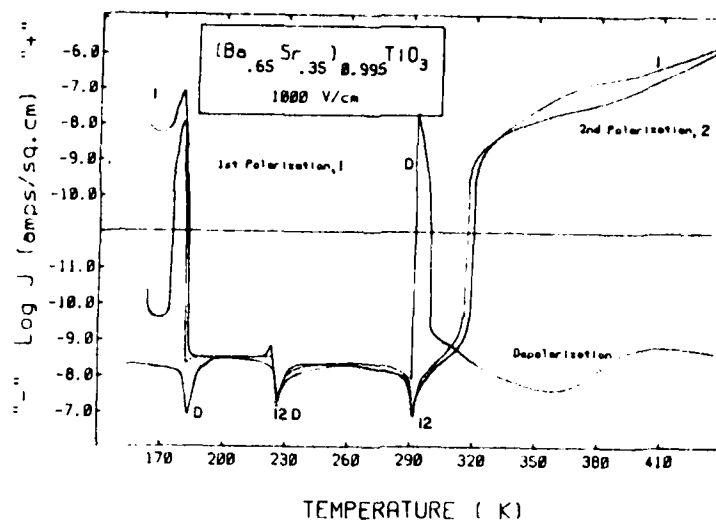
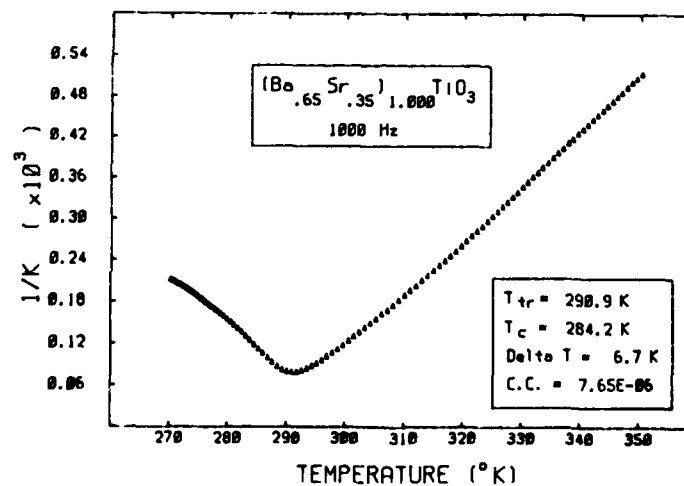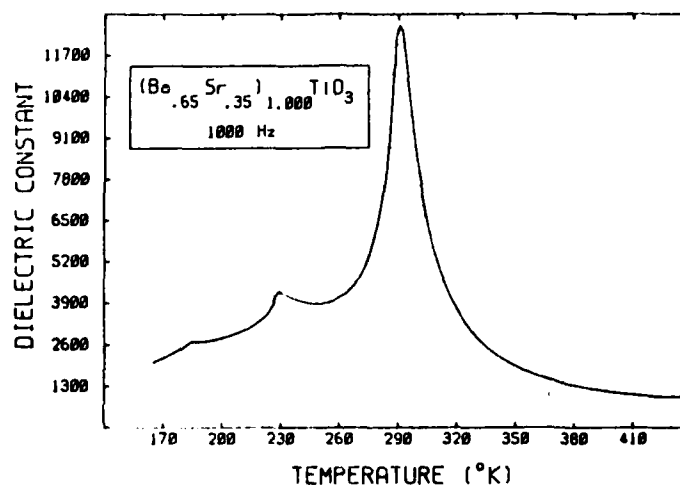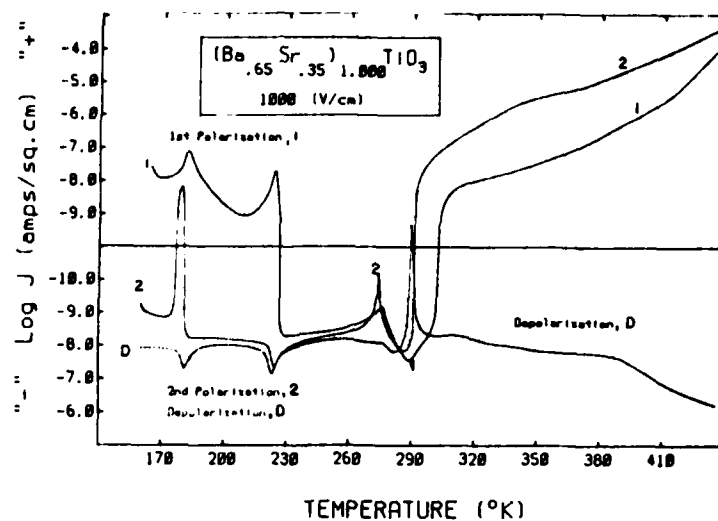Figure 4.3.5g: TSPC/DC, dielectric constant, and Curie-Weiss vs. temperature plots for Sr = 0.35, A:B = .995.

Figure 4.3.5h: TSPC/DC, dielectric constant, and Curie-Weiss vs. temperature plots for Sr = 0.35, A:B = 1.000.

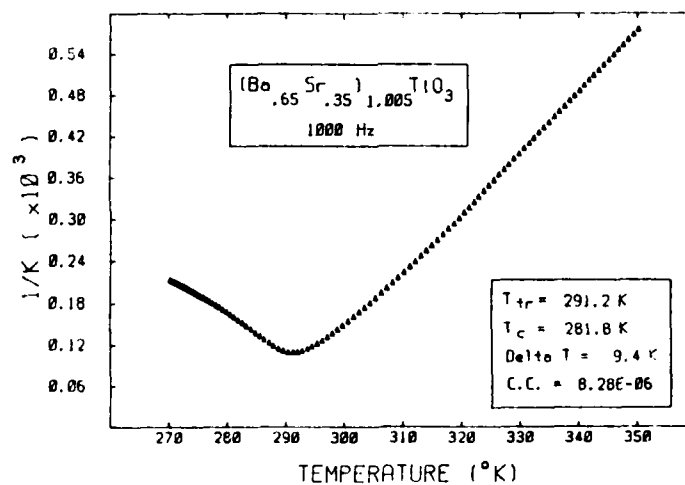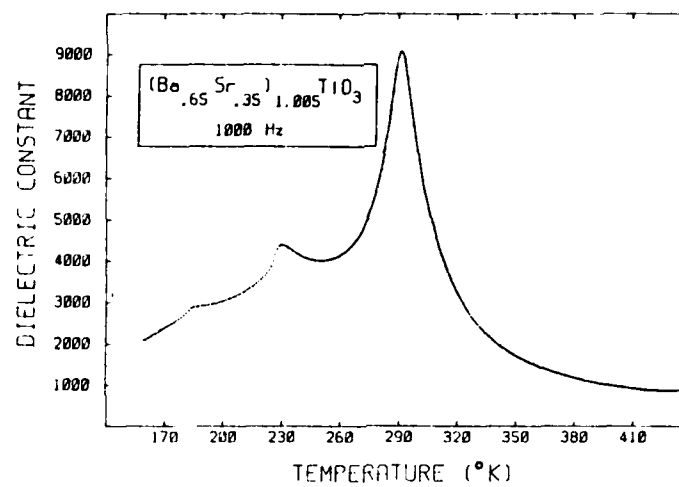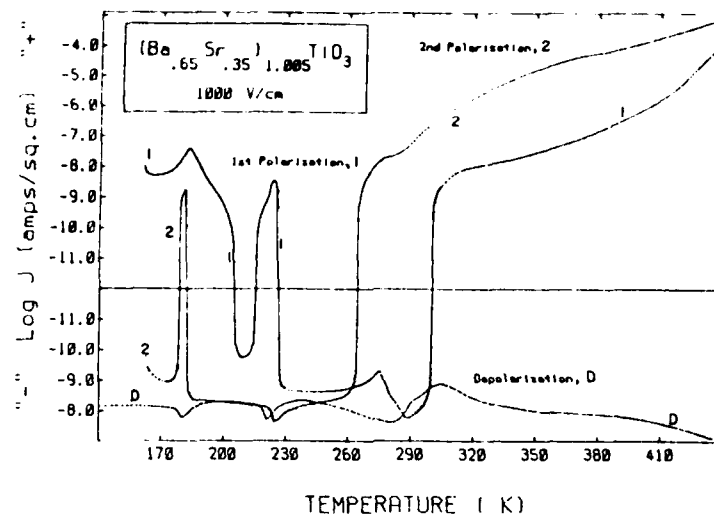**Figure 4.3.51:** TSPC/DC, dielectric constant, and Curie-Weiss vs. temperature plots for Sr = 0.35, A:B = 1.005.

the clues we need to understand why such a high dielectric constant is observed. We think that TSPC/DC measurements combined with dielectric constant and P_S vs. temperature, and $Q_{i,j}$ measurements will allow us to determine the reason. Any conclusions drawn to date must necesarily be tentative ones due to lack of complete experimental work, and insufficient knowledge concerning the interpretation of the TSPC/DC results themselves.

4.4 TSPC/DC Measurements and Their Relationship to Degradation

Low-voltage degradation measurements of commercial capacitors were carried out first in our research program and hence TSPC/DC measurements on "good" and "bad" capacitors were made. It was hoped in the low-voltage program that some of the commercial capacitors would exhibit the classic "short", due to a dendritic growth which can be cleared with application of a voltage high enough to vaporize the metal. These dendrites grow along structural imperfections (i.e. delaminations, cracks, open porosity) which we thought the TSPC/DC apparatus might be able to detect. Unfortunately, no classic shorts have been detected as described in Section 1.

Microstructural analysis showed that the commercial capacitors exhibited very little porosity and a total lack of delaminations. The commercial capacitors are excellent in terms of lack of physical flaws. It appears that in order to prove whether or not TSPC/DC measurements can distinguish between capacitors with or without physical flaws we'll have to manufacture our own "good" and "bad" units. Personnel at PSU are

-223-

currently working on a project to purposely induce porosity and delaminations into multilayer capacitors in a controlled fashion; we hope to participate in this program by life-testing some of the units, and measuring their TSPC/DC behavior. Until this time no definitive conclusions can be drawn concerning whether or not TSPC/DC measurements can detect physical inhomogeneities. Based upon all of our results, it appears TSPC/DC measurements are much more sensitive to material properties, as compared to physical properties.

The only "failures" generated during life-testing were those capacitors (compositionally NPO or BX units)which exhibited a gradual increase in conductivity, in most cases changing 2-3 orders of magnitude. These capacitors still had a room temperature resistance of 10^{6-8} ohms. TSPC/DC measurements on these capacitors showed a distinctive difference after degradation when compared to passed units, but unfortunately none of the capacitors which exhibited this gradual increase were run on the TSPC apparatus before life testing. The following section describes the differences between the spectra of "failed" and "passed" capacitors.

4.4.1 NPO Capacitor "Failure"

Figures 4.4.1a-b represent unencapsulated NPO capacitors from the same lot; the first was subjected to no accelerated life testing while the second "failed" the 85 ^{O}C / 85% R.H. 1.5 VDC life test. The untested unit was later life-tested and passed.
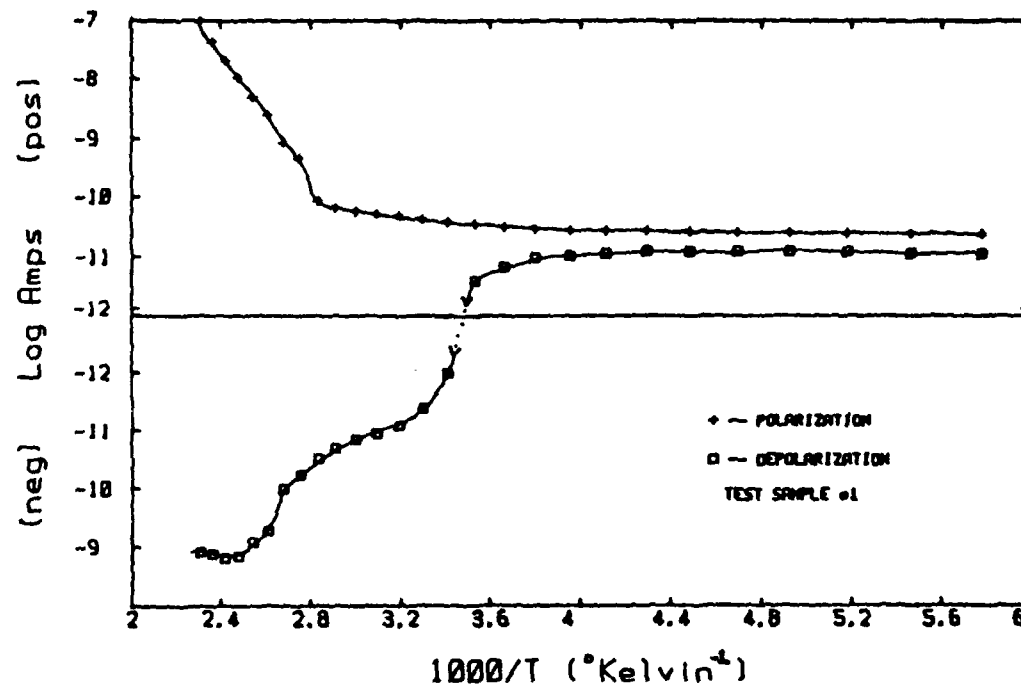
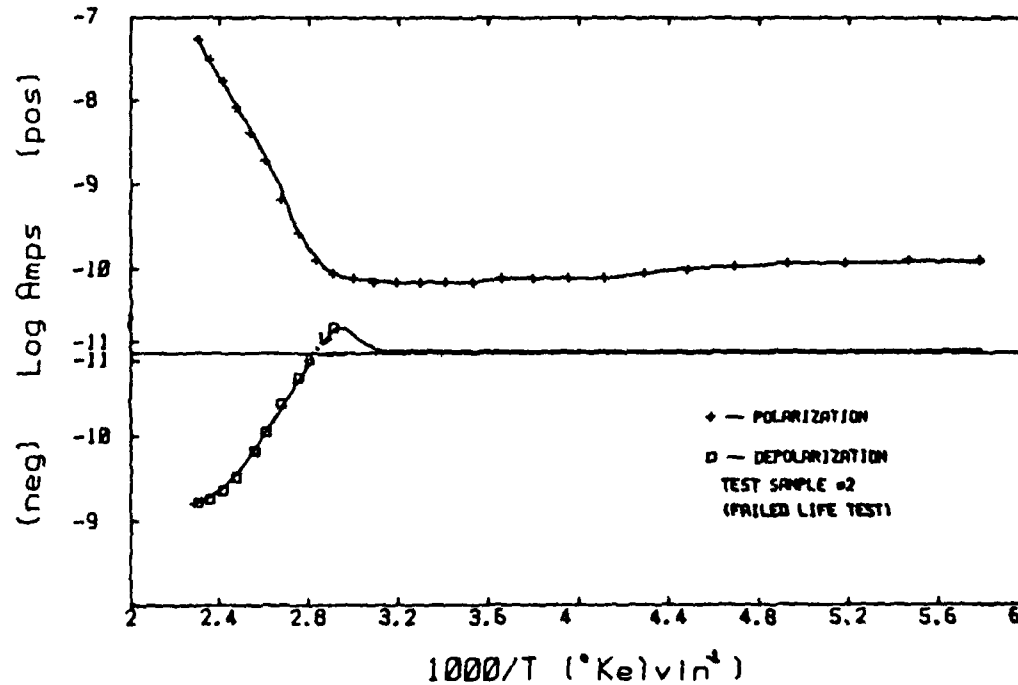Figure 4.4.1a: NPO capacitor which passed the 85/85 life test.

Figure 4.4.1b: NPO capacitor which initially failed the 85/85 life test, then recovered upon heating.

Both exhibit a stable polarization current over the region which they have a constant capacitance, with an increase in current above $\approx$ 85 ^{O}C corresponding to the dominance of the leakage current. Activation energies for the two specimens were the same. The sample which failed exhibited virtually no discharge current until $\approx$ 85 ^{O}C, at which point it again duplicated the behavior of the untested unit. Note the current levels are the same.

Based upon these results it appears the TSPC/DC measurement shows no difference between untested and failed units. However, measurement of the resistance of the "failed" unit showed it had reverted back to $\approx$ 10 ^{13} ohms following the TSPC/DC measurement. This is a strong indicator that water was the culprit in this failure; the TSPC/DC procedure undoubtedly dried the capacitor out during evacuation and heating at 165 ^{O}C. Still then, in this case the TSPC/DC measurement does not appear to distinguish between a good capacitor and one prone to failure.

4.4.2 BX Capacitor Failures

Figures 4.4.2a-e are results of TSPC/DC studies performed on unencapsulated BX capacitors from the same lot which were found to be failure prone during the 85/85 1.5VDC life test. Figure 4.4.2a is of an untested BX capacitor from this lot. Similiar to the BX capacitor described in Section 4.3.2, the TSPC/DC spectrum reflects the compositional nonhomogeneities which result in the flattening and broadening of the tetragonal-cubic transition.

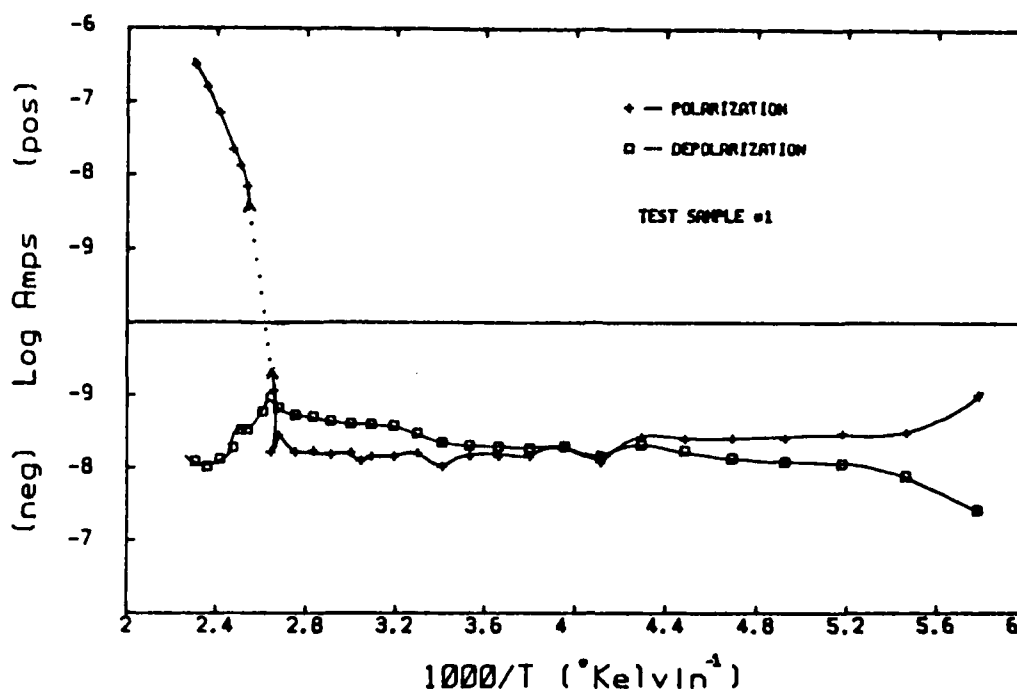Figures 4.4.2b-d exhibit the effects of life testing on the

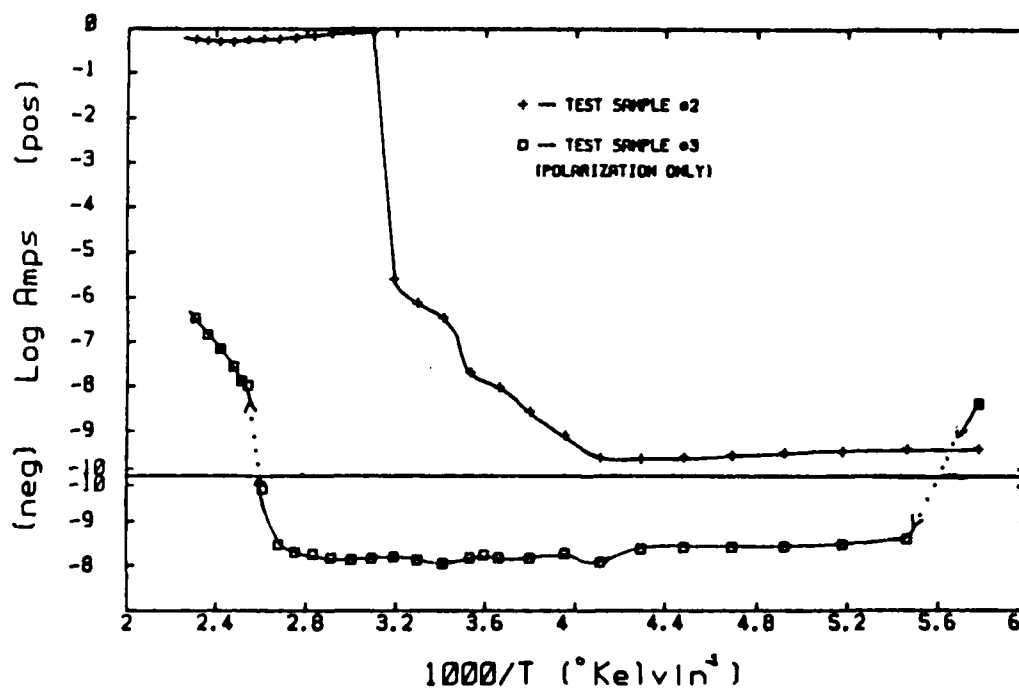**Figure 4.4.2a:** BX capacitor not subjected to the 85/85 test.

Figure 4.4.2b: BX capacitors subjected to accelerated life testing.

current spectra. Figure 4.4.2b shows the results of accelerated life testing. Sample #2 was subjected to 1000 VDC for 17 hours; sample #3 was subjected to 800 VDC for 42 hours. Both specimens passed these life tests, however, their TSPC/DC results differ. Sample #3 exhibits normal behavior, with no appreciable deviation from the untested specimen. Sample #2 was completely different; it exhibited no negative current characteristic of charging. The BX capacitor has become a resistor, losing its capacity to store charge. Note, however, that a leakage current measurement at room temperature would have shown a normal, low value. Increasing the temperature to $\approx$ 60 $^{\circ}$C resulted in a sharp rise in current, with an eventual short; the breakdown voltage of the dielectric was reached.

Figure 4.4.2c shows the results of samples which were life-tested 1000 hours at 85 $^{\circ}$C / 85 % RH, 1.5 VDC; sample #4 failed the life test while sample #5 did not. Again a large difference in the TSPC behavior is seen. Sample #4 is behaving as a typical, nonferroelectric ceramic; the linear increase in current reflects the activation energy.

Figure 4.4.2d shows the results of a BX capacitor which was not life tested but failed during the TSPC run. At $\approx$ -20 $^{\circ}$C the sample abruptly changed resistivity. A second polarization run showed the sample remained in the low resistivity condition. Water could not be the cause of this failure due to the moisture-free environment, nor could it be the result of a dendritic growth; metals increase in resistance with increasing temperature. None of the capacitors which had failed life
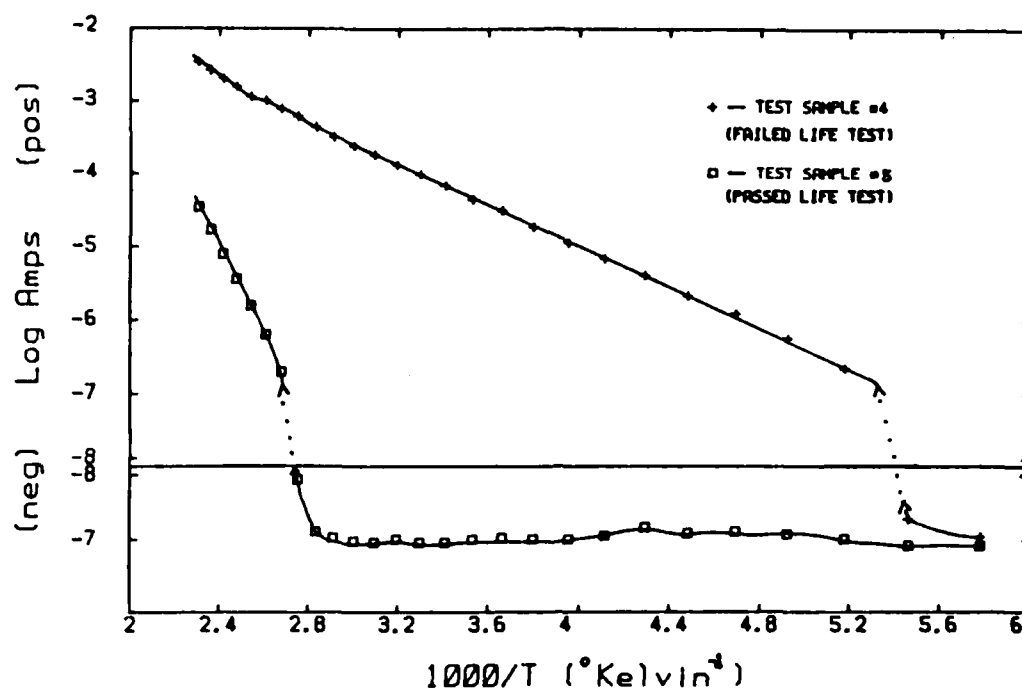
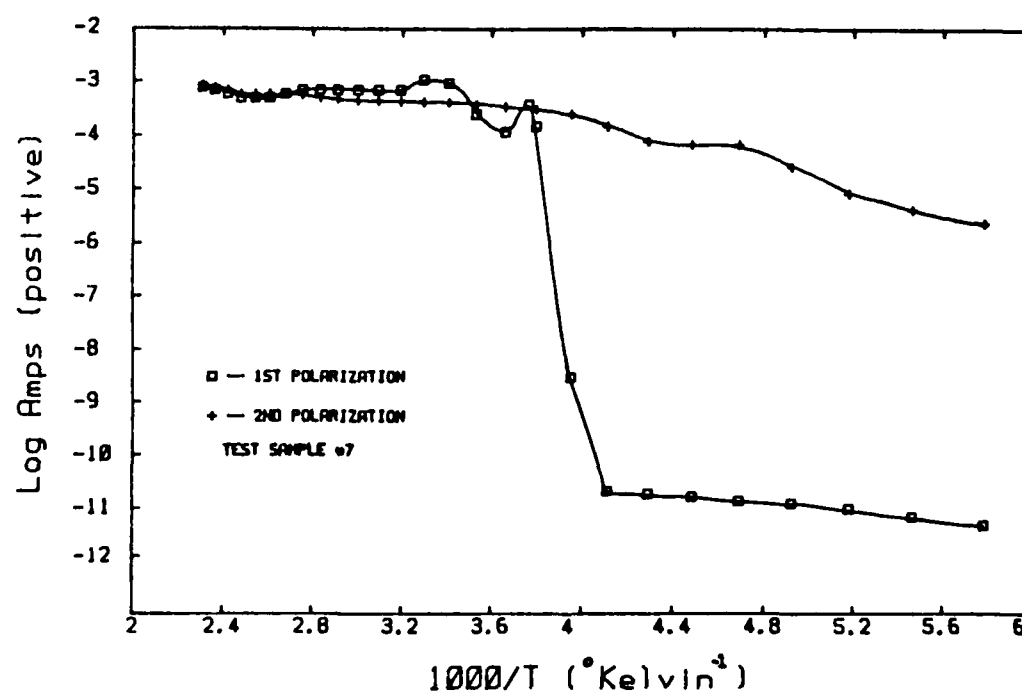Figure 4.4.2c: BX capacitors #4 and #5; #4 failed the 85/85 test while #5 passed.

Figure 4.4.2d: BX capacitor which failed duing the TSPC/DC measurement.

testing exhibited evidence of dendritic growths; the TSPC measurement would show the high leakage current decreasing with increasing temperature if this were the case.

Figure 4.4.2e shows the TSPC spectrum of a BX capacitor which failed methanol testing following thermal shock treatment . Although we could not find the cause of this failure, this specimen did not fail the life test nor show a change in TSPC behavior.

4.4.3 Degradation of BaTiO$_3$

In accordance with the high-voltage testing program we have been measuring the change in TSPC/DC behavior of degraded vs. non-degraded specimens. Figure 4.4.3a is a typical graph of the kind of results we have obtained from these studies, in this case for pure BaTiO$_3$, density = 94.9 % theoretical. From the high voltage studies we know this sample does not degrade at fields 2000 V/cm at 85 ^{O}C, but it does degrade for fields 1000 V/cm at 150 ^{O}C. Correspondingly, the TSPC run at 500 V/cm shows normal behavior, and does not change if run repeatedly, or if the run is halted at a temperature and the current monitored. All are indicative of a lack of degradation.

At 1800 V/cm the specimen shows an increase in leakage current levels which is expected, but Ohm's law would predict only an increase of $\approx$ 1/2 an order of magnitude, not the 1-2 order of magnitude increase observed in both the ferroelectric and paraelectric regions of the TSPC spectrum. Degradation of the specimen is occurring; repeating the TSPC/DC measurement of
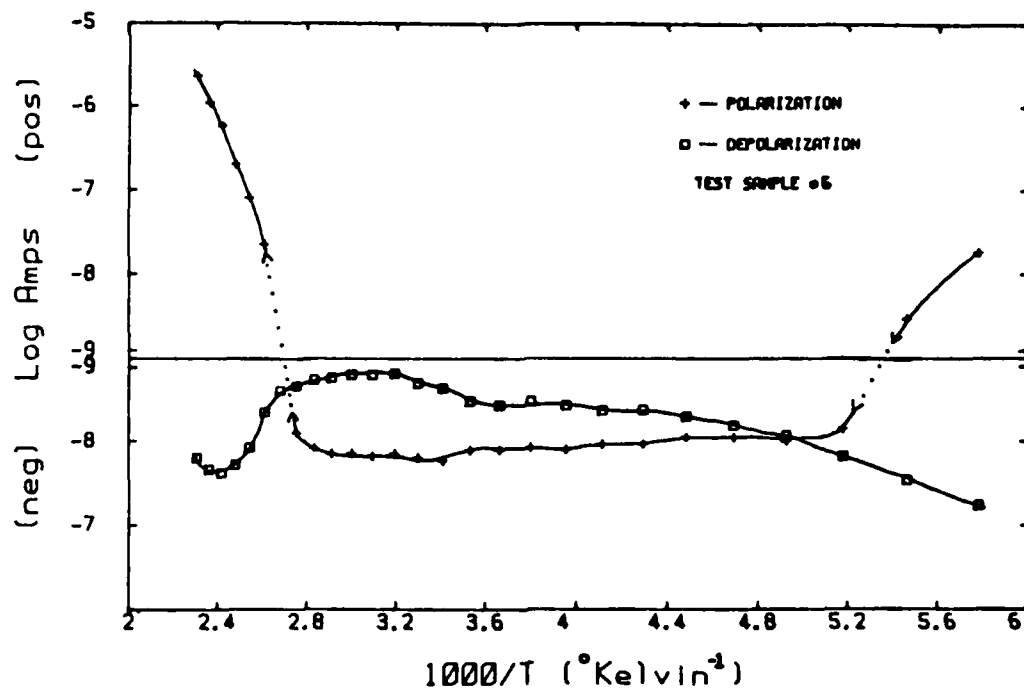
Figurwe 4.4.2e: Bx capacitor which failed the methanol test, _after_ being thermal shocked.
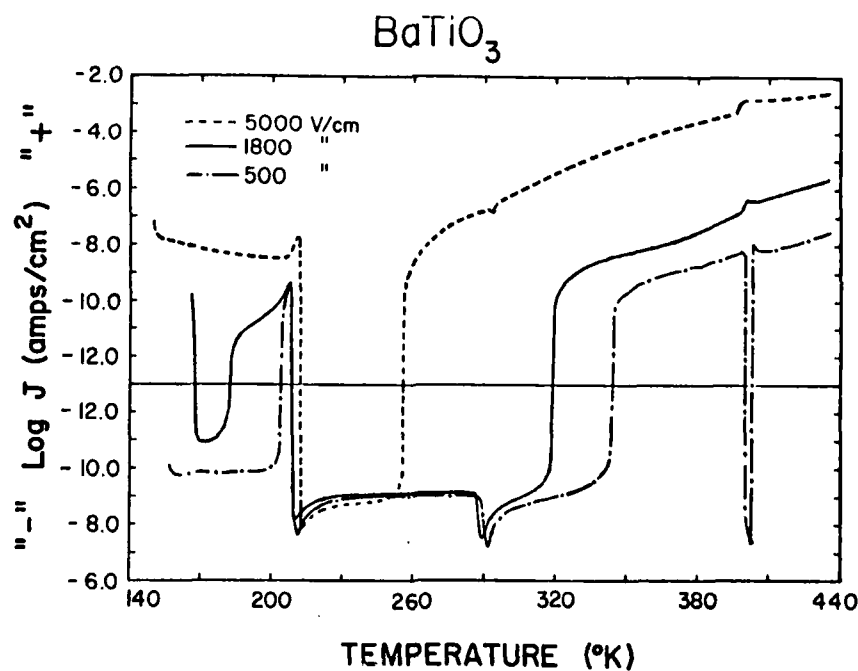

Figure 4.4.3a TSPC behavior of $BaTiO_3$ measured at various fields; degradation is occurring.

this specimen at 1800 V/cm results in ever increasing leakage currents. Note the current peak at the Curie point is eliminated; this could indicate either the high current levels are masking the previously observed behavior, or degradation is resulting in a major change in the crystalline structure or defect chemistry. The $BaTiO_3$ specimen is essentially turning from a capacitor into a resistor.

At 5000 V/cm the spectrum continues to exhibit the effect of degradation occurring; now the orthorhombic-tetragonal peak is disappearing. The transition from negative to positive current is occurring at lower temperatures, indicative of the increasing conductivity as degradation occurs.
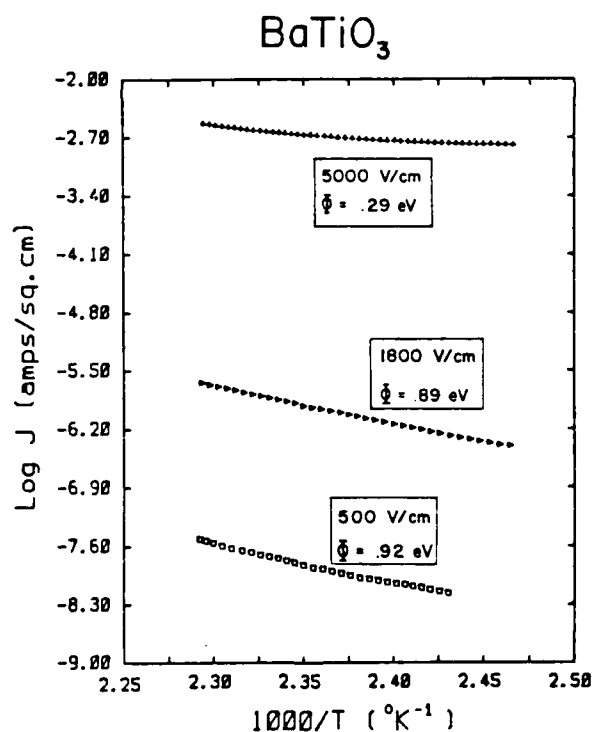
$BaTiO_3$

Figure 4.4.3b: Variation of the activation energy for $BaTiO_3$ in the paraelectric region with field.

-232-

Figure 4.4.3b shows how the activation energy of conduction decreases in the paraelectric region as the field is increased and degradation occurs. This is undoubtedly due to the increase in mobility of the migratory species causing degradation. This agrees with the results we have obtained in our high voltage studies.

These results are representative of all the $BaTiO_3$ compositions which degrade and have been run on the TSPC/DC apparatus. The results of our measurements using TSPC/DC behavior to study degradation phenomena can be summarized as follows:

Summary of TSPC/DC Behavior as it Relates to Degradation

1) TSPC/DC measurements have not been found capable of detecting the structural flaws which lead to low voltage degradation. Therefore it is not a useful technique to predict capacitor reliability.

2) TSPC/DC measurements do exhibit a large difference between those capacitors which failed the life test and those which did not. This is also true for those $BaTiO_3$ compositions which do and do not degrade. Therefore, TSPC/DC measurements are useful tools for studying degradation behavior, but not predicting it.

3) None of the commercial capacitor failures from the low voltage life testing program were due to dendritic growths. The TSPC spectrum would have exhibited decreasing leakage current levels with increasing temperature if this were the

case.

We hope to use TSPC/DC measurements to determine whether or not degradation is destroying the ferroelectric behavior of $BaTiO_3$ in some manner, or if it simply masks it. Remember the disappearance of the characteristic current peaks exhibited during structure changes as degradation occurs. This would be an important finding, as it may confirm or reject our suspicions that the degradation is due to grain boundary phenomena, and not necessarily due to the defect chemistry of the primary phase.

4.5 Activation Energy Determination from TSPC Measurements

Two of the easiest quantities to derive from TSPC measurements are the low temperature resistivity and activation energy of the conduction process. The resistivity at any temperature is found by:

$$\rho = \frac{E}{J} \qquad\qquad (1)$$

where ρ = resistivity (ohm-cm)
       E = applied field (volts/cm)
       J = current density (amps/cm^2)

Note the current necessarily needs to be positive, i.e. leakage current. The activation energy is found by simply plotting Log J (amps/cm^2) vs. Inverse Temperature. The slope of this line is equal to $-\phi/k$, where ϕ is the activation energy of the conduction process, and k the Boltzman constant.

Table 4.5 contains the activation energies determined in the paraelectric region of the undoped $BaTiO_3$ compositions, Ba:Ti = 0.96 to 1.04, and the acceptor and donor-doped $BaTiO_3$'s. In general, compositions with excess Ti have an activation energy less than one, and compositions with excess Ba greater than one. Ba:Ti = 1.002 and 1.02 are exceptions to this general behavior. These numbers agree well with a degradation study carried out by Keck[27], and are useful in terms of analyzing degradation behavior. No attempt will be made here to explain why the activation energy values vary as they do.

Composition	Applied Field (V/cm)	Activation Energy (eV)
$Ba_{.96}TiO_3$	500	.51
$Ba_{.97}TiO_3$	500	.71
$Ba_{.98}TiO_3$	500	.61
$Ba_{.99}TiO_3$	500	.90
$Ba_{.995}TiO_3$	500	.91
$Ba_{.998}TiO_3$	500	.94
$Ba_{1.000}TiO_3$	500	1.09
$Ba_{1.002}TiO_3$	500	.98
$Ba_{1.005}TiO_3$	500	1.10
$Ba_{1.01}TiO_3$	500	1.34
$Ba_{1.02}TiO_3$	500	.76
$Ba_{1.03}TiO_3$	500	1.05
$Ba_{1.04}TiO_3$	500	1.10
$BaTi_{.99}Al_{.01}O_3$	500	1.58
$BaTi_{.95}Al_{.05}O_3$	500	1.06
$BaTi_{.99}Nb_{.01}O_3$	500	.37
$BaTi_{.95}Nb_{.05}O_3$	500	.90

TABLE 4.5: Activation energies of various doped and undoped barium titanates.
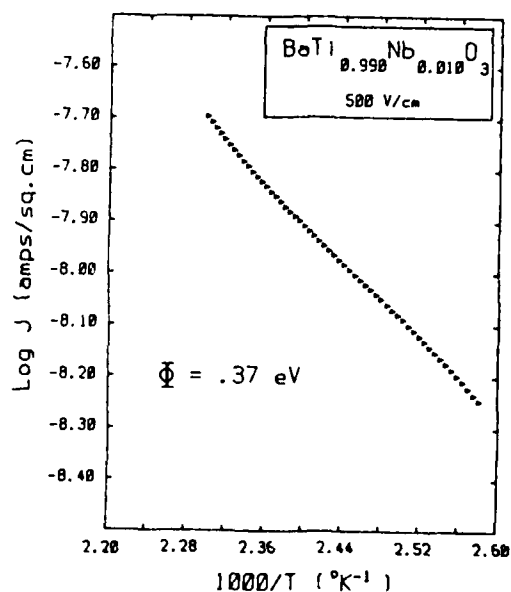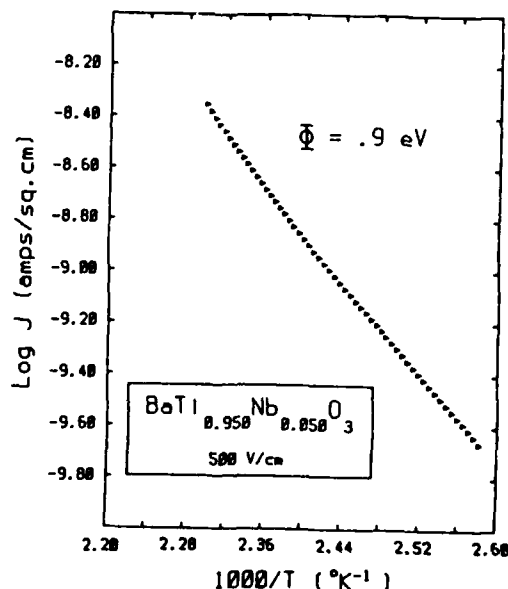
Figure 4.5a   Figure 4.5b

Figures 4.5a and b are activation energy plots for the Nb-doped $BaTiO_3$ compositions, which constitutes donor-doping. Note at the 1 mole % doping level the activation energy is only .37 eV, with a transition to .90 eV with 5 mole % donor additions. This is indicative of the two compensation mechanisms; partially electronic for the 1 % level, and ionic for the 5 % level. The activation energy for the electronically compensated $BaTiO_3$ reflects the depth of the donor level more so than the ionically compensated $BaTiO_3$, whose activation energy is composed more so of a mobility term.

Figures 4.5c and d are activation energy plots for the Al^{+3}-doped $BaTiO_3$, which constitutes acceptor doping. At 1 mole % levels the activation energy is quite high, 1.58 eV, which is
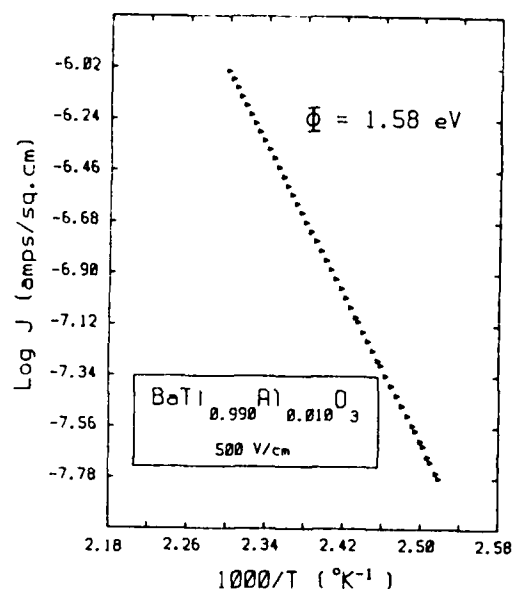
Figure 4.5c
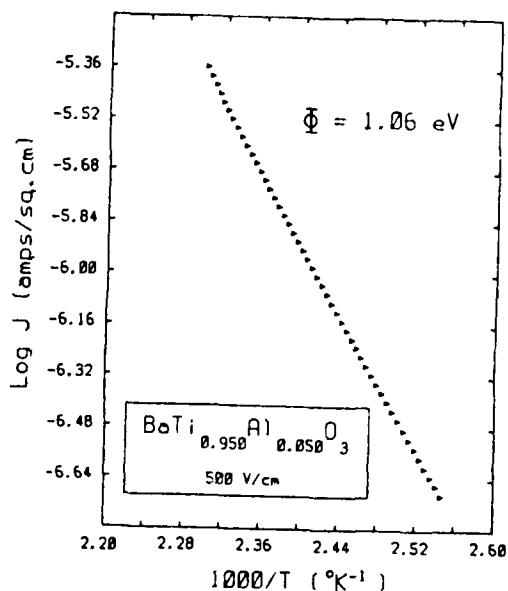
Figure 4.5d

probably indicative of an electronic compensation mechanism; the acceptor centers are acting as electron traps. Increasing the dopant level to 5 mole % decreases the activation energy to 1.06 eV, which is probably indicative of the a transition to the ionic compensation mechanism; i.e. the creation of an $V_o^{..}$ for every two Al^{+3} ions added.

Figure 4.5e is an activation energy plot for $Ba_{.99}TiO_3$ which exhibits an important point. The two lines represent the temperature dependence of the current in the ferroelectric and paraelectric states. Note the activation energy is different; lower in the ferroelectric state compared to the paraelectric state. This may be due to the internal strains and fields in the
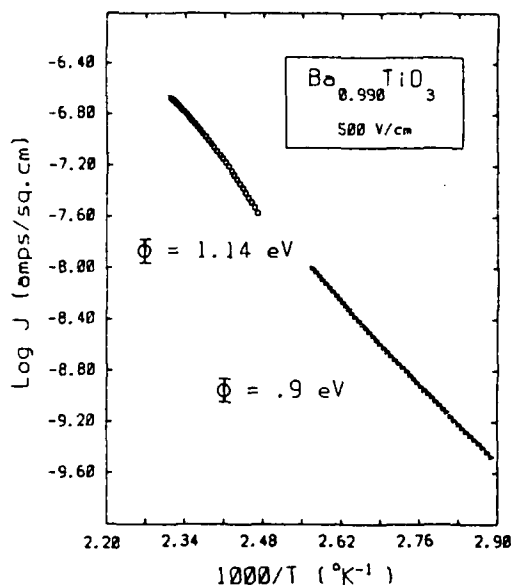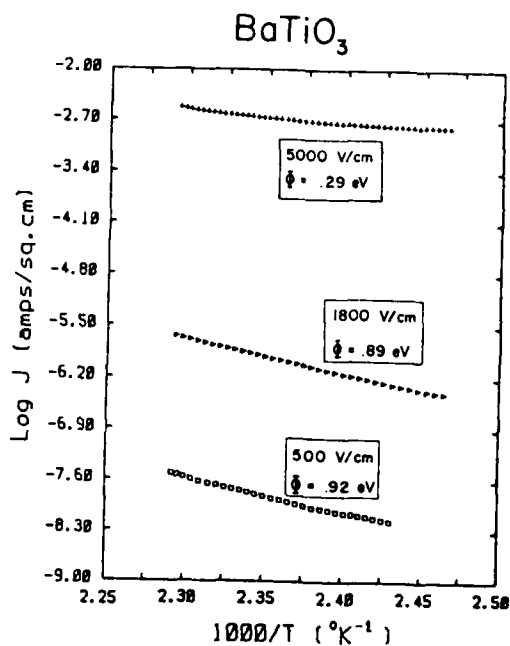
BaTiO$_3$

Figure 4.5e   Figure 4.5f

ferroelectric state somehow altering the mobility of the carrier.

Figure 4.5f is an activation plot for BaTiO$_3$ which illustrates another important point. The activation energy is dependent upon the applied field. This could be indicative of either a field-enhanced mobility, or carrier concentration. Figures 4.5e and f illustrate effectively the importance of defining the conditions under which the activation energy is measured. AC resistivities were not measured, but undoubtedly would yield another value for the activation energy.

This section was included to illustrate the TSPC measurement's ability to yield low temperature activation energies. We have used this technique to measure other ceramic materials such as LaCrO$_3$ and LaMnO$_3$, with excellent results.

-239-

4.6 Summary of Results from the TSPC/DC Measurements

TSPC/DC and capacitance measurements have been carried out on a wide variety of specimens, including single crystals, commercial capacitors, and doped, undoped, and shifted $BaTiO_3$'s. The results from these experiments can be summarized as follows:

1) TSPC/DC measurements are capable of determining:

- the temperature at which phase transitions occur

- the formulation of a commercial capacitor (i.e. NPO, BX, Z5U) and its useful temperature range of constant capacitance

- the order of the tetragonal-cubic phase transition in $BaTiO_3$; i.e. first or second order. This is an indirect measurement of P_S vs. temperature.

- whether or not $BaTiO_3$ is stoichiometric; which is judged through the grain size and its effect on the presence of current peaks

- the effects of donors and acceptors on the ferroelectric behavior, resistivity, and activation energy

- the effects of shifters and depressors on the ferroelectric behavior

- distinguishing between "good" and "bad" capacitors following life testing

- the low temperature resistivity and activation energy

2) TSPC/DC measurements cannot predict the ability of a capacitor to pass life testing.

4.7 Future Studies

In addition to the many things we have already found TSPC/DC measurements useful for, we feel these measurements can also yield a great deal of information concerning domain switching rates, aging phenomena, and ferroelectric theory. The real crux of the matter in studying these phenomena lies in interpreting the TSPC/DC results in terms of the thermodynamic and lattice dynamics theories of ferroelectricity. This will require the completion of a large set of auxiliary experiments. In addition, we wish to expand the TSPC/DC program to include all the variables listed for study earlier in this section. Therefore, our future studies include:

1) Integrating the Sawyer-Tower measurement system into our computerized test setup in order to obtain P_S vs. temperature dependencies, as well as hysteresis effects.

2) Completion of the $Q_{I,J}$ measurements at Penn State University.

3) Studying TSPC/DC behavior as a function of:

   - applied field
   - heating rate
   - grain size and distribution
   - porosity
   - poling field and subsequent aging

4) Preparing a larger set of Zr-shifted $BaTiO_3$'s and measuring their behavior.

5) Obtaining more single crystal specimens and measuring them.

6) Measuring donor and acceptor-doped specimens in which electronic compensation is occurring.

REFERENCES

1. Brennan, T.F., "Ceramic Capacitor Insulation Failure accelerated by Low Voltage", Proc. of the 16TH Annual Reliability Physics Symposium, April 1978.

2. Holladay, A.M.,"Unstable Insulation Resistance in Ceramic Capacitors", Proc. of the Symposium on Capacitor Technology, Applications, and Reliability, NASA Conf. Pub. 2186, 1981.

3. Sato, K. et.al. "A Low-Voltage Screening of Ceramic Capacitors From Leakage Failure", Proc. of the International Symposium for Testing and Failure Analysis, 1981.

4. Sato, K. et.al., "Mechanism of Ceramic Capacitor Leakage Failure Due to Low DC Stress", Proc. of the 18th International Reliability Physics Symposium, 1980.

5. Ropiak, S., "Low Voltage Failure Mechanisms for Ceramic Capacitors", Proceedings, International Society for Testing and Failure Analysis Symposium, Los Angeles, 1982.

6. Murata et.al, "Low-Voltage Failure of Monolithic Ceramic Capacitors and Their Screening Method", Proc. of the International Symposium for Testing and Failure Analysis, 1981.

7. Chittick, R.C., Gray, E., and Alexander, J.H. , "Non-destructive Screening for Low-Voltage Failure in Multilayer Capacitors", Proc. of the 3RD Annual Capacitor and Resistor Technology Symposium, March 1983.

8. Chittick, R.C. and Gray, E., "Improved Moisture Resistance of Multilayer Ceramic Capacitors Encapsulated by On-Line Screening", Proc. of the 4th Annual Capacitor and Resistor Technology Symposium, March 1984.

9. Ewell, G.J. and Demeo, D.A., "Electrical Parameters of Capacitors Failing the $85^{o}C$ / 85% RH / 1.5 VDC Test ", Proc. of the 2nd Annual Capacitor and Resistor Technology Symposium, March 1982.

10. Ewell, G.J. and Demeo, D.A., "Extended Electrical Characteristics of Ceramic Capacitor Failure Under Low-Voltage Conditions", Proc. of the International Symposium for Testing and Failure Analysis, October 1982.

11. Hughes Aircraft Co., " A Study of Unstable Insulation Resistance in Multilayer Ceramic Capacitors", Final Report on NASA Contract NAS8-34364, October 1982.

12. Straessle, R.C. and Ewell, G.J., "The $85^{o}C$-85 % R.H.-1.5 VDC Bias Test: Can Ceramic Capacitors Pass This New Screen ?",

Proc. of the 3rd Annual Capacitor and Resistor Technology Symposium, March 1983.

13. Sahu, Kasum, and Lunchnick, A., "Evaluation of Multilayer Ceramic Capacitors for Low-Voltage Type Failures", Proc. of the 4th Annual Capacitor and Resistor Technology Symposium, March 1984.

14. Bradley, F.N., "Ultrasonic Scanning of Multilayer Ceramic Chip Capacitors", Proc. of the Symposium on Ceramic Technology, Applications, and Reliability, NASA Conf. Pub. 2186, 1981.

15. Vahaviolos, S.J., "In-Process Capacitor Flaw Determination with Acoustic Emission", Phys. Acoust. Corp. Tech. Report TR-19, 1979.

16. Kahn, S.R., and Checkaneck, R.W.,"Acoustic Emission Testing of Multilayer Ceramic Capacitors", IEEE Transactions on Components, Hybridr, and Manufacturing Technology, Vol. CHMT-1, 1978.

17. Vorres, C.L. et.al ,"Re-evaluation of Ceramic Capacitors with the Scanning Laser Acoustic Microscope Following Life Testing", Proc. of the 3rd Annual Capacitor and Resistor Technology Symposium, March 1983.

18. Wei, D.T.Y. , "Identification of Ceramic Capacitor Shorts by Voltage Contrast in The Scanning Electron Microscope", Proc. of the 3rd Annual Capacitor and Resistor Technology Symposium, March 1983.

19. Burton, L.C., private communication.

20. Burton, L.C., "Intrinsic Mechanisms of Multilayer Ceramic Capacitor Failure", Annual Report ONR Contract No. N00014-83-K-0168, April 1984

21. Branwood, A. and Tredgold, R., Proc. Phys. Soc.,76 93 (1960).

22. Gruver, A., et. al. , State of the Art Review on Ferooelectric Ceramic materials, Tech. Report AFML-66-164, Linden Laboratories, Inc., State College, PA. (1966).

23. Lehovic, K., and Shirn, G.J., J. Appl. Phys., 33, 2036 (1962)

24. Glower, C., and Heckman, G., J. Chem. Phys., 41,877 (1964)

25. Payne, D.,"Concerning the Physics of Failure of Barium Titanate Capacitors", Proceedings of the Sixth Annual Reliability Physics Symposium, Los Angeles, CA, (1967)

26. MacChesney, J., et.al., J. Amer. Cer. Soc., 46,197 (1963)

27. Keck, J., "Electrical Degradation of High Purity Barium Titanate", Ph.D. Dissertation, Univ. of Mo - Rolla, 1976

28. Hickmott, T.W., J. Appl. Phys.,51, 4269 (1980)

29. Emtage, P. and Tantraporn, N., Phys. Rev. Letters, 8 267, April 1962

30. Lengyel, G., J. Appl. Phys., 37 807 (1966)

31. Tantraporn, W., and Harris, J.Appl. Phys.,

32. Hacskaylo, M., J. Appl. Phys.,35 2943 (1964)

33. Johansen, I.T., J. Appl. Phys., 37 499 (1966)

34. Fisher, J., and Giaever, I., J. Appl. Phys. 32 172 (1961)

35. Ekrut, H., and Hahn, A., J. Appl. Phys. 51 1686 (1980)

36. Maserjian, J., and Zamani, N., J. Appl. Phys., 53 559 (1982)

37. Matsuoka, M., "Progress in Research and Development of ZnO Varistors", Grain Boundary Phenomena in Electronic Ceramics, Vol. 1, pp. 290-308, The American Ceramic Society (1981).

38. Child, C.D., Phys. Rev., 32 492 (1911)

39. Mott, N.F., and Gurney, R.W., Electronic Processes in Ionic Crystals, Oxford Univ. Press, London 1940.

40. Rose, A., Phys. Rev., 97 15 (1955)

41. Lampert, M., and Mark., P., Current Injection in Solids, Academic Press, New York (1970)

42. O'Reilly, T.J., DeLucia, J., Sol. State Electronics, 18 965 (1975)

43. Rosenthal, A, and Sapar, A., J. Appl. Phys., 45 2787 (1974)

44. Edwards, D.A., and Jones, P.L., Sol. State Electronics,21 1163 (1978)

45. Smith, R. and Rose, A., Phys. Rev., 97 1531 (1955)

46. Branwood, A.,et.al.,Proc. Phys. Soc., 79 1161 (1962)

47. Rhys-Roberts, C. and Tredgold, R., Proc. Phys. Soc.,76 497 (1960)

48. Nespurek, S., and Sworakowski, J., J. Appl. Phys., 51 2098 (1980)

49. Mathur, V. and Dahura, K., Sol. State Electronics, <u>42</u> 61 (1979)

50. Kroger, F.A. and Vink, H.J., <u>Solid State Physics Vol. 3</u>, Edited by F. Seitz and D. Turnbull, Academic Press, New York, 1956, pp. 307-435.

51. Chan, N.H. and Smyth, D.M., J. Amer. Cer. Soc., <u>67</u> 285 (1984)

52. Long, S.A., and Blumenthal, R.N., J. Amer. Cer. Soc., <u>54</u> 515 (1971)

53. Long, S.A. and Blumenthal, R.N., J. Amer. Cer. Soc., <u>54</u> 577 (1971)

54. Chan, N.H. and Smyth, D.M., <u>123</u> 1584 (1976)

55. Eror, N.G. and Smyth, D.M., <u>The Chemistry of Extended Defects in Non-Metallic Solids</u>, Edited by L. Eyring and M. O'Keefe, North Holland, Amsterdam, 1970.

56. Sharma, R.K. et.al., J. Amer. Cer. Soc., <u>64</u> 448 (1981)

57. Chan, N.H., et.al., J. Amer. Cer. Soc., <u>64</u> 556 (1981)

58. Chan, N.H., et.al., J. Amer. Cer. Soc., <u>65</u> 167 (1982)

59. Eror, N.G., and Smyth, D.M., J. Sol. State Chem., <u>24</u> 235 (1978)

60. Bois, G.V. et. al., Inorg. Materials, <u>12</u> 1302 (1976)

61. Graham, H.C., and Tallan, N.M., J. Amer. Cer. Soc., <u>54</u> 548 (1971)

62. Anderson, H.U. and Sorrell, C.A., "Development and Characterization of High Temperature Electrically Conducting Oxides", Progress Report DOE/ER/10598-3, October 1982.

63. Negal, R. et. al., J. Sol. State Chem., <u>9</u> 297 (1974)

64. O'Bryan, H.M. and Thompson, J., J. Amer. Cer. Soc., <u>57</u> 522 (1974)

65. Rase, D.E., and Roy, R., J. Amer. Cer. Soc., <u>38</u> 102 (1955)

66. Kulcsar, F., J. Amer. Cer. Soc., <u>39</u> 13 (1956)

67. Smyth, D.M., J. Sol. State Chem., <u>16</u> 73 (1976)

68. Smyth, D.M., J. Sol. State Chem., <u>20</u> 359 (1977)

69. Anderson, H.U. private communication.

70. Ruddleson, S.N., and Popper, P., Acta. Crystallog.,11 54 (1958)

71. Gallagher, P., et.al., J. Amer. Cer. Soc., 46 359 (1963)

72. Subbaro, E., and Shirane, G.J., J. Amer. Cer. Soc., 42 279 (1959)

73. Jonker, G., Sol. State Elec., 7 895 (1964)

74. Bratschun, W., J. Amer. Cer. Soc., 45 611 (1962)

75. Miller, C.A., J. Matl. Science, 3 436 (1968)

76. Anderson, H.U., J. Amer. Cer. Soc., 48 118 (1965)

77. Hyatt, E.P. et.al., Cer. Bull., 46 732 (1967)

78. Kulcsar, F., J. Amer. Cer. Soc., 39 13 (1956)

79. Anderson, H.U., and Payne, D.H., J. Amer. Cer. Soc., 50 491 (1967)

80. Huebner, W., et. al., "Electrical Degradation of High Purity $BaTiO_3$", Proc. 4th Annual Capacitor and Resistor Symposium, 1984.

81. Smyth, D.M. et. al., 1984 Amer. Cer. Soc. National Convention, Pittsburgh, PA.

82. Devonshire, A.F., Phil. Mag.,40 1040 (1949)

83. Cochran, W., Advan. Phys., 9 987 (1960)

84. Hong, C. and Day, D.E., J. of Matl's Science, 14 2493 (1979)

85. Fatuzzo, E. and Merz, W.J., Ferroelectricity, North Holland Pub. Co., Amsterdam, 1967.

86. Chen, R., J. Matl's Science, 11 1521 (1976)

87. Shindo, K., Mem. Shiga Univ., 27 1 (1978)

88. Hong, C. and Day, D.E., J. Amer. Cer. Soc., 64 61 (1981)

89. Agarwal, A. and Day, D.E., J. Amer. Cer. Soc., 65 231 (1982)

90. Bucci, C. and Fieschi, R., Phys. Rev., 148 816 (1966)

91. McKeever, and Hughes, D.M., J. of Phys. D; Appl. Phys., 8 1520 (1975)

92. Hino, T., "Thermally Stimulated Characteristics in Solid Dielectrics", <u>IEEE Transactions on Electrical Insulation</u>. EI-15, 1980, pp. 301-311.

93. Morin, F.J., and Oliver, "Energy Levels of Iron and Aluminum in Strontium Titanate", <u>Physical Review B</u>, 8, #12, 1973, pp.5847-5854

94. Siegwarth, J.D. and Morrow, A.J., J. Appl. Phys.,<u>47</u> 4784 (1976)

95. Lebevda, N.N., et.al., Sov. Phys., Sol. State, <u>19</u> 2152 (1977)

END

FILMED

2-85

DTIC